Structural characterization of chiral molecules using vibrational circular dichroism spectroscopy

Lassen, Peter Rygaard

Publication date:
2006

Document Version
Publisher's PDF, also known as Version of record

Peter Rygaard Lassen

Structural Characterization of Chiral Molecules Using Vibrational Circular Dichroism Spectroscopy

Ph.D. Thesis, July 2006

Quantum Protein Centre
Department of Physics
Technical University of Denmark
DK-2800 Lyngby, Denmark

Supervisors:

Professor Henrik Bohr[a]
Associate Professor Lars Hemmingsen[a,b]
Associate Professor Per-Ola Norrby[c]

[a]*Quantum Protein Centre, Department of Physics, Technical University of Denmark*
[b]*Department of Natural Sciences, The Royal Veterinary and Agricultural University*
[c]*Department of Chemistry, Technical University of Denmark*

Typeset in LaTeX 2ε
Printed in Denmark by Vester Kopi, DTU, Lyngby
Available online at http://hjem.get2net.dk/c971779/phd.pdf

Revised version

"Saglighed er godt nok, men lidt salighed er ikke at foragte."
-Klaus Rifbjerg

Cover illustration: Four of the molecular structures investigated during this project: Ginkgolide B, nyasol, curcuphenol dimer, and a rhenium(V) complex.

Preface

This thesis is submitted as part of the requirements for obtaining the Ph.D. degree from the Technical University of Denmark (DTU). The work presented here has been carried out from August 2003 to July 2006 at the Department of Physics, DTU, under supervision of Prof. Henrik Bohr and Assoc. Prof. Lars Hemmingsen (now Department of Natural Sciences, The Royal Veterinary and Agricultural University), as well as Assoc. Prof. Per-Ola Norrby, Department of Chemistry, DTU. A Ph.D. grant from DTU has sponsored the project. Some of this work has been published, and these papers are included as appendices, along with two preliminary manuscripts.

Part of this work was carried out at the Department of Chemistry at Syracuse University, Syracuse, New York, where I had the opportunity to spend two semesters (fall of 2004 and spring 2005) in the world's leading FT-VCD group, supervised by Professors Laurence A. Nafie and Teresa B. Freedman.

Outline of the Thesis

Chapter 1 introduces the fundamental concept of chirality and some research areas where it is significant. Chapter 2 reviews the theoretical and experimental methods used in this project. Chapter 3 describes some studies of small or medium-sized organic molecules, followed by larger metal complexes and myoglobin in Chapter 4. The appendices include a list of abbreviations and some Unix scripts written during the project. An English and Danish abstract is also given. Finally, a number of papers and manuscripts are attached.

Acknowledgments

I would like to thank my supervisors: Henrik Bohr for his enthusiasm, encouragement and entertainment; Lars Hemmingsen for his clear-sightedness, overview and useful suggestions; Per-Ola Norrby for his chemical intuition and for classes on computational chemistry and spectroscopic methods.

During my time at DTU, I have enjoyed sharing my office with two postdocs, Peter W. Thulstrup and later Niels H. Andersen. I thank them for their company, co-operation and discussions we had. I also appreciate Tobias M. Johansen for taking care of the computer cluster, Assoc. Prof. Karl J. Jalkanen for introducing me to VCD, and Assoc. Prof. Salim Abdali for providing the contact with Syracuse University.

Special thanks go to Professors Larry Nafie, Tess Freedman and Dr. Xiaolin Cao at Syracuse University (SU) for having me in their lab, where I also enjoyed the opportunity to work with two nice Ph.D. students, Yanan He and Rosina Lombardi. Dr. Tim Korter is acknowledged for instrument time on his FT-IR spectrometer.

When project supervisor Lars Hemmingsen moved to The Royal Veterinary and Agricultural University during my stay abroad, a desk was provided for me by the Bioinorganic group at the Department of Natural Sciences. I thank all of them for their hospitality and for sharing their expertise during my frequent visits.

Finally, I wish to thank all the other co-workers, fellow students and friends both in Denmark and Syracuse, whose company I have enjoyed during my Ph.D. work.

Kgs. Lyngby, July 2006 *Peter Rygaard Lassen*

Contents

List of Figures

Chapter 1

Introduction

1.1 Chirality

At the beginning of this thesis we need to define a central term which the project revolves around as it progresses. *Chirality* means 'handedness' and is a phenomenon of great importance in biology and chemistry. Just like our left and right hands are non-superimposable mirror images of one another, so can chiral molecules exist in pairs called *enantiomers*. The phenomenon of chirality cannot occur for objects with less than three dimensions. If there are several chiral features, and some (not all) of them are inverted, one has a *diastereomer*. Both diastereomers and enantiomers are *stereoisomers*. The *absolute configuration* of a molecule is a complete specification of its chiral features.

An even mixture of opposite enantiomers is called *racemic* or a *racemate*. If the mixture contains a surplus of one enantiomer, the term *enantiomeric excess* (abbreviated *ee*) is used to quantify the composition. An *ee* of 100 % means a pure enantiomer, whereas 0 % *ee* is the racemate.

Before defining the different types of chirality, we recommend a review about the science of chiral molecules in the past century [107].

1.1.1 Forms of Chirality

All the amino acids and sugars occuring in living organisms display a form of chirality called *central chirality*, *i.e.*, one or more carbon atoms with four different groups attached. Histidine is shown as an example in Figure 1.1. Each such tetrahedral carbon (or other chiral centre) can be characterized by a letter (*R*) or (*S*) based on the so-called Cahn-Ingold-Prelog rules.

Another form of chirality is *axial chirality*. It arises when four groups sit in a non-planar arrangement about a *chiral axis*. One example is aromatic rings connected via a single bond. Depending on the twist around the axis defined by that bond, such an arrangement can be classified as (*P*) or (*M*). If such a distinction is to have any value, there must be steric hindrance preventing the groups from rotating between the two orientations. This will make them a kind of stereoisomers called *atropisomers* from the Greek words for *not* and *turn*. See

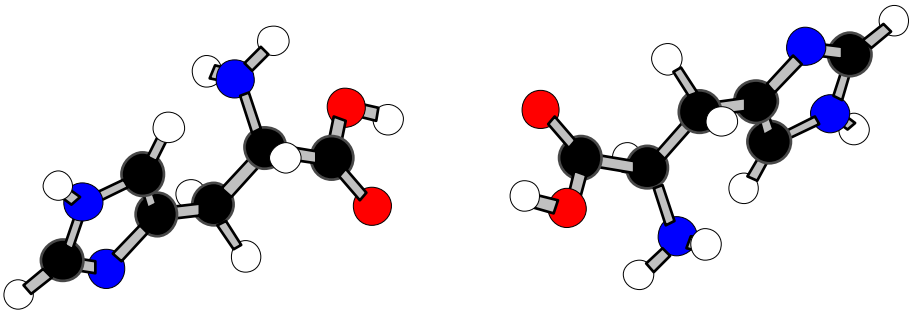

Figure 1.1: The two enantiomers of histidine, a common amino acid. (*S*)-histidine is shown to the left and (*R*)-histidine to the right.

Figure 3.14 on page 41 for an example structure.

Finally, there is *helical chirality*. A helix, propeller or screw can be twisted left (minus, *M*) or right (plus, *P*) around its axis. Famous examples are the double-stranded DNA structure and the α-helical secondary structure element found in most proteins. Obviously, helical chirality is of a more macroscopic nature.

1.1.2 Symmetry Breaking

There are several fundamental asymmetries in Nature which one would not expect on purely statistical grounds. As mentioned above, some of the most abundant molecules in living organisms (amino acids and sugars) are chiral. If these molecules were synthesized by random processes from achiral starting materials, we would find equal amounts of each enantiomer. But in living organisms there is (almost) perfect enantiomeric purity, such that only left-handed amino acids[1] and right-handed sugars occur.[2]

Another mystery is the helical structure of DNA, which always has a right-handed twist. Of course, once we have a functioning living organism, we would expect it to pass its symmetry breaks on to future generations. But how these symmetry breaks first came about poses a problem to those who believe that life originated by chance. Many explanations have been invoked [70], among them the weak nuclear force, which has turned out to be chiral [71,99].

The example from Nature is a case of *parity violation*. Within quantum mechanics, *parity* is the property of a wave function that it is unchanged or at most negated by an inversion of all spatial coordinates. It is also called space inversion symmetry. If a wave function does not obey this rule, it is referred to as parity violation. Such a fundamental asymmetry occurs at the sub-atomic level, more specifically it has turned out that the weak nuclear force violates the parity principle. One way this has been observed is in the β-decay of nuclei.

[1] One of the 20 common amino acids, glycine, is achiral.

[2] Some bacteria produce proteins that break this rule, such as the antiviral protein gramicidin which has interchangeably left- and right-handed amino acids [125].

We will not go into details with this, but mention it here because the weak nuclear force is expected to break the symmetry of some molecular vibrations, as we will touch upon later in Section 4.2. Interested readers are referred to a review [14].

1.2 Outline of VCD Development

It may be appropriate at this point to define the term chiroptical:

> A term referring to the optical techniques (using refraction, absorption or emission of anisotropic radiation) for investigating chiral substances [*e.g.* measurements of optical rotation at a fixed wavelength, optical rotatory dispersion (ORD), circular dichroism (CD), and circular polarization of luminescence (CPL)].[3]

The simplest and oldest form of chiroptical spectroscopy is *optical rotation*, which simply measures the (mole specific) angle of rotation of incident linearly polarized light on a sample. The information content of such a measurement is rather limited, though. By making this measurement in a range of wavelengths, one gets *optical rotatory dispersion*.

Experimentally, *circular dichroism* (CD) is defined as the difference in absorbance of left and right circularly polarized (LCP and RCP) light. As one can imagine, these two polarization states will be absorbed differently by opposite chiral features—almost like our left and right hands fit differently into opposite gloves. ECD or *electronic circular dichroism* is the original form of CD[4], which probes electronic transitions using visible or ultraviolet light [75]. By using the term *vibrational circular dichroism*, one specifies that vibrational transitions are studied, in which case one gets the advantage of many more bands. These bands resonate with infrared (IR) radiation. However, VCD signals appear only as small variations on top of an ordinary (unpolarized) IR absorption spectrum. The difference is 3–4 orders of magnitude, placing high demands on the measuring apparatus.

The VCD spectroscopic technique has been gradually refined over the past three decades since its discovery [55, 80], and there are several recent reviews on the topic [28,38,63,85,110]. Today, VCD is a well-established technique, but not very wide-spread, even though spectrometers are commercially available from several companies: BioTools (Wauconda, IL), Bruker Optics (Billerica, MA), Jasco (Easton, MD), and Thermo Electron (Madison, WI).

The applicability of VCD has greatly increased with the development of software capable of calculating VCD spectra from first principles, because that allows for direct comparison of experimental and calculated VCD signals. This means that the absolute configuration of a sample molecule can be unambiguously determined. Relevant software packages are Gaussian (Gaussian, Inc.

[3] IUPAC Compendium of Chemical Terminology, 2nd Edition (1997)

[4] In the literature, sometimes CD is understood as electronic CD. But in this thesis, CD is used as a common term for ECD and VCD.

Wallingford, CT), The Cambridge Analytic Derivatives Package (CADPAC)[5], and Dalton[6]. Compared to VCD, ECD has the advantage of stronger signals, but on the other hand calculations are more troublesome.

Another, rather complex technique is *Raman optical activity* (ROA), which considers four types of Raman scattering of circularly polarized light [7,76]. It was discovered about the same time as VCD, but the development of both instrumentation and *ab initio* software has been slower, and only recently has a commercial instrument appeared from BioTools (Wauconda, IL).

In Chapter 2, we introduce the theory and instrumentation of VCD in the context of optical spectroscopy of chiral molecules. Additionally, the theoretical methods used are outlined.

1.3 Applications of VCD in Drug Development

Central to the development of new drugs is their 3-dimensional structure, since this will determine their interactions with, *e.g.*, membrane-bound receptors in our cells. Therefore, it is important to characterize new candidate drug molecules in terms of prevalent conformers and absolute configuration. These compounds are often relatively small and chiral, which makes them very suitable for vibrational circular dichroism studies combining the experimental and theoretical approaches [28,38,69]. There are other methods used for absolute configuration determination—primarily X-ray crystallography, which requires crystallization of the compound—but VCD is a good alternative, because it can be used for samples in solution and amorphous states [38,105]. For very simple molecules, optical rotation can be used.

Another useful application of VCD is the determination of enantiomeric excess or *ee*. If one has a reference VCD spectrum of a sample with a known, high *ee*, then the *ee* of an unknown mixture of the enantiomers can be determined from simple interpolation of the VCD spectra.

A number of small to medium-sized organic molecules have been examined with theoretical and experimental VCD during this project, and these studies are presented in Chapter 3 as well as in Papers 1–4.

1.4 Bioinorganic Chemistry in Nature

At first glance, the term bioinorganic sounds like an oxymoron: What does inorganic matter have to do with biology? However, "inorganic" should not be understood here as though nothing organic is involved. Rather, it means that there are elements such as transition metal ions embedded in organic compounds. Bioinorganic chemistry is highly relevant to biological processes such as metabolism and gene regulation [11]. Metal centres enable metalloenzymes

[5] www-theor.ch.cam.ac.uk/software/cadpac.html
[6] www.kjemi.uio.no/software/dalton/

to perform their catalytic processes at such high rates that we are only beginning to pick up the trick. Apparently the combination of the bulk protein and the electronic properties of metal ions provides ideal active sites that are both (stereo)specific and fast. The production of the natural products considered in Chapter 3 very likely involve several such catalytic steps, although little is known about these processes [112, 115].

As an example, some of the methyl-substituted phenyloxirane samples in Section 3.2 were actually synthesized using a chiral manganese complex as enantioselective catalyst, see Figure 1.2 [43, 124].

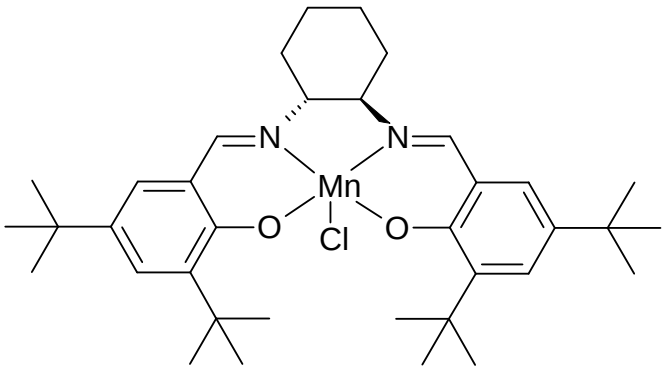

Figure 1.2: The Mn(salen) catalyst (known as "Jacobsen's catalyst") used by Peter Fristrup for synthesis of methyl-substituted phenyloxiranes. Hydrogens are omitted.

Metalloproteins provide good study cases when trying to elucidate the functioning of large biomolecules, because various spectroscopic techniques can probe the metal ion and hence the active site directly. VCD spectroscopy has entered the league of methods used for resolving the structure of chiral metal sites, although the sample preparation can be more tricky than for the smaller molecules considered in Chapter 3.

In order to understand how metal ions contribute to biological systems, we need to consider their electron orbitals. But a molecule the size of a protein is still too large to analyze in detail with quantum mechanical methods. Hence, we have to turn to more limited systems, which hopefully retain most of the structural and electronic properties. It would of course be wonderful if we could synthesize smaller metal complexes capable of competing with real metalloenzymes in terms of catalytic efficiency. But that may not be possible, since the apoprotein apparently plays a role too in terms of providing a specific binding pocket or suitable environment for the specific task of that protein [16].

Chapter 4 contains our studies of bioinorganic systems in the form of transition metal complexes or metalloproteins. Figure 1.3 indicates which transition metals are present in the compounds studied. The size of these complexes border on what can be analyzed theoretically with present computers. Hence, the protein experiments are only compared to calculations of smaller model systems.

1 H																	2 He
3 Li	4 Be											5 B	6 C	7 N	8 O	9 F	10 Ne
11 Na	12 Mg											13 Al	14 Si	15 P	16 S	17 Cl	18 Ar
19 K	20 Ca	21 Sc	22 Ti	23 V	24 Cr	25 Mn	26 **Fe**	27 **Co**	28 **Ni**	29 Cu	30 **Zn**	31 Ga	32 Ge	33 As	34 Se	35 Br	36 Kr
37 Rb	38 Sr	39 Y	40 Zr	41 Nb	42 Mo	43 Tc	44 Ru	45 Rh	46 Pd	47 Ag	48 Cd	49 In	50 Sn	51 Sb	52 Te	53 I	54 Xe
55 Cs	56 Ba	57 La	72 Hf	73 Ta	74 W	75 **Re**	76 Os	77 Ir	78 Pt	79 Au	80 Hg	81 Tl	82 Pb	83 Bi	84 Po	85 At	86 Rn

Figure 1.3: Part of the periodic table of the elements, with the transition metals considered in this project highlighted.

Chapter 2

Methods

2.1 Theoretical Methods

2.1.1 Molecular Mechanics

This approach to modelling molecules is classical in origin: It considers the atoms as hard spheres with springs between them [44]. One can then evaluate the forces between atoms based on the bond lengths, valence angles and torsional angles. Figure 2.1 illustrates these bonding interactions that need to be parameterized. The force constants for these springs can be determined empirically from vibrational spectra or by a more advanced modelling approach. The simplest possible description of the springs comes from the well-known Hooke's law (or sine functions in the case of dihedral angles). It is also necessary to consider non-bonding interactions like van der Waals or electrostatic forces, which are often only considered for atoms within an appropriate cutoff-distance. The entire set of parameters is called a *force field*, which can include some or all atoms to different levels of sophistication. Some force fields are targeting metal complexes, which are more tricky than purely organic compounds [87].

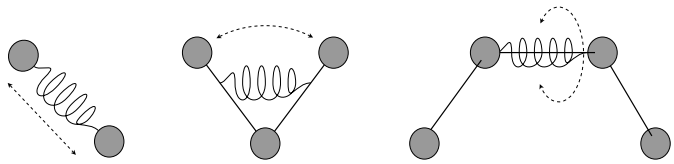

Figure 2.1: The classical picture of molecular mechanics, showing an interatomic bond stretch (left), valence angle bending (middle) and torsional bending (right).

Among the force fields applied during this project is the Merck molecular force field (MMFF) [46], which gives reliable results compatible with higher-level calculations [47].

Two different computer programs have been used for our molecular mechanics (MM) investigations: MacroModel (Schrödinger, Portland, OR) [73] and HyperChem (Hypercube, Inc., Gainesville, FL). The latter was used to

generate the images of molecular structures in this thesis, but unfortunately it does not indicate bond orders.

MM allows for a simple and fast determination of molecular structure. Since electrons are not treated explicitly, MM cannot be used to calculate the spectroscopic properties of interest here. We have only used the technique as a starting point in optimizing the geometry of theoretical molecular structures, and therefore we will not discuss it in further detail. Instead, we will turn to the more advanced methods.

2.1.2 Quantum Mechanics

Here, we briefly introduce some fundamental concepts, which are described more thoroughly in various textbooks [35, 65]. In principle, quantum mechanics (QM) allows for an exact solution to the problem of how electrons and nuclei behave in the electrostatic potential created by their spatial arrangement. In terms of the *Hamiltonian* or energy operator $\hat{H}$, the time-independent Schrödinger equation below gives the wave function Ψ and energy E of a system of n electrons and N nuclei as a function of their coordinates $\vec{r}_i$ and $\vec{R}_I$, respectively, as

$$\hat{H}\Psi(\vec{r}_1, \vec{r}_2, \ldots, \vec{r}_n, \vec{R}_1, \vec{R}_2, \ldots, \vec{R}_N) = E\Psi(\vec{r}_1, \vec{r}_2, \ldots, \vec{r}_n, \vec{R}_1, \vec{R}_2, \ldots, \vec{R}_N), \tag{2.1}$$

$$\hat{H} = -\frac{1}{2}\sum_i \nabla_i^2 - \frac{1}{2}\sum_I \nabla_I^2 - \sum_i \sum_I \frac{Z_I}{r_{iI}} + \sum_i \sum_{j>i} \frac{1}{r_{ij}} + \sum_I \sum_{J>I} \frac{Z_I Z_J}{r_{IJ}} \tag{2.2}$$

The terms in the Hamiltonian are the electronic and nuclear kinetic energy operators followed by three potential terms describing the Coulomb interaction between electrons i, j and nuclei I, J with atomic numbers Z_I. Atomic units are being used.

The Born-Oppenheimer Approximation

Often, the *Born-Oppenheimer* approximation is invoked. It takes advantage of the fact that the electron mass is almost 2000 times smaller than that of the nucleons. This allows us to regard the nuclei as fixed in space and only consider the electronic wave function ψ with the Schrödinger equation and Hamiltonian simplified to

$$\hat{H}_e\psi(\vec{r}_1, \vec{r}_2, \ldots, \vec{r}_n) = E_e\psi(\vec{r}_1, \vec{r}_2, \ldots, \vec{r}_n), \tag{2.3}$$

$$\hat{H}_e = -\frac{1}{2}\sum_i \nabla_i^2 - \sum_i \sum_I \frac{Z_I}{r_{iI}} + \sum_i \sum_{j>i} \frac{1}{r_{ij}} = \hat{T}_e + V \tag{2.4}$$

where the kinetic energy operator $\hat{T}$ and potential V have been introduced. From this equation, information such as the electron probability distribution $|\psi|^2$ can be derived—at least in principle.

The Variational Principle

The Schrödinger equation can only be solved analytically for a two-particle hydrogen-like system (with a nucleus and an electron), in which case one gets the stationary states (orbitals) and their energies. Introducing more nuclei would make the potential V more complex, and each additional electron would add 3 independent variables to ψ. Therefore, to treat even a single molecule, one has to resort to numerical methods—which can be done quite efficiently on computers.

In practice, one approaches the solution to the Schrödinger equation (2.3) by making use of the *variational principle*, according to which any guess at a solution ψ different from the true ground state ψ_0 will have an energy E_e greater than the ground state energy E_0. Using the shorthand Dirac notation for the integrals, one has:

$$\left\langle \psi \left| \hat{H}_e \right| \psi \right\rangle = E_e \geq E_0 = \left\langle \psi_0 \left| \hat{H}_e \right| \psi_0 \right\rangle \tag{2.5}$$

This equation introduces the concept of a *functional*, which is a "function of a function", *i.e.* it takes a function (ψ) as argument and returns a number (E_e). The trick, then, is to make intelligent guesses among a properly chosen set of wave functions.

One (conceptually) simple way of guessing at a many-electron wave function is the *Hartree-Fock approximation*, which combines molecular orbitals into a normalized, antisymmetric product called a *Slater determinant* Φ:

$$\psi(\vec{r}_1, \vec{r}_2, \ldots, \vec{r}_n) \approx \Phi = \frac{1}{\sqrt{n!}} \begin{vmatrix} \phi_1(\vec{r}_1)\sigma(1) & \phi_2(\vec{r}_1)\sigma(1) & \ldots & \phi_n(\vec{r}_1)\sigma(1) \\ \phi_1(\vec{r}_2)\sigma(2) & \phi_2(\vec{r}_2)\sigma(2) & \ldots & \phi_n(\vec{r}_2)\sigma(2) \\ \vdots & \vdots & \ddots & \vdots \\ \phi_1(\vec{r}_n)\sigma(n) & \phi_2(\vec{r}_n)\sigma(n) & \ldots & \phi_n(\vec{r}_n)\sigma(n) \end{vmatrix} \tag{2.6}$$

which consists of one-electron orbitals $\phi(\vec{r})$ and spin functions $\sigma(i)$, where the latter indicates the spin of electron i, which is either $\alpha(i)$ (spin up) or $\beta(i)$ (spin down). The elements of the Slater determinant are called spin orbitals. Having chosen this form of the wave function, one applies the variational principle and tries to find the set of one-electron orbitals which minimizes the total potential and kinetic energy $\left\langle \Phi \left| \hat{H}_e \right| \Phi \right\rangle$ of the electrons. This is done iteratively in a computer by a procedure called the *self-consistent field* (SCF) method, because the solution is only implicitly given: The Hamiltonian depends on the wave function.

2.1.3 Density Functional Theory

The variational principle reveals that the ground state energy can be determined in principle from knowledge of just the potential V (given by the nuclei) and number of electrons n for the system of interest. But there's more good news: There exists a shortcut around the wave function ψ. One can consider the

electron density $\rho(\vec{r})$ instead of the wave function, which in principle simplifies the job because $\rho(\vec{r})$ is a function of position in space rather than the coordinates of every electron. Thus, in principle one can introduce more electrons at a much lower computational cost. Besides, the electron density is much easier to comprehend than some many-dimensional wave function. It has been shown that the electron density fully characterizes a system in the ground state—just as the wave function. In other words, there is a one-to-one correspondence between these two characterizations. Indeed, this is a surprising and substantial contribution to the field of computational chemistry, which earned Walter Kohn the 1998 Nobel Prize in Chemistry, along with John A. Pople [66, 98].[1]

In the present work, we have used DFT as implemented in the Gaussian 03 software (Gaussian, Inc., Wallingford, CT) [41]. Different computers have been used, predominantly the 16-CPU Linux cluster at QuP and the IBM cluster at Centre for Scientific Computing, Aarhus, Denmark.

2.1.4 Functionals

The major drawback of DFT is that the functional which gives the energy in equation (2.5) is not explicitly known. More specifically, it is the exchange-correlation part of the functional which is unknown. Several terms have been swept under this carpet, including electron-electron interaction contributions beyond the classical electrostatics and kinetic energy of non-interacting electrons [65, 66]. Much effort goes into developing better explicit approximations to this functional, which increase the accuracy while minimizing the computational cost.

One example of a functional is the very successful three-parameter hybrid functional B3LYP proposed by Becke, which mixes Hartree-Fock exchange with DFT exchange-correlation (Lee, Yang and Parr) [9]. Another hybrid functional is B3PW91 [96], which uses the Perdew/Wang 91 correlation functional instead. These two functionals have proven successful for calculating vibrational spectra [110].

2.1.5 Basis Sets

In QM calculations, the wave function is typically represented by a linear combination of basis functions that are relatively easy to manipulate in a computer. Almost like a three-dimensional analogue of Taylor series, they approximate the orbitals of real molecules, which cannot be expressed analytically. This concept of *basis sets* are introduced in any decent textbook on DFT [35, 65].

Usually, linear combinations of gaussian functions are used as approximations of atomic orbitals. Each such basis function or *contraction* can consist of one or more so-called gaussian *primitives*. A minimal basis set has one basis function for each occupied orbital. We have only used *split valence* basis sets,

[1] See http://nobelprize.org/chemistry/laureates/1998/press.html for the entire press release by the Nobel Committee.

which include extra basis functions for each valence orbital in order to vary its size. In *double zeta* basis sets there are two basis function per orbital, while *triple zeta* basis sets have three, etc.

In addition to changing the orbital size, one can allow for changes in shape by including some orbital character of the higher angular momentum, *i.e.*, p-orbital contributions to s-orbitals, d-orbital contribution to p-orbitals, etc. These contributions are called *polarization functions* and are important when modelling atomic bonds.

Sometimes, a further increase of orbital size can be necessary, *e.g.*, to treat systems with negative charges. To that end, *diffuse functions* are added, which have the form of s- or p-orbitals.

Finally, to treat atoms heavier than Ar in an efficient way, one often uses basis sets which do not handle the inner core electrons explicitly, but rather put them into an *effective core potential* (ECP). The rationale for this is that primarily the valence orbitals are needed to describe bonding. At the same time, relativistic effects can be included more efficiently.

Name	Description	Reference
6-31G	Valence double-zeta basis set of Pople *et al.*	[26]
6-31G(d,p)	6-31G with d- and p-polarization functions	[48]
6-31++G(d,p)	6-31G(d,p) with two diffuse functions	[40,53]
D95V	Dunning/Huzinaga valence double-zeta	[30]
SDD	D95V (H–Ar) and Stuttgart/Dresden ECPs	[30]
LanL2DZ	D95V (H–Ne), Los Alamos ECP + DZ (Na–Bi)	[30,121]
cc-pVDZ	Dunning's correlation consistent basis set	[29]
aug-cc-pVDZ	double-zeta cc-pVDZ with diffuse functions	[64]
aug-cc-pVTZ	triple-zeta cc-pVTZ with diffuse functions	[64]

Table 2.1: Standard basis sets in Gaussian 03 used in this study.

Name	Primitives → Contractions	Reference
Stuttgart RSC 1997 ECP	(8s,7p,6d,1f) → [6s,5p,3d,1f]	[27]
Hay-Wadt VDZ (n+1) ECP	(5s,5p,5d) → [3s,3p,2d]	[50,121]
Ahlrichs TZV	(17s,10p,6d) → [6s,3p,3d]	[102]
Ahlrichs VTZ	(14s,9p,5d) → [8s,5p,3d]	[101]
Bauschlicher ANO	(20s,15p,10d,6f,4g) → [7s,6p,4d,3f,2g]	[8]
CRENBL ECP	(7s,6p,6d)	[57]

Table 2.2: Basis sets used for the first-row transition metals Fe, Co, and Ni in this study.

A range of such gaussian basis sets has been applied throughout this study. Some of them are standard basis sets implemented in Gaussian—these are briefly listed in Table 2.1.

Of the basis sets in Table 2.1, 6-31G(d), LanL2DZ and SDD have also been used for transition metals. Additional basis sets for transition metals have been

Name	Primitives → Contractions	Reference
Stuttgart RSC 1997 ECP	(8s,7p,6d) → [6s,5p,3d]	[2]
Hay-Wadt VDZ (n+1) ECP	(5s,6p,5d) → [3s,3p,2d]	[50, 121]

Table 2.3: Basis sets used for Re in Section 4.2, in addition to SDD and LanL2DZ.

downloaded from the Extensible Computational Chemistry Environment Basis Set Database [1]. These are listed in Tables 2.2–2.3.

2.2 Optical Spectroscopy

Classical physics is insufficient to explain the phenomena observed when light (or electromagnetic radiation in general) interacts with molecules. We need to understand the discrete nature of molecular energy levels, the electron spin, and the orbital shapes.

About a century ago, Max Planck introduced the idea that the interaction between matter and electromagnetic radiation is quantized. Accordingly, the frequencies of radiation absorbed or emitted would have to correspond to a specific transition between two states with energies E_1 and E_2:

$$\Delta E = E_2 - E_1 = hf \tag{2.7}$$

where f is the frequency and h is (not surprisingly) Planck's constant. This is the key to modern molecular spectroscopy.

Molecules are not static entities, as they contain numerous charged particles that are orbiting, vibrating and rotating mainly due to electrostatic forces. These particles can generate both electronic and magnetic *dipole moments*. Electronic dipole moments result from displaced charges upon atomic binding, whereas magnetic moments are due to rotating charges. Hence, interactions with electromagnetic radiation can take place, which cause transitions in the molecule between different states. During a transition, charge is redistributed, leading to electric transition dipole moments (for linear displacements) and magnetic transition dipole moments (for circular displacements). If the electric (magnetic) transition dipole moment is zero, one refers to the transition as electric (magnetic) dipole forbidden [100].[2] Information about the molecule can be obtained by probing those transitions, and this gives rise to three families of electromagnetic spectra with different energy ranges, as discussed in the sections below (except for the rotational spectra).

When measuring a spectrum, a number of lines will appear at the frequencies which obey equation (2.7). These lines are broadened due to ensemble averaging of molecules that are present in many slightly different states at finite temperatures. To avoid this, one would have to look at an isolated single

[2] "Forbidden" does not mean that such transitions never occur: Not all electrons obey the laws we put up.

molecule, in which case only the inevitable broadening due to the Heisenberg uncertainty principle will remain.

It seems intuitive to some extent, that chiral molecules will scatter or absorb the two opposite circular polarizations differently, much like a hand fits better into one glove than the other. We should expect that oppositely spiraling electromagnetic waves will interact differently with the chiral arrangements of oscillating and rotating charges it encounters. Linearly polarized light is also affected, because it can be seen as a superposition of LCP and RCP light.

A simple way of distinguishing samples of opposite enantiomers is to measure their optical rotation, *i.e.*, the angular shift of incident linearly polarized light (usually the orange sodium D line), which is due to different velocities of left and right circularly polarized light. If the angle is positive, the sample is designated with a (+) or D for dextrorotatory, otherwise with (−) or L for levorotatory. Unfortunately, there is no known correlation between optical rotation and absolute configuration. Besides, there is very little information content in the angle of optical rotation, although it can be measured as a function of wavelength, which is what ORD is about. For our purposes, though, we need to turn to more advanced techniques.

One chiroptical technique very recently made commercially available is Raman optical activity (ROA), which considers different kinds of scattering of circularly polarized light during vibrational transitions and so is the chiral counterpart of ordinary Raman spectroscopy. We have not used these scattering techniques in this project, but refer interested readers to a review [76].

2.2.1 Electronic Spectra

Electronic transitions in atoms and molecules usually take place in the visible or ultraviolet range of the electromagnetic spectrum, and these give rise to most of the colours that we perceive (and our very ability to perceive them). Figure 2.2 shows the familiar colours of light in the visible part of the electromagnetic spectrum.

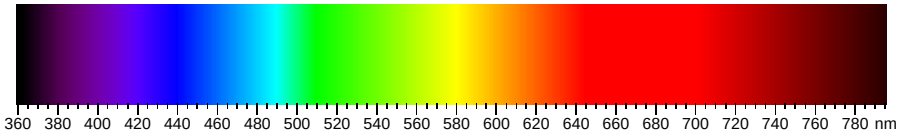

Figure 2.2: The visible range of the electromagnetic spectrum.

The absorption of electromagnetic radiation by electronic transitions gives rise to ultraviolet/visible (UV-Vis) absorption spectroscopy, which usually goes down to around 200 nm, depending on the available UV sources. We have only used this spectroscopic technique once (Section 3.3) and so will not introduce it in more detail.

2.2.2 Vibrational Spectra

The vast majority of vibrational transitions in molecules resonate with infrared radiation, which is sometimes called heat radiation, because we perceive it as heat. On the molecular level, heat manifests itself as random vibrations and constant exchange of infrared radiation.

For a molecule with n atoms, the number of independent vibrational patterns (*normal modes*) is $3n - 6$ ($3n - 5$ for a linear molecule), since we have 3 degrees of freedom for each atom minus the displacements and rotations of the whole molecule.

Unlike UV-Vis spectroscopy, the abscissa unit of vibrational spectra is usually *wavenumbers* $\bar{\nu}$ (in cm^{-1}), *i.e.*, reciprocal wavelength $1/\lambda$, which may be called frequency by some in the heat of battle, although the correct relation between them is the familiar $c = f\lambda = f/\bar{\nu}$, where c is the speed of light and f is the frequency (Hz). Part of the confusion may arise from the letter ν being used by some to denote frequency. At least there is a one-to-one correspondence, so ambiguity can be avoided. Not all spectroscopists are used to thinking in terms of wavenumbers, but there is a simple relation between λ (in nm) and $\bar{\nu}$ (in cm^{-1}), namely $\lambda\bar{\nu} = 10^7$.

Interatomic vibrations are often modelled by the harmonic oscillator (the *harmonic approximation*), which in the classical case is just Hooke's law with energy E in terms of the force constant k and deviation from equilibrium $r - r_{eq}$:

$$E = \frac{1}{2}k(r - r_{eq})^2 \tag{2.8}$$

From quantum mechanics, we know that such an oscillator has the allowed energy states [5]

$$E_l = \left(l + \frac{1}{2}\right)\frac{h}{2\pi}\sqrt{\frac{k}{\mu}} \tag{2.9}$$

where k is the force constant, μ the reduced mass, and $l = 0, 1, 2, \ldots$ is the vibrational quantum number. We recall that there is a *zero-point energy* for $l = 0$ and an identical energy spacing ΔE between subsequent levels. Furthermore, the *selection rules* only allow transitions, for which $\Delta l = \pm 1$.

Real interatomic potentials have an anharmonic shape close to the empirical *Morse potential*

$$E = E_{diss}(1 - e^{a(r_{eq} - r)})^2 \tag{2.10}$$

where E_{diss} is the dissociation energy, r_{eq} is the equilibrium distance, and a defines the steepness of the potential well. Contrary to the harmonic oscillator, the Morse potential has a decreasing ΔE with increasing l. Furthermore, the selection rules allow for *overtones*, since $\Delta l = \pm 1, \pm 2, \ldots$, but the intensity of the overtones ($\Delta l > 1$) is rapidly diminished as l grows. Additionally, there is a possibility for combination bands, *i.e.* weak absorbances at the sum of two or more wavenumbers. If two bands (either fundamentals, overtones or combination bands) are closely spaced, they may easily exchange energy. This is known as *Fermi resonance* [5].

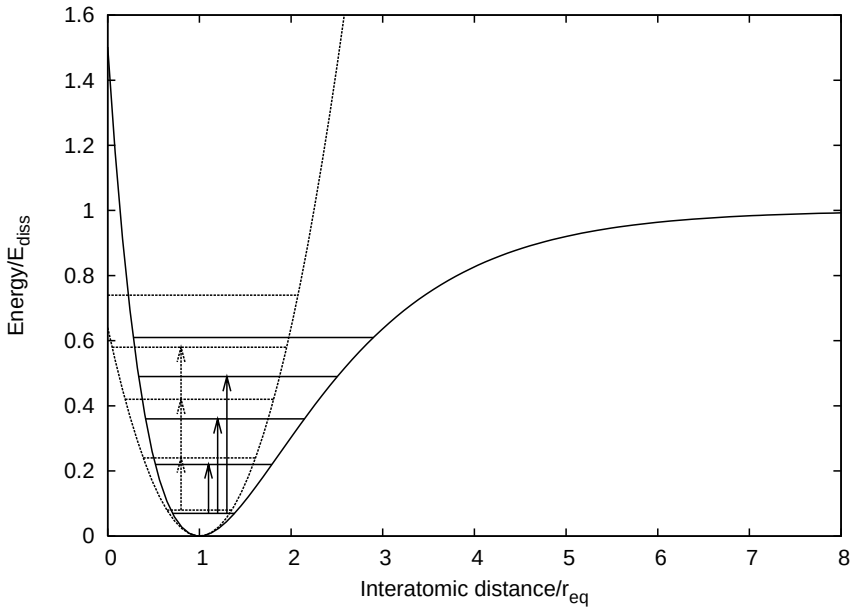

Figure 2.3: The Morse potential (—) and harmonic approximation (····) to the energy of an interatomic bond, with some vibrational levels included to illustrate the different energy spacing and some absorption processes to show the selection rules.

A Morse potential is compared to an approximating harmonic oscillator in Figure 2.3. Some allowed vibrational levels and transitions for each of them are included to illustrate the zero-point energies, energy spacing and selection rules. From the asymmetric shape of the Morse potential, one can infer that vibrating atoms spend more time on the far side of equilibrium separation, because the restoring force is lower there.

Around room temperature, the population of the electronic and vibrational ground state dominates, according to the Boltzmann distribution. Hence, we can allow ourselves to disregard absorptions starting from the $l = 1$ level or higher (called hot bands).

Infrared Spectroscopy

Infrared (IR) spectroscopy gives information about the vibrational modes of molecules. It is also known as vibrational absorption (VA) spectroscopy, since the molecular energy levels probed are predominantly vibrational. The absorbance $A(\bar{\nu})$ or *transmittance* $T(\bar{\nu})$ quantifies the amount of radiation absorbed by a sample as a function of wavenumber:

$$A(\bar{\nu}) = -\log \frac{I(\bar{\nu})}{I_0(\bar{\nu})} = -\log T(\bar{\nu}) \tag{2.11}$$

where $I(\bar{\nu})$ and $I_0(\bar{\nu})$ are the intensities measured with and without the sample present, respectively, and $T(\bar{\nu})$ is simply the fraction of light transmitted by the sample. The single-beam signal $I_0(\bar{\nu})$ is the IR source output dampened

by optical components along the light path—including the sample cell with solvent, if such are being used. In that case, one should subtract a spectrum of the solvent from that of the sample solution in order to obtain the pure sample spectrum.

Many available texts are useful when trying to assign observed normal modes to specific chemical groups [21, 95]. In recent years, software has also become available, which allows one to animate calculated normal modes of molecules on the computer screen. Examples are GaussView (Gaussian, Inc., Wallingford, CT), Molden[3], Molekel[4], and Jmol[5].

2.2.3 Circular Dichroism Spectroscopy

The definition of CD is simply the difference in absorbance of left and right circularly polarized light:

$$\Delta A = A_L - A_R \tag{2.12}$$

Vibrational CD can be understood both as an extension to electronic circular dichroism (ECD) and as a specialization of IR spectroscopy. Just as ECD probes the effect of chirality on electronic transitions, VCD probes the chirality of vibrational transitions. In other words, VCD is to IR spectroscopy what ECD is to UV-Vis spectroscopy. Since the mid-infrared (MIR) vibrational levels outnumber UV-Vis electronic levels, VCD provides more information than ECD. One further advantage of VCD over ECD is that high quality vibrational spectra can be obtained without treating excited electronic states.

Unfortunately, VCD has the disadvantage compared to ECD, that the CD signals relative to the parent absorption spectrum are smaller. VCD is usually around 4 orders of magnitude smaller than the parent IR absorption, this factor is known as the *anisotropy ratio* g [80]:

$$g = \frac{\Delta A}{A} \tag{2.13}$$

An alternative definition of g will appear below, which is more suited for theoretical results. Needless to say, VCD requires careful optimization of instruments. The starting point for obtaining a VCD spectrum is to have a good IR spectrum, otherwise the small absorbance difference ΔA will not be detected.

If a sample molecule is replaced with its enantiomer, it corresponds to interchanging A_L and A_R in (2.12), so obviously the VCD will change sign. A racemate has zero VCD signal, at least in theory. In practice there will be small artifacts, which one can eliminate from a VCD spectrum of a chiral sample by subtracting its racemate spectrum or even better—if one has the opposite enantiomer—by subtracting the average spectrum of the two enantiomers, which is equivalent to taking half their difference.

Since our project has focused on VCD rather than ECD, only the theory of the former will be reviewed in the following section.

[3] www.cmbi.ru.nl/molden/molden.html

[4] www.cscs.ch/molekel/

[5] http://jmol.sourceforge.net/

2.3 Theory of IR and VCD

Calculations of IR and VCD spectra usually employ the harmonic approximation, where the potential energy around each equilibrium atomic bond length is approximated by a parabola. This information is derived from the *Hessian* matrix, which contains the second derivatives of the energy with respect to position, *i.e.*, the force constants. In reality, the shape of the potential along interatomic bonds is rather like the Morse potential we saw in Section 2.2.2.

The anisotropy ratio g introduced in (2.13) can also be given as

$$g = \frac{4R}{D} \tag{2.14}$$

since the *rotational strength* R and *dipole strength* D for a given transition is proportional to the integrated VCD and IR intensity, respectively. The dipole and rotational strengths are defined below in terms of the electric and magnetic dipole transition moments. The electric dipole transition moment is the net linear charge displacement during a transition, and the magnetic dipole transition moment is the net charge circulation [100]. For the transition from the electronic and vibrational ground state to the first excited vibrational level of normal mode a, the dipole and rotational strength are (using Dirac's notation) [84, 85]

$$D_{01}^a = \left| \left\langle \psi_0^a \left| \hat{\mu} \right| \psi_1^a \right\rangle \right|^2 \tag{2.15}$$

$$R_{01}^a = \Im \left(\left\langle \psi_0^a \left| \hat{\mu} \right| \psi_1^a \right\rangle \cdot \left\langle \psi_1^a \left| \hat{m} \right| \psi_0^a \right\rangle \right) \tag{2.16}$$

where $\Im$ means the imaginary part, ψ_0 and ψ_1 are the vibrational ground and 1st excited state wave functions, and $\hat{\mu}$ and $\hat{m}$ are the electric and magnetic dipole moment operators, respectively:

$$\hat{\mu} = \sum_n q_n \vec{r}_n \tag{2.17}$$

$$\hat{m} = \sum_n \frac{q_n}{2m_n c} \vec{r}_n \times \vec{p}_n \tag{2.18}$$

where q_n, m_n, $\vec{r}_n$ and $\vec{p}_n$ is the charge, mass, position and momentum of electron n, respectively (disregarding the nuclear contributions).

In the following, we use Einstein summation notation, where repeated Greek subscripts means implicit summation over cartesian components x, y, z. Starting with the electric dipole transition moment, it can be expanded in terms of atomic polar tensor elements and nuclear displacement vectors as [74, 84]

$$\left\langle \psi_0^a \left| \hat{\mu}_\beta \right| \psi_1^a \right\rangle = \sqrt{\frac{\hbar}{2\omega_a}} \sum_A P_{\alpha\beta}^A S_{A\alpha,a} \tag{2.19}$$

where the atomic polar tensor (APT) consist of electronic and nuclear terms (subscript 0 means evaluation at equilibrium nuclear positions):

$$P_{\alpha\beta}^A = \left(\frac{\partial \mu_\beta}{\partial R_{A\alpha}} \right)_0 = E_{\alpha\beta}^A + Z_A e \delta_{\alpha\beta} \tag{2.20}$$

and the S-vector or displacement vector for nucleus A and normal mode a is given by

$$S_{A\alpha,a} = \left(\frac{\partial R_{A\alpha}}{\partial Q_a}\right)_{Q=0} = \left(\frac{\partial \dot{R}_{A\alpha}}{\partial \dot{Q}_a}\right)_{\dot{Q}=0} = \left(\frac{\partial \dot{R}_{A\alpha}}{\partial P_a}\right)_{P=0} \tag{2.21}$$

where $\dot{Q}_a = P_a$ is the conjugate vibrational momentum. The nuclear contribution $Z_A e\delta_{\alpha\beta}$ to the APT is simply the charges added to the diagonal elements. The electronic contribution $E^A_{\alpha\beta}$ to the APT is, expressed in terms of electronic energy E_{el} and electric field $\vec{E}$:

$$E^A_{\alpha\beta} = -\left(\frac{\partial^2 E_{\text{el}}}{\partial \vec{E}_\beta \partial R_{A\alpha}}\right)_0 \tag{2.22}$$

Similarly, the magnetic dipole transition moment can be expanded as [74,84]

$$\left\langle \psi_0^a \middle| \hat{\mathfrak{m}}_\beta \middle| \psi_1^a \right\rangle = i\sqrt{\frac{\hbar\omega_a}{2}} \sum_A M^A_{\alpha\beta} S_{A\alpha,a} \tag{2.23}$$

where the atomic axial tensor (AAT) components $M^A_{\alpha\beta}$ consist of electronic and nuclear terms:

$$M^A_{\alpha\beta} = \left(\frac{\partial m_\beta}{\partial \dot{R}_{A\alpha}}\right)_0 = I^A_{\alpha\beta} + \frac{Z_A e}{2c}\varepsilon_{\alpha\beta\gamma} R^0_{A\gamma} \tag{2.24}$$

The electronic contributions to the AAT is, expressed in terms of electronic energy E_e and magnetic field $\vec{H}$:

$$I^A_{\alpha\beta} = -\left(\frac{\partial^2 E_{\text{el}}}{\partial \vec{H}_\beta \partial \dot{R}_{A\alpha}}\right)_0 \tag{2.25}$$

Here appears the problem of taking a derivative with respect to nuclear velocity $\dot{R}$, which is obviously beyond the Born-Oppenheimer approximation. Several theoretical formalisms for VCD exist, and they deal with this problem in different ways. Among them are vibronic coupling theory (VCT) [83], magnetic field perturbation (MFP) [108] and nuclear velocity perturbation (NVP) [74]. These theories have also been reviewed [84]. Here, we briefly present the VCT formalism, since this one is best suited for understanding the enhancement phenomena in the following section. The formally equivalent MFP formulation is the one incorporated into the Gaussian 03 software.

In the VCT formalism, the electronic AAT contribution (2.25) is given as [78]

$$I^A_{\alpha\beta} = 2i\hbar \sum_{e\neq g} \frac{\left\langle \psi_g^0 \middle| \hat{\mathfrak{m}}_\beta \middle| \psi_e^0 \right\rangle \left\langle \psi_e^0 \middle| \left(\frac{\partial \psi_g}{\partial R_{A,\alpha}}\right)_0 \right\rangle}{E_e^0 - E_g^0} \tag{2.26}$$

where ψ_g^0 and ψ_e^0 are the vibrational ground states of the electronic ground and first excited state with energies E_g^0 and E_e^0, respectively. At this point, we are ready to extend the VCD theory to account for the resonance case when the denominator becomes small. This will be done mostly in qualitative terms, since this theory has yet to be implemented in software for practical use.

2.3.1 Resonance-Enhanced VCD

A few years after the discovery of VCD, it was observed that some transition-metal compounds displayed differing VCD intensities for different transition metals, while the IR intensity remained the same. This was first observed in a sparteine complex [6]. The effect, which typically amounts to an order of magnitude, was also associated with sign changes for some of the transitions. Two decades later the same compounds were re-investigated in a broader spectral range as well as theoretically, and the unenhanced VCD has been calculated using quantum mechanics implemented in Gaussian [52]. Unfortunately, the theory needed to reproduce the enhancement is not yet fully implemented. In some cases, however, the present theory is able to reproduce at least part of the enhancement, as we shall see later (section 4.3).

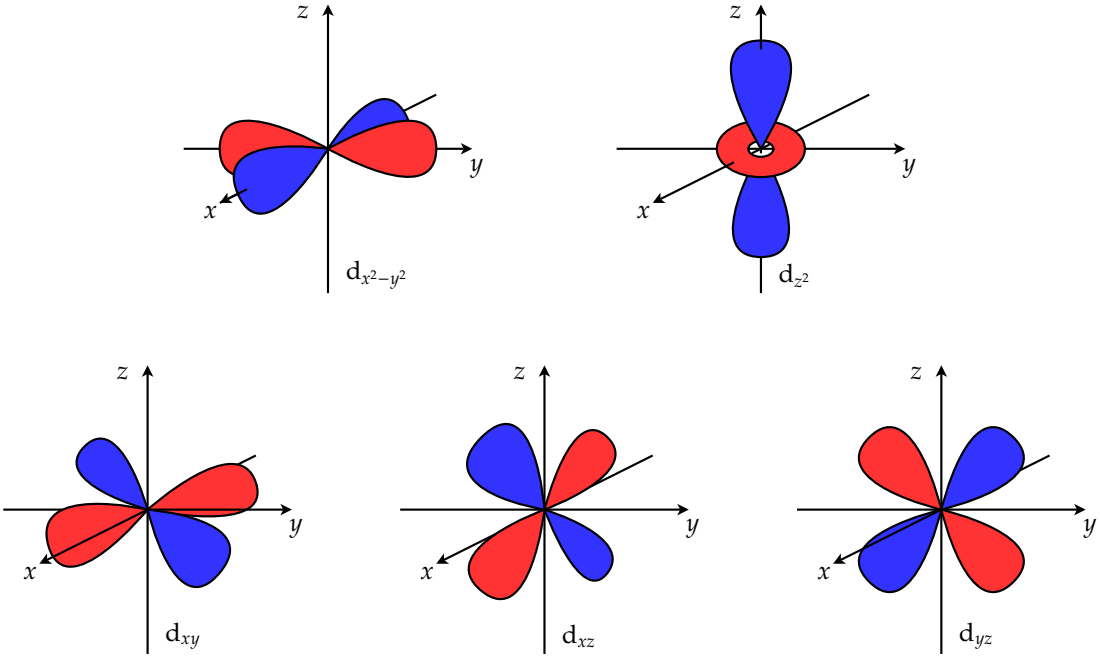

Figure 2.4: The approximate electron density clouds of the five d-orbitals.

Equation (2.26) above suggests that we may expect increased VCD intensities when the energy denominator becomes small—just before the theory breaks down. Recently, a full theory for the emergence of enhanced VCD intensities appeared, which includes non-Born-Oppenheimer terms [78]. According to this theory, which is based on the VCT formalism, VCD enhancement can be explained from the presence of underlying electronic CD in the infrared or near-infrared (NIR) region. The effect has therefore been termed resonance-enhanced VCD or REVCD. Usually, electronic transitions in molecules take place at considerably higher energies than vibrational transitions, which is also assumed in current computational implementations. However, in some situations there can be low-lying (NIR or IR) electronic transitions, usually associated with transition metal d-orbitals. In 1994 it was proposed that such

low-lying d–d transitions could couple with vibrational transitions to enhance the anisotropy ratio [109]. Only part of this enhancement is taken into account in existing MFP implementations of VCD, hence one cannot yet expect reliable comparisons of theory and experiment when there are low-lying d–d transitions (or f–f transitions in rare earth elements).

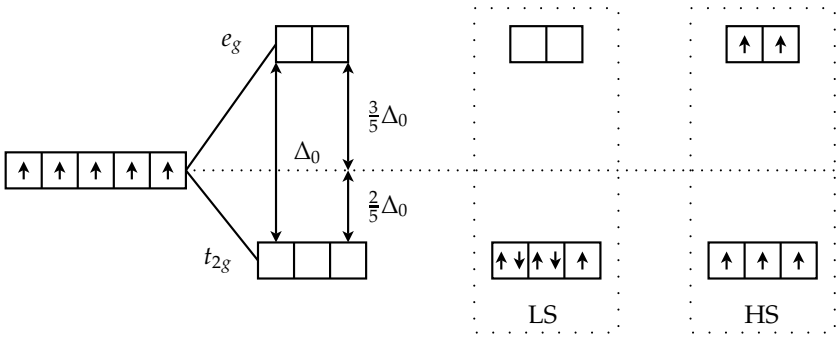

Figure 2.5: The ligand field splitting of the five d-orbitals in an octahedral coordination geometry. As an example, the low-spin (LS) and high-spin (HS) electron distribution is shown for a d^5 element such as Fe(III).

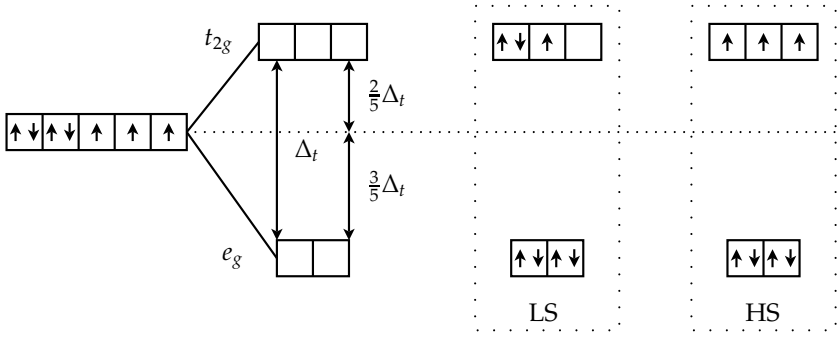

Figure 2.6: The ligand field splitting of the five d-orbitals in a tetrahedral coordination geometry. As an example, the low-spin (LS) and high-spin (HS) electron distribution is shown for a d^7 element such as Co(II).

These low-lying electronic states, which are electric dipole forbidden and magnetic dipole allowed [78], may appear when the symmetry of the ligand field around a transition-metal ion is broken. In an isolated transition metal atom, the d-orbitals (Figure 2.4) are degenerate. Upon coordination, the orbitals split into different energy levels with some degree of degeneracy depending on the symmetry of the ligand field. For instance, in octahedral coordination with six identical ligands, the d-orbitals can be shown to split into three degenerate lower energy levels and two degenerate upper levels [23]. These levels are referred to as t_{2g} and e_g, respectively (Figure 2.5). If the energy spacing Δ_0 is large enough, the electrons prefer to sit in the t_{2g} levels (*low-spin* configuration), otherwise Hund's rule causes them to populate the e_g levels as well (*high-spin*

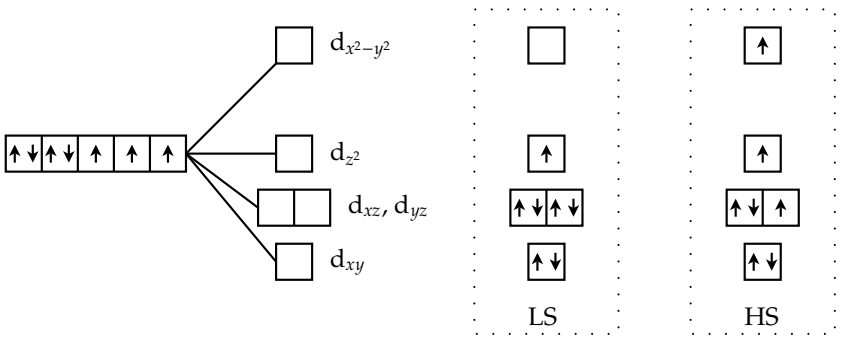

Figure 2.7: The ligand field splitting of the five d-orbitals in a symmetric square planar coordination geometry with the ligands along the x- and y-axes. As an example, the low-spin (LS) and high-spin (HS) electron distribution is shown for a d^7 element such as Co(II).

configuration). In tetrahedral coordination, the t_{2g} and e_g levels change places (Figure 2.6). When the coordination symmetry is broken due to chirality at the metal ion, the degeneracy of the t_{2g} and e_g levels is lifted, and if the appeared electronic transitions are near resonance with infrared or near-infrared radiation, enhanced VCD signals will result.

Square planar coordination can be thought of as a perturbation of the octahedral geometry, where the z-axis ligands have been pulled infinitely far apart. This gives a more complicated splitting pattern with at most two degenerate levels and other levels which are often close enough to allow electronic transitions in the IR. An example of an energy diagram is shown in Figure 2.7.

When low-lying electronic states are taken into account, equation (2.26) gets modified with a correction term depending on the vibrational frequency ω_a of normal mode a [78]:

$$I^A_{\alpha\beta}(\omega_a) = 2i\hbar \sum_{e\neq g} \frac{\left\langle \psi^0_g \middle| \hat{\mathrm{m}}_\beta \middle| \psi^0_e \right\rangle \left\langle \psi^0_e \middle| \left(\frac{\partial \psi_g}{\partial R_{A,\alpha}}\right)_0 \right\rangle}{E^0_e - E^0_g} \left(1 + \frac{\omega_a^2}{(\omega^0_e - \omega^0_g)^2 - \omega_a^2}\right) \tag{2.27}$$

This expression, where the bandwidth dependency is left out, is within 1 % of equation (2.26) when $\omega_e \geq 10\omega_a$, *i.e.*, when no low-lying electronic states are present. Damping terms can be included to avoid division by zero if $\omega_e = \omega_g$.

The term enhanced VCD does not mean simply that the anisotropy ratio of every band is similarly increased. Only some of the bands show enhancement, and occasionally they seem to change sign as well [52]. There is a spatial dependence involved, which only enhances those vibrational modes that can couple with the orbitals undergoing low-lying electronic transitions. If these ECD bands are indeed the underlying mechanism, there is obviously a dependence on their frequency—and possibly on intensity and sign. However, the exact nature of the dependencies is not clear.

2.3.2 Processing Calculated Results

Frequency data calculated by Gaussian are given in arrays of wavenumbers and the properties of that normal mode (force constant, reduced mass, IR intensity etc.). When calculating a VCD spectrum, the dipole strength D_i and rotational strength R_i is added for each normal mode i. The dipole and rotational strengths, given in terms of electrostatic units as esu^2cm^2, can be converted into the more convenient *molar absorption coefficient* (also known as molar absorptivity or molar extinction coefficient) ϵ (with units of $\text{L mol}^{-1}\text{ cm}^{-1}$) using the equations

$$D_i \approx 9.2 \cdot 10^{-39} \epsilon_i \frac{\gamma}{\bar{\nu}_i} \pi \tag{2.28}$$

$$R_i \approx 2.3 \cdot 10^{-39} \Delta\epsilon_i \frac{\gamma}{\bar{\nu}_i} \pi \tag{2.29}$$

where γ is the half-width (HWHM) of a Lorentzian band centered at the wavenumber $\bar{\nu}_i$ with the peak height ϵ_i (for IR) or $\Delta\epsilon_i$ (for VCD) [85]. Thus, we use the dipole strength rather than the IR intensity values from Gaussian (which are in units of km/mol).

Experimental intensities can be converted from absorbance A to molar absorption coefficient using *Lambert-Beer's law*

$$A = \epsilon\, c\, l \tag{2.30}$$

where c is the concentration and l is the path length (in cm). In this way, calculated and experimental intensities can be directly compared. We now have three equivalent expressions for the anisotropy ratio, relating experiment to theory:

$$g = \frac{\Delta A}{A} = \frac{\Delta\epsilon}{\epsilon} = \frac{4R}{D} \tag{2.31}$$

The calculated spectral data can be plotted as a series of spikes. However, to facilitate graphical comparison of calculated and experimental spectra, we use the values of ϵ and $\Delta\epsilon$ from equations (2.28)–(2.29) and convolute them with Lorentzians (which is the natural band shape of IR absorption). A Unix script has been written for this purpose, as described below. It generates a Lorentzian for the IR and VCD signal of each normal mode and adds them into two functional expressions (the IR and VCD spectra), which are then tabulated in columns of wavenumber $\bar{\nu}$, molar absorption coefficient ϵ, and molar absorption coefficient difference $\Delta\epsilon$.

Calculated wavenumbers are typically scaled by a so-called *frequency scaling factor*, which originates from the fact that calculated normal modes have systematic frequency deviations from reality, typically a few percent. The reasons for this are the approximate electron structure calculation and the harmonic approximation, which is assumed for the atomic bonds. Scaling factors for a range of calculation methods have been tabulated.[6]

[6] For a comprehensive list, see http://srdata.nist.gov/cccbdb/vibscale.asp.

When comparing calculated and experimental spectra, it is very useful to visualize the calculated vibrational modes in order to assign them. Therefore, we have made use of the free Java program Jmol, which can open output files from Gaussian and animate the atomic displacements.

Unix Scripts

Besides the Unix script mentioned above, we have written several other scripts for various purposes, and they are briefly described here. Their code is listed in appendix B.

When several conformers of a molecule have been geometry optimized, the script `g03energies.bash` can extract the SCF energies from these files and print a table comparing their relative energies (converted to kJ/mol) as well as the corresponding population fraction in case of a Boltzmann distribution.

The script `g03toCSV.bash` reads the output of a Gaussian frequency calculation and also takes a frequency scaling factor and half-width γ as arguments. Then it converts the IR and VCD into ϵ and $\Delta\epsilon$ values tabulated in the 400–4000 cm^{-1} wavenumber range.

To make a plot of the spectral data generated by `g03toCSV.bash`, one can use the script `plotCSV.bash`, which returns a list of commands for the plotting program GnuPlot.[7] Furthermore, the scripts `annotateIR.bash` and `annotateVCD.bash` allows for annotating each normal mode in the above plot with its number. These three scripts simply return the lines of GnuPlot commands to use, so they are only of relevance to GnuPlot users.

To extract a table of vibrational data (wavenumbers and any properties calculated), the script `g03toFrq.bash` can be used. It stores the table in a text file. The scripts for annotation in GnuPlot need this table as input.

2.4 VCD Instrumentation

As mentioned previously, VCD requires carefully optimized instruments. The starting point for obtaining a VCD spectrum is to have a good IR spectrum with an absorbance within about 0.2–0.8. If the IR bands absorb more, too little radiation may reach the detector, and poor signal-to-noise ratio (S/N) will result. Additionally, longer scan times are needed than for IR spectroscopy.

Two different Fourier transform VCD spectrometers have been used during the course of this project; one at QuP and one at the Department of Chemistry at SU. Their characteristics are briefly outlined here, followed by a discussion of key components and techniques.

The instrument at QuP is a Thermo-Nicolet Nexus 870 FT-IR instrument (Thermo Electron Corp., Madison, WI) equipped with a VCD accessory module. This module contains 3 mirrors, a linear polarizer, PEM-90 modulator, BaF_2 lens, and a detector.

[7] GnuPlot is freeware and available from http://www.gnuplot.info.

The instrument used at SU is a modified Chiral*IR* spectrometer (BioTools, Inc., Wauconda, IL), equipped with two sources [79] for better S/N and two photoelastic modulators. The second PEM is used for baseline improvement.

In addition, we have used a Thermo-Nicolet Magna-IR 850 spectrometer (Thermo Electron Corp., Madison, WI) at the Department of Chemistry at SU for higher-resolution IR spectroscopy.

2.4.1 Dispersive vs. Fourier Transform Instruments

Generally, there are two types of VCD instruments, the *dispersive* and the *Fourier transform* (FT) spectrometers. The former uses a monochromator to select one narrow range of IR wavelengths at a time, thereby scanning through the spectral region of interest. Of course, the wider that region, the longer time it takes to collect a spectrum.

A Fourier transform spectrometer, on the other hand, uses a Michelson-Morley interferometer to simultaneously irradiate the sample with a multitude of wavelengths given by the pattern of constructive and destructive interference. This is called the multiplex advantage. The pattern changes continually as one of the mirrors in the interferometer is scanned back and forth. A longer movement range gives a better resolution (the two are inversely proportional [5]), and a lower mirror speed increases the S/N. The interferogram modulation typically takes place at a frequency of a few kHz [3,81]. A computer is used to collect and demodulate the signal.

Recent developments have allowed for FT-VCD measurements in the continuous spectral range from 800–10000 cm^{-1}, *i.e.* into the NIR, by combining three instruments optimized in different regions [15, 82].

Since we have not used dispersive spectrometers, the following discussion will not deal specifically with that kind of instrument.

2.4.2 Polarization Modulation

In order to measure the difference in absorption of LCP and RCP radiation, we need to change the polarization state periodically. The modulation of polarization state between RCP and LCP has to take place at a frequency different from the Fourier modulation in order for the two modulations to be separated. To that end, an optical component called a *photoelastic modulator* (PEM) is used (Hinds Instruments, Hillsboro, OR), which consists of a crystalline slab of material (in our case ZnSe) with tunable birefringence depending on the stress applied to the crystal (Figure 2.8). By periodically changing the stress with attached piezo elements, incoming light from a linear polarizer is modulated via elliptic to circular polarization of both orientations (Figure 2.9). Depending on the amplitude of the stress, the PEM will have its optimum at different wavenumbers, allowing VCD measurements to be made in a region about $\pm 600\,cm^{-1}$ from the optimum.

We have used PEMs from Hinds Instruments, Inc. (Hillsboro, OR), which

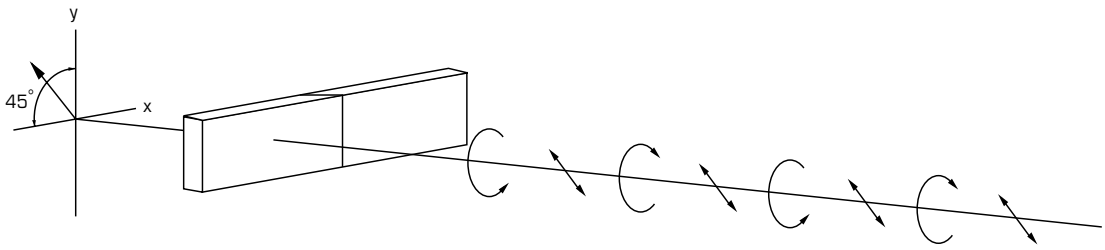

Figure 2.8: Schematic of a photoelastic modulator (PEM), which consists of an octahedral slab of crystalline material attached to a piezo element. The incoming light is linearly polarized 45° from the symmetry axis of the crystal. Courtesy of Hinds Instruments.

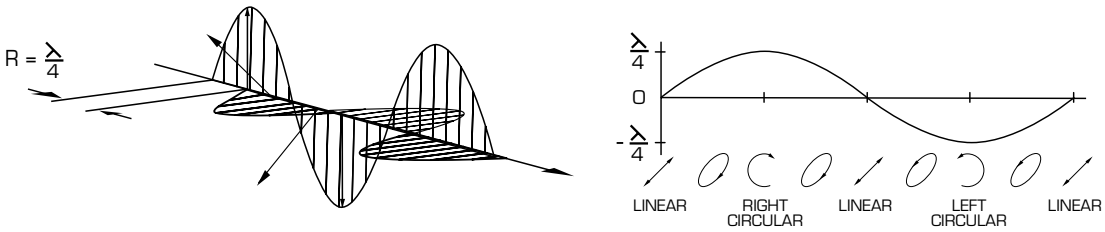

Figure 2.9: For the purpose of VCD spectroscopy, the photoelastic modulator is driven at periodic quarter-wave retardation (left), which generates interchangeably LCP and RCP radiation with intermediate states of linear and elliptic polarization. Courtesy of Hinds Instruments.

typically operate around 50 kHz, *i.e.*, an order of magnitude above the Fourier modulation. A lock-in amplifier and demodulator is provided with the PEM.

It is possible to use two PEMs simultaneously; one before and one after the sample, with separate lock-in amplifiers. This allows for a better baseline with almost no linear birefringence artifacts and thus is especially valuable when one does not have the racemate or opposite enantiomer of a sample available for baseline correction. The method implies driving the two PEMs at slightly different frequencies (37.3 kHz ±15 Hz), whereby two simultaneous VCD signals are collected and subtracted in real-time [77]. The retardation of the second PEM can be adjusted to tune the baseline.

2.4.3 Detection

Obviously, a fast detector is needed to keep up with the PEM frequency. Therefore, we have used HgCdTe (also called MCT) detectors cooled with liquid nitrogen. This type of detector has a spectral range of operation in the MIR region around 800–4000 cm^{-1}, though not optimal above 2000 cm^{-1} [15]. It is not sensitive to the frequency or polarization state of impinging radiation.

Recorded VCD intensities have to be calibrated to account for the wavenumber dependency of the PEM. The standard method of calibration is to use a sample consisting of a quarter-wave plate followed by a linear polarizer. Two

single-beam spectra are then measured, with the sample rotated so that its polarizer is parallel or orthogonal to the polarizer before the PEM. When the resolution or PEM optimum is changed, a new calibration curve has to be obtained. Any recorded VCD spectrum must then be divided by this curve [62].

There are several ways to improve the S/N. The simplest is to measure for a longer time. Increasing the acquisition time by a factor n increases the S/N by $\sqrt{n}$ [5]. There are alternatives to this trade-off, as described below, but some of them are costly.

If possible, on can increase the S/N by increasing the IR source intensity and hence the dynamic range. However, this may saturate the detector, so in order to avoid that one can use optical filters to remove especially the NIR part of the light source. This allows one to selectively increase the intensity of radiation in the mid-infrared (MIR) region under study. For a liquid nitrogen cooled MCT detector, a long-wave pass filter with a cutoff above 2000 cm^{-1} can be used if the C–H stretching region is not being considered.

There is a more intelligent way of removing irrelevant photons from the bundle of radiation hitting the detector, whereby the S/N can be increased further (actually doubled) [79]. One can use two simultaneous light sources at adjacent corners of a four-port interferometer, with orthogonal linear polarizers in front of them. This makes the interferometer yield two orthogonal interferograms, which are then passed through the PEM and sample. A standard FT-VCD instrument has a linear polarizer in front of the PEM, and in that case, rotating the polarizer by 90° would interchange the RCP and LCP radiation and thus negate the VCD spectrum. With two orthogonally polarized sources, one removes the linear polarizer in front of the PEM and essentially subtracts the arising pair of opposite VCD signals. What happens is that the polarization modulated parts of radiation leaving the sample in the ideal case combine positively, whereas the rest combines negatively. So the VCD part of the signal increases at the expense of the ordinary IR part. Since the detector noise level remains the same, the VCD S/N has increased.

Chapter 3

Small Organic Molecules and Pharmaceuticals

3.1 Introduction: The Lesson From Thalidomide

Multicellular organisms have a host of small signalling molecules, which are chiral, typically because they are peptides. Therefore chirality is a crucial aspect of drug development, which has been apparent ever since the thalidomide disaster in the mid-20th century. Thalidomide was a drug used as sleeping aid and to prevent morning sickness of pregnant women. But it turned out to cause serious birth defects to their children. The reason was that thalidomide was a chiral drug, and one of its enantiomers had the desired medical effect, whereas the other caused birth defects [33]. So these days, new drugs have to be enantiomerically pure in the US[1] and many other countries. In the case of thalidomide, that would in fact not be possible, since the enantiomers interconvert [33].

This chapter is devoted to the work carried out on small to medium-sized organic molecules during the course of the project. All of them came from collaborators who were interested mainly in determining or verifying the absolute configuration. The methyl-substituted phenyloxiranes were synthesized by Ph.D. student Peter Fristrup from the Department of Chemistry at DTU as part of a project on asymmetric catalysis. The remaining compounds are natural products of pharmaceutical interest, extracted in enantiomerically pure form by collaborators. Nyasol was supplied by Prof. Søren B. Christensen from the Department of Medicinal Chemistry at The Danish University of Pharmaceutical Sciences (DFU). The curcuphenol monomer and dimers were supplied by Dr. Robert Cichewicz at University of California, Santa Cruz. They were sent to Prof. Nafie's lab at SU, where we examined them. Finally, ginkgolide B was supplied by Assoc. Prof. Kristian Strømgaard at DFU.

[1] FDA's policy statement for the development of new stereoisomeric drugs. *Chirality 4* (1992), 338–40.

3.2 Methyl-Substituted Phenyloxiranes

This project is related to studies of asymmetric catalysis taking place at the Department of Chemistry, DTU. A collaboration was established in order to determine the absolute configuration of the three possible methyl-substituted phenyloxiranes. These are small, fairly rigid molecules with 1–2 chiral centres as shown in Figure 3.1. Synthesis of enantioenriched samples was done by Peter Fristrup from the Department of Chemistry [42], whereas IR/VCD measurements and most QM calculations were carried out at the Quantum Protein Centre (QuP), Department of Physics at DTU. The objective was to determine the absolute configuration by comparison of theoretical and experimental VCD spectra. A paper on our joint efforts has been published and is enclosed in appendix E as Paper 1.[2]

Three samples were provided in both enantioenriched and racemic form: α-MePhOx (95 % *ee*), *cis*-β-MePhOx (89 % *ee*) and *trans*-β-MePhOx (99 % *ee*), where MePhOx is short for methylphenyloxirane. The *cis*-β-MePhOx sample was known to contain 10 % of its (1*S*,2*S*)-diastereomer with 73 % *ee*.

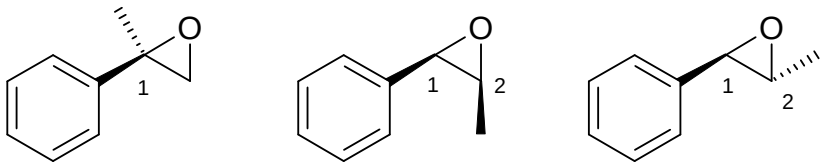

Figure 3.1: Chemical structure of the three methyl-substituted phenyloxiranes studied: (*R*)-1-methylphenyloxirane (α-MePhOx, left), (1*R*,2*S*)-2-methylphenyloxirane (*cis*-β-MePhOx, middle) and (1*R*,2*R*)-2-methylphenyloxirane (*trans*-β-MePhOx, right). These are the enantiomers investigated by theoretical methods.

3.2.1 Theoretical and Experimental Methods

The conformational flexibility of the compounds is limited to phenyl and methyl rotations relative to the oxirane ring. Initial DFT energy calculations of different geometries were carried out by Peter Fristrup using B3LYP/6-311++G(d,p) implemented in Jaguar 4.2 (Schrödinger, Inc., Portland, OR). Subsequent DFT geometry optimizations and frequency calculations were performed with Gaussian 03 [41] on the Linux cluster at QuP. An earlier study of phenyloxirane concludes that the B3LYP functional is better than B3PW91 [4], hence we used B3LYP in the present work.

An extensive theoretical study of methyloxirane using different functionals and basis sets for HF and DFT calculations has been published [18], which recommends using the aug-cc-pVDZ or 6-311++G(2d,2p) basis set rather than

[2] In the paper, the acronym VA has been used, whereas this thesis uses the synonymous IR. Here, we also use molar absorption coefficient instead of molar extinction coefficient to be consistent with the rest of the thesis.

the common 6-31G(d). We have thus included aug-cc-pVDZ in our list of basis sets, along with its triple-zeta cousin aug-cc-pVTZ, and 6-31++G(d,p).

Gas phase calculations were carried out by Karl Jalkanen and Lars Hemmingsen, and are included in Paper 1. Here, we present our additional Gaussian 03 calculations, which are identical to the above except for inclusion of a self-consistent reaction field (SCRF) polarizable continuum (PCM) solvent model for CCl_4. These calculations were carried out to investigate whether implicit solvation would improve the fit to experimental data. Calculated peaks were scaled to account for systematic frequency deviations and convoluted with Lorentzian shapes assuming a half-width of $4\,\mathrm{cm}^{-1}$. Furthermore, two Unix scripts were used for numbering of calculated normal modes (section B.5–B.6) in order to facilitate comparison with experiments.

IR and VCD spectroscopic measurements were carried out at QuP on the Thermo-Nicolet Nexus 870 FT-IR with a PEM accessory module. Only the spectra of neat samples are included here, as the solution spectra were measured by co-authors. Neat samples were contained in a BaF_2 cell with $\approx 15\,\mu\mathrm{m}$ path length and measured at a resolution of $4\,\mathrm{cm}^{-1}$ for 8 h. Racemate spectra were used for VCD baseline correction. Experimental intensities were calibrated and converted from absorbance to molar absorption coefficient. To that end, we use Lambert-Beer's law (2.30) in a form more suited for neat samples:

$$A = \epsilon\, c\, l = \epsilon\, \frac{l\,\rho}{d\,MW} \tag{3.1}$$

where ρ is the density and d is a dilution factor ($d = 1$ for neat samples). The MW is 134.2 g/mol for all three compounds, and their densities are $1.02\,\mathrm{g/cm}^3$ for α-MePhOx and $1.01\,\mathrm{g/cm}^3$ for both *cis*-β-MePhOx and *trans*-β-MePhOx.

3.2.2 Results and Discussion

The initial conformational search by Peter Fristrup identified only one conformer of each of the methylphenyloxiranes, as shown in Paper 1, Figure 3. The DFT optimized geometries from our B3LYP/aug-cc-pVTZ calculation of the three enantiomers from Figure 3.1 are shown in Figure 3.2. There is no noticeable structural difference compared to the calculation without solvent model. Furthermore, it turned out that the calculated IR and VCD spectra barely changed upon inclusion of an implicit solvent model.[3]

Figures 3.3–3.5 compare our experimental IR and VCD spectra of neat samples to our calculated spectra of the above enantiomers. Calculated wavenumbers are scaled by 0.98, since that brings the peaks very close to the experimental ones. Calculated VCD intensities are scaled with the known *ee* of the corresponding sample. In the case of *cis*-β-MePhOx, the known diastereomeric purity was corrected for in the calculated IR/VCD spectra by adding/subtracting 10 % of the calculated (1*R*,2*R*)-2-MePhOx IR/VCD, respectively (taking the 73 % *ee* of the diastereomer into account).

[3]These calculations were performed after submission of our paper and are therefore not included in the final version.

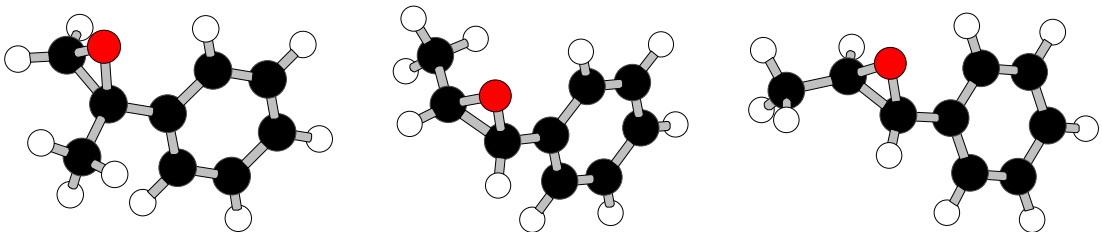

Figure 3.2: Optimized structures of three methylphenyloxiranes calculated using B3LYP/aug-cc-pVTZ: (*R*)-1-MePhOx (left), (1*R*,2*S*)-2-MePhOx (middle) and (1*R*,2*R*)-2-MePhOx (right).

It is apparent from the three comparisons, that we can assign the absolute configurations of the three samples to be (*R*)-1-MePhOx, (1*R*,2*S*)-2-MePhOx and (1*R*,2*R*)-2-MePhOx, respectively. Detailed discussion of the observed and calculated spectra is given in Paper 1.

A major problem during this project was the rather disappointing S/N characteristics of the VCD measurements, which made it difficult to obtain detailed spectra. It does not seem possible to measure much better spectra with the present experimental setup. Other people using the same spectrometer and VCD accessory seem to have noise problems as well [32]. However, one of our colleagues, Dr. Niels H. Andersen, has recently been able to improve the S/N of the spectrometer by implementing a set of optical filters. Further improvements would be rather comprehensive or costly, such as linearizing the design of the PEM accessory module to avoid the use of mirrors or installing a second PEM for artifact reduction.

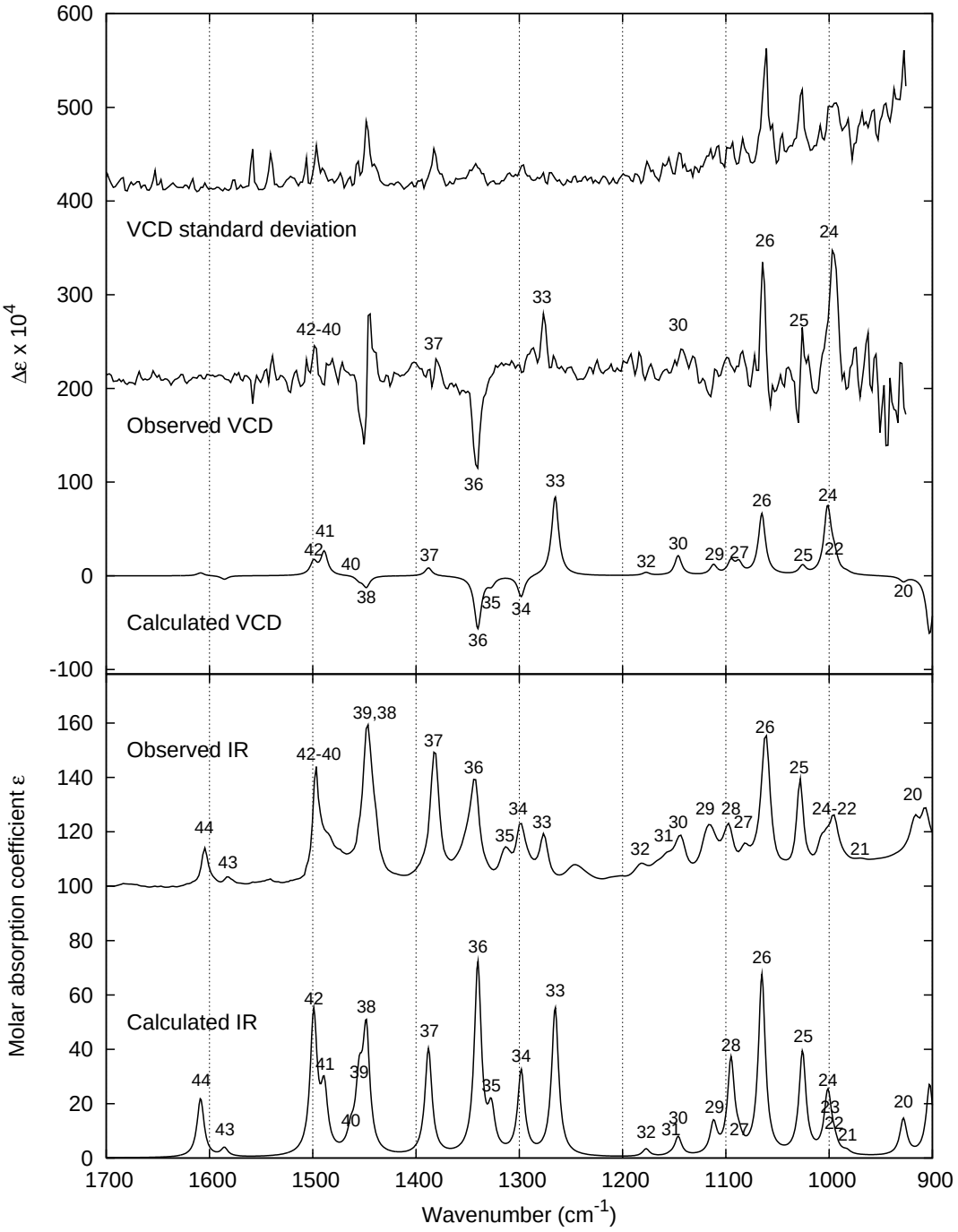

Figure 3.3: Comparison of experimental and calculated IR (bottom) and VCD (top) spectra of α-methylphenyloxirane. Calculated spectra are for the (*R*)-enantiomer with 95 % *ee*, using B3LYP/aug-cc-pVTZ with an implicit solvent model, using 4 cm^{-1} half-width and a frequency scaling factor of 0.98. Most fundamentals are numbered. Experimental spectra are of neat samples, measured for 8 h using 4 cm^{-1} resolution and a 17.3 μm path length.

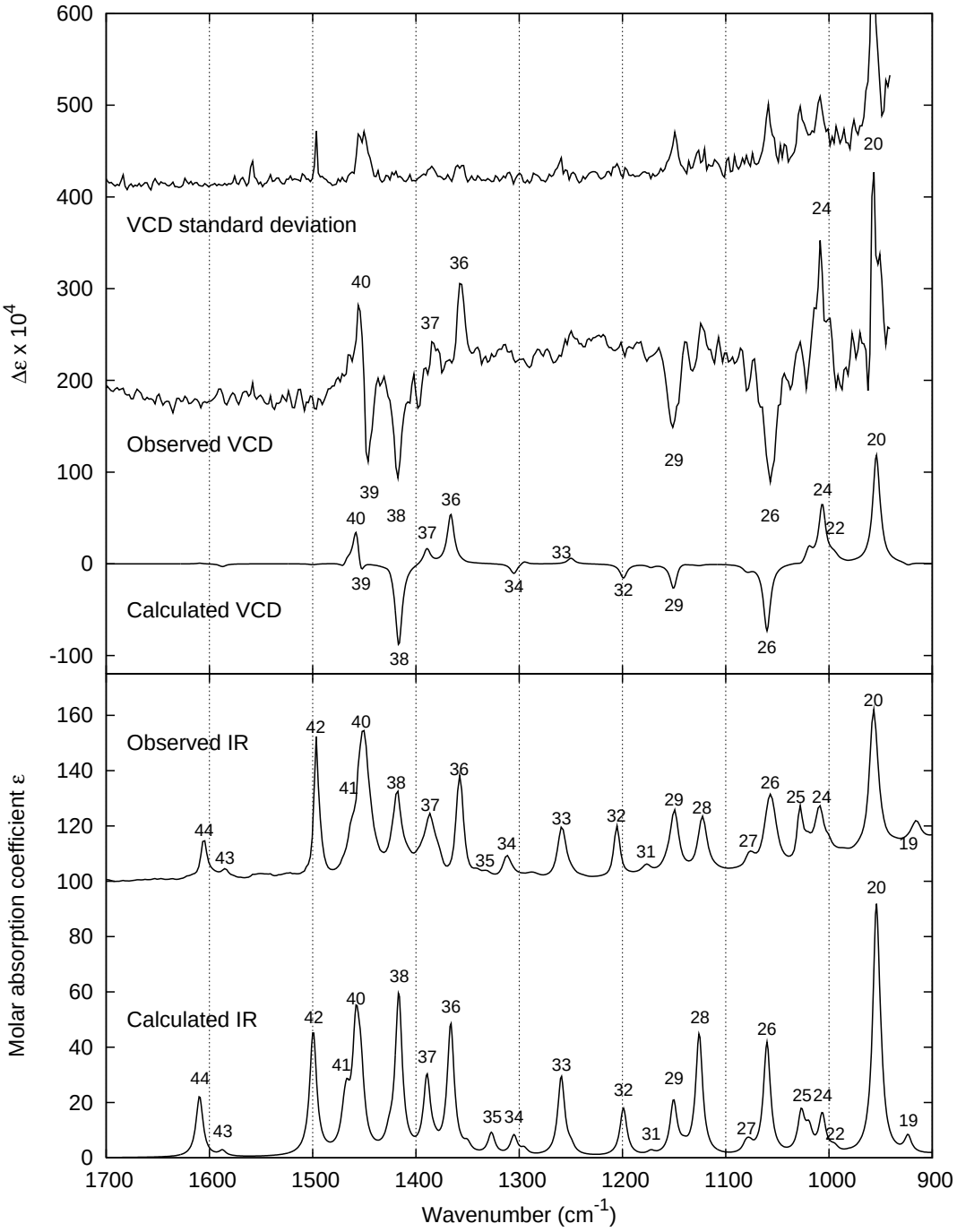

Figure 3.4: Comparison of experimental and calculated IR (bottom) and VCD (top) spectra of *cis*-*β*-methylphenyloxirane. Calculated spectra are for the (1*R*,2*S*)-enantiomer with 89 % *ee*, but include 0.73×10 % of the (1*S*,2*S*)-diastereomer spectra to account for its presence in the sample. The DFT method was B3LYP/aug-cc-pVTZ with an implicit solvent model, using 4 cm^{-1} half-width and a frequency scaling factor of 0.98. Fundamentals for *cis*-*β*-MePhOx are numbered. Experimental spectra are of neat samples, measured for 8 h using 4 cm^{-1} resolution and a 16.5 μm path length.

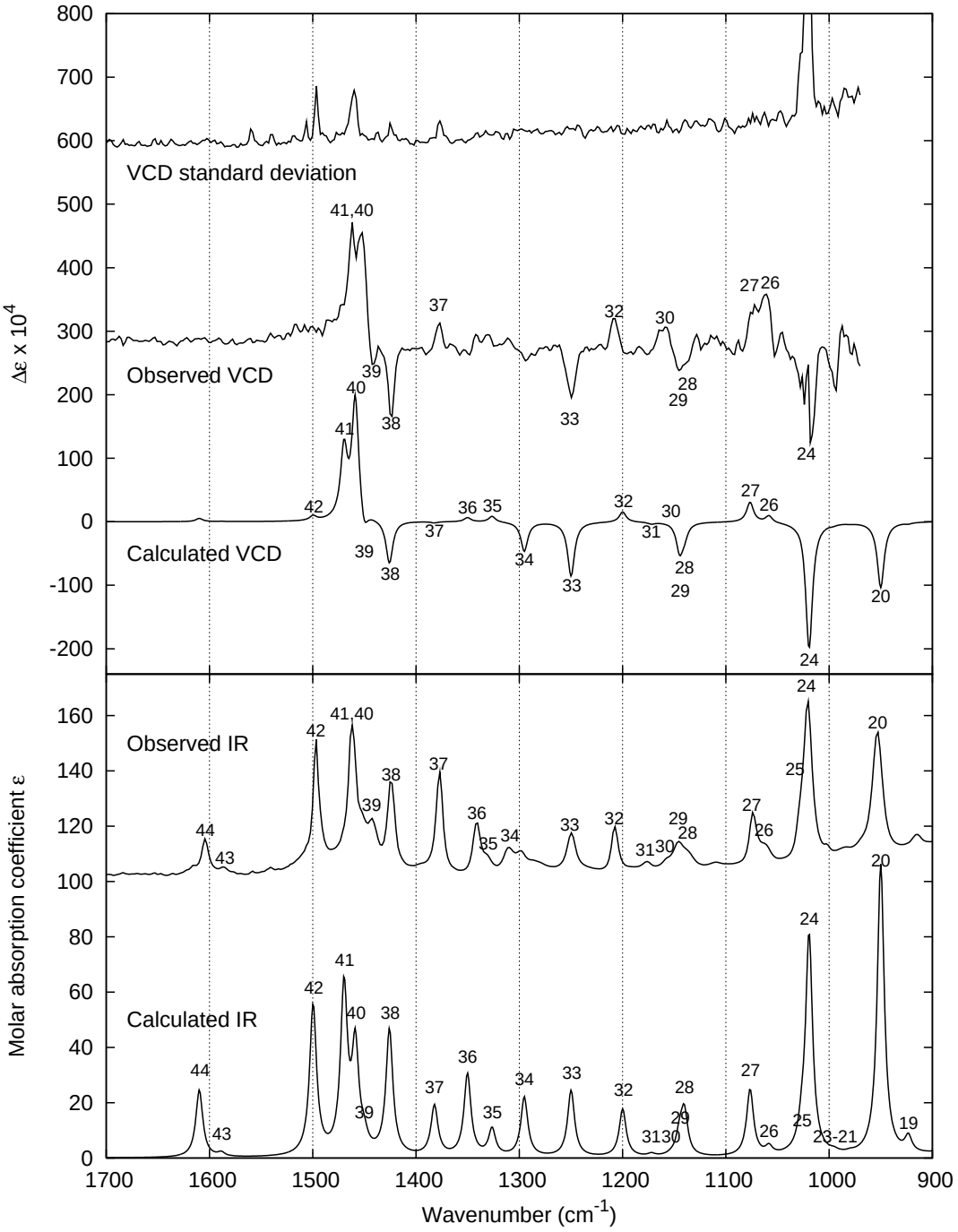

Figure 3.5: Comparison of experimental and calculated IR (bottom) and VCD (top) spectra of *trans*-β-methylphenyloxirane. Calculated spectra are for the (1*R*,2*R*)-enantiomer with 99 % *ee*, using B3LYP/aug-cc-pVTZ with an implicit solvent model, using 4 cm^{-1} half-width and a frequency scaling factor of 0.98. Most fundamentals are numbered. Experimental spectra are of neat samples, measured for 8 h using 4 cm^{-1} resolution and an 18.6 μm path length.

3.3 Nyasol

The compound nyasol is a natural product with antiplasmodial and antifungal activity, and both of its enantiomers can be derived from different plants [58, 61, 90, 94, 118]. The IUPAC name of the compound is (*Z*)-1,3-bis(4-hydroxyphenyl)-1,4-pentadiene, and its structure is shown in Figure 3.6, where a single chiral centre can be seen. Our objective was to determine the absolute configuration of (+)-nyasol from *Asparagus africanus* and thereby resolve the uncertainty in a previous attempt to do so [72] and allow for tests of differing biological activity of the enantiomers. This project was carried out in collaboration with the Department of Medicinal Chemistry at the Danish University of Pharmaceutical Sciences (DFU), from where the sample was provided. IR and VCD Measurements were carried out both at QuP and at the Department of Chemistry at Syracuse University (SU). Our results have been published and are included as Paper 2.

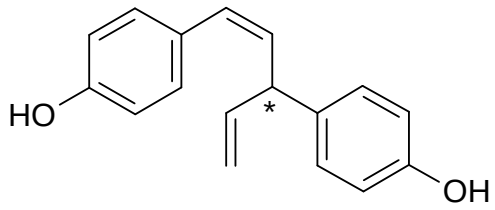

Figure 3.6: The chemical structure of nyasol, (*Z*)-1,3-bis(4-hydroxyphenyl)-1,4-pentadiene. An asterisk indicates the chiral centre.

Nyasol is soluble in DMSO, acetonitrile, and methanol, but insoluble in chloroform. The compound is colourless, but is reported to turn red on exposure to air [90].

3.3.1 Conformational Analysis and DFT Calculations

A Systematic Unbounded Multiple Minimum (SUMM) conformational search (details are in Paper 2) revealed 26 conformers in the gas phase within an energy range of 20 kJ/mol, 12 of which were within 6 kJ/mol from the ground state (see Table 1 and Figure 1 of Paper 2). Thus, nyasol is very flexible in spite of its modest size, and many conformers have to be taken into account when calculating theoretical spectra. Subsequent DFT geometry optimization using B3LYP/6-31G(d,p) brought 16 conformers within that energy range due to pronounced energy shifts when going from MM to DFT methods. These 16 conformers could be divided into groups of four based on their aliphatic dihedral angles, with each group containing 2×2 different hydroxy group orientations. The lowest energy structure is shown in Figure 3.7. The 8 lowest energy conformers were reoptimized using B3LYP/aug-cc-pVDZ, which is a larger basis set with diffuse functions and therefore assumed to yield more reliable results. For the purpose of Boltzmann weighting, the SCF energies

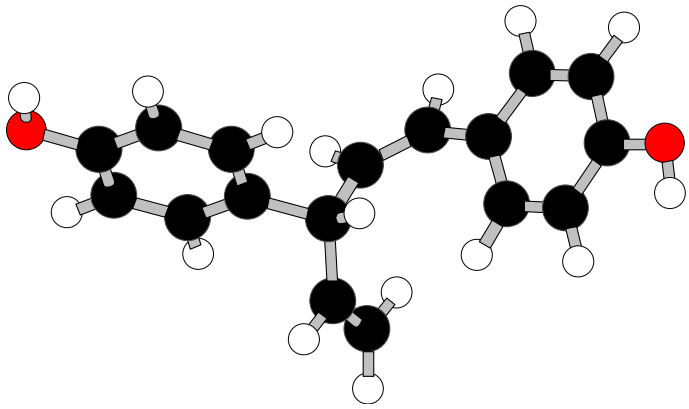

Figure 3.7: Optimized structure of (*S*)-nyasol in its lowest energy conformer, calculated using B3LYP/6-31G(d,p).

from the larger basis set were corrected with zero-point energy and Gibbs free energy contributions from the 6-31G(d,p) frequency calculations as suggested by a recent DFT study [91].

IR and VCD spectra were calculated using both B3LYP/6-31G(d,p) and B3LYP/aug-cc-pVDZ, as well as B3LYP/6-31G(d,p) with a self-consistent reaction field (SCRF) solvent model for DMSO.

3.3.2 Results and Discussion

The significant number of conformers posed a problem for recording a good VCD spectrum of nyasol, because their signals in some cases cancel each other. The calculated IR and VCD spectra of the 8 lowest energy conformers are shown in Figure 3.8, from which we can identify the spectral regions where VCD signals cancel or add up. The latter regions tell us where to look in an experimental VCD spectrum in order to determine the absolute configuration. Such regions are the strong positive signal at 1530 cm^{-1}, as well as 800–1000 and 1590–1650 cm^{-1}.

There is no substantial difference between the spectra calculated with these basis sets, but their peak positions are slightly different, as can be seen in Paper 2, Figure 4.

Our (+)-nyasol sample had turned red when we received it, indicating some degree of chemical change. An NMR spectrum was recorded at the Department of Chemistry at DTU, which identified the sample as nyasol, but with 10–20 % of pollution.[4] However, our UV-Vis spectrum (Paper 2, Figure 6) is in agreement with previous results [72].

IR and VCD spectra were recorded both in DMSO-d_6 and in a KBr pellet, using a Chiral*IR* instrument at SU to get improved baseline and S/N. Only the KBr pellet reveals the spectral region 800–1000 cm^{-1}, which is blocked by BaF_2 windows and DMSO-d_6. In Figure 3.9, the observed spectra are compared to

[4] Per-Ola Norrby, personal communication (data not shown).

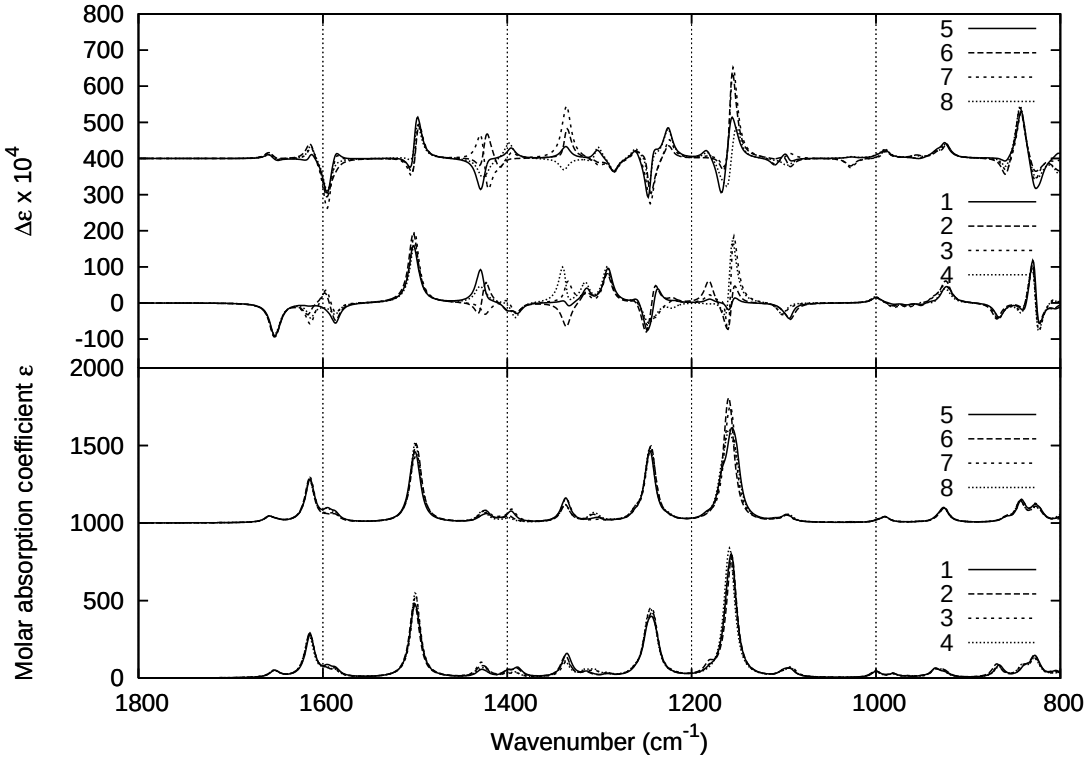

Figure 3.8: Calculated IR (bottom) and VCD (top) spectra of the 8 lowest energy conformers of (*S*)-nyasol in the gas phase, using B3LYP/aug-cc-pVDZ without frequency scaling. The spectra of conformers 5–8 are offset for clarity.

the Boltzmann weighted averages of the calculated IR and VCD from Figure 3.8. Calculated wavenumbers have been scaled by 0.97.[5] Paper 2, Table 2 gives assignments of most of the peaks present in the calculated spectra of the lowest energy conformer.

When comparing the calculated and experimental spectra, the crucial VCD spectral regions identified above display good agreement, especially in the 800–1000 cm^{-1} region of the KBr pellet measurement and around 1500 cm^{-1} in DMSO-d_6. Based on this comparison, we can assign the absolute configuration of the sample as (*S*)-(+)-nyasol.

There are some discrepancies in other spectral regions, which can be explained by examining the IR spectra. The intense modes calculated around 1185 cm^{-1} arise from O–H bending, which appear to be quenched by hydrogen bonding in both solution and KBr. There is also considerable broadening of the C–O stretching band around 1250 cm^{-1}, which we likewise suspect to be influenced by hydrogen bonding. In the KBr pellet, the sample molecules are still in proximity and can hydrogen bond.[6]

[5] According to the Computational Chemistry Comparison and Benchmark DataBase (CCCBDB), http://srdata.nist.gov/cccbdb/vibrations.asp.

[6] We can compare the pellet to a slice of salami, where the sample molecules are the red

A strange observation is the broad negative VCD signals around 1000–1100 cm^{-1}. The only reason we can think of is stress-induced birefringence artifacts from the KBr pellet.

The proposed effect of hydrogen bonding has been verified by DFT calculations with an explicit DMSO-d_6 molecule next to each OH group, see Figure 3.10, which compares implicit and explicit solvent inclusion. The latter is not shown in Paper 2. The overall agreement with the experimental IR spectrum improves with explicit solvent molecules, since the intensity of the 1185 cm^{-1} bands has decreased considerably, and the broad features in the 1200–1300 cm^{-1} region are better reproduced. The DMSO-d_6 modes introduced are primarily at 860, 1000, and 1040 cm^{-1}, *i.e.*, outside the spectral range of the measurement. Thus, our calculations with explicit solvent molecules work better than the SCRF (PCM) implicit solvation calculation shown in Paper 2 (Figure 4), because they take the specific solvent-solute interaction into account. In fact, the continuum solvent model turns out to intensify the discrepancy at 1185 cm^{-1}.

The calculated VCD spectrum of the lowest energy conformer with explicit DMSO-d_6 is of little use due to considerable artifacts, which probably arise because the single nyasol-DMSO-d_6 arrangement considered is not representative of reality. Rather than considering an ensemble of arrangements, we have only one, thereby losing isotropy and introducing artificial VCD signals from the chiral nyasol-DMSO-d_6 arrangement. The only recognizable experimental feature seems to be the 1510 cm^{-1} band. Considerable improvement of the fit is achieved by including the next three conformers and averaging, which apparently make most of the DMSO-d_6 artifacts cancel each other. The two corresponding IR spectra look similar, as we would expect from their insensitivity to the additional chirality introduced.

"meat" and the KBr particles play the role of the fatty bits.

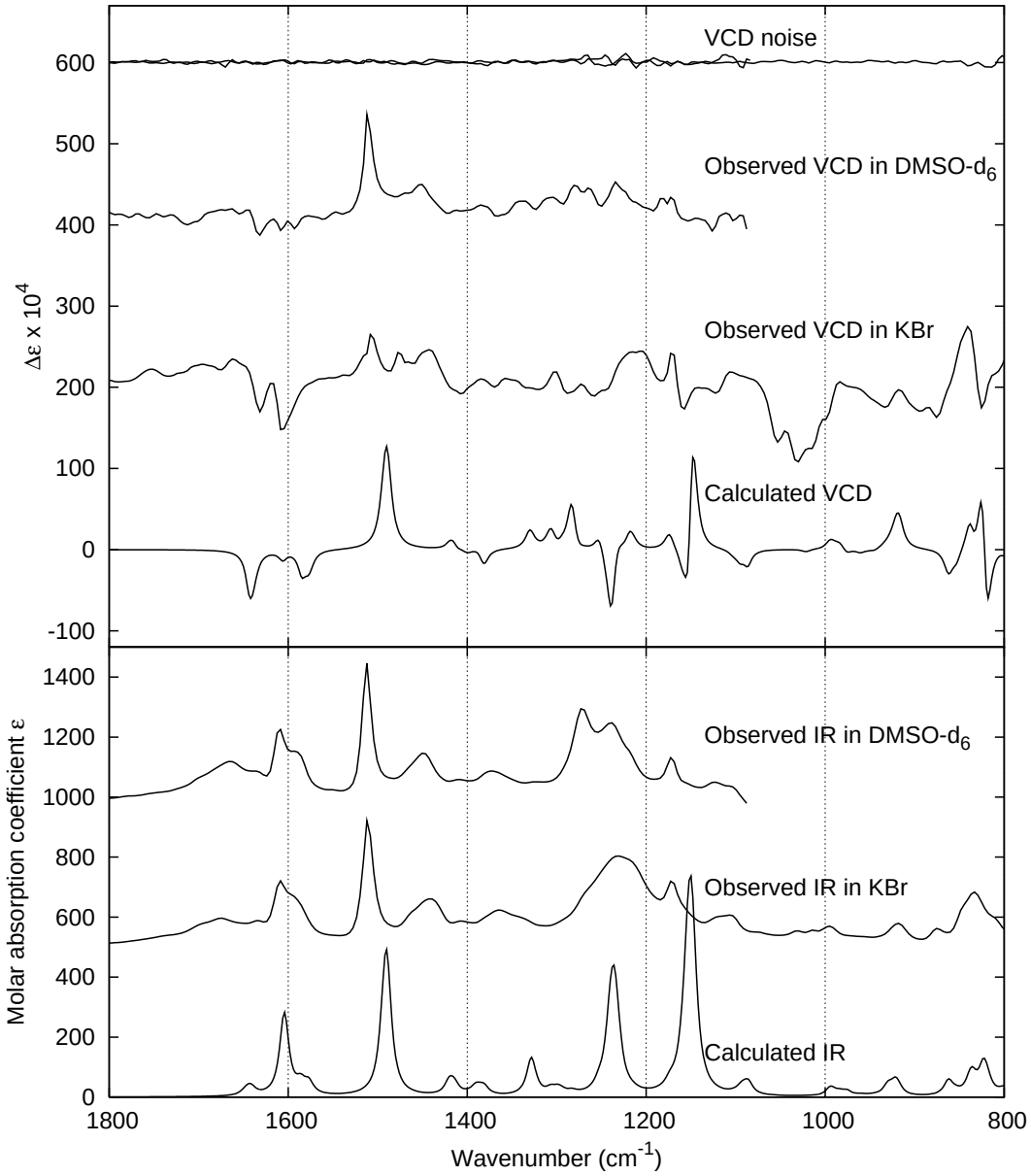

Figure 3.9: IR (bottom) and VCD (top) spectra of nyasol. Calculated spectra are Boltzmann weighted averages of the 8 lowest conformers of (*S*)-nyasol using B3LYP/aug-cc-pVDZ, with wavenumbers scaled by 0.97 and a half-width of 6 cm^{-1}. Samples measured are 0.20 M nyasol in DMSO-d_6 solution (5.0 mg of nyasol in 100 µL DMSO-*d*6 in a BaF_2 cell with 100 µm path length) as well as a KBr pellet (≈2 mg nyasol in 250 mg KBr, ⌀ 13 mm × 1 mm). Spectra were measured with 8 cm^{-1} resolution and the PEMs set at 1400 cm^{-1}, using an acquisition time of 9 h in solution and 31 h for the KBr pellet. Spectra in DMSO-d_6 have had the solvent signals subtracted, and the KBr pellet spectra have been converted to molar absorption coefficient by scaling the absorbance to match that of the solution.

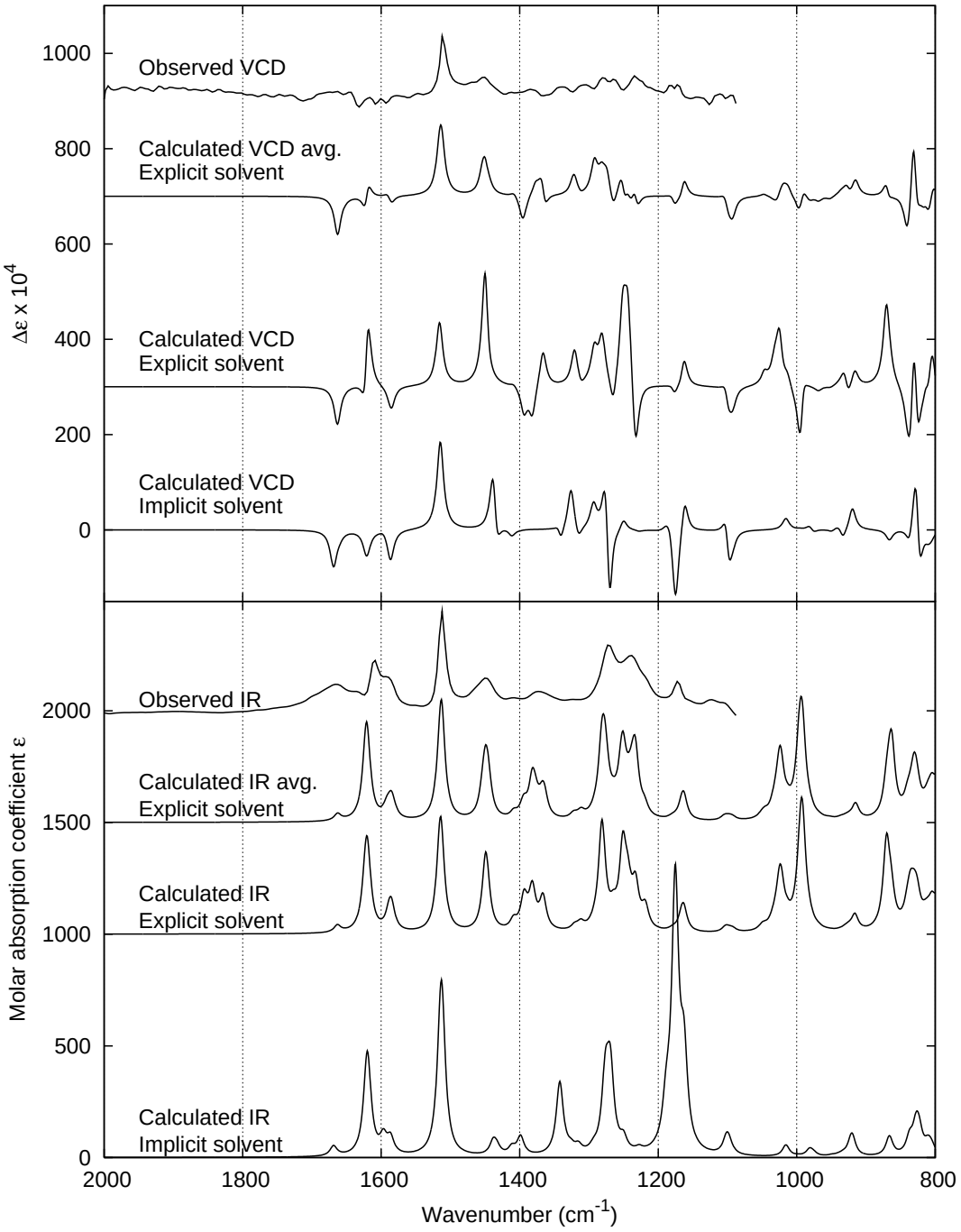

Figure 3.10: Calculated IR (bottom) and VCD (top) spectra of (*S*)-nyasol with an implicit PCM solvation model using B3LYP/6-31G(d,p), as well as explicit solvent calculations with 2 DMSO-d_6 molecules for both the lowest energy conformer and the four lowest (averaged), using B3LYP/6-31G(d,p). Calculated wavenumbers are scaled by 0.97 and peaks broadened to 6 cm^{-1}. Experimental spectra in DMSO-d_6 solution (solvent background subtracted) are shown above (same data as in Figure 3.9).

3.4 Curcuphenol Dimer

As part of the collaboration with Prof. Nafie and Freedman's lab at SU, we were asked to investigate the curcuphenol dimer isolated from the marine snail *Didiscus aceratus* by a group from University of California, Santa Cruz [49]. A range of pharmaceutically interesting compounds had been isolated from this snail, all of which were derivatives of (*S*)-(+)-curcuphenol with the IUPAC name 2-((S)-1,5-Dimethyl-hex-4-enyl)-5-methyl-phenol [123]. Specifically, we were asked to elucidate the axial chirality of two curcuphenol dimer atropisomers, which hereafter will be referred to simply as the dimers. Samples of monomeric (*S*)-curcuphenol and both of its dimers were received. The structure of (*S*)-curcuphenol and its dimer are shown in Figure 3.11. The dimer has two chiral centres in addition to the chiral axis, which emerges upon dimerization and is fixed in (*P*) or (*M*) configuration by steric hindrance. Below, we describe our part of the investigations, which are included in a publication. This paper is enclosed as Paper 3.

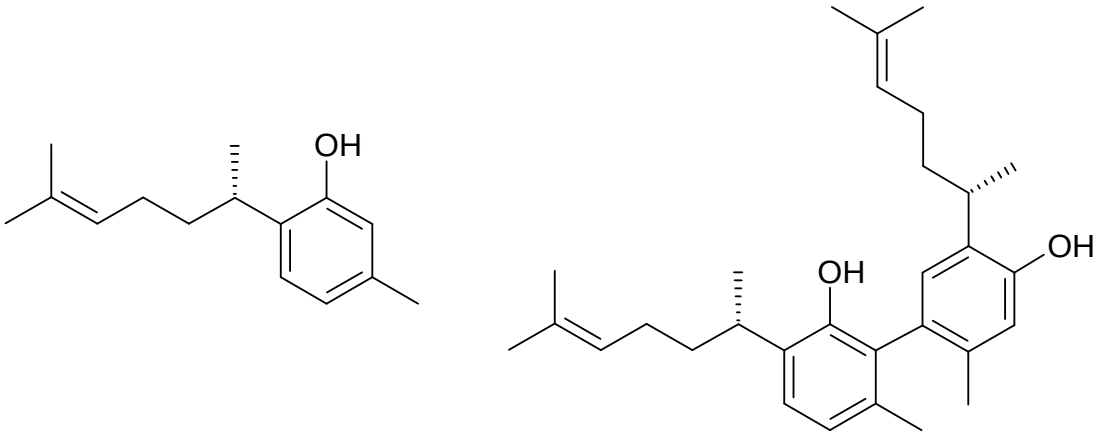

Figure 3.11: Chemical structure of (*S*)-curcuphenol (left) and its dimer (right). The dimer has a chiral axis along the bond connecting the phenol rings, which gives two possible stereoisomers (atropisomers).

3.4.1 Theoretical Model Compound

The optimized structure of one conformer of a dimer is shown in Figure 3.12, and it suggests the problem of a large conformational space. Each half of the dimer has five variable dihedral angles in addition to the methyl groups, so this is an even greater challenge than nyasol (treated in Section 3.3). A conformational search with HyperChem using the force field MM+ [54] or the semi-empirical method PM3 [111] gave 20 conformers in the gas phase for curcuphenol alone, so we could not calculate VCD spectra of all possible dimer conformers. We also cannot be sure that the conformer displayed in Figure 3.12 is the lowest energy state.

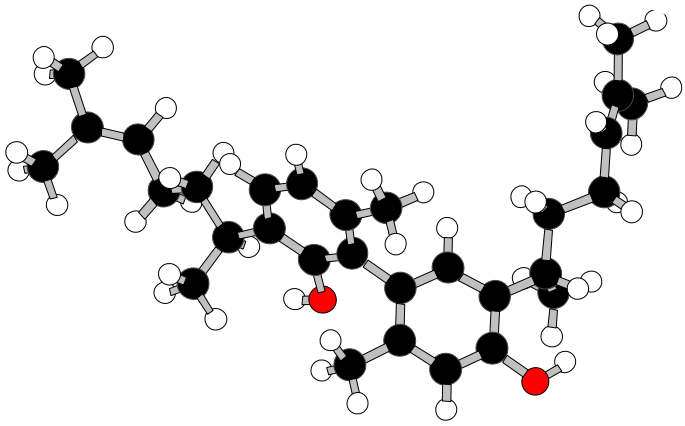

Figure 3.12: DFT optimized structure of a curcuphenol dimer, calculated using B3LYP/6-31G(d).

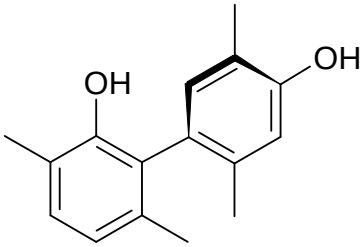

Figure 3.13: Chemical structure of 3,6,2′,5′-tetramethyl-biphenyl-2,4′-diol, a truncated model compound for the (*P*)-dimer of curcuphenol. It has axial chirality, but no chiral centres.

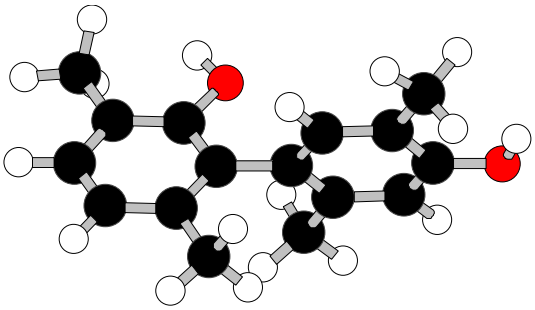

Figure 3.14: DFT optimized structure of the truncated model compound for the (*P*)-atropisomer of the curcuphenol dimer, calculated using B3LYP/6-31G(d).

Rather, we chose only to conduct DFT calculations of the most relevant fraction of the dimer, which contains the axial chirality but cuts away the flexible chains and chiral centers by turning the latter into methyl groups. This theoretical model structure is shown in Figure 3.13. The idea was to calculate the VCD of this chiral axis structure and compare it to the measured difference VCD of the dimers. Since the axial chirality of the dimers is opposite whereas their central chirality is identical, this subtraction was hoped to leave us with

spectral features pertaining primarily to the axial chirality. This strategy turned out to be successful.

The model compound has very limited conformational flexibility: the lone pairs of each oxygen can point towards or away from the neighbouring methyl group. The former orientation is favoured by a total of 18 kJ/mol over the latter, when both structures are optimized using DFT with the B3LYP functional and 6-31G(d) basis set. Thus, it was assumed adequate to consider only the lowest energy state. Figure 3.14 shows this optimized structure.

3.4.2 Experimental and Calculated Spectra

DFT calculations of the IR and VCD of the model compound above were carried out with Gaussian 03 at the B3LYP/6-31G(d) level of theory. The vibrational frequencies output by Gaussian were scaled by 0.97.[7] Furthermore, the calculated IR and VCD intensities (given in terms of dipole and rotational strength) were converted into Lorentzians with a half-width of 6 cm^{-1} for comparison to experiment.

The measured IR and VCD spectra of curcuphenol and its dimers are shown in Figure 3.15, with the experimental conditions outlined in Table 3.1. Because the VCD signals of curcuphenol are largest between 1100–1300 cm^{-1}, we must expect that region of the VCD spectra for the dimers to be a poor indicator of the axial chirality. In turn, only the dimers have significant VCD bands above 1400 cm^{-1}, so these must arise from the chiral interaction of the two monomers and therefore bear a fingerprint of the axial chirality. This is confirmed by the opposite sign of those VCD bands. The dimer VCD signals below 1400 cm^{-1} are not opposite in sign, because the identical chiral centers contribute nearly equally. Thus, the region above 1400 cm^{-1} will be the most important one to compare with the calculated spectra.

The IR spectrum of curcuphenol has many similarities with those of the dimers, since they have large parts in common. The two dimer IR spectra look almost identical, except for minor discrepancies around 1000–1050 cm^{-1} and 1700 cm^{-1}, arising either from impurities or the fact that the dimers are diastereomers.

Sample	Concentration	Path length	Acq. time
Curcuphenol	0.59 M (8.4 mg in 65 μL)	54 μm	20 h
Dimer #1	0.11 M (8.3 mg in 180 μL)	98 μm	10 h
Dimer #2	0.23 M (10.8 mg in 110 μL)	98 μm	10 h

Table 3.1: Experimental conditions for spectra of (*S*)-curcuphenol and its atropisomer dimers. All spectra were recorded using $CDCl_3$ solutions in BaF_2 cells, with the same acquisition time for sample and solvent. The resolution was 4 cm^{-1}, and the two PEMs of the Chiral*IR* instrument were set at 1400 cm^{-1}.

[7] This scaling factor lies within the range suggested by the CCCBDB database, http://srdata.nist.gov/cccbdb/vibrations.asp.

The calculated VCD spectrum of the model compound can be compared to difference VCD spectra of the two atropisomers, because this subtraction almost eliminates the spectral features of the alkyl side chains and their chiral centers, which are identical in the two atropisomers. The calculated spectra of the model compound along with the dimer IR and difference VCD (#2 – #1)/2 of the atropisomers is shown in Figure 3.16. The overall agreement between observed and calculated VCD indicates that dimer #2 is the (*P*)-atropisomer (and *vice versa*).

Although the calculated and observed IR spectra do not pertain to the same compound and so do not have to coincide, the bands around 1500 cm^{-1} and higher compare well.

The success of this VCD comparison is partly because some spectral features of the axial chirality are in a spectral region with negligible signals from the chiral centres. But even the spectral region below 1400 cm^{-1} shows very good agreement between calculated and experimental spectra, confirming the assumption made about the cancellation of central chirality features.

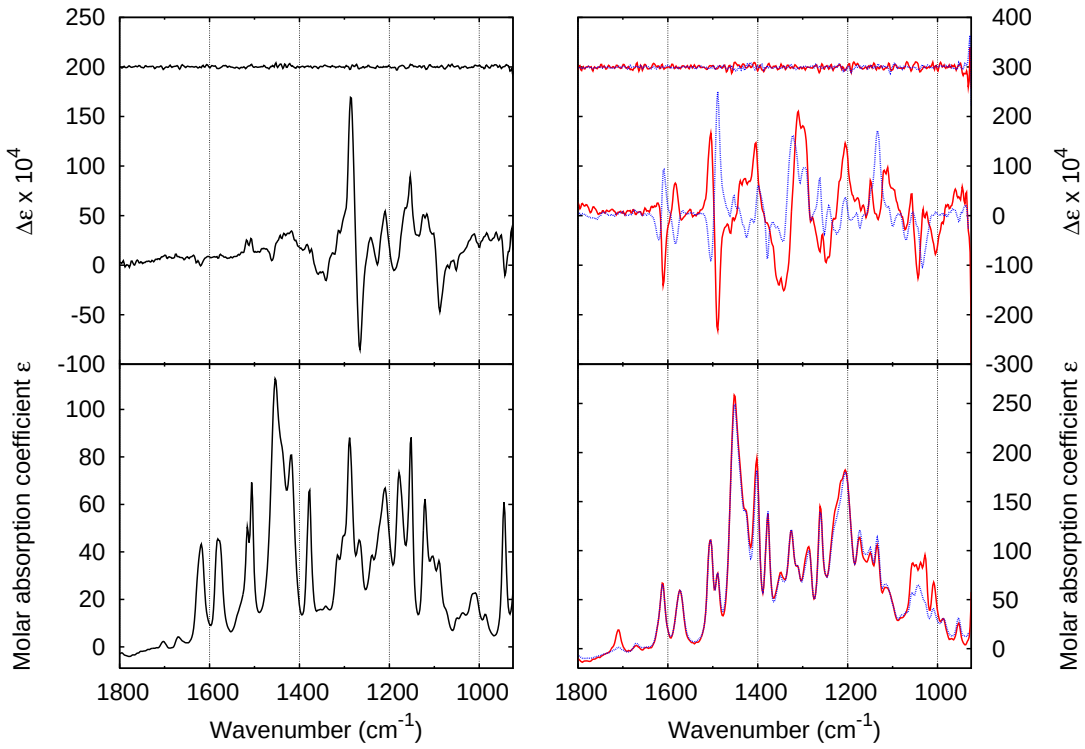

Figure 3.15: Observed IR (lower traces) and VCD spectra (upper traces, with the VCD noise level shown above) of (*S*)-curcuphenol (left) and its dimers (right), #1 (—) and #2 (····). Experimental conditions are given in Table 3.1 above. Solvent spectra are subtracted, and absorbance converted into molar absorption coefficient using Lambert-Beer's law (2.30).

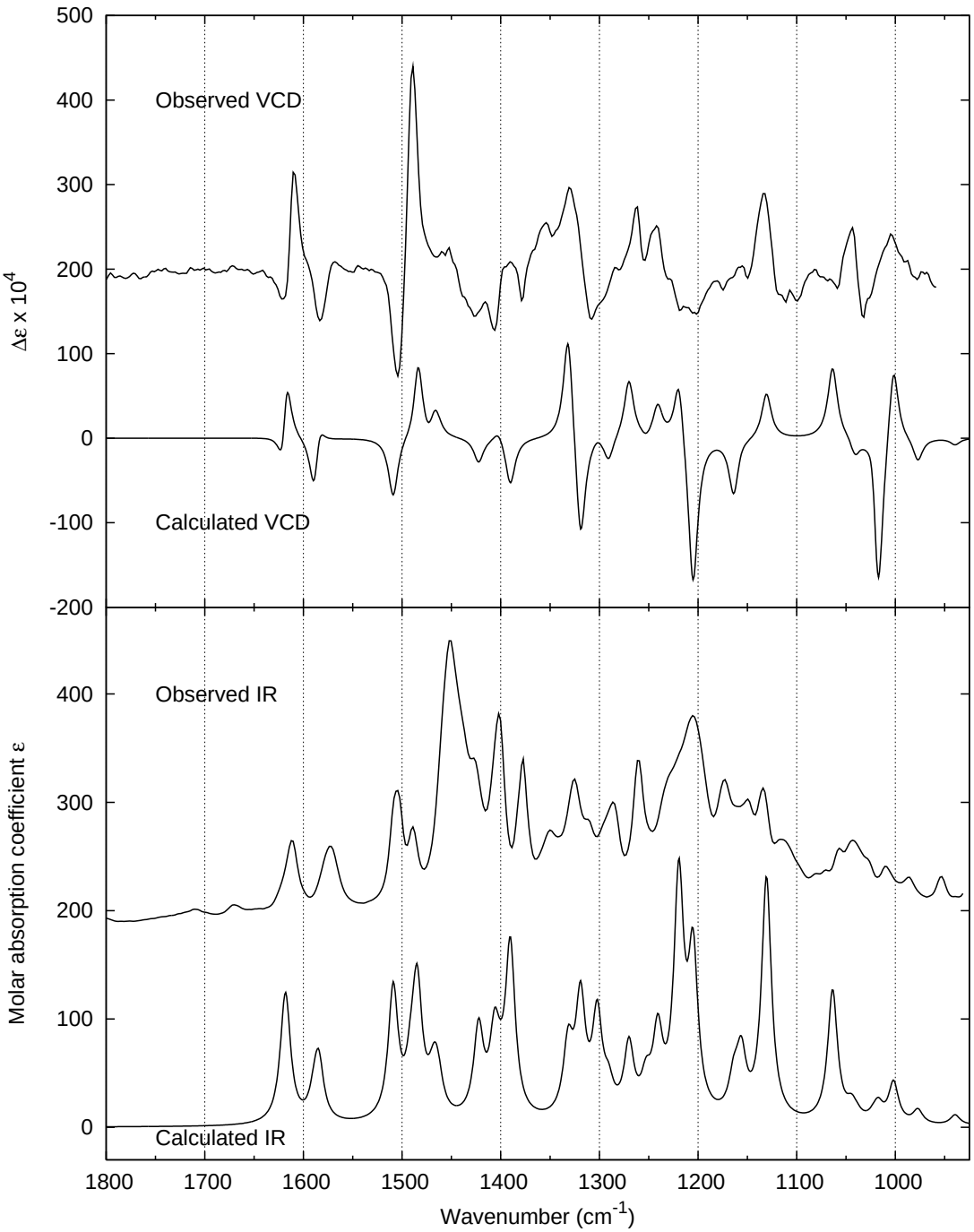

Figure 3.16: Observed IR spectrum (bottom) and difference VCD (#2 – #1)/2 of the atropisomers (top) vs. DFT calculated spectra for the (*P*)-atropisomer of the model compound in Figure 3.13, using B3LYP/6-31G(d). Experimental conditions are given in Table 3.1.

3.5 Ginkgolide B

We have embarked on another collaboration with the Department of Medicinal Chemistry at DFU, where Assoc. Prof. Kristian Strømgaard is involved in investigating derivates of ginkgolides [113,114,120], which are natural products from the *Ginkgo biloba* tree. Extracts from this tree have been used for medical purposes for millenia. The benefits should include anti-asthmatic effects and memory improvement [60,86,112]. A number of terpene trilactones have been extracted from *Ginkgo biloba*, among them the ginkgolides. Most of their known physical properties and spectroscopic data are summarized in a recent review [119]. However, to the best of our knowledge no VCD spectra have been published previously.[8]

We were asked to obtain theoretical and experimental VCD spectra to verify the absolute configuration of Ginkgolide B (GB), one of several related ginkgolides as illustrated in Figure 3.17. Dr. Niels H. Andersen initiated measurements of GB and one of the ginkgolide derivates under study at DFU. Part of our measurements were carried out at SU. Our VCD studies are presented in a preliminary manuscript attached as Paper 4.

Of the compounds studied during this Ph.D. project, GB is the one with the most chiral features, since it has an impressive 11 chiral centres among its 54 atoms. The absolute configuration is known from the published X-ray structure [31]. A DFT study of the structure and IR spectrum of GB has also been published, where a conformational search and subsequent geometry optimization of the lowest energy structure matched the X-ray structure [126]. There are two intramolecular hydrogen bonds, one of which becomes intermolecular upon crystallization.

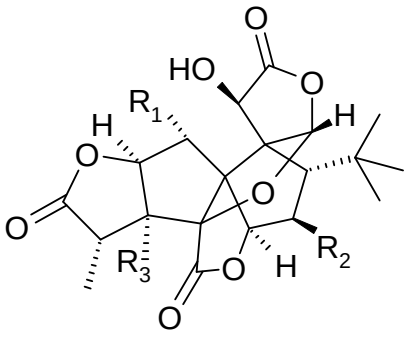

Structure	R_1	R_2	R_3
Ginkgolide A	H	H	OH
Ginkgolide B	OH	H	OH
Ginkgolide C	OH	OH	OH
Ginkgolide J	H	OH	OH
Ginkgolide M	OH	OH	H

Figure 3.17: Chemical structure of a family of ginkgolides [119], where the residues R_1–R_3 differ as listed to the right. Hydrogens at chiral centres are shown for clarity. Depending on the residues, there are 10–12 chiral centres. Only ginkgolide B (with 11 chiral centres) has been studied in the present work.

[8] Readers looking for the references should be aware that two of them have been published with typos in their titles [31,86].

3.5.1 Theoretical and Experimental Methods

DFT calculations were performed with Gaussian 03 [41], using the B3LYP functional and 6-31G(d,p) basis set. An augmented basis set of Dunning, aug-cc-pVDZ [29], was also tried but failed to converge. A set of six conformers were provided, optimized with B3LYP/6-31G(d).[9] We calculated the IR and VCD spectra of the lowest energy conformer using the 6-31G(d) and 6-31G(d,p) basis sets.

Ginkgolides are very stable compounds, soluble in CH_3OH, CH_3CN, DMSO and others, but insoluble in CH_3Cl and CCl_4 [119]. In order to reduce solvent absorbance and solvent-solute interactions, we decided to use deuterated acetonitrile, CD_3CN, wherein 1.8 mg of GB was dissolved to obtain a total volume of 50 μL, corresponding to an 85 mM solution when using the calculated MW = 424.4 g/mol.

After measuring the IR and VCD spectra in CD_3CN, the sample was restored by letting the solvent evaporate. Roughly half of the GB left was then ground with 250 mg KBr in a Wig-L-Bug® for 30 s and pressed into a pellet under 13000 lbs for 4 min in order to record the solid-state spectra of GB.

The spectra presented below were measured on the modified Chiral*IR* FT-VCD at SU, using a resolution of 4 cm^{-1} with the instrument optimized at 1400 cm^{-1} and acquisition times of 4–12 h.

3.5.2 Results and Discussion

A population analysis of the provided B3LYP/6-31G(d) conformers using one of our Unix scripts (section B.1) found of a dominating lower energy conformer (95 %), with energy differences 7.3 kJ/mol and 16 kJ/mol from the next available conformers (the structural difference lies in the orientation of the three OH groups). Hence, it was reasonable only to consider the dominating conformer, the structure of which is shown in Figure 3.18.

Reoptimization and VCD calculation of the lowest energy conformer with the 6-31G(d,p) basis set gave only minor changes compared to the 6-31G(d) calculated, most notably a slight intensity increase at 1250 cm^{-1}. So the extra polarization functions do not contribute much, and in fact the fit to the experimental band at 1250 cm^{-1} is better with 6-31G(d,p). Figure 3.19 compares the experimental spectra in CD_3CN solution and KBr pellet to the B3LYP/6-31G(d) calculation. We have used a frequency scaling factor of 0.98 for the calculated spectra, which is a compromise between the higher and lower wavenumber regions, where the scaling factor seems too high or too low, respectively. Ideally, one should use a nonuniform scaling. Our scaling factor deviates from the factor 0.945 suggested in an earlier IR study [126]. Their spectrum was of poorer quality, though.

The IR spectra have many bands that overlap, and the condensed ring structure of GB also makes a rigorous assignment difficult. But a good overall

[9] From a master student project by Niels Johan Christensen.

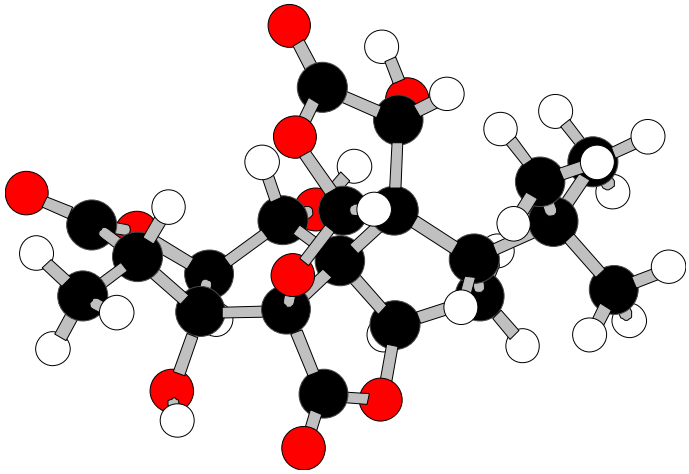

Figure 3.18: DFT optimized structure of ginkgolide B in the lowest energy structure, using B3LYP/6-31G(d,p).

agreement can be seen. The most notable difference is improper scaling of the lactone C=O stretches just below 1800 cm^{-1}, which also do not appear as a doublet band in CD_3CN, presumably due to hydrogen bonding or other solute-solute interactions. Such interactions are also likely to influence the O–H bending modes, one of which (1170 cm^{-1}) appears too intense in the calculation.

Water traces can be seen in the IR of the KBr pellet at 1625 cm^{-1}, and the CD_3CN solution seems to have a small negative band there, suggesting that the solvent spectrum used for subtraction had more water than the sample. Both KBr and CD_3CN are hygroscopic, so this is not unusual, even though care was taken to keep the samples dry.

As we turn to the VCD spectra, we see very good agreement, in particular between calculation and measurement in solution. The aforementioned discrepancies of C=O stretch frequency scaling and O–H bending persist. In turn, the C=O stretching VCD couplet is resolved also in CD_3CN, where the IR doublet was not. For the KBr pellet, the VCD features in this region are sharper, as one would generally expect for the solid state, but there is also a broad positive feature just above 1700 cm^{-1}, which has no visible parent IR absorbance and is not readily interpreted. The calculated spectrum has two closely spaced negative bands at 1867 and 1874 cm^{-1} and one positive band at 1892 cm^{-1}, which matches the sign pattern of the sharp features, because there is a shoulder on the negative band. So the origin of the broad feature is uncertain.

From the excellent agreement of calculated and observed VCD spectra, we have verified the absolute configuration of GB. That is an impressive achievement, considering the 11 chiral centres present, and it would most likely not be possible if there had been more conformational flexibility in the compound.

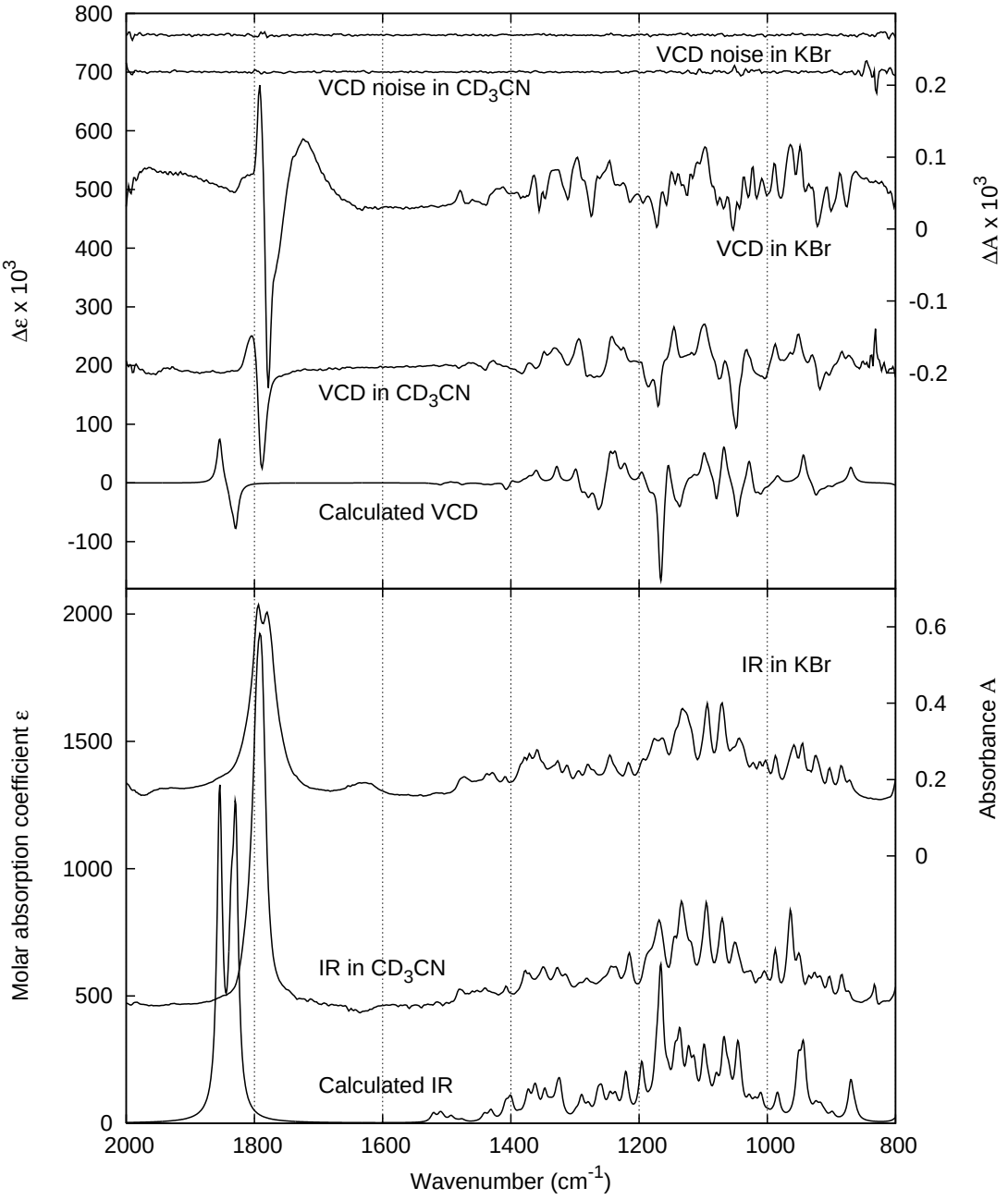

Figure 3.19: Observed vs. DFT calculated IR (bottom) and VCD (top) spectra of ginkgolide B. Calculated spectra are for the lowest energy conformer in the gas phase, using B3LYP/6-31G(d) with a scaling factor of 0.98 and half-width 5 cm^{-1} (left axis). Experimental spectra are recorded in CD_3CN solution (solvent subtracted, left axis) and in a KBr pellet (right axis). VCD noise levels are shown at the very top. Spectra were measured on the modified Chiral*IR* instrument, with 4 cm^{-1} resolution and the PEMs set at 1400 cm^{-1}. Further conditions for the CD_3CN solution: 1.8 mg GB in 50 µL (85 mM), in a 54 µm BaF_2 cell using 12 h acquisition time for sample and solvent. For the KBr pellet: ≈1 mg GB in 250 mg KBr (⊘ 13 mm × 1 mm, pressed for 4 min at a load of 13000 lbs) using 4 h acquisition time.

3.6 Summary

During this chapter, we have studied several small or medium-sized molecules (from a DFT viewpoint). Their number of chiral centres ranges from 1 to 11, and their conformational degrees of freedom range from 1 to 11 dihedral angles, as can be seen from table 3.2, which compares the basic features of the organic sample molecules studied.

Sample	Atoms	MW (g/mol)	Angles	Chiral features
α-Me-phenyloxirane	20	134.2	1	1 centre
cis-β-Me-phenyloxirane	20	134.2	1	2 centres
trans-β-Me-phenyloxirane	20	134.2	1	2 centres
Nyasol	35	252.3	6	1 centre
Curcuphenol dimer	74	434.7	11	2 centres, 1 axis
Ginkgolide B	54	424.4	4	11 centres

Table 3.2: Comparison of physical properties of the molecules treated in this chapter. "Angles" is the number of variable dihedral angles apart from methyl rotations.

Since the size and conformational flexibility of these samples vary considerably, we have provided a good overview of the capabilities of the methods used, primarily for absolute configuration determination.

In all cases, we have successfully determined or verified their absolute configuration by comparing experimental and calculated VCD intensities. The IR spectra have also been compared as a structural fingerprint. Although IR lacks the information on chirality, often other features are more clearly seen in IR than VCD, such as the presence of water contamination or whether calculated wavenumbers have been scaled appropriately.

We have used two different experimental setups, either the Thermo-Nicolet Nexus 870 FT-IR spectrometer at QuP or a BioTools Chiral*IR* FT-VCD instrument in Syracuse, NY. The latter has a more advanced setup with simultaneous operation of two IR sources and two PEMs, and it obviously outperforms the other instrument in terms of S/N and baseline flatness.

Some solvent effects have been observed. Polar solvents interact more with the solute, as we saw primarily in the case of nyasol in DMSO-d_6, where O–H bending features were disturbed by intermolecular hydrogen bonding. Explicit inclusion of solvent molecules resolved some discrepancies between gas phase calculations and solution measurements. On the other hand, using implicit solvent models gave only minor corrections to the gas phase calculations.

The use of a solid-state matrix (KBr pellets) allowed for spectroscopy in the solid phase, although for a viscous sample like nyasol it was rather like a neat sample. KBr has the benefits of allowing a wider spectral range and usually better resolved peaks than in solution. But the pellet also influences the VCD measurements by introducing birefringence artifacts which cannot be subtracted using a pure KBr pellet, since the two pellets would not have identical stress profiles. So there is less reproducibility.

Our most flexible sample was the curcuphenol dimer, in which case we did not bother to perform a conformational analysis, because the subsequent number of DFT jobs was anticipated too large to be feasible. Fortunately, we were able to come up with a smaller model structure able to reproduce the spectral features in question. Hence, nyasol was our most computationally demanding DFT study so far, with 26 conformers geometry optimized using B3LYP/6-31G(d).

The largest molecule studied was the curcuphenol dimer, but a smaller model strategy provided the theoretical foundation of the conclusion. So ginkgolide B with its 11 chiral centres is the largest structure, for which we have calculated IR/VCD spectra in this chapter. That could be achieved within about a week. So we have not reached the system size limit of the present QM methods. The next chapter will bring us closer to that limit as we bring heavy metal centres into play, with their many electrons and different spin states—not to mention the large complexes they form.

Chapter 4

Transition Metal Complexes and Metalloproteins

4.1 Introduction

VCD calculations on metal complexes have only recently been undertaken, pioneered by our collaborators at SU [39,52]. The ability to compare experimental and calculated VCD spectra of such (usually electron-rich) compounds opens new possibilities, especially when REVCD theory becomes implemented in DFT software to yield more reliable calculations of complexes with low-lying electronic transitions.

We became involved in some studies of transition metal complexes and metalloproteins while staying at SU, the results of which are presented in this chapter. First, there is a thorough characterization of some rhenium ($Z = 75$) complexes. These are not of direct biological relevance, except for the use of rhenium in radiopharmaceuticals [68]. These rhenium compounds are used in a search for parity violation (PV) at the sub-atomic level, which indirectly may be highly relevant to biology if PV turns out to have an influence on what we may call the enantiomeric excess of life, *i.e.*, the overwhelming natural predominance of one enantiomer over the other in the basic building blocks in biology [71,99].

REVCD effects were not the issue with the rhenium complexes, but were observed in several other cases, which are reviewed in Sections 4.3–4.4. Two complexes were being studied experimentally, while we were running DFT calculations on them. Additionally, we ran a series of VCD experiments on myoglobin with different ligands, where new REVCD features were observed. Unfortunately, proteins are well beyond the exponential wall of DFT [66], so we were restricted to running calculations on just the heme group and ligands, hoping that they would reproduce some of the observed REVCD in spite of the presently lacking theoretical implementations.

4.2 Rhenium(V) Complexes

The rhenium complexes studied in this project are part of an ongoing search for parity violation (PV) in IR spectroscopy, *i.e.*, slightly different absorption frequencies of opposite enantiomers induced by interaction with the weak nuclear force, which is chiral in itself. The absorption frequency difference is predicted by the standard model to be infinitesimal, requiring very advanced techniques for its observation, which are currently investigated in a French lab [24, 25, 106]. More specifically, the Re=O stretching mode of several chiral oxorhenium(V) complexes is studied with an ultra-stable tunable CO_2 laser. It has turned out that the PV energy difference scales with atomic number approximately as Z^5, therefore the present rhenium samples are very promising candidates for its observation [24, 103, 104].

Here, we present our benchmark analysis of two oxorhenium(V) complexes containing the hydrotris(1-pyrazolyl)borate (Tp) ligand. We recorded IR and VCD spectra of the compounds and performed density functional theory (DFT) calculations of those same spectra using several basis sets in order to find a good methodology for further studies. The synthesis was done by collaborators in France, and our spectroscopic measurements were carried out at the Department of Chemistry at SU, while calculations were running in Denmark. These studies are included in the attached Paper 5, which describes some newer rhenium complexes as well. To the best of our knowledge, this is the first VCD study involving rhenium compounds.

Previous publications containing DFT calculations on Re complexes have used different functionals, primarily B3LYP [45, 67, 93, 122], but also BPW91 [122] and B3PW91 [20]. Basis sets used for Re include LanL2DZ [67], SDD [122], Hay-Wadt VDZ (n+1) ECP [45], and Stuttgart basis sets [20, 104]. We present a comparison of spectra calculated using these four basis sets at the B3LYP level.

Four samples (two enantiomeric pairs) were received: (S_{Re},$S_{O\text{-}C}$,$R_{C\text{-}N}$)-TpReO(ephedrine), (S_{Re},S_C)-TpReO(proline) and their enantiomers, which we refer to as (S,S,R)-**1**, (R,R,S)-**1**, (S,S)-**2** and (R,R)-**2**, respectively.[1] They were synthesized in enantiopure form according to literature procedures [34], and their structures are shown in Figure 4.1. The calculated MW is 578.45 g/mol for **1** and 528.35 g/mol for **2**.

4.2.1 Theoretical and Experimental Methods

IR and VCD spectra of all samples were recorded under several conditions, both in solid state (in KBr pellets) and in solution ($CHCl_3$ and $CDCl_3$) contained in BaF_2 cells. KBr pellets were prepared by grinding 3 mg of the sample, then mixing that with dry KBr and grinding again. Part of that mixture was then mixed with more KBr to yield a pellet with the desired level of absorbance. Pellets were pressed for typically 5 min at a load of 13000 lbs. The IR and VCD

[1] When assigning an *R* or *S* to the chiral Re centre, the Tp ligand can be considered as a whole, allowing one to use the Cahn-Ingold-Prelog rules.

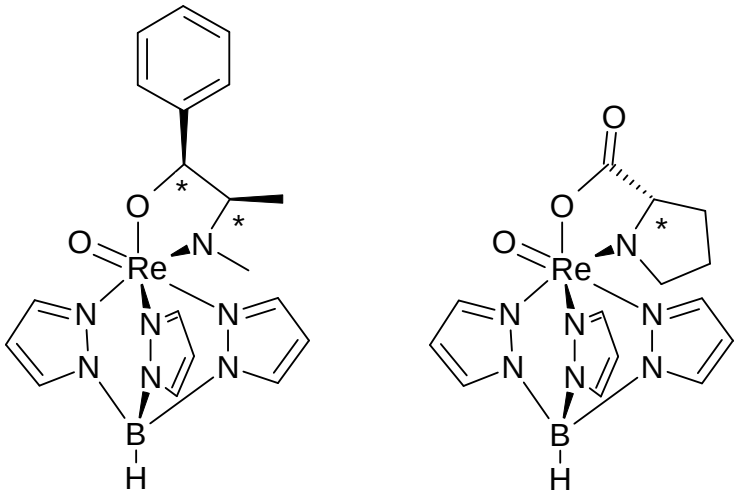

Figure 4.1: Chemical structures of the two rhenium complexes studied in this thesis: (S_{Re},$S_{O\text{-}C}$,$R_{C\text{-}N}$)-TpReO(ephedrine) (**1**, left) and (S_{Re},S_C)-TpReO(proline) (**2**, right), where Tp=hydrotris(1-pyrazolyl)borate. In addition to Re being a chiral centre, the ephedrine and proline ligands add 2 and 1 chiral centre, respectively, where indicated.

Solvent/matrix	Chloroform		KBr pellets	
Sample amount	≈5 mg in 150 μL		≈0.5 mg in 250 mg	
Spectrometer	Chiral*IR*	Magna-IR 850	Chiral*IR*	Magna-IR 850
Path length	94 μm	106 μm	1 mm	1 mm
Spectral range (cm^{-1})	800–2000	800–4000	800–2000	400–4000
Acquisition time	12 h	90 min	5–20 h	35–90 min

Table 4.1: Experimental conditions for IR and VCD spectroscopy of the rhenium(V) complexes.

spectra were obtained on a Chiral*IR* spectrometer with two PEMs optimized at 1400 cm^{-1}. The resolution was 4 cm^{-1}. Higher resolution (0.25 cm^{-1}) IR spectra were recorded on a Magna-IR 850 spectrometer (Thermo Nicolet, Madison, WI), where the actual data spacing was 0.12 cm^{-1}. Further experimental conditions are given in Table 4.1.

Prior to running DFT calculations, structures of the sample molecules were constructed in HyperChem, and their possible conformers were considered. The proposed structures were relaxed in HyperChem using the MM+ force field [54], with Re temporarily replaced by Mn because no force field for Re was available. These two elements have similar valence and coordination properties, so apart from the size difference, the geometry estimate should be useful. Both complexes have distorted octahedral coordination around Re(V).

DFT calculations were carried out with Gaussian 03 [41] using the B3LYP functional and different basis sets: either LanL2DZ or SDD for all atoms, or 6-31G(d) for elements H through O combined with a larger basis set for Re (Hay-Wadt VDZ (n+1) ECP or Stuttgart RSC 1997 ECP [1]). Molecular geome-

tries were optimized, and vibrational spectra for isolated (gas phase) species were calculated, primarily utilizing the IBM cluster at Centre for Scientific Computing, Aarhus, Denmark. The calculated vibrational frequencies were scaled by 0.97, a typical value for B3LYP calculations. Furthermore, the calculated IR and VCD intensities were converted into Lorentzians (HWHM=5 cm^{-1}) for comparison with experiments.

4.2.2 Conformers and IR/VCD Spectra

Only one conformer for **1** was identified (**1a**), whereas **2** has two different ways of puckering the five-membered proline ring (**2a** and **2b**). The optimized structures from Gaussian 03 are shown in Figure 4.2. In the gas phase, the calculated energies for the latter two conformers differ by 0.4696 kJ/mol according to the LanL2DZ basis set, corresponding to a 55 vs. 45 % population, if we assume a Boltzmann distribution. With the Stuttgart and 6-31G(d) basis sets, the difference is smaller: 0.0548 kJ/mol, suggesting almost equal populations. We denote the two conformers **2a** and **2b**, where **2a** has the lower energy. No systematic conformation search was performed, so there could be more conformers possible. However, two other proline ring conformers were investigated, but they both converged back to one of the previous ones. Similarly, an alternative orientation of the phenyl group in **1a** was tried, but it converged to the one previously found. Very little variation is seen in the structures when different basis sets are used for geometry optimization.

We also calculated the energy of alternative diastereomers by inverting the chirality of the rhenium, which is equivalent to removing the bidentate proline or ephedrine ligand and putting it back the other way around. Geometry optimization with B3LYP/LanL2DZ resulted in a **1a** diastereomer 12.6 kJ/mol higher in energy, suggesting a population fraction of 0.6 %. For **2a**, the difference was even more pronounced: 21.2 kJ/mol. Thus, it is reasonable to assume diastereomeric purity of the samples. IR and VCD spectra were calculated for both conformers **2a** and **2b**, since they were expected to be present in roughly equal amounts and thus both contribute to the observed spectra.

We obtained good quality experimental IR and VCD spectra, especially for the samples in solution. $CHCl_3$ and $CDCl_3$ are chemically identical but have different spectral windows, allowing us to get continuous spectral coverage from 800–4000 cm^{-1}. Because the BaF_2 windows cut off below 800 cm^{-1}, only the KBr pellets can be studied in the region 400–800 cm^{-1}, and only with the Magna-IR 850 instrument, because this region is outside reach of the VCD instruments used, which both have a BaF_2 lens in front of the detector.

Generally, the enantiomeric pairs of **1** and **2** yield practically indistinguishable IR spectra and negated VCD spectra, as exemplified by their IR and raw VCD spectra in $CDCl_3$ solution shown in Figure 4.3. These VCD spectra are very close to opposite (within a low noise level), when one takes the baseline shift and curving into account. To eliminate absorption artifacts, one can either use the solvent or racemic VCD as baseline. Thus, the average VCD spectrum

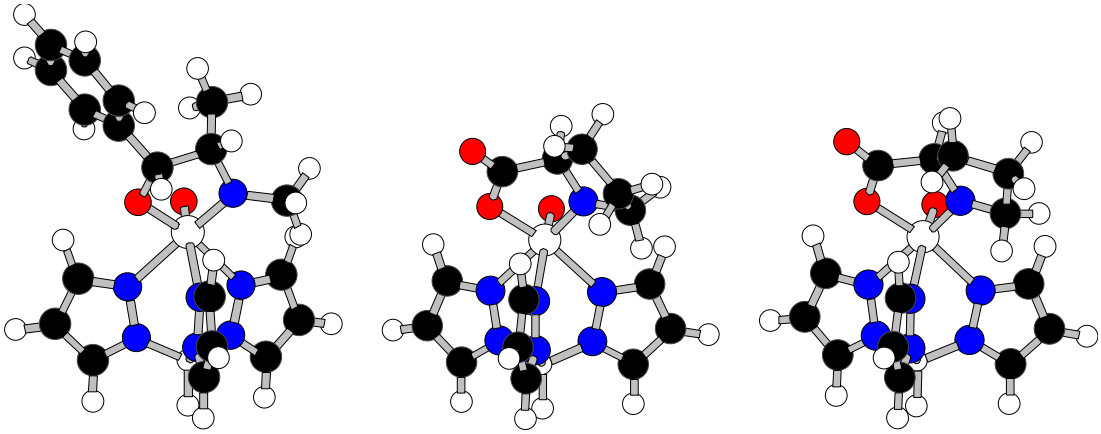

Figure 4.2: DFT optimized geometries of the two Re(V) complexes, calculated using B3LYP/6-31G(d) with Stuttgart RSC 1997 ECP for rhenium. Only one conformer of (R_{Re},$R_{O\text{-}C}$,$S_{C\text{-}N}$)-TpReO(ephedrine) was found (**1a**, left), whereas (R_{Re},R_C)-TpReO(proline) has two (**2a**, middle and **2b**, right).

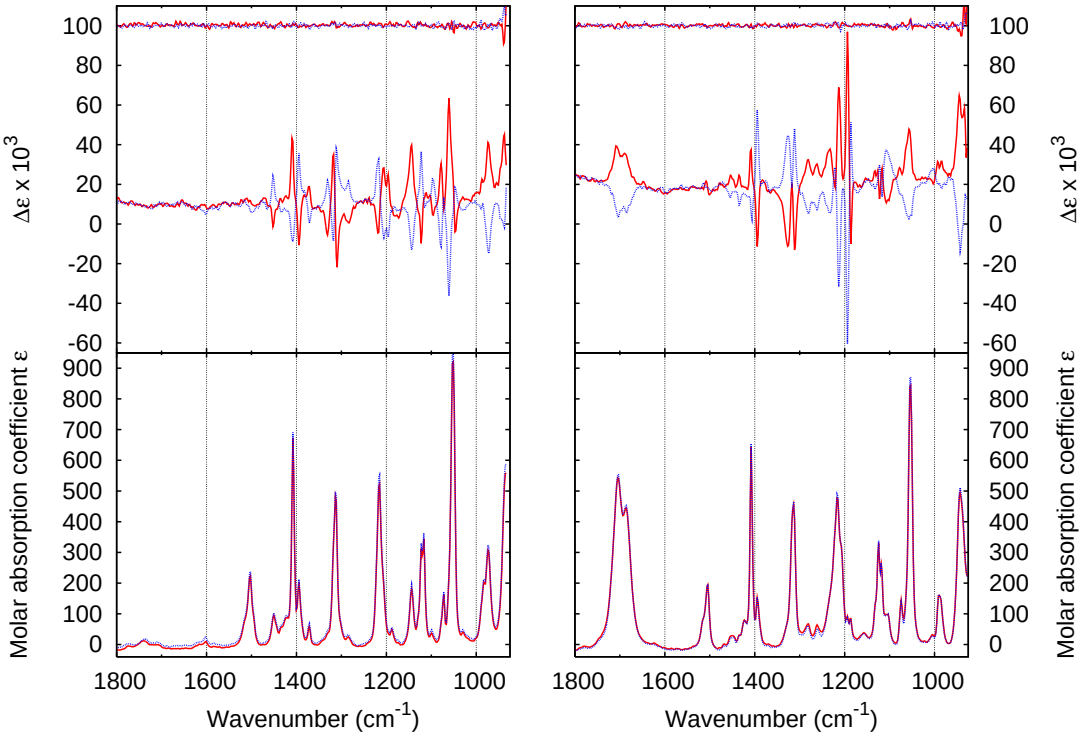

Figure 4.3: Observed IR (lower traces) and VCD spectra (upper traces, with the VCD noise level shown above) of each enantiomer of TpReO(ephedrine) (left) and TpReO(proline) (right) in $CDCl_3$ solutions. Solvent IR spectra have been subtracted. The resolution was 4 cm^{-1}, with the instrument optimized at 1400 cm^{-1}. Collection time is 12 h. The region below 925 cm^{-1} has been left out because of high solvent absorbance and thus higher noise.

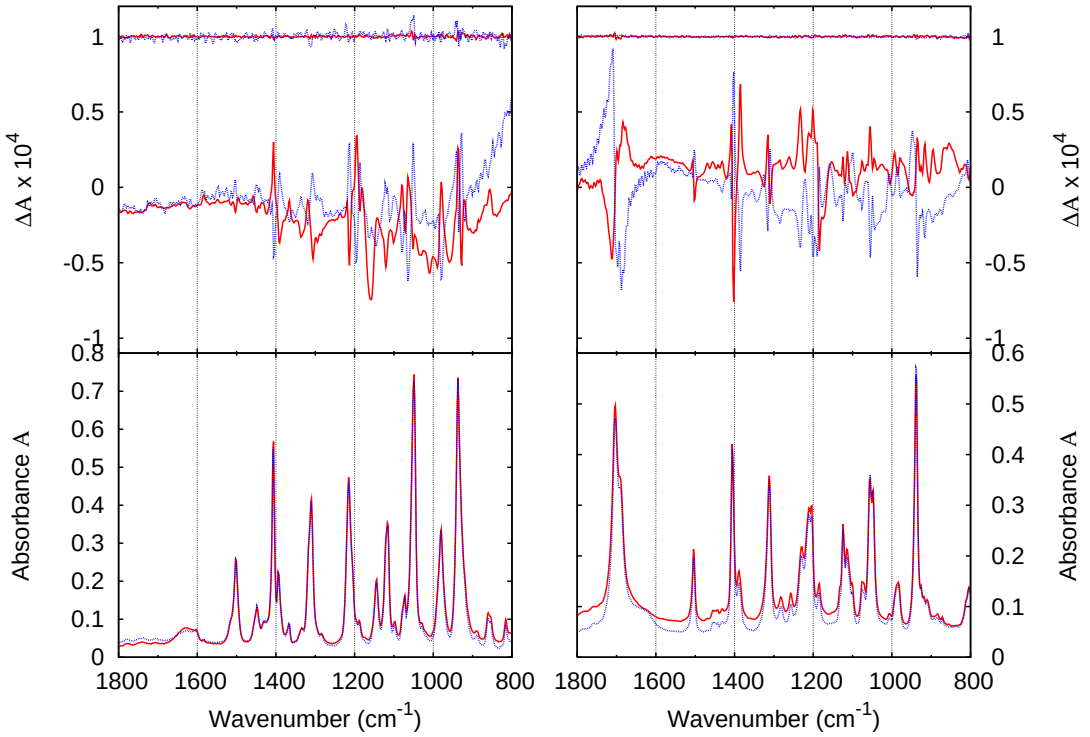

Figure 4.4: Observed IR (lower traces) and VCD spectra (upper traces, with the VCD noise level shown above) of both enantiomers of TpReO(ephedrine) (left) and TpReO(proline) (right) in KBr pellets containing ≈0.5 mg of sample in 250 mg KBr. Collection times are 12–20 h at a resolution of 4 cm^{-1}, with the instrument optimized at 1400 cm^{-1}. VCD baselines have been adjusted for two of the measurements using a straight line.

(corresponding to the racemic sample) was subtracted from the pair of VCD spectra, yielding a pair of exactly opposite spectra with a better S/N. The VCD spectra in solution in the subsequent figures have been subtracted in that way.

The IR and VCD spectra measured for the same samples in KBr pellets are shown in Figure 4.4. Both pellets of **1** and **2** have narrower bands compared to spectra in solution, which is expected. However, there is no clear indication of crystal field splitting, *e.g.*, a doubling of peaks if there are two molecules in the unit cell. There is a weak water band at 1625 cm^{-1} and more notably at 3300-3600 cm^{-1} (not shown).

In the VCD spectra, we can clearly see bands of opposite sign, but the baselines are less well defined than in solution due to sample inhomogeneity. Strain-induced birefringence cannot be completely avoided, and there is less reproducibility in pellet preparation. Although the anisotropy ratio goes up by about three times compared to the solution state, the VCD spectra are somewhat noisier and have less well-defined baselines. For KBr pellets, sometimes baseline shift due to scattering can be observed, thus two of the VCD baselines in Figure 4.4 have been adjusted.

An interesting difference between solution and solid state spectra appears in the two carbonyl (C=O) VCD signals for **2** around 1700 cm^{-1}, which are of the same sign in solution, but bisignate in the KBr pellets. We were unable to explain that feature.

When comparing the observed IR and VCD spectra to the array of calculated ones (Figures 4.5–4.6), we can verify the absolute configuration of the samples and assign most of the observed peaks. Experimental spectra from both $CHCl_3$ and $CDCl_3$ are shown combined. A progressively better fit to the experimental spectra can be seen when increasing the basis set size. One basis set has been left out (the B3LYP/SDD calculation), because those results look very similar to the B3LYP/LanL2DZ calculation. In general, the comparison is very reasonable. However, the C=O stretching frequency observed for **2** is systematically wrong by about 100 cm^{-1} (Figure 4.6); but it is underestimated by LanL2DZ and SDD, and overestimated by 6-31G(d). Other spectral regions have incorrectly scaled frequencies, but the uniform scaling factor corrects most of it. Furthermore, the relative intensities of VCD peaks differ somewhat between the observed and calculated spectra. We find the best agreement using the combination of the Stuttgart basis set for rhenium and 6-31G(d) for the other elements. In the region around 1200 cm^{-1} there are several bands involving the proline, which are not readily assigned, but a larger basis set on the light elements should improve the fit.

The observed C=O stretch has a splitting not reproduced by the calculations. Two distinct peaks are observed at 1689 and 1704 cm^{-1}, indicating two significantly different environments, which could be either two conformers or an intermolecular association. Indeed, we have identified two possible conformers of **2**, but their calculated C=O stretches differ by 2 cm^{-1}, which is too little to explain the observed splitting of 15 cm^{-1}. Furthermore, the relative intensities of the observed C=O bands is more like 1:4 than the 1:1 suggested by gas phase population analysis.

Apart from that, it appears that the average of the **2a** and **2b** conformers indeed fits the experiments better than any one of them, suggesting that the gas-phase population estimate is valid in solution. The calculated spectra for **2a** and **2b** do not differ much, but the observed IR has two adjacent peaks around 1500 cm^{-1}, whereas only one band is found there in each of the two calculated IR spectra. If both conformers are present in solution with a larger frequency separation than calculated, that would explain the observation. Furthermore, only the calculated **2b** VCD has a negative VCD feature at 980 cm^{-1}, corresponding to the observed feature at 1000 cm^{-1}, so we cannot rule out the presence of **2b**.

The two large basis sets for rhenium yield different results for the Re=O vibrations at ≈930 cm^{-1}. In the case of Hay-Wadt, they are less reliably reproduced than by the Stuttgart basis set (which has an additional 15 basis functions), since the calculated Re=O frequency for **1a** is too close to and coupled with the C–O stretch vibration at 970 cm^{-1}, whereas for **2a**–**b** the Re=O is coupled with the proline breathing mode at 980 cm^{-1}, judging from the assign-

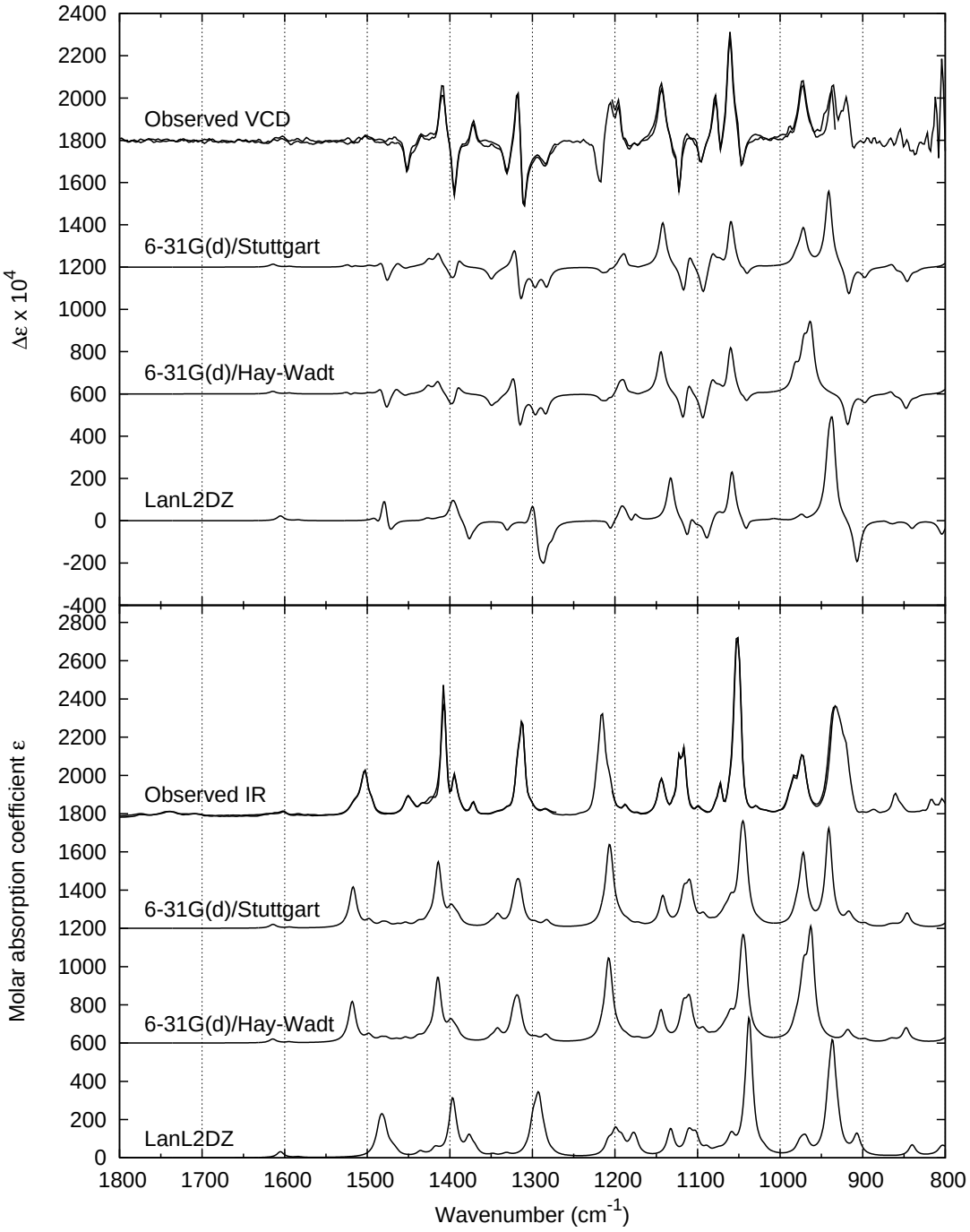

Figure 4.5: Observed vs. calculated IR (bottom) and VCD (top) spectra for TpReO(ephedrine), **1**. The calculated spectra are at the DFT/B3LYP level with different basis sets: either LanL2DZ on all atoms or 6-31G(d) on elements H through O, with Hay-Wadt VDZ (n+1) ECP or Stuttgart RSC 1997 ECP on Re. Observed IR spectra are solvent subtracted ($CHCl_3$ and $CDCl_3$), and VCD is baseline corrected using the average of the two enantiomers. The resolution is 4 cm^{-1}, with the instrument optimized at 1400 cm^{-1}. Collection time is 12 h for both the sample and its enantiomer.

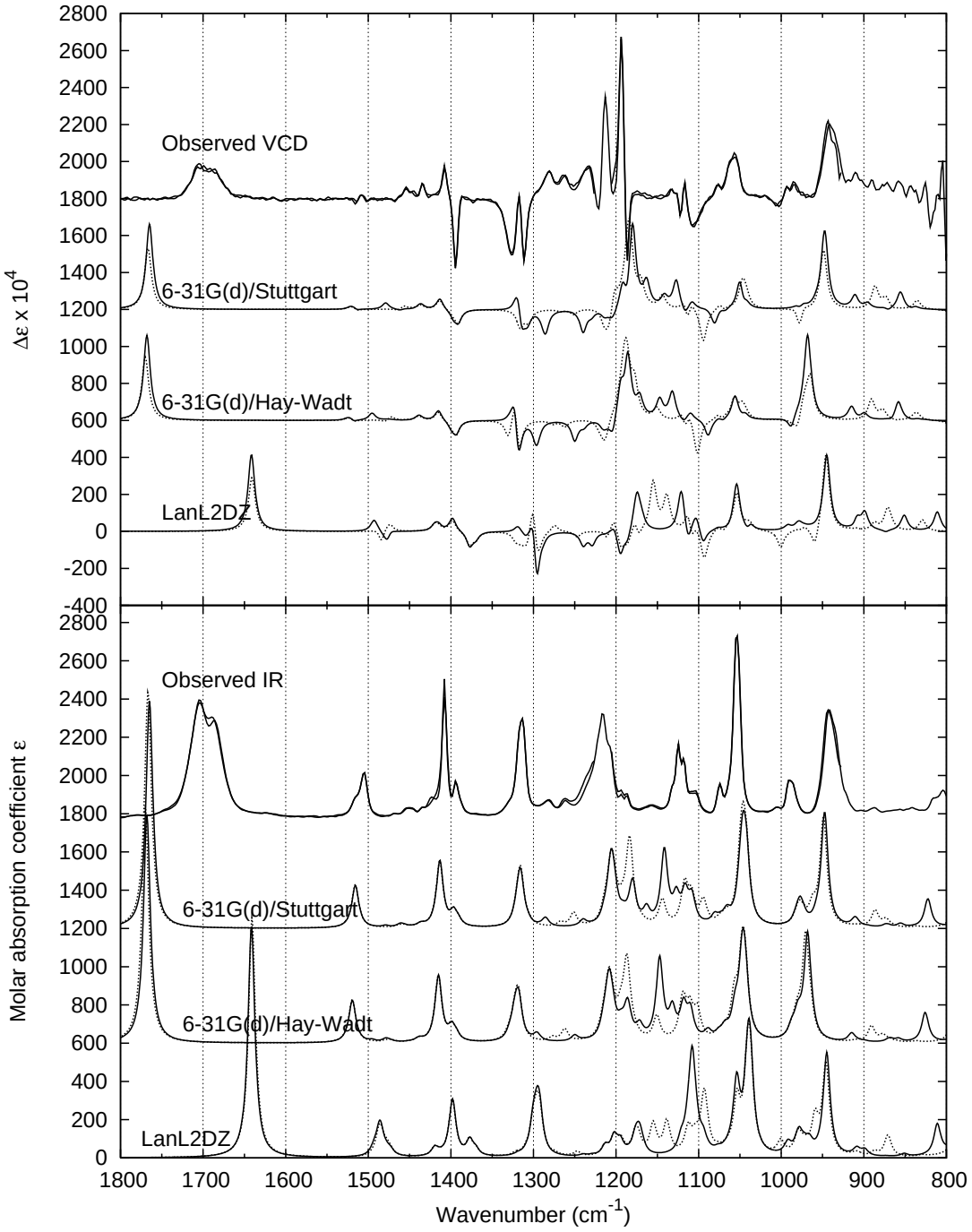

Figure 4.6: Observed vs. calculated IR (bottom) and VCD (top) spectra for TpReO(proline), **2**. The calculated spectra are at the DFT/B3LYP level with different basis sets: either LanL2DZ on all atoms or 6-31G(d) on elements H through O, with Hay-Wadt VDZ (n+1) ECP or Stuttgart RSC 1997 ECP on Re. Both conformers are included: **2a** (—) and **2b** (····). Observed IR spectra are solvent subtracted ($CHCl_3$ and $CDCl_3$), and VCD is baseline corrected using the average of the two enantiomers. The resolution is 4 cm^{-1}, with the instrument optimized at 1400 cm^{-1}. Collection time is 12 h for both the sample and its enantiomer.

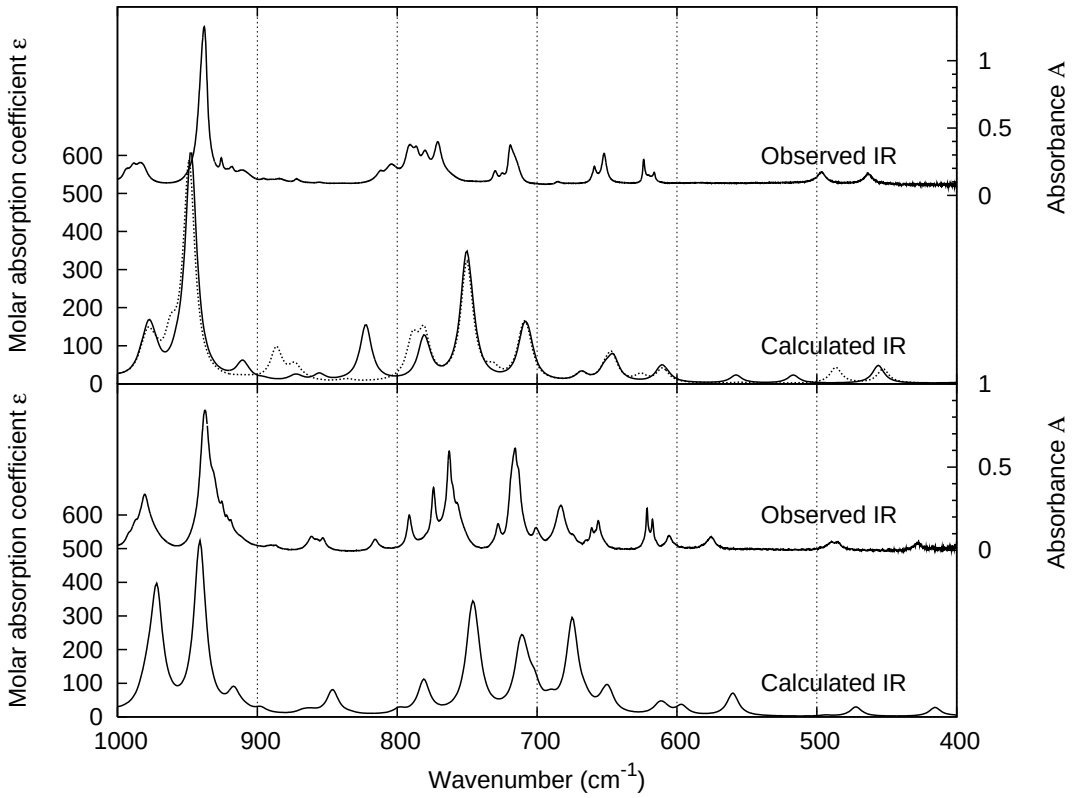

Figure 4.7: Experimental vs. calculated IR spectra of Re(V) complexes (*R,R,S*)-**1** (bottom) and (*R,R*)-**2** (top) in KBr pellets, showing the 400–1000 cm^{-1} region compared to the B3LYP/6-31G(d)/Stuttgart RSC 1997 ECP calculations. Both conformers **2a** (—) and **2b** (····) are included. The experimental resolution is 0.25 cm^{-1}, and the collection times 90 min.

ments by Gaussian 03. An earlier publication erroneously assigned the Re=O stretches to be around 980 cm^{-1} [34]. The overestimated frequency from the Hay-Wadt basis set can be lowered by reducing the force constant of the Re=O stretch, the effect of which was simulated by substituting the oxygen with its ^{17}O isotope and evaluating the vibrations using the Gaussian 03 freqchk utility. Doing so brings the Re=O stretching frequencies calculated with Hay-Wadt very close to those calculated with the Stuttgart basis set (data not shown).

4.2.3 Higher resolution IR spectra

On closer inspection, the Re=O stretching bands at ≈930 cm^{-1} reveal several shoulders on the lower wavenumber side, just below the $CDCl_3$ cutoff, which are not readily assigned by the calculations. This inspired us to measure a series of higher (though not ultra-high) resolution IR spectra, using the Magna-IR 850 spectrometer at 0.25 cm^{-1} resolution. The Re=O stretching band is the primary target for the ultra-high resolution IR spectroscopy in France, so a thorough characterization here is obviously of interest.

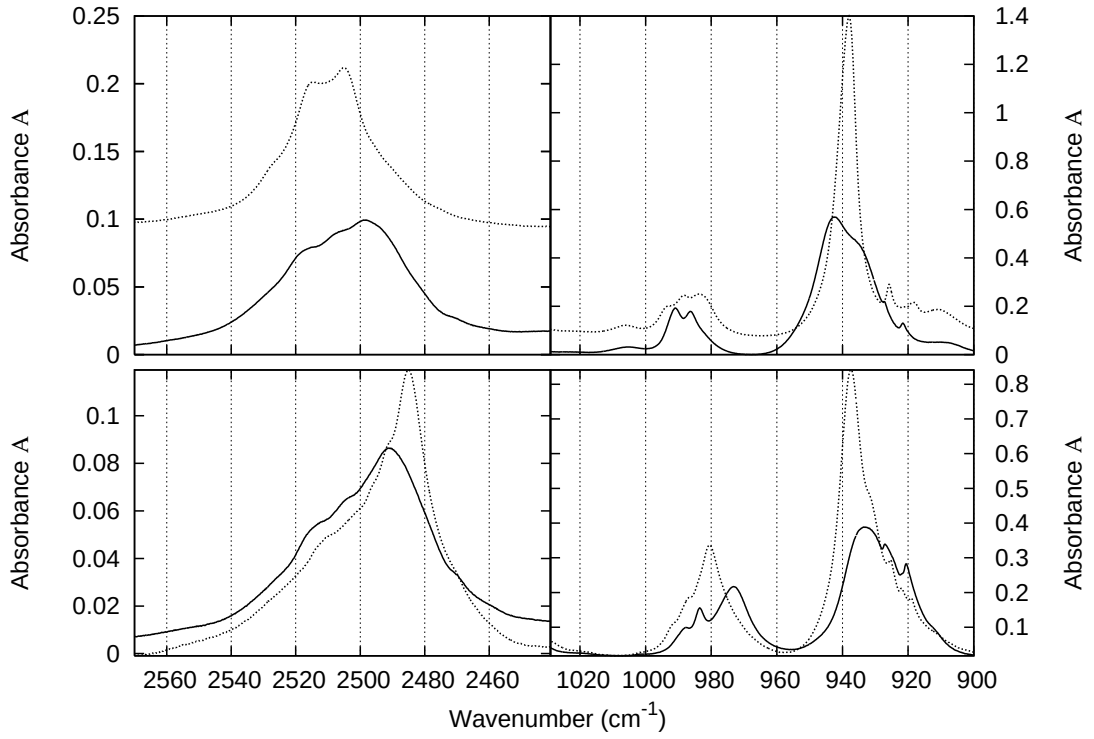

Figure 4.8: Experimental IR spectra of Re(V) complexes (*R,R,S*)-**1** (bottom) and (*R,R*)-**2** (top) in $CHCl_3$ (—) and KBr pellets (····), showing the B–H stretching (left) and Re=O stretching regions (right). The resolution is 0.25 cm^{-1}, and the collection times 90 min.

The calculated and experimental IR in the lower wavenumber region 400–1000 cm^{-1} are shown in Figure 4.7, where the spectra of KBr pellets are compared to the B3LYP/6-31G(d)/Stuttgart calculations. Towards lower $\bar{\nu}$, the applied uniform frequency scaling factor of 0.97 becomes too low, but we can still correlate nearly all of the peaks.

It turns out that there is fine structure not only in the Re=O stretch, but also in the region of the lone B–H stretch around 2500 cm^{-1}. The latter is theoretically the only normal mode between the fingerprint and C–H stretching regions, so no other bands should be around. The fine structure of the bands around 930 cm^{-1} might be due to nearby normal modes, which are found in the calculations, but their calculated IR intensity is 2 orders of magnitude smaller than the Re=O stretching intensity. These spectral features are shown in detail in Figure 4.8 in both $CHCl_3$ solution and KBr pellets (notice that the Re=O bands are the ones below 960 cm^{-1}). All four samples seem to display at least three shoulders on the lower $\bar{\nu}$ tail of the Re=O stretch and two or three on the higher $\bar{\nu}$ tail of the B–H stretch band, with an additional shoulder to lower $\bar{\nu}$.

Several explanations must be invoked in order to explain the observed shoulders. Both rhenium and boron have naturally occurring stable isotopes, *i.e.*, 37 % ^{185}Re and 20 % ^{10}B, which will generate shoulder bands when present. The size of these wavenumber shifts can be estimated from the reduced masses

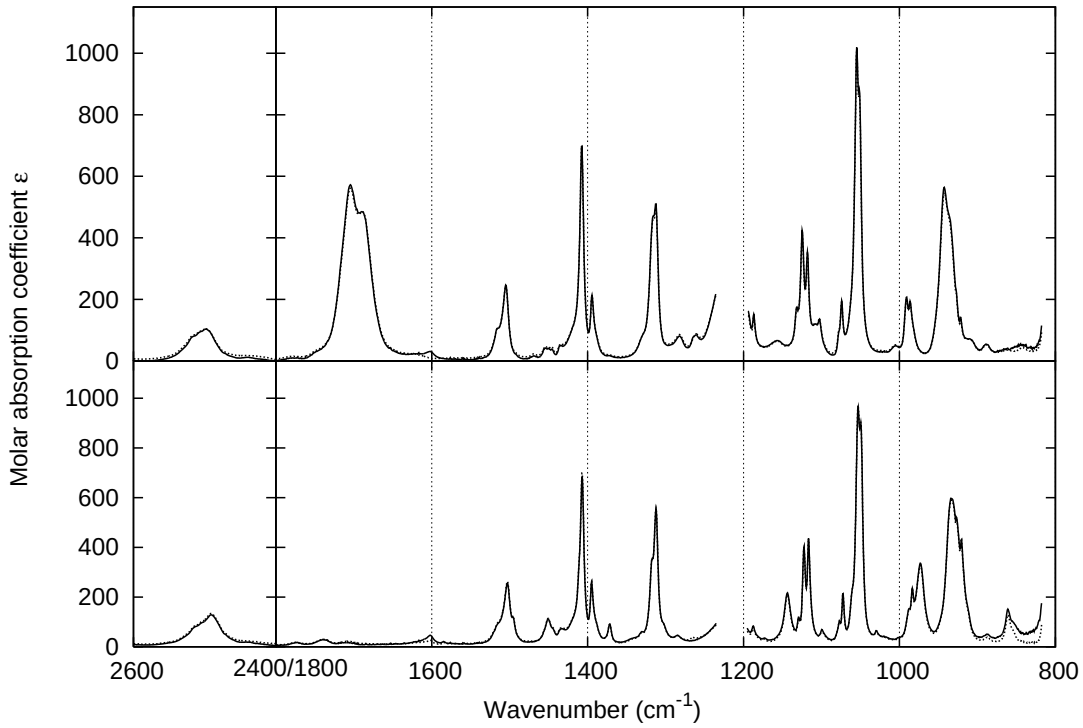

Figure 4.9: Experimental IR spectra of Re(V) complexes (*S*,*S*,*R*)-**1** (bottom) and (*S*,*S*)-**2** (top) in $CHCl_3$, using lower (—) and normal (····) concentrations (**1**: 61 mM vs. 4.3 mM; **2**: 95 mM vs. 4.7 mM). The intense $CHCl_3$ band around 1200 cm^{-1} has been blanked. The resolution is 1 cm^{-1}, and the collection times 35–90 min.

or calculated by Gaussian (using freqchk) to be +0.37 cm^{-1} for Re=O and +11 cm^{-1} for B–H, making only the B–H shift noticeable here. Additional splitting may come from Fermi resonance with overtones and combination bands of B–H deformations, which indeed are assigned by the calculation at around half the stretching frequency. Also the Re=O shoulders can be due to Fermi resonance, since the calculated Re=O stretching at 970 cm^{-1} (unscaled) matches combination bands of 146 and 823 cm^{-1} (involving the N-Re=O angle), as well as 301 and 669 cm^{-1} (involving ephedrine chelate ring deformation).

The calculated Re=O and B–H stretching frequencies of the conformers **2a** and **2b** nearly coincide: $\Delta\bar{\nu}$ for the largest basis set is 1.5 and 0.06 cm^{-1}, respectively. So this is an insufficient explanation. Besides, the same effect is seen for **1** with its single conformer.

Alternatively, the observed splitting could be an intramolecular effect. Because no hydroxyl groups are present and only tertiary amines, there is no obvious possibility for hydrogen bonding as the splitting mechanism. Besides, hydrogen bonding tends to broaden rather than split bands. However, there is negative partial charge on the oxygens and positive partial charge on the boron hydrogen, so some splitting may result. There could also be interactions with solvent molecules, which could cause splitting even in KBr pellets, if the sample

has crystallized with solvent molecules in the unit cell. The published crystal structures have two complexes in the unit cells, but no solvent molecules [34]

In an attempt to reduce the degree of solute-solute interactions, two IR spectra at a roughly 15 times lower concentration were recorded. As can be seen in Figure 4.9, there is practically no difference when converting absorbance to molar absorption coefficient (which makes the peak heights independent of concentration). So whatever the interactions are, they persist at lower concentration. This evidence supports the possibility of intramolecular effects like Fermi resonance and precludes solute-solute interactions.

4.3 Chiral Schiff-Base Complexes

As part of our collaboration with the lab of Professors Nafie and Freedman at SU, we performed theoretical studies of some transition metal complexes which were being synthesized and characterized spectroscopically, primarily by Ph.D. student Yanan He [51].

Early observations of an enhancement effect in VCD spectroscopy were made in the C–H stretching region on transition metal complexes with (−)-M(sparteine)Cl_2 in 1980 (M=Co, Ni, Zn) [6]. Another kind of VCD enhancement involving ring currents rather than transition metals was found a few years later [37]. The mechanism under study here is the resonance-enhanced type (REVCD) from transition elements, cf. Section 2.3.1.

The first combined theoretical and experimental study of REVCD revisited the sparteine complexes above, but in a broader spectral range, where it was found that the enhancement effect reaches into the fingerprint region as well [52]. Calculations of VCD spectra were made, but only compared favourably for the unenhanced (closed shell) Zn(II) complex [51], because current DFT implementations of VCD (using MFP) do not include the full enhancement theory. Yet, it will appear below that in some cases part of the observed enhancement can be reproduced by calculations, depending on the geometric details and choice of method. We cannot offer any solid explanation to why this is so, except that there could be some fortuitous cancellation of errors in the MFP formalism. Several Schiff-base complexes with REVCD effects have been studied at SU and are described in the manuscript enclosed as Paper 6. In this section, we review our contribution to that work.

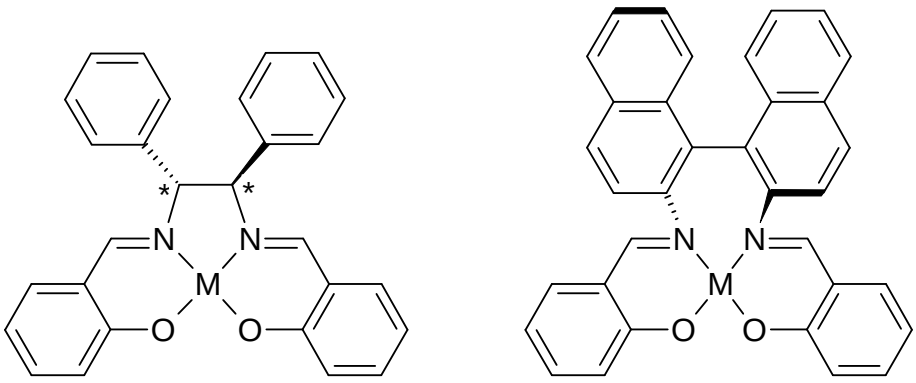

Figure 4.10: Chemical structures of the (R,R)-saldiphenyl complex (left) and (R)-salbinaphtyl complex (right), where M indicates the metal centre.

The chemical structures of the transition metal complexes considered in this section are shown in Figure 4.10. These complexes reveal enhanced VCD for Co(II) relative to Ni(II) (and Zn(II) in the case of salbinaphtyl), and this is explained by the presence of low-lying d–d transitions in Co(II) [51]. We present VCD calculations which reproduce part of that enhancement.

4.3.1 Co(II)saldiphenyl Complex

The IUPAC name of this complex is [*N*, *N*'-Bis(salicylidene)-1,2-diphenyl-1,2-ethanediaminato]-Co(II). A crystal structure of this complex has been published (with Ni(II) though) [56]. The complex features two chiral centres, which prefer to have the same chirality. Contrary to the Ni(II) complex, its Co(II) cousin has a low-lying electronic transition at 2100 cm^{-1} [51]. The low-spin cobalt centre is in distorted square planar coordination (cf. Figure 2.7 on page 21) and therefore effectively chiral, which makes it an interesting study case for REVCD. Given that the orbitals below $d_{x^2-y^2}$ are closely spaced at the outset and only shift a little by the structural perturbation, we may expect REVCD effects.

Conformers and Geometries

Two distinct conformers of both the Co(II) and Ni(II) complexes were constructed in HyperChem, with the phenyls in axial or equatorial position, *i.e.*, directed perpendicular or parallel to the salen moiety. Their geometries were subsequently DFT optimized in the gas phase using unrestricted B3LYP with 6-31G(d) on H through O and Ahlrichs VTZ on the metal [101].

The electronic energy of the equatorial conformer is 4.84 kJ/mol higher than that of the axial one. This indicates that 87 % of a Boltzmann distributed ensemble would be the axial conformer. When calculated thermal free energies are taken into account, the energy gap grows to 7.94 kJ/mol. We chose to calculate the VCD spectra of both structures.

It turned out that the (*R*, *R*)-axial and (*S*, *S*)-equatorial conformers have similar distortion of the tetrahedral coordination site. Therefore, these configurations are compared below. Their optimized geometries are shown in Figure 4.11.

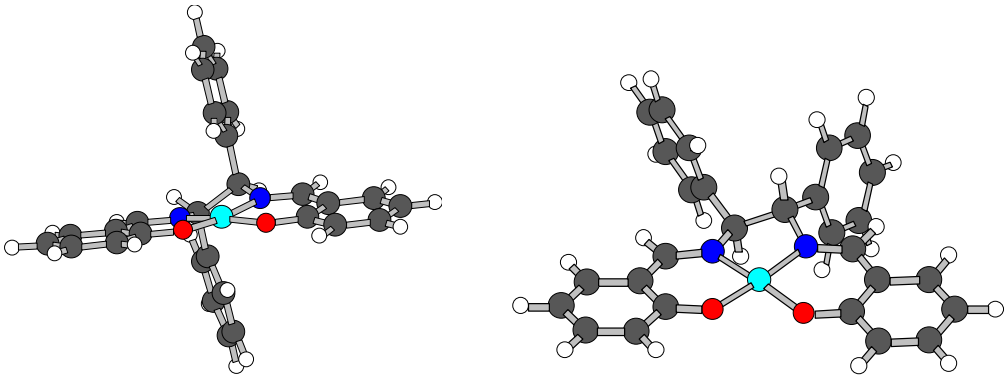

Figure 4.11: Geometries of Co(II)saldiphenyl in the conformers with axial/equatorial phenyls, optimized using B3LYP/6-31G(d) with Ahlrichs VTZ on Co. The enantiomers shown are (*R*, *R*)-axial (left) and (*S*, *S*)-equatorial (right).

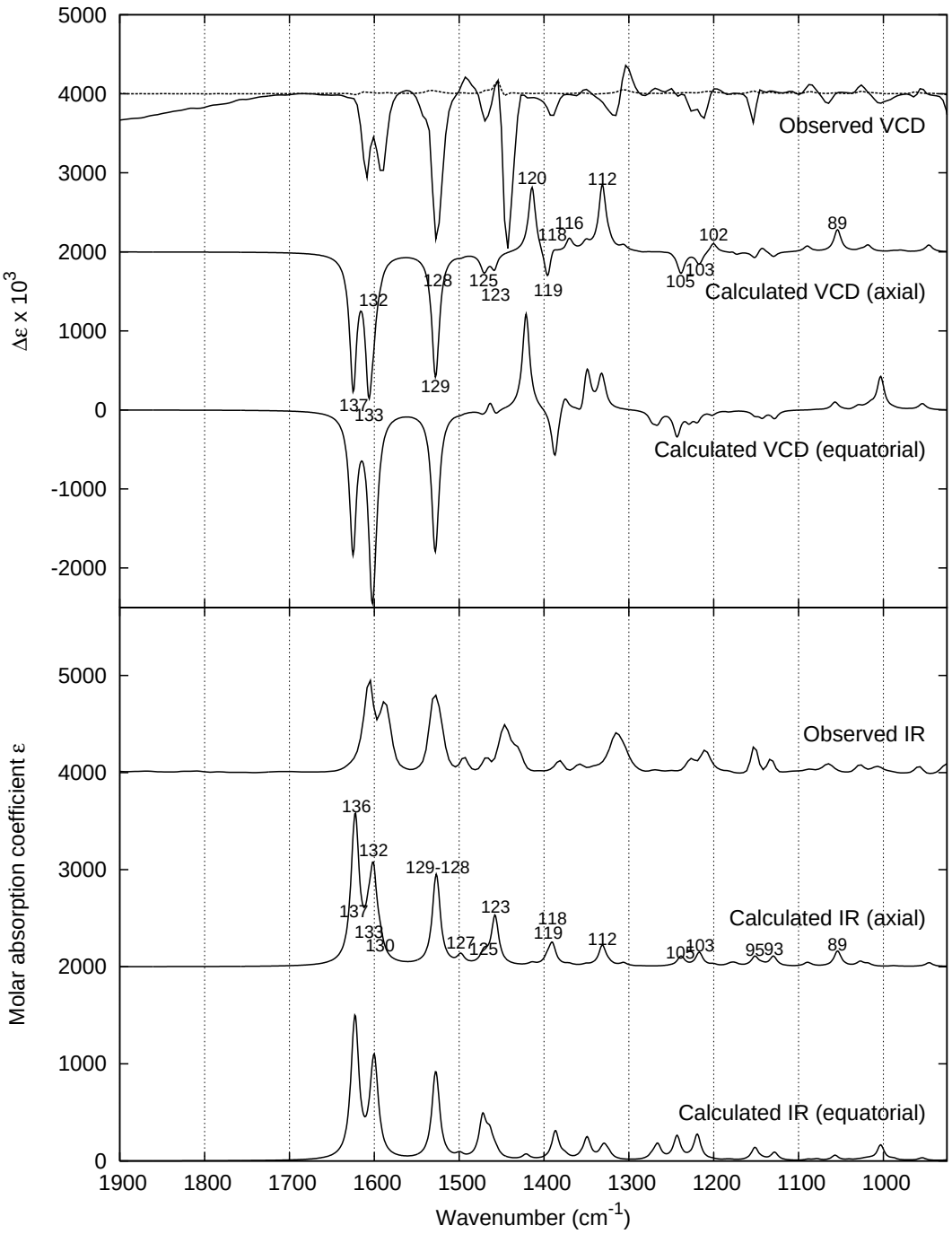

Figure 4.12: Observed vs. calculated IR (bottom) and VCD (top) spectra of Co(II)saldiphenyl. Calculated spectra (using B3LYP with 6-31G(d) on H through O and Ahlrichs VTZ on Co) are for the (*R*, *R*)-axial and (*S*, *S*)-equatorial conformers, with a frequency scaling factor of 0.97 and 5 cm^{-1} half-width. Experimental spectra of both the Co(II) (—) and Ni(II) complexes (····) are shown for their (*R*, *R*)-enantiomers (0.12 M in $CDCl_3$), courtesy of Yanan He [51]. The acquisition time was 6 h, using 54 μm path length at 8 cm^{-1} resolution with the PEMs at 2000 cm^{-1}.

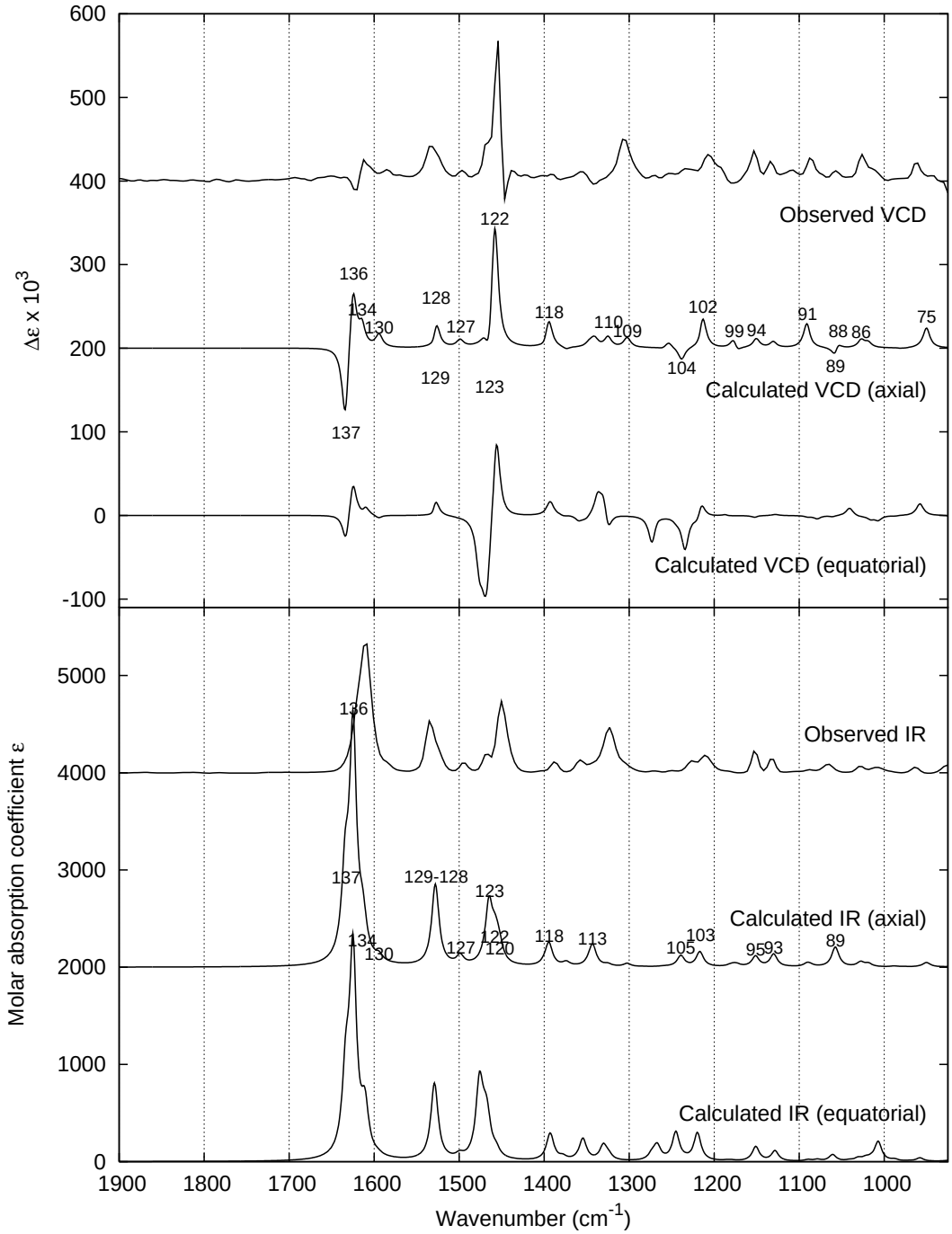

Figure 4.13: Observed vs. calculated IR (bottom) and VCD (top) spectra of Ni(II)saldiphenyl. Calculated spectra (using B3LYP with 6-31G(d) on H through O and Ahlrichs VTZ on Ni) are for the (*R*, *R*)-axial and (*S*, *S*)-equatorial conformers, with a frequency scaling factor of 0.97 and 5 cm^{-1} half-width. Experimental spectra of the (*R*, *R*)-enantiomer (0.12 M in $CDCl_3$) are courtesy of Yanan He [51]. The acquisition time was 6 h, using 54 μm path length at 8 cm^{-1} resolution with the PEMs at 2000 cm^{-1}.

Calculated IR and VCD Spectra

Our calculated spectra are shown in Figure 4.12, compared to experimental data for the (*R*, *R*)-enantiomer. The experimental VCD of the unenhanced Ni(II) complex has been included and looks very flat on this scale. One can see the tail of the broad negative ECD band above 1700 cm^{-1}, which is suspected of causing the observed enhancement. Prominent normal modes for the axial conformer have been numbered. It turns out that the Ahlrichs VTZ calculation yields REVCD for both conformers considered. Moreover, the enhanced peaks have the same sign even though the absolute configurations are opposite. We ascribe this to the similar distortion of the coordination site.

In order to take Boltzmann weighting into account for the (*R*, *R*)-enantiomer, one should combine the calculated VCD spectra as 0.87×(*R*, *R*)-axial minus 0.13 × (*S*, *S*)-equatorial. Doing so renders the calculated VCD intensities closer to reality, but otherwise there are small changes, because the conformers have very similar spectra.

From the calculation of the (*R*, *R*)-axial conformer, we can assign some of the observed REVCD modes. Numbers in parentheses refer to calculated normal modes. Except for an ethylendiamine C–H bending mode at 1390 cm^{-1} (119), there are salen in-plane deformations at 1610 cm^{-1} (137), 1590 cm^{-1} (133, with C=N stretching), 1520 cm^{-1} (129, with C=C stretching), and 1300 cm^{-1} (112, with C–O stretching). All of these vibrations occur in the vicinity of the Co(II) centre, and so it is reasonable that they experience enhancement.

Figure 4.13 compares the calculated and experimental data for the Ni(II)saldiphenyl complex, which has no REVCD. As seen clearly in Figure 4.12, these VCD intensites are more than an order of magnitude smaller. Again, prominent normal modes have been numbered for the axial conformer, and the vertical position of these numbers (roughly corresponding to the intensity) indicate that some VCD bands are cancelled by their neighbours. Apparently the Ahlrichs VTZ basis set also reproduces the unenhanced signals well, although some of the experimental VCD intensities (around 1310 and 1625 cm^{-1}) look more like the equatorial than the axial conformer. The electronic energy difference is 5.65 kJ/mol in favour of the axial conformer, suggesting a 91 % population.

The most prominent observed VCD modes can be assigned to phenyl in-plane deformation at 1460 cm^{-1} (122) and salen in-plane deformations at 1620 cm^{-1} (137), 1610 cm^{-1} (136), and 1530 cm^{-1} (128), in the latter case dominated by C=C stretching.

For direct comparison, most of the calculated normal modes and anisotropy ratios of the two saldiphenyl complexes are given in Table 4.2. The normal modes for the two complexes often correspond if their number is identical, but one should rather match the pattern of IR intensities—or even better, animate each normal mode for direct comparison (which would be rather tedious). For the Co(II) complex, the maximum g is 0.135 at normal mode #120.

In conclusion, we have achieved a good fit of the calculations to given experimental data, and we demonstrated the ability of the Ahlrichs VTZ basis set to reproduce both unenhanced VCD and some enhanced signals.

Co(II)Saldiphenyl					Ni(II)Saldiphenyl				
#	$\bar{\nu}$	ε	$\Delta\varepsilon \cdot 10^3$	$g{\cdot}10^3$	#	$\bar{\nu}$	ε	$\Delta\varepsilon \cdot 10^3$	$g{\cdot}10^3$
74	945	8.030	22.520	11.22	74	947	2.173	0.743	1.37
75	946	28.189	44.733	6.35	75	950	32.757	28.212	3.45
84	1018	12.424	49.134	15.82	84	1018	16.839	-0.698	-0.17
85	1018	11.756	28.887	9.83	85	1019	15.097	6.742	1.79
86	1027	27.053	18.798	2.78	86	1027	25.524	10.827	1.70
87	1028	19.173	0.653	0.14	87	1028	22.294	-1.722	-0.31
88	1052	14.014	4.183	1.19	88	1055	13.659	11.539	3.38
89	1054	146.132	274.783	7.52	89	1058	193.244	-14.818	-0.31
90	1086	5.952	0.040	0.03	90	1087	17.486	-3.861	-0.88
91	1090	35.875	69.787	7.78	91	1091	28.772	31.617	4.40
93	1130	99.462	-63.053	-2.54	93	1130	121.709	9.070	0.30
94	1143	16.310	74.848	18.36	94	1151	3.282	15.368	18.73
95	1151	95.856	-88.423	-3.69	95	1151	103.742	-4.760	-0.18
98	1174	13.723	-45.480	-13.26	98	1173	16.371	-7.737	-1.89
99	1177	20.242	38.764	7.66	99	1177	20.904	11.950	2.29
100	1180	9.660	-22.142	-9.17	100	1181	9.096	0.936	0.41
102	1200	16.257	120.922	29.75	102	1213	6.459	40.520	25.09
103	1217	140.262	-154.991	-4.42	103	1217	148.475	-8.600	-0.23
104	1237	36.784	-82.460	-8.97	104	1238	42.212	-16.217	-1.54
105	1239	65.090	-195.013	-11.98	105	1240	72.026	1.298	0.07
109	1306	31.544	60.427	7.66	109	1302	31.910	11.873	1.49
110	1324	18.851	80.214	17.02	110	1325	17.861	12.291	2.75
112	1331	209.120	826.169	15.80	112	1340	9.844	8.063	3.28
113	1342	2.526	1.364	2.16	113	1343	209.376	3.470	0.07
115	1350	13.584	97.811	28.80	115	1348	21.401	3.255	0.61
116	1370	15.789	169.928	43.05	116	1374	39.208	-3.082	-0.31
118	1390	214.101	124.105	2.32	118	1394	236.975	33.807	0.57
119	1396	65.128	-418.042	-25.68	119	1400	20.560	-6.108	-1.19
120	1414	25.073	843.485	134.57	120	1453	130.861	-4.995	-0.15
121	1456	66.233	49.989	3.02	121	1456	84.796	7.302	0.34
122	1456	11.060	41.329	14.95	122	1458	206.731	150.972	2.92
123	1458	436.517	-275.169	-2.52	123	1465	603.687	-38.158	-0.25
125	1471	99.926	-186.549	-7.47	125	1472	20.283	-0.132	-0.03
126	1498	28.423	-41.718	-5.87	126	1499	27.462	-3.711	-0.54
127	1498	65.385	18.348	1.12	127	1499	66.356	12.171	0.73
128	1526	497.635	-293.189	-2.36	128	1527	396.322	50.398	0.51
129	1528	496.448	-1328.950	-10.71	129	1529	456.576	-28.090	-0.25
130	1593	136.007	-18.650	-0.55	130	1594	55.165	15.666	1.14
131	1594	13.713	-95.801	-27.94	131	1595	4.028	-0.440	-0.44
132	1601	816.504	-536.873	-2.63	132	1612	206.402	-3.449	-0.07
133	1607	274.455	-1486.030	-21.66	133	1613	26.796	-3.194	-0.48
134	1613	8.487	10.631	5.01	134	1614	142.207	36.915	1.04
135	1613	24.115	19.238	3.19	135	1616	20.406	-6.729	-1.32
136	1622	1121.600	94.321	0.34	136	1625	2377.730	80.764	0.14
137	1625	489.860	-1714.350	-14.00	137	1634	840.954	-93.791	-0.45

Table 4.2: Comparison of selected calculated normal modes for Co(II)Saldiphenyl (left) and Ni(II)Saldiphenyl (right), using unrestricted B3LYP/6-31G(d) with Ahlrichs VTZ on the metal. Entries are (scaled) wavenumbers $\bar{\nu}$/ cm^{-1}, IR intensities ε/ M^{-1}cm^{-1}, VCD intensities $\Delta\varepsilon$/ M^{-1}cm^{-1}, and anisotropy ratios g.

4.3.2 Co(II)salbinaphtyl Complex

Complexes like this are useful in asymmetric catalysis, as described in a recent review [17]. Similar complexes were reported as early as 1968 [88]. The synthesis of the present complex was reported 10 years ago [10]. It has the IUPAC name [[2,2′-[[1,1′-binaphthalene]-2,2′-diylbis(nitrilomethylidyne)]bis[4,6-dichlorophenolato]](2-)-*N*,*N*′,*O*,*O*′]-Co(II). The literature has differing nomenclature regarding the chirality. There are no chiral centres, but the tetradentate ligand consists of two identical halves with axial chirality, and their interconnection is also a chiral axis. The Co(II) centre is distorted tetrahedral, and thus we may expect low-lying d–d transitions introduced by the lifted degeneracy (cf. Figure 2.6 on page 20). Indeed, there is an electronic transition centered at 2540 cm^{-1}, with positive ECD for the (*R*)-enantiomer [51].

Conformers

The binaphtyl bridge assures very limited conformational flexibility, hence only one conformer was constructed in HyperChem and subsequently geometry optimized using DFT/B3LYP. To that end, we used both LanL2DZ and 6-31G(d) basis sets, in the latter case combined with Ahlrichs VTZ on Co. The optimized geometries are shown in Figure 4.14, which also illustrates our chirality nomenclature.

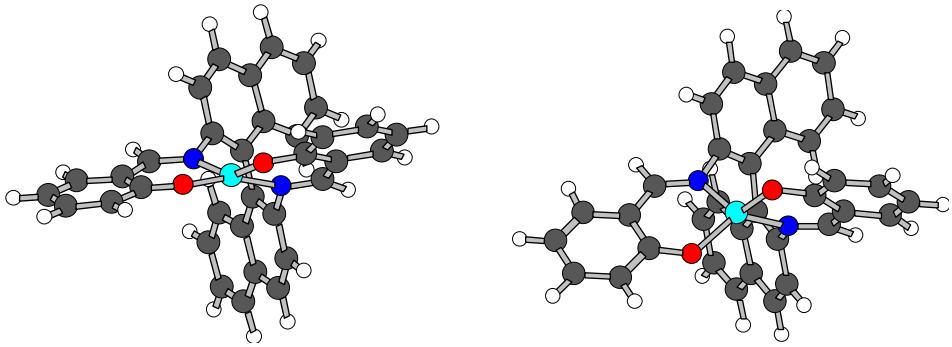

Figure 4.14: DFT optimized geometries of the (*R*)-Co(II)salbinaphtyl complex in low-spin (left) and high-spin (right) states, calculated using B3LYP/6-31G(d) with Ahlrichs VTZ on Co.

Depending on the spin state of the complex, the coordination around Co(II) becomes either distorted square planar (for LS) or distorted tetrahedral (for HS), which appear to be the only conformers possible. The basis sets used give only minor structural differences.

Calculated IR and VCD Spectra

Our calculated IR and VCD spectra of (*R*)-Co(II)salbinaphtyl in the high-spin state are shown in Figure 4.15, compared to experimental spectra. The latter shows a tail towards higher $\bar{\nu}$ of the aforementioned positive ECD band.

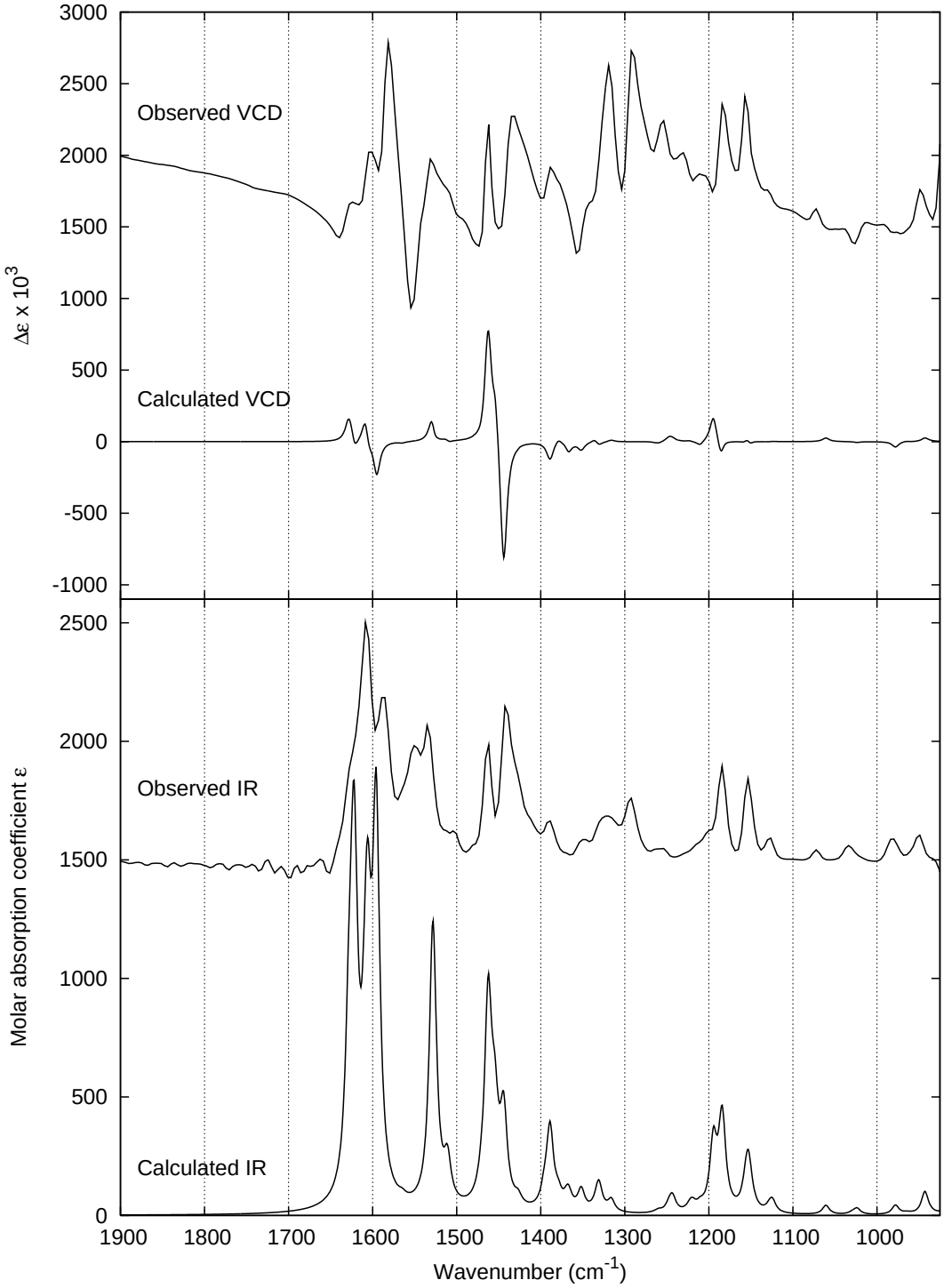

Figure 4.15: Observed vs. calculated IR (bottom) and VCD (top) spectra of (*R*)-Co(II)salbinaphtyl, using B3LYP with 6-31G(d) on H through O and Ahlrichs VTZ on Co), with a frequency scaling factor of 0.97 and 5 cm^{-1} half-width. Experimental spectra (95 mM in $CDCl_3$ solution) are shown, courtesy of Yanan He [51]. The acquisition time was 6 h, using 54 μm path length at 8 cm^{-1} resolution with the PEMs at 2000 cm^{-1}.

Spectra of the low-spin complex were calculated by Prof. Freedman and are shown in Paper 6 (Figure 18). In both the LS and HS calculations, there is good agreement with the experimental IR, but only poor agreement with the VCD, although both calculated VCD spectra seem to have REVCD effects, since the signals around 1450 cm^{-1} are about as intense as the observed spectrum. In the present calculation, there is a couplet consisting of two positive and two negative VCD signals. The remaining VCD bands are relatively small. The absolute configuration cannot be verified based on this comparison, since only some of the sign patterns agree.

Both the distorted square planar geometry (LS) and the distorted tetrahedral coordination (HS) reveal similar calculated VCD intensities. They do not differ enough to discern which spin state matches the experiment better, although the coordination is reported to be nearly tetrahedral, *i.e.*, high-spin [17]. To make things worse, the calculated VCD is not quite reproducible, since the HS calculation by Prof. Freedman (included in Paper 6) shows two positive bands around 1450 cm^{-1}. This interesting (though somewhat disillusioning) result suggests that even structural variations within the convergence criteria are sufficient to markedly perturb the subsequent VCD calculation. Apart from this notable discrepancy, the smaller VCD signals of the two HS calculations agree perfectly.

Compared to the previous case of Co(II)saldiphenyl, this agreement is less favourable. It serves to illustrate that unexpected results may occur when we approach the limits of current DFT implementation of VCD theory in Gaussian 03. In the following section about myoglobin, even more pronounced variations in calculated VCD will appear.

4.4 Myoglobin and Ligands

A research area that can obviously benefit from REVCD is the study of metalloproteins, where signals from the active site can stand out in VCD spectra if there are suitable IR electronic transitions to resonate with.

The primary example of enhanced VCD in metalloproteins is myoglobin (Mb), which is properly called metmyoglobin (metMb) when the Fe is oxidized to Fe(III). Enhanced VCD intensities have been observed for ligand stretching modes when azide (N_3^-) or cyanide (CN^-) is bound, and several explanations were proposed before the theory of REVCD was established [12, 13, 116, 117]. Interestingly, both of these systems have a low-spin Fe(III) centre with octahedral coordination (cf. Figure 2.5 on page 20), which is subject to distortions of the heme plane (called hemin in its oxidized form) by the surrounding apoprotein as well as upon ligand binding. In metMb-N_3, there is a temperature-dependent equilibrium between LS and HS Fe(III) with N_3^- absorption bands at 2043 and 2021 cm^{-1}, respectively, of which only the latter (LS form) has strong VCD [116].

Low-lying electronic transitions have been calculated from ESR data for the above mentioned systems; at 959 cm^{-1} and 2375 cm^{-1} for metMb-N_3 and at 340 cm^{-1} and 1264 cm^{-1} for metMb-CN [92]. We believe that such transitions may cause REVCD in heme proteins, appearing as an enhancement of LS Fe(III) relative to HS Fe(III).

Fragments of published metMb structures from the Protein Data Bank (PDB) are shown in Figure 4.16, including the hemin active site, proximal histidine (His93), and distal azide or cyanide ligand, as well as a few nearby amino acids.

In this project, we made a survey of a range of small ligands in order to determine whether they would bind metMb and possibly reveal enhanced VCD signals. We were focusing on distal ligand-induced spectral changes in the fingerprint region, where several bands attributed to hemin and ligands have displayed REVCD for cytochrome c, another heme protein [51]. Hence, we are expanding the spectral region of metMb VCD studies.

Alongside the experiments, DFT calculations on model systems consisting of just the hemin group and ligands were carried out. Our theoretical studies were primarily concentrated on the diatomic ligands azide and cyanide. These calculations are on the border of what is feasible with our current computer resources.

4.4.1 Experimental Methods

Horse skeletal muscle myoglobin was purchased in lyophilized form from Sigma (M0630-1G). Mb was dissolved in 0.135 M phosphate buffer at pH 8.41 with a metMb concentration of 11 mM (200 mg/mL). We used a 22 μm demountable CaF_2 cell (BioTools) to get a suitable absorbance in the 1000–1500 cm^{-1} region. CaF_2 windows cut off below 1000 cm^{-1}. The amide II and especially amide I regions have higher absorbance and should ideally be studied at a lower concentration (possibly in D_2O) or shorter path length.

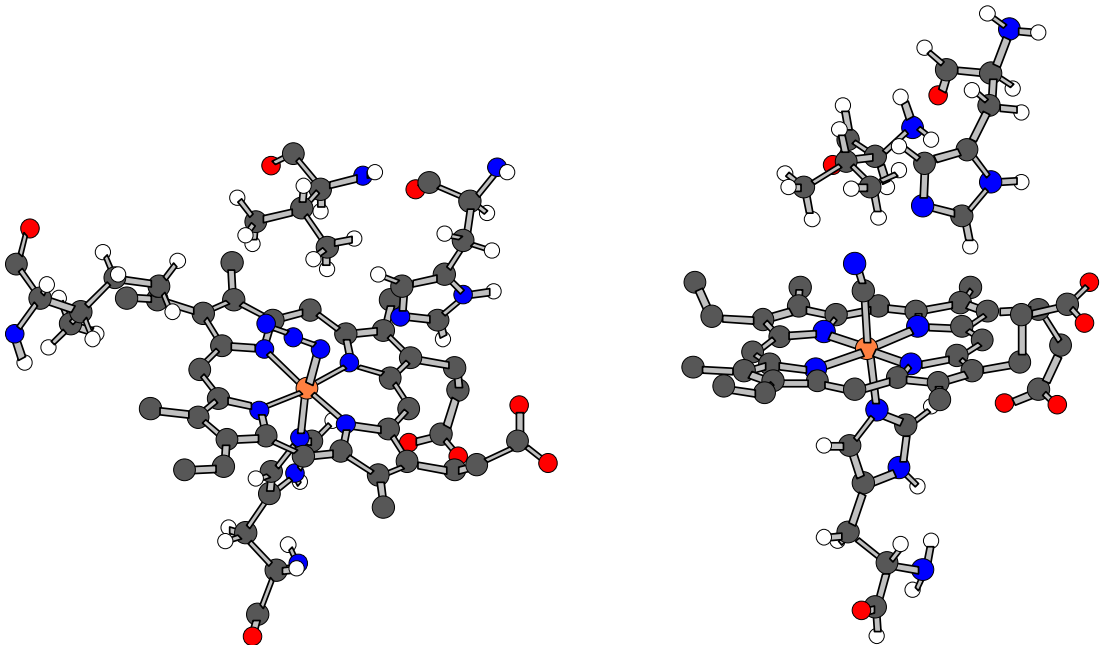

Figure 4.16: Crystal structure fragments from a) metMb-N_3 (left, PDB ID 1AZI) and b) metMb-CN (right, PDB ID 1EBC), showing hemin with proximal histidine (His93), distal ligand and nearby amino acid residues. Hydrogens are omitted from the hemins for clarity.

A number of ligands were considered and added to metMb solutions: Azide (N_3^-), thiocyanate (SCN^-), imidazole (Im), 1-Me-Im, 2-Me-Im, 4-Me-Im, and pyridine (Py). The deuterated varieties Py-d_5 and Im-d_4 were also considered (the latter becomes Im-d_3 in solution, since the acidic deuterium will be exchanged). The chemical structures of all but the linear molecules are shown in Figure 4.17.

The strong UV-Vis heme absorption band around 430 nm (the Soret band) is known to shift upon ligand binding [36], especially if the ligand changes the spin state of Fe(III) from HS to LS. In such cases we can directly see if there is binding, as the colour turns more red.

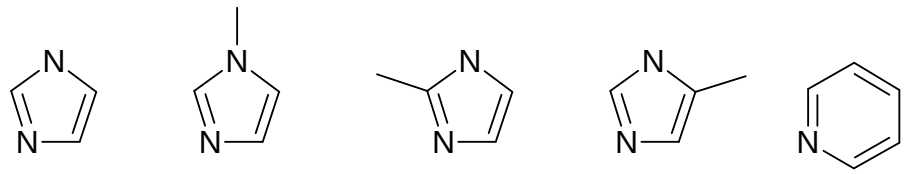

Figure 4.17: Chemical structures of the small metMb ligands considered. From the left: imidazole, 1-Me-imidazole, 2-Me-imidazole, 4-Me-imidazole, pyridine. Deuterated imidazole and pyridine were also used. The nitrogens towards the bottom are possible coordinating atoms.

IR and VCD spectra were recorded on a modified Chiral*IR* (BioTools) at SU. The resolution was 8 cm^{-1}, and the spectral range was 1000–3000 cm^{-1} or 1000–2000 cm^{-1} when an optical filter was used. Both PEMs were set at 1400 cm^{-1}, and the acquisition time was up to 12 h.

4.4.2 Computational Model Structures

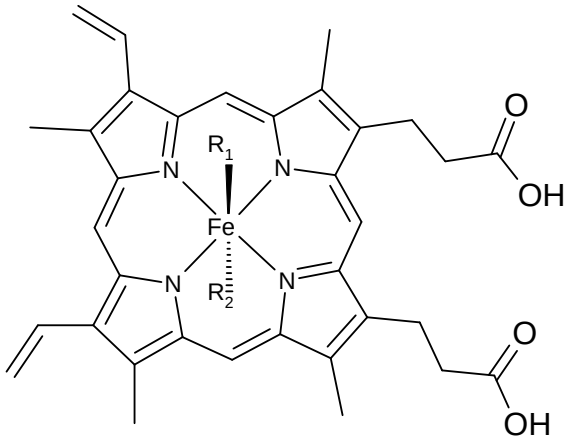

Figure 4.18: The chemical structure of heme, with proximal and distal binding sites R_1 and R_2, respectively (as defined in Figure 4.16).

Figure 4.18 shows the chemical structure of heme *b*, also known as protoporphyrin IX, which is a widespread prosthetic group [16]. In reduced form (with an Fe(II) centre) it is called heme, whereas the oxidized Fe(III) form is often called hemin.

The hemes in proteins will be more or less distorted from steric interactions with the peptide chain. Therefore, rather than starting a DFT geometry optimization from a hemin group taken out of the azidometMb crystal structure 1AZI (Figure 4.16a), we built a hemin group in the gas phase and then positioned the Fe(III) ligands according to the crystal structures. The primary difference in hemin structure from the native protein is that the propionic acids form an intramolecular hydrogen bond on the distal side rather than hydrogen bonding to amino acid residues on either side. The proximal and distal sides are defined by the two histidines in the crystal structure. Imidazole was used in place of proximal histidine (His93) for simplicity, and different distal ligands were substituted. At the pH 8.4 used experimentally, His and Im should be protonated [59].

The geometries were optimized using Gaussian 03, and vibrational spectra were calculated. We used the B3LYP functional and different basis sets: LanL2DZ and in a few cases 6-31G(d). For isolated ligand molecules, 6-31G(d) or 6-31++G(d,p) was used. The calculated intensities were convoluted with Lorentzians with a half-width of 5 cm^{-1}.

Ligand	Ligand:protein ratio	Colour change	K_{eq}/dm^{3}mol^{-1}
Azide	1:1	Yes	$43.3 \cdot 10^3$
Imidazole	10:1	Yes	255
1-Me-imidazole	10:1	Yes	
2-Me-imidazole	10:1 and 100:1	No	
4-Me-imidazole	10:1	Yes	
Pyridine	10:1	No	
Thiocyanate	10:1	No	277

Table 4.3: Overview of the metMb ligand binding attempts, indicating the relative concentrations of ligand and protein, our observed colour changes and some reported equilibrium constants K_{eq} [97].

4.4.3 Results and Discussion

As expected, most of our ligands were readily able to bind metMb and simultaneously change the spin state from the native HS to LS (Table 4.3) or at least an equilibrium in favour of LS. Samples with pyridine or thiocyanate added in 10-fold excess did not change the spin state, but SCN^- has been shown to bind metMb [22]. However, it binds to Fe(III) in the HS state, so even though it has a strong IR band at 2006 cm^{-1}, there is no observable VCD [116]. Pyridine (Py) does not bind very easily; Fe(III) is in rapid equilibrium between LS and HS, and the protein may denaturate [19]. Most of the imidazoles bind, but 2-Me-Im did not seem to bind even at 100-fold excess, which is presumably due to the methyl group next to the coordinating N (Figure 4.17). Therefore, no spectra of this sample were recorded.

Our recorded VCD spectra in the fingerprint region of metMb with and without ligand are shown in Figure 4.19. The IR spectra are not included, because they have only vanishing contributions from the ligands in this region and therefore look practically identical.

Samples of metMb with Py or SCN^- added in 10-fold excess, which showed no colour change as an indication of entering the LS state, also show VCD spectra identical to that of metMb (within the noise level). On the other hand, all remaining five spectra (with N_3^- or imidazoles) reveal several new spectral features, which we interpret as REVCD due to the LS Fe(III) centre. Some of these new signals are similar among the different ligands: Positive bands at 1090, 1210, 1235, 1250, 1375 and 1400 cm^{-1}, and a negative band at 1100 cm^{-1}. Apart from metMb-Im and metMb-Im-d_3 having more negative VCD at 1515 cm^{-1}, this seems to be the only place where the REVCD signals are negative. These similar signals supposedly arise from hemin or the proximal ligand, while differing signals must be attributed to the distal ligands. The couplet around 1100 cm^{-1} is more intense for N_3^- than for the other ligands, which may be due to the more ionic character of the former.

Figure 4.20 compares the difference VCD spectra of metMb with Im and Im-d_3 bound, *i.e.*, the metMb-ligand VCD spectra with metMb VCD subtracted.

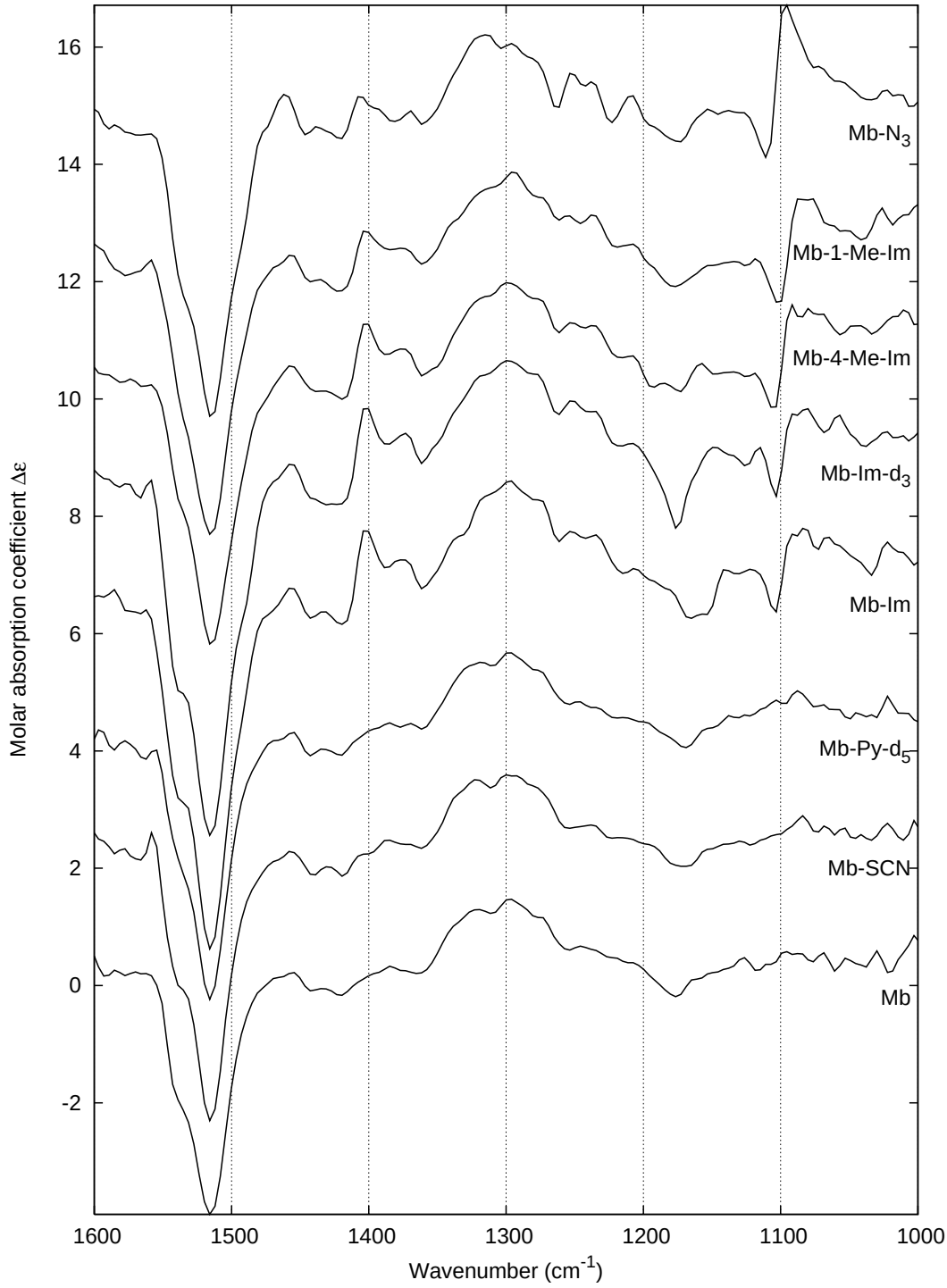

Figure 4.19: Experimental VCD spectra of metMb (11 mM metMb in 0.135 M phosphate buffer at pH 8.4 with 22 μm path length) and metMb with various distal ligands: Thiocyanate, pyridine, and the imidazoles are added in 10-fold excess, whereas azide is equimolar. MetMb, metMb-SCN and metMb-Py-d_5 have HS Fe(III) centres (Py-d_5 may not be bound). The resolution was 8 cm^{-1}, with the PEMs set at 1400 cm^{-1} and 12 h acquisition time. Spectra are offset for clarity, but not solvent subtracted.

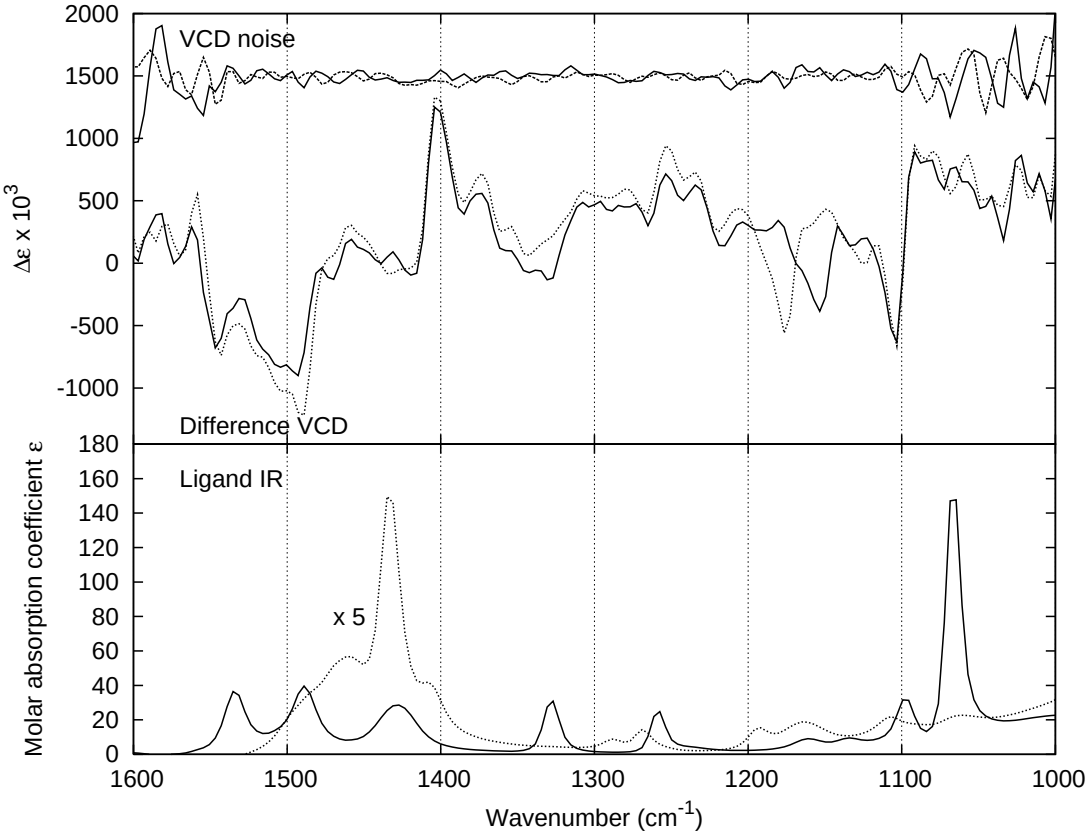

Figure 4.20: Experimental VCD difference (metMb subtracted) spectra of metMb-Im (—) and metMb-Im-d_3 (····) (top), compared to IR spectra of ligands Im (—) and Im-d_3 (····) (bottom) in 0.44 M and 1.8 M solutions, respectively. The resolution is 8 cm^{-1}, with the PEMs set at 1400 cm^{-1}. All spectra are solvent subtracted. An optical filter with cutoff above 2000 cm^{-1} was used.

This makes the REVCD and any other different features stand out, and should be comparable to calculations on just hemin and ligands. VCD noise levels are included to show which bands are reliable. The noise increases towards the CaF_2 cutoff at 1000 cm^{-1} and the intense water/amide I bands above 1600 cm^{-1}.

In the present case of imidazoles, we did not perform model DFT calculations and therefore merely compare experiments to each other. The IR spectra of the ligands alone have been included in Figure 4.20, in order to see whether some of the enhancement occurs at ligand vibrational modes. For Im, this is the case at 1135 and 1330 cm^{-1}, which are assigned by a B3LYP/6-31G(d) calculation (not shown) as ring breathing and C–N stretching at the coordinating N, respectively. A very similar story goes for Im-d_3, which has two breathing modes at 1160 and 1190 cm^{-1} and C–N stretching at 1430 cm^{-1}, all of which seem to arise in VCD as well. Caution should be exercised in these assignments, as the normal mode positions of ligands in solution and bound states will shift to some degree. But it sounds plausible that the above modes, if any, should be enhanced.

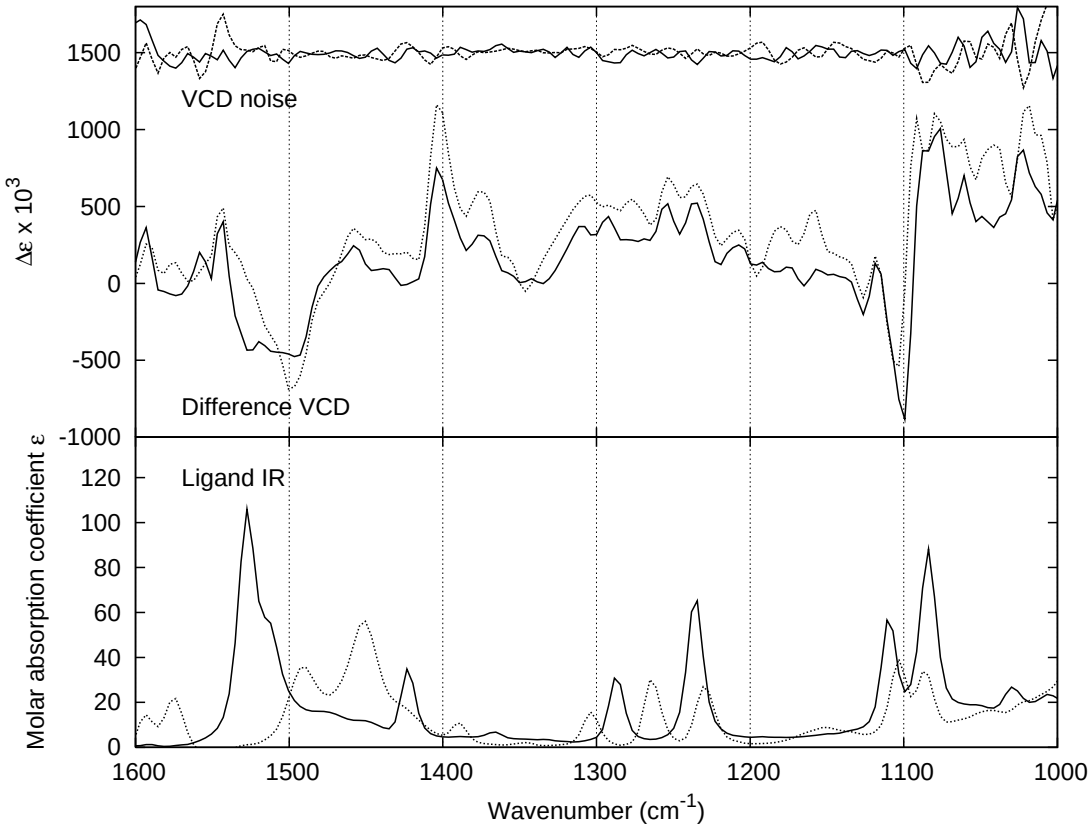

Figure 4.21: Experimental VCD difference (metMb subtracted) spectra of metMb-1-Me-Im (—) and metMb-4-Me-Im (····) (top), compared to IR spectra of ligands 1-Me-Im (—) and 4-Me-Im (····) (bottom) in 1.9 M solutions. The resolution is 8 cm^{-1}, with the PEMs set at 1400 cm^{-1}. All spectra are solvent subtracted.

The difference VCD spectra of metMb-1-Me-Im and metMb-4-Me-Im are compared to ligand IR spectra in Figure 4.21. Once again, we have calculated the ligand IR spectra at the B3LYP/6-31G(d) level in order to assign the ligand modes. There are not many significant differences between the two VCD spectra overall. But for 1-Me-Im, the prominent C=C IR band at 1525 cm^{-1} matches a distinct VCD signal. Also the C–N stretch at 1110 or the ring breathing at 1085 cm^{-1} could cause the sharp negative VCD band there. In case of 4-Me-Im, there is a similar correspondence between C=C stretching and negative VCD at 1595 cm^{-1}. The weak, broad feature at 1150 cm^{-1} seems associated with a positive VCD signal, but is not readily assigned by the calculated ligand IR. It could be both an N–H bending mode or (less likely) C–N stretching.

To summarize, we have identified common REVCD signals for all the low-spin Fe(III) metMb-ligand complexes investigated, as well as distinct enhanced VCD signals for each of them which coincide with ligand IR modes. In the following paragraphs, we look closer at the metMb-N_3, metMb-CN and metMb-H_2O complexes, for which model calculations have been undertaken.

Azidometmyoglobin

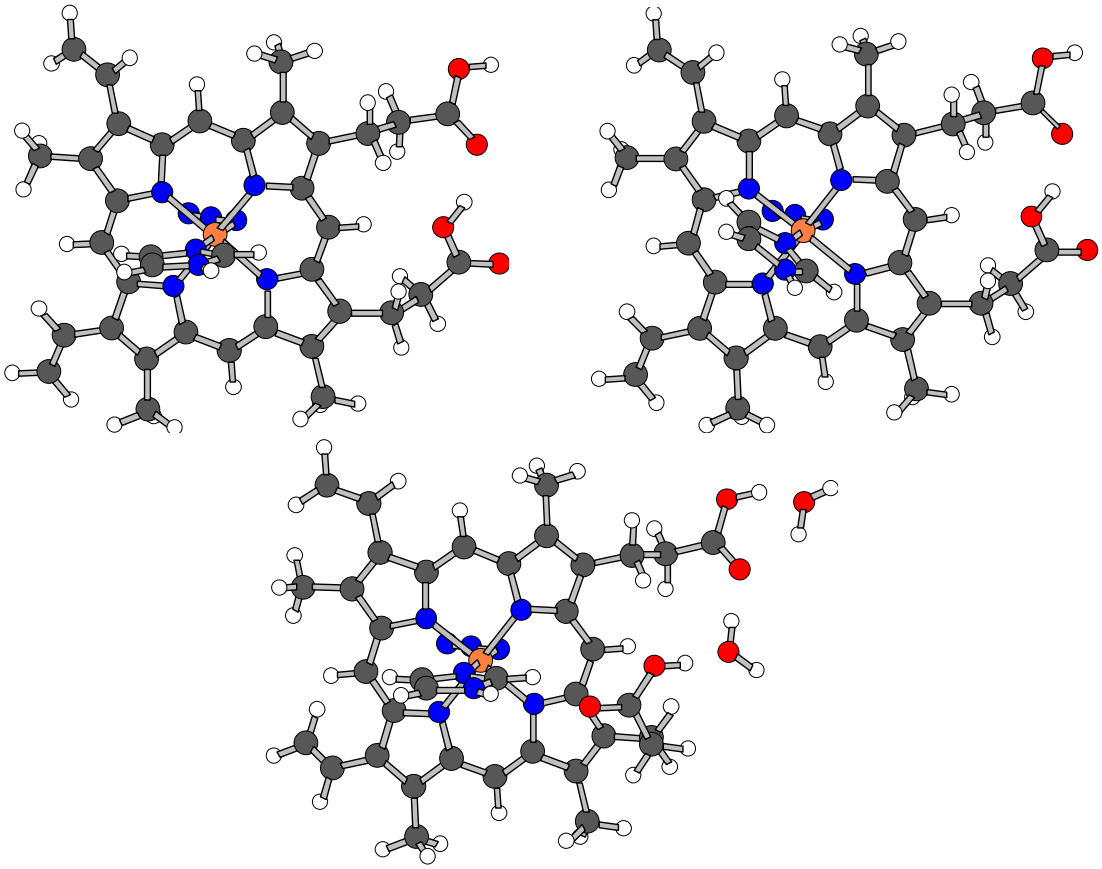

Figure 4.22: DFT optimized structures of hemin-Im-N_3, calculated using B3LYP/LanL2DZ. a) Without geometry constraints (top left). b) With Im fixed in the dihedral angle of His93 from 1AZI (top right). c) With two explicit water molecules near the propionic acids and no geometry constraints (bottom).

When the hemin-Im-N_3 complex was geometry optimized without constraints (Figure 4.22a), the proximal Im rotated 45° (around the coordination bond) from the 1AZI starting orientation to become coplanar with azide. The calculated IR/VCD spectra of this structure are shown in Figure 4.23a. Spectra calculated with proximal 4-Me-Im are almost indistinguishable from the case with just Im (data not shown).

In order to maintain Im in the right orientation, its torsional angle was fixed and geometry optimization repeated (Figure 4.22b). As expected, the frequency calculation of the resulting structure gives one imaginary mode corresponding to Im rocking. The calculated spectra (Figure 4.23b) look almost identical to the case without geometry constraints, except for the VCD showing a three times more intense N_3^- stretching mode at 1990 and a very significant Im in-plane deformation mode at 1500 cm^{-1}. Calculated N_3^- anisotropy ratios are $-3.54 \cdot 10^{-5}$ (a), $-1.08 \cdot 10^{-4}$ (b), and $-6.84 \cdot 10^{-5}$ (c). They are all below the range of experimental values, which is -6.4– $-9.5 \cdot 10^{-3}$ [12, 116].

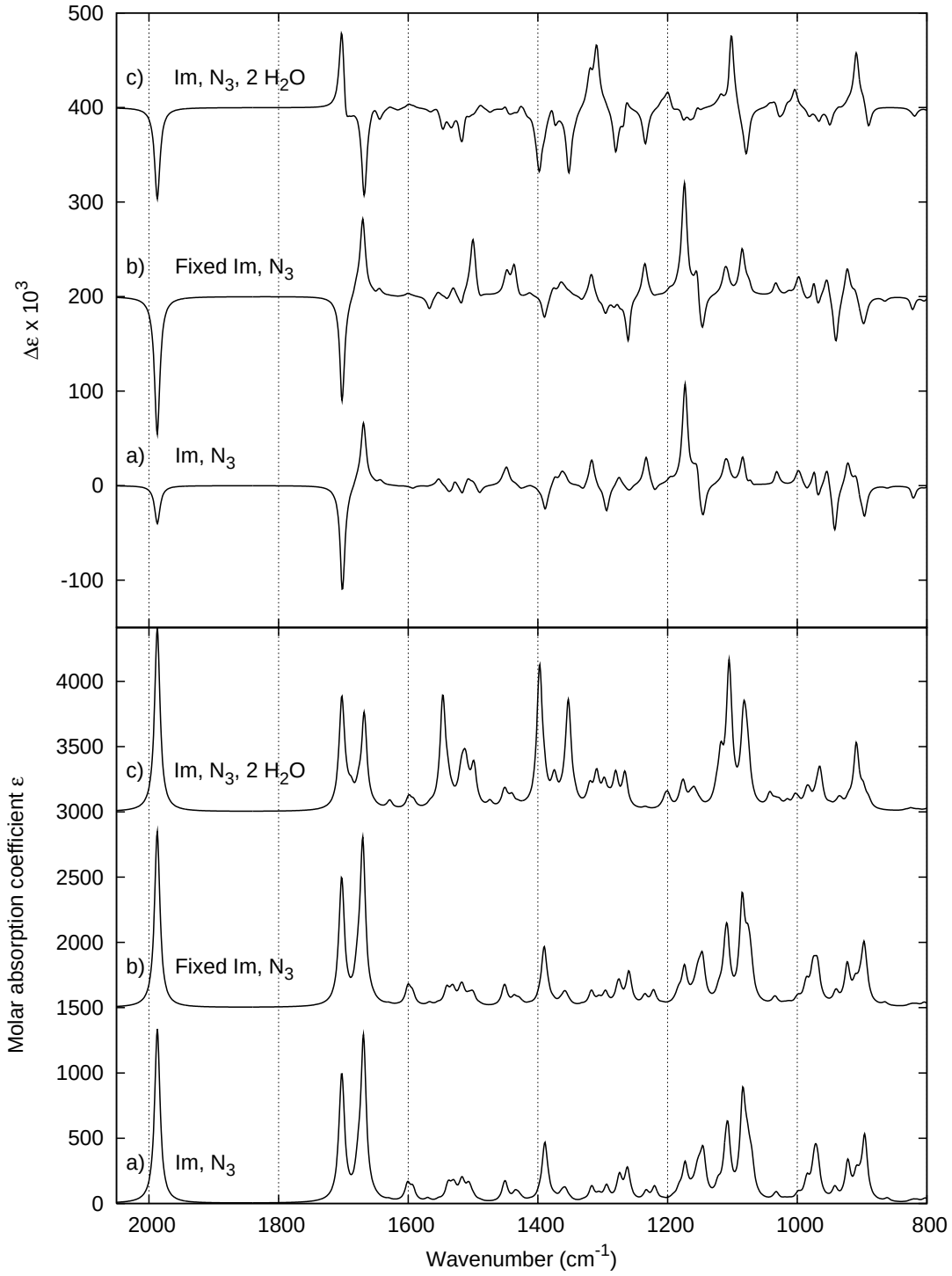

Figure 4.23: Calculated IR (lower half) and VCD (upper half) spectra of low-spin hemin with distal azide and other ligands as indicated. The DFT/B3LYP/LanL2DZ level was used, with no frequency scaling and Lorentzian broadening (HWHM=5 cm^{-1}). a) Without fixed Im, its rotation is 45° off from 1AZI His93. b) With fixed Im (1 imaginary frequency at Im rocking). c) With 2 explicit water molecules holding the propionic acids in place.

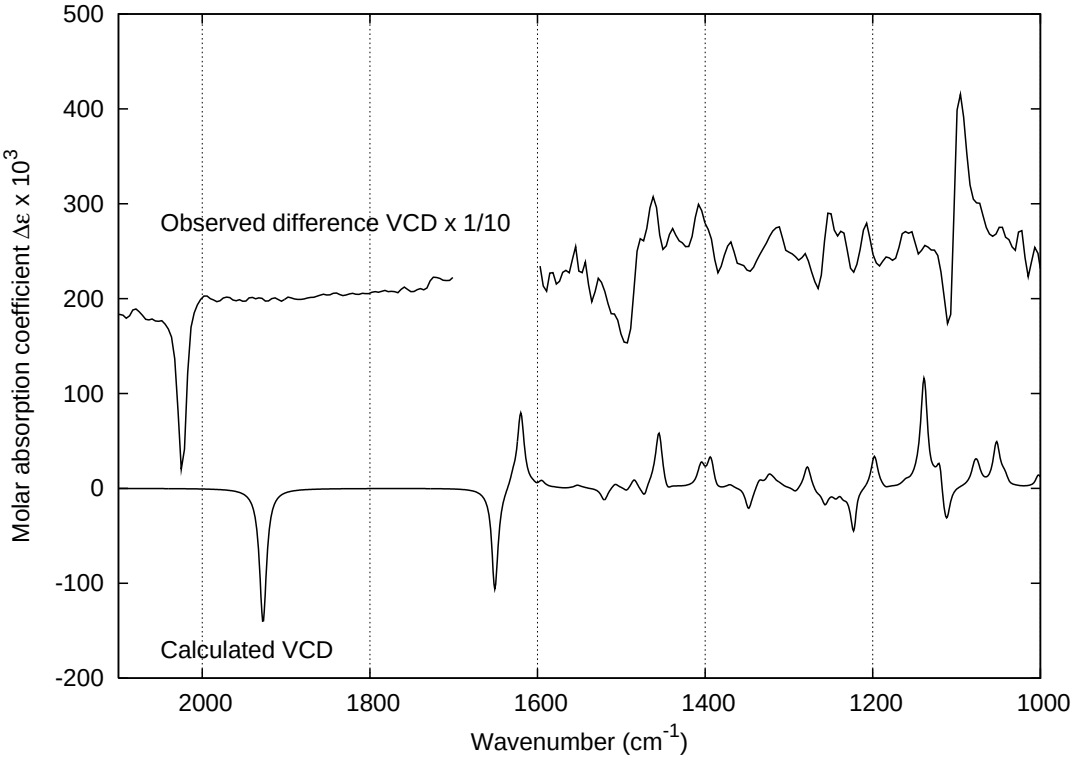

Figure 4.24: Experimental VCD difference of metMb-N_3 and metMb vs. calculated VCD of low-spin hemin-Im-N_3 at the DFT/B3LYP/LanL2DZ level, with frequency scaling factor 0.97 and HWHM=5 cm^{-1}. The experimental resolution was 8 cm^{-1}, and the acquisition time was 12 h for both samples, with the PEMs set at 1400 cm^{-1}. The very noisy amide I region has been left out.

Finally, a geometry optimization of hemin-Im-N_3 was started out from the 1AZI structure, with two explicit water molecules added to keep the propionic acids in place. They succeeded in doing so by forming a hydrogen bonding chain, but at the same time Im rotated 45° away from its starting orientation (Figure 4.22c). The calculated spectra at this geometry, shown in Figure 4.23c, not surprisingly introduce several strong O–H bending modes, some of which give strong VCD signals too (at 1100, 1350, and 1400 cm^{-1}). Additionally, in the VCD the propionic C–H bending is prominent at 1310 cm^{-1}, and the signs of the propionic C=O stretches at 1670–1700 cm^{-1} are inverted. We tend to believe that the stronger VCD features are O–H artifacts rather than REVCD effects.

The experimental VCD of azidometMb is shown in Figure 4.24, where the VCD of metMb has been subtracted to obtain only the enhanced VCD signals from hemin and ligands. Calculated VCD for hemin-Im-N_3 at the B3LYP/LanL2DZ level is shown, with the Im fixed (similar to Figure 4.23b, but with wavenumbers scaled by 0.97). The experimental VCD is 10 times more intense, and beyond that the correspondence is not convincing, although some of the sign pattern fits. We tentatively assign the intense 1100 cm^{-1} couplet to calculated hemin in-plane deformations at 1110–1115 cm^{-1}. The C=O stretches

cannot be seen in the experiment because they are buried in the water/amide I region, but the azide stretch at 1925 cm^{-1} has the correct sign. Other interesting calculated modes are Im N=C–N stretch at 1455 cm^{-1}, Im N–H bending at 1390 cm^{-1}, hemin deformation coupled to N_3^- stretch at 1220 cm^{-1} and O–H bend at 1200 cm^{-1}. From the poor ability to reproduce the observed intensities, it seems that LanL2DZ is an insufficient basis set for calculating REVCD. A paper on sparteine complexes reached a similar conclusion [52].

Cyanometmyoglobin

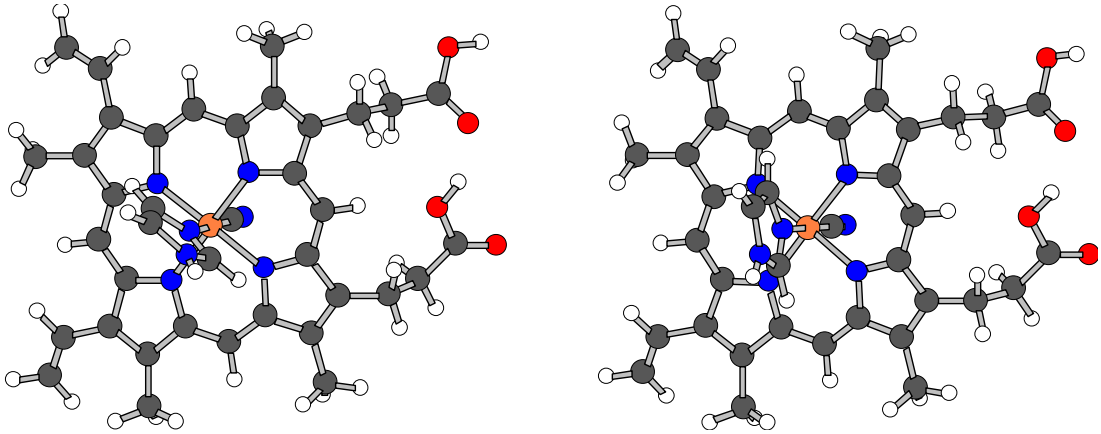

Figure 4.25: DFT optimized structure of hemin-Im-CN without geometry constraints. With B3LYP/LanL2DZ, Im stays oriented as in the crystal structures (left), but with B3LYP/6-31G(d) Im rotates 45° away (right).

Figure 4.16b shows a crystal structure fragment from sperm whale cyanometMb (PDB ID 1EBC), since no crystal structure of the cyanide complex with horse heart Mb was found. But the hemin is distorted in a fashion roughly similar to 1AZI, and the proximal His is similarly oriented. As our starting structure for gas phase DFT calculations we took the already optimized hemin-Im-N_3 and simply replaced the distal ligand. In the crystal structure, CN^- is not quite normal to the heme plane, but inclines by 9° due to electrostatic interactions with His64.

During geometry optimization, CN^- came to lie along the ligand axis normal to hemin. Depending on the starting orientation of the proximal Im, it was able to find at least two equilibrium orientations, either in the correct one or about 90° away from it. Their electronic energies differ by merely 7.5 J/mol. Interestingly, when a reoptimization was performed with the 6-31G(d) basis set, Im rotated 45° to lie between the first two orientations. Furthermore, the hemin became slightly saddle shaped. Figure 4.25 compares two of these structures.

The calculated VCD spectra in the three optimized structures are compared in Figure 4.26. Remarkably, the VCD of the two alternative structures at the B3LYP/LanL2DZ level differ by an order of magnitude and have somewhat

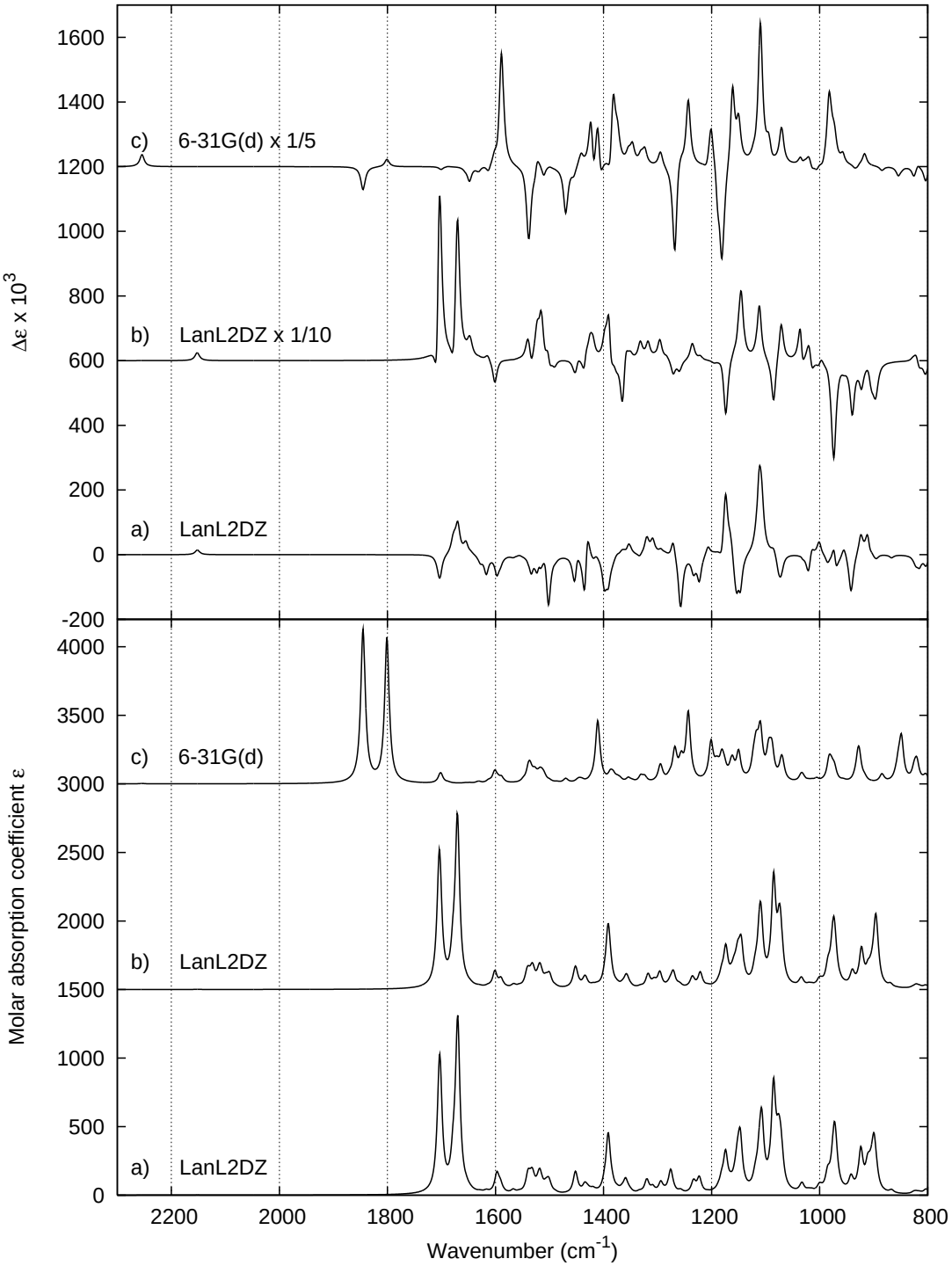

Figure 4.26: Calculated IR (lower half) and VCD (upper half) spectra of low-spin hemin with proximal Im and distal cyanide. The DFT/B3LYP level was used with basis sets as indicated and Lorentzian broadening (HWHM=5 cm^{-1}) without frequency scaling. a) With Im rotated 90° off from 1EBC His93. b) With Im oriented as 1EBC His93. c) With Im rotated 45° off and 1 imaginary frequency (Fe–C≡N bending mode).

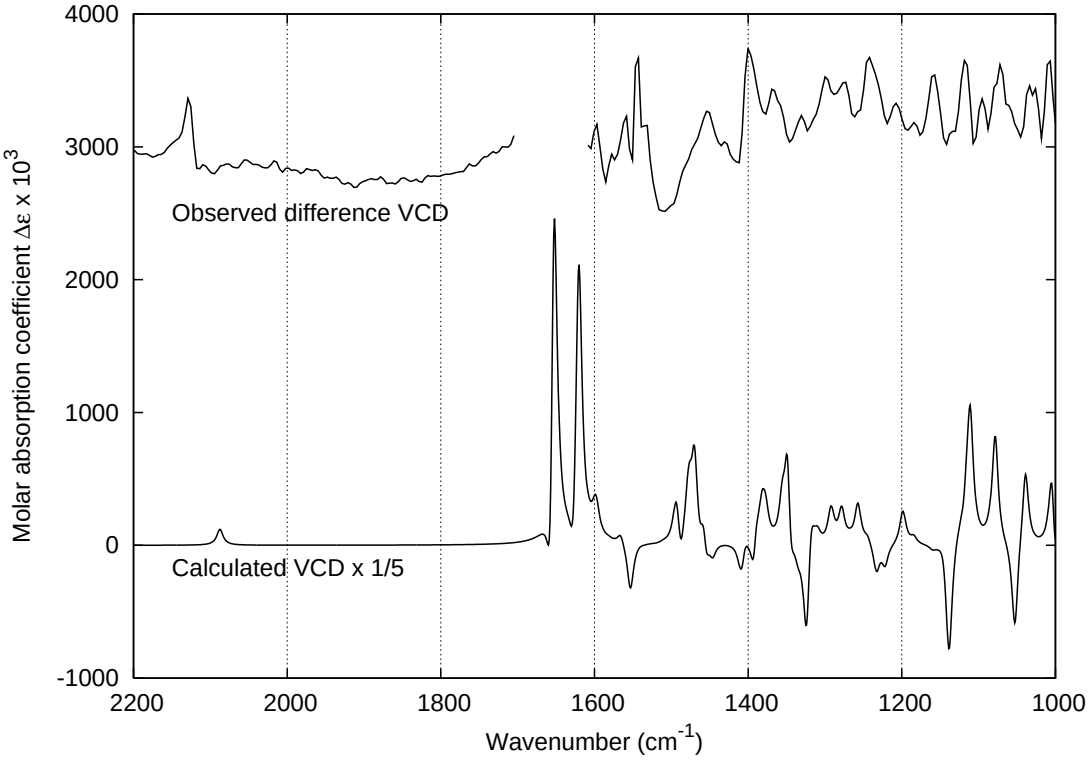

Figure 4.27: Experimental VCD difference of metMb-CN and metMb vs. calculated VCD of low-spin hemin-Im-CN at the DFT/B3LYP/LanL2DZ level, with frequency scaling factor 0.97 and HWHM=5 cm^{-1}. The experimental resolution was 8 cm^{-1} at 11 mM concentration and 30.4 μm path length. Acquisition times were 28 h, with the PEMs set at 1200 or 2000 cm^{-1} respectively. The very noisy amide I region has been left out. Experimental data courtesy of David A. Dunmire/Teresa B. Freedman.

differing sign patterns, while their IR spectra look indistinguishable. We also note that the positions of the cyanide and C=O stretching modes are considerably higher for the 6-31G(d) basis set, a pattern seen earlier for a Re(V) complex (Figure 4.6). The cyanide stretching mode is too weak to be discerned in the IR spectra, but is visible in the VCD. This mode has a theoretical anisotropy ratio g, which varies by an order of magnitude among the calculations as 0.012 (a), 0.23 (b), and 0.028 (c). Part of this variation may be due to the uncertainty of dividing two small numbers. Two of these g values are similar to reported values of $2.4–2.8 \cdot 10^{-3}$ [13,116], but recent measurements suggest a value as large as 0.01 (David A. Dunmire, Syracuse University, unpublished result).

Just before the 6-31G(d) frequency calculation, the structure took one step away from the located minimum with Im turned 45°, resulting in one imaginary normal mode (Fe–C≡N bending). This makes the calculated results less reliable.

A comparison of experimental VCD difference (kindly provided from David A. Dunmire) to the B3LYP/LanL2DZ calculation with Im in correct orientation is shown in Figure 4.27. Remarkably, the roles are reversed compared to the

previous case of azidometMb (Figure 4.24): This theoretical VCD spectrum has higher intensity overall than the experimental results, which seems to overturn the previous conclusion about the LanL2DZ basis set showing no REVCD.

Our calculated CN^- stretching mode at 2090 cm^{-1} has both correct intensity and sign. Other modes that appear to correspond to experiment (apart from the intensity discrepancy) are hemin in-plane breathing at 1470 cm^{-1} and deformations at 1220, 1230, 1350, 1360, 1380, 1390, 1480, and 1550 cm^{-1}, propionic acid C–H twisting, wagging and scissoring at 1260–1290, 1352, and 1490 cm^{-1}, respectively. Modes involving Im include in-plane ring deformation at 1320 cm^{-1} and N–H bending at 1390 cm^{-1}. We would expect such vibrations to experience enhancement. Even the propionic acid modes may not be too far away for that. Experiments with Co(II)salbinaphtyl and Co(II)Cl_4salbinaphtyl show that the metal site orbitals are sensitive to substitutions taking place 5–7 Å away [51].

High-Spin Hemin Calculations

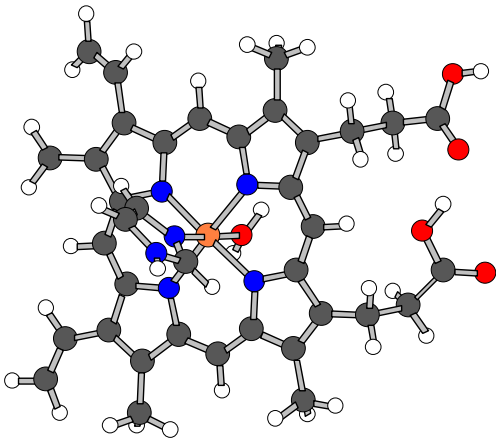

Figure 4.28: DFT optimized structure of hemin with proximal Im and distal H_2O bound, calculated using B3LYP/LanL2DZ.

As a final example of unexpected VCD intensities, we show a calculation of hemin with proximal Im and either distal H_2O bound or no distal ligand, which should have a HS Fe(III) centre [89]. The optimized structure with distal water is shown in Figure 4.28, where the proximal Im stays in the correct orientation during optimization. When water is removed, Fe is simply pulled slightly out of the hemin towards Im. Our calculated IR and VCD spectra of these structures are displayed in Figure 4.29. Apparently, the structure with water bound has an order of magnitude larger VCD intensity overall, with only minor differences in the IR spectra.

No enhanced VCD was expected in these HS complexes. The reason for the intense VCD in the case with distal water could simply be the fact that this geometry is more chiral around the Fe(III). Possibly, we are seing artificial VCD signals because only one orientation of the water molecule is considered,

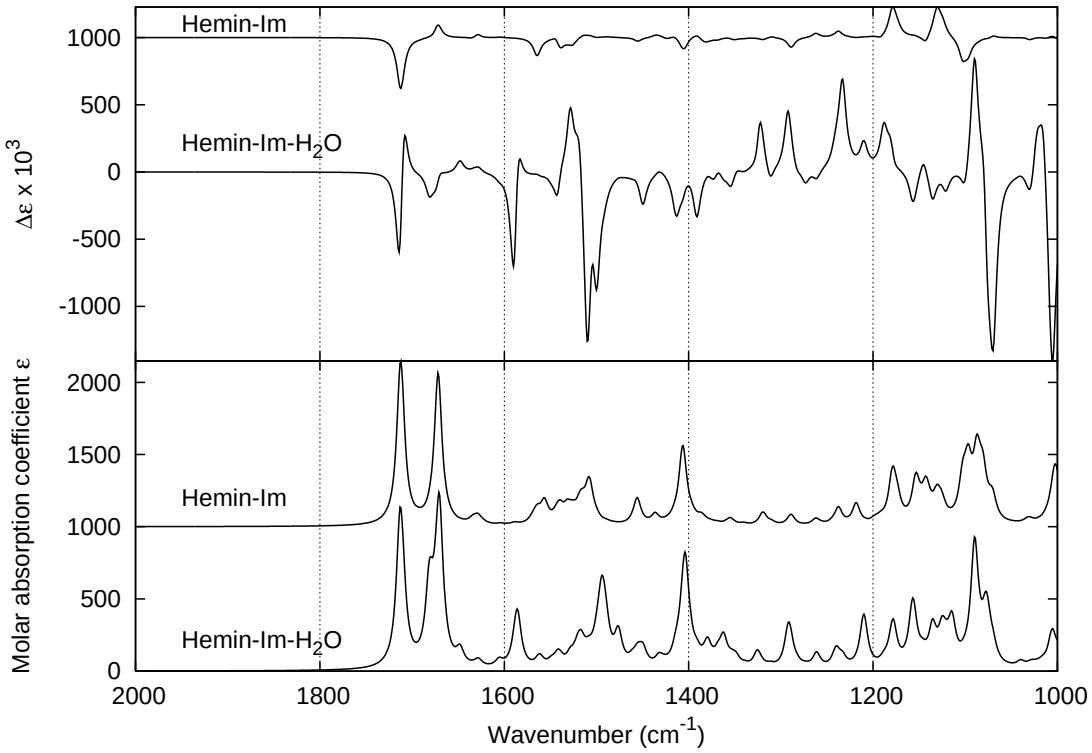

Figure 4.29: Calculated IR (bottom) and VCD (top) of HS Fe(III) hemin with proximal Im and either distal H_2O or no distal ligand, calculated using B3LYP/LanL2DZ.

whereas in reality it is most likely more dynamic and therefore may average out some of the artifacts.

4.5 Summary

To the best of our knowledge, this chapter has presented the first VCD spectra of rhenium compounds, both experimentally and theoretically. We have made a DFT/B3LYP survey of the performance of different basis sets and successfully reproduced our experimental spectra of two Re(V) complexes by using the Stuttgart RSC 1997 ECP basis set on Re, thereby verifying their absolute configuration and predominant conformers. Thus, the applicability of VCD has been expanded to heavy elements, which may become a valuable tool for investigations of chiral transition metal complexes.

In the subsequent sections, we have continued undergoing research at SU into the effect of resonance-enhanced VCD (REVCD). Our first study case was purely theoretical, since corresponding measurements were already being carried out. We therefore calculated the IR and VCD spectra of some Schiff-base transition metal complexes, for which REVCD is seen in case of Co(II), but not with Ni(II) or Zn(II). Here, the Co(II) complexes are the only ones which have low-lying (IR) electronic CD signals from d–d transitions. We successfully

calculated enhanced VCD intensities of Co(II)saldiphenyl and unenhanced VCD of Ni(II)saldiphenyl using B3LYP/6-31G(d) with the Ahlrichs VTZ basis set on the metal, which verified the absolute configurations and established the predominant conformers of the samples. In the case of Co(II)salbinaphtyl, we found two possible geometries with different spin states, but were only able to reproduce part of the observed VCD enhancement with the same method as before.

We also got involved in a major project about metmyoglobin (metMb) and various small ligands, with which a range of VCD measurements were carried out, along with theoretical calculations on just hemin and ligands. We have seen effects of REVCD in both cases and were able to correlate the results to some degree. With various imidazole ligands, we measured characteristic REVCD features, some of which were coincident with ligand IR modes. Other REVCD modes were assigned to hemin or ligand modes by DFT/B3LYP calculations on isolated hemin with proximal imidazole and distal N_3^- or CN^-. Theoretical anisotropy ratios for the CN^- stretching were similar to experimental values. Strangely, when comparing metMb-N_3 and metMb-CN results, the calculated VCD with LanL2DZ misses the experimental REVCD intensities by about an order of magnitude, but in opposite direction. Hence, LanL2DZ may be an insufficient basis set. This is hard to judge yet, with an incomplete computational implementation and system sizes on the border of what is tractable, since frequency calculations often exceeded a month of CPU time. Besides, using the 6-31G(d) basis set for comparison was not always feasible.

Currently, the VCD intensities one gets from calculations of systems with low-lying d–d transitions seem somewhat random, depending partly on basis set and partly on minor structural changes. Apparently, these calculations become difficult due to size, shallow energy minima and the fact that we are approaching the limit of the MFP theory, which does not entirely take the low-lying electronic transitions into account.

With the discovery of REVCD, the applicability of VCD might become expanded to include transition metal complexes embedded in biological systems, *i.e.*, metalloproteins. Our hope for REVCD is to get a selective probe of their active sites, if the present teething troubles can be overcome by a reliable implementation of recent theory in DFT software.

Chapter 5

Concluding Remarks

This Ph.D. thesis has investigated a number of organic and bioinorganic molecules by using the VCD technique experimentally as well as theoretically. We have used this combined method on several pharmaceutically interesting cases, thereby further illustrating the applicability of VCD in drug development, where structural elucidation is essential. Several small molecules were studied, and their absolute configurations were determined, along with identification of prominent conformers. These molecules range from 20 to 74 atoms in size, and some are challenging cases either by being very flexible (nyasol and curcuphenol dimers), whereas another (ginkgolide B) has 11 chiral centres.

Most of our DFT calculations were carried out in the gas phase, but solvent effects have also been treated at different levels. Implicit solvation models gave only minor changes compared to gas phase spectra, whereas introduction of explicit solvent molecules was more successful.

Much of our research during the stay at SU was devoted to the study of transition metal complexes containing primarily Re(V) or Co(II). In these cases, the absolute configurations were known from elsewhere and verified by VCD analysis, whereas the conformers in solution were not fully identified. Very few examples of VCD applied to transition metal complexes exist, so our work was mainly feasibility studies. Thus, we have successfully measured the first VCD spectra of rhenium compounds and reproduced them theoretically. Furthermore, we have looked into the phenomenon of resonance-enhanced VCD (REVCD), which has been observed for several complexes having partly filled d-orbitals with associated infrared electronic transitions. At present, commercial DFT software does not have the full theory needed to account for the contributions of these electronic states to the VCD. However, we were able to reproduce some of the observed enhancement using the current VCD implementation (magnetic field perturbation).

Transition metals with open d-shells are often present in biology (metalloproteins), where they take part in various catalytic or transportation processes. Here, REVCD might become a selective probe of the active sites around metal ions. We have studied metmyoglobin with a number of small ligands bound, some of which reveal markedly different VCD in the fingerprint region. It is believed that the Fe(III) centre can cause REVCD in its low-spin state. DFT

calculations on model systems consisting of hemin and ligands were carried out, and they revealed considerable VCD intensity variations while the IR spectra remained similar. It seems like the anisotropy ratio is very sensitive to geometrical details and maybe the basis set employed.

Bibliography

[1] Basis sets were obtained from the Extensible Computational Chemistry Environment Basis Set Database, Version 02/25/04, as developed and distributed by the Molecular Science Computing Facility, Environmental and Molecular Sciences Laboratory which is part of the Pacific Northwest Laboratory, P.O. Box 999, Richland, Washington 99352, USA, and funded by the U.S. Department of Energy. The Pacific Northwest Laboratory is a multi-program laboratory operated by Battelle Memorial Institute for the U.S. Department of Energy under contract DE-AC06-76RLO 1830. Contact Karen Schuchardt for further information. http://www.emsl.pnl.gov/forms/basisform.html.

[2] Andrae, D., Haussermann, U., Dolg, M., Stoll, H., and Preuss, H. Energy-adjusted ab initio pseudopotentials for the second and third row transition elements. *Theoretica Chimica Acta 77*, 2 (1990), 123–41.

[3] Andrews, S. S., and Boxer, S. G. Analysis of noise for rapid-scan and step-scan methods of FT-IR difference spectroscopy. *Applied Spectroscopy 55*, 9 (2001), 1161–5.

[4] Ashvar, C. S., Devlin, F. J., and Stephens, P. J. Molecular structure in solution: An ab initio vibrational spectroscopy study of phenyloxirane. *Journal of the American Chemical Society 121*, 12 (1999), 2836–49.

[5] Banwell, C. N., and McCash, E. M. *Fundamentals of molecular spectroscopy*, 4th ed. McGraw-Hill, 1994.

[6] Barnett, C. J., Drake, A. F., Kuroda, R., Mason, S. F., and Savage, S. Vibrational-electronic interaction in the infrared circular dichroism spectra of transition-metal complexes. *Chemical Physics Letters 70*, 1 (1980), 8–10.

[7] Barron, L. D., Bogaard, M. P., and Buckingham, A. D. Raman scattering of circularly polarized light by optically active molecules. *Journal of the American Chemical Society 95*, 2 (1973), 603–5.

[8] Bauschlicher, C. W. Large atomic natural orbital basis sets for the first transition row atoms. *Theoretica Chimica Acta 92*, 3 (1995), 183–98.

[9] Becke, A. D. Density-functional thermochemistry. III. The role of exact exchange. *Journal of Chemical Physics 98*, 7 (1993), 5648–52.

[10] Bernardo, K., Leppard, S., Robert, A., Commenges, G., Dahan, F., and Meunier, B. Synthesis and characterization of new chiral Schiff base complexes with diiminobinaphthyl or diiminocyclohexyl moieties as potential enantioselective epoxidation catalysts. *Inorganic Chemistry 35*, 2 (1996), 387–96.

[11] Bertini, I., Gray, H. B., Lippard, S. J., and Valentine, J. S. *Bioinorganic Chemistry*. University Science Books, 1994.

[12] Bormett, R. W., Asher, S. A., Larkin, P. J., Gustafson, W. G., Ragunathan, N., Freedman, T. B., Nafie, L. A.; Balasubramanian, S., Boxer, S. G., Yu, N.-T., Gersonde, K., Noble, R. W., Springer, B. A., and Sligar, S. G. Selective examination of heme protein azide ligand-distal globin interactions by vibrational circular dichroism. *Journal of the American Chemical Society 114* (1992), 6864–7.

[13] Bormett, R. W., Smith, G. D., and Asher, S. A. Vibrational circular dichroism measurements of ligant vibrations in haem and non-haem metalloenzymes. *Faraday Discussions 99* (1994), 327–39.

[14] Bouchiat, M.-A., and Bouchiat, C. Parity violation in atoms. *Reports on Progress in Physics 60*, 11 (1997), 1351–94.

[15] Cao, X., Shah, R. D., Dukor, R. K., Guo, C., Freedman, T. B., and Nafie, L. A. Extension of Fourier transform vibrational circular dichroism into the near-infrared region: Continuous spectral coverage from 800 to 10 000 cm^{-1}. *Applied Spectroscopy 58*, 9 (2004), 1057–64.

[16] Chapman, S. K., Daff, S., and Munro, A. W. Heme: The most versatile redox centre in biology? In *Metal Sites in Proteins and Models*, H. A. O. Hill, P. J. Sadler, and A. J. Thomson, Eds. Springer-Verlag Berlin Heidelberg, 1999.

[17] Che, C.-M., and Huang, J.-S. Metal complexes of chiral binaphthyl Schiff-base ligands and their application in stereoselective organic transformations. *Coordination Chemistry Reviews 242*, 1-2 (2003), 97–113.

[18] Cheeseman, J. R., Frisch, M. J., Devlin, F. J., and Stephens, P. J. Hartree-Fock and density functional theory ab initio calculation of optical rotation using GIAOs: basis set dependence. *Journal of Physical Chemistry A 104*, 5 (2000), 1039–46.

[19] Chen, Y., Liu, G., and Tang, W. ^{1}H NMR studies of pyridine binding to metmyoglobin. *Inorganica Chimica Acta 249*, 2 (1996), 239–43.

[20] Clot, E., Besora, M., Maseras, F., Megret, C., Eisenstein, O., Oelckers, B., and Perutz, R. N. Bond energy M-C/H-C correlations: dual theoretical and experimental approach to the sensitivity of M-C bond strength to substituents. *Chemical Communications 3*, 4 (2003), 490–1.

[21] Coates, J. Interpretation of infrared spectra, a practical approach. In *Encyclopedia of Analytical Chemistry*, R. A. Meyers, Ed. John Wiley & Sons, 2000, pp. 10815–37.

[22] Conti, E., Moser, C., Rizzi, M., Mattevi, A., Lionetti, C., Coda, A., Ascenzi, P., Brunori, M., and Bolognesi, M. X-ray crystal structure of ferric Aplysia limacina myoglobin in different liganded states. *Journal of Molecular Biology 233*, 3 (1993), 498–508.

[23] Cotton, F. A. *Chemical applications of group theory*, 3rd ed. Wiley, New York, 1990.

[24] Crassous, J., Chardonnet, C., Saue, T., and Schwerdtfeger, P. Recent experimental and theoretical developments towards the observation of parity violation (PV) effects in molecules by spectroscopy. *Organic & Biomolecular Chemistry 3*, 12 (2005), 2218–24.

[25] Crassous, J., Monier, F., Dutasta, J. P., Ziskind, M., Daussy, C., Grain, C., and Chardonnet, C. Search for resolution of chiral fluorohalogenomethanes and parity-violation effects at the molecular level. *ChemPhysChem 4*, 6 (2003), 541–8.

[26] Ditchfield, R., Hehre, W. J., and Pople, J. A. Self-consistent molecular-orbital methods. IX. An extended Gaussian-type basis for molecular-orbital studies of organic molecules. *Journal of Chemical Physics 54*, 2 (1971), 724–8.

[27] Dolg, M., Wedig, U., Stoll, H., and Preuss, H. Energy-adjusted ab initio pseudopotentials for the first row transition elements. *Journal of Chemical Physics 86*, 2 (1987), 866–72.

[28] Dukor, R. K., and Nafie, L. A. Vibrational optical activity of pharmaceuticals and biomolecules. In *Encyclopedia of Analytical Chemistry*, R. A. Meyers, Ed. John Wiley & Sons, 2000, pp. 662–676.

[29] Dunning, Thom H., J. Gaussian basis sets for use in correlated molecular calculations. I. The atoms boron through neon and hydrogen. *The Journal of Chemical Physics 90*, 2 (1989), 1007–23.

[30] Dunning Jr, T. H., and hay, P. J. Gaussian basis sets for molecular calculations. In *Modern Theoretical Chemistry*, H. F. Schaefer III, Ed. Plenum, New York, 1976, pp. 1–28.

[31] Dupont, L., Dideberg, O., Germain, G., and Braquet, P. Structure of ginkgolide B (BN 52021) monohydrate, a highly specific PAF/acether receptor antagonist isolated from Ginkgo biboba L. *Acta Crystallographica Section C 42*, 12 (Dec 1986), 1759–62.

[32] Ellzy, M. W., Jensen, J. O., Hameka, H. F., and Kay, J. G. Correlation of structure and vibrational spectra of the zwitterion L-alanine in the presence of water: an experimental and density functional analysis. *Spectrochimica Acta Part A: Molecular and Biomolecular Spectroscopy 59*, 11 (2003), 2619–33.

[33] Eriksson, T., Bjorkman, S., and Hoglund, P. Clinical pharmacology of thalidomide. *European Journal of Clinical Pharmacology 57*, 5 (2001), 365–76.

[34] Faller, J. W., and Lavoie, A. R. Diastereoselective synthesis and electronic asymmetry of chiral nonracemic rhenium(V) oxo complexes containing the hydrotris(1-pyrazolyl)borate ligand. *Organometallics 19*, 19 (2000), 3957–62.

[35] Foresman, J. B., and Frisch, Æ. *Exploring Chemistry with Electronic Structure Methods*, 2nd ed. Gaussian, Inc., 1996.

[36] Franzen, S., and Boxer, S. G. On the origin of heme absorption band shifts and associated protein structural relaxation in myoglobin following flash photolysis. *Journal of Biological Chemistry 272*, 15 (1997), 9655–60.

[37] Freedman, T. B., Balukjian, G. A., and Nafie, L. A. Enhanced vibrational circular dichroism via vibrationally generated electronic ring currents. *Journal of the American Chemical Society 107*, 22 (1985), 6213–22.

[38] Freedman, T. B., Cao, X., Dukor, R. K., and Nafie, L. A. Absolute configuration determination of chiral molecules in the solution state using vibrational circular dichroism. *Chirality 15*, 9 (2003), 743–58.

[39] Freedman, T. B., Cao, X., Young, D. A., and Nafie, L. A. Density functional theory calculations of vibrational circular dichroism in transition metal complexes: Identification of solution conformations and mode of chloride ion association for (+)-Tris(ethylenediaminato)cobalt(III). *Journal of Physical Chemistry A 106*, 14 (2002), 3560–5.

[40] Frisch, M., Pople, J., and Binkley, J. Self-consistent molecular orbital methods. XXV. Supplementary functions for Gaussian basis sets. *Journal of Chemical Physics 80*, 7 (1984), 3265–9.

[41] Frisch, M. J., Trucks, G. W., Schlegel, H. B., Scuseria, G. E., Robb, M. A., Cheeseman, J. R., Montgomery, J. A., J., Vreven, T., Kudin, K. N., Burant, J. C., Millam, J. M., Iyengar, S. S., Tomasi, J., Barone, V., Mennucci, B., Cossi, M., Scalmani, G., Rega, N., Petersson, G. A., Nakatsuji, H., Hada, M., Ehara, M., Toyota, K., Fukuda, R., Hasegawa, J., Ishida, M., Nakajima, T., Honda, Y., Kitao, O., Nakai, H., Klene, M., Li, X., Knox, J. E., Hratchian, H. P., Cross, J. B., Adamo, C., Jaramillo, J., Gomperts, R., Stratmann, R. E., Yazyev, O., Austin, A. J., Cammi, R., Pomelli, C., Ochterski, J. W., Ayala, P. Y., Morokuma, K., Voth, G. A., Salvador, P., Dannenberg, J. J., Zakrzewski, V. G., Dapprich, S., Daniels, A. D., Strain, M. C., Farkas, O., Malick, D. K., Rabuck, A. D., Raghavachari, K., Foresman, J. B., Ortiz, J. V., Cui, Q., Baboul, A. G., Clifford, S., Cioslowski, J., Stefanov, B. B., Liu, G., Liashenko, A., Piskorz, P., Komaromi, I., Martin, R. L., Fox, D. J., Keith, T., Al-Laham, M. A., Peng, C. Y., Nanayakkara, A., Challacombe, M., Gill, P. M. W., Johnson, B., Chen, W., Wong, M. W., Gonzalez, C., and Pople, J. A. Gaussian 03, Revision B.04. Gaussian, Inc., Pittsburgh PA, 2003.

[42] Fristrup, P. *Selective Homogeneous Catalysis in Asymmetric Synthesis*. PhD thesis, Technical University of Denmark, February 2006.

[43] Fristrup, P., Dideriksen, B. B., Tanner, D., and Norrby, P.-O. Probing competitive enantioselective approach vectors operating in the Jacobsen-Katsuki epoxidation: A kinetic study of methyl-substituted styrenes. *Journal of the American Chemical Society 127*, 39 (2005), 13672–9.

[44] Goodman, J. M. *Chemical Applications of Molecular Modelling*. Royal Society of Chemistry, 1998.

[45] Gray, T. G., Rudzinski, C. M., Meyer, E. E., Nocera, D. G., and Holm, R. H. Spectroscopic and photophysical properties of hexanuclear rhenium(III) chalcogenide clusters. *Journal of the American Chemical Society 125*, 16 (2003), 4755–70.

[46] Halgren, T. A. Merck molecular force field. I. Basis, form, scope, parameterization, and performance of MMFF94. *Journal of Computational Chemistry 17*, 5-6 (1996), 490–519.

[47] Halgren, T. A. MMFF. VII. Characterization of MMFF94, MMFF94s, and other widely available force fields for conformational energies and for intermolecular-interaction energies and geometries. *Journal of Computational Chemistry 20*, 7 (1999), 730–48.

[48] Hariharan, P. C., and Pople, J. A. The influence of polarization functions on molecular orbital hydrogenation energies. *Theoretica Chimica Acta 28*, 3 (1973), 213–22.

[49] Harrison, B., and Crews, P. The structure and probable biogenesis of helianane, a heterocyclic sesquiterpene, from the indo-pacific sponge haliclona ?fascigera. *Journal of Organic Chemistry 62* (1997), 2646–48.

[50] Hay, P. J., and Wadt, W. R. Ab initio effective core potentials for molecular calculations. Potentials for K to Au including the outermost core orbitals. *Journal of Chemical Physics 82*, 1 (1985), 299–310.

[51] He, Y. *Enhanced VCD in Transition Metal Complexes and Metalloproteins*. PhD thesis, Syracuse University, July 2005.

[52] He, Y., Cao, X., Nafie, L. A., and Freedman, T. B. Ab initio VCD calculation of a transition-metal containing molecule and a new intensity enhancement mechanism for VCD. *Journal of the American Chemical Society 123*, 45 (2001), 11320–1.

[53] Hehre, W., Ditchfield, R., and Pople, J. Self-consistent molecular orbital methods. XII. Further extensions of Gaussian-type basis sets for use in molecular orbital studies of organic molecules. *Journal of Chemical Physics 56*, 5 (1972), 2257–61.

[54] Hocquet, A., and Langgård, M. An evaluation of the MM+ force field. *Journal of Molecular Modeling 4*, 3 (1998), 94–112.

[55] Holzwarth, G., Hsu, E. C., Mosher, H. S., Faulkner, T. R., and Moscowitz, A. Infrared circular dichroism of carbon-hydrogen and carbon-deuterium stretching modes. observations. *Journal of the American Chemical Society 96*, 1 (1974), 251–2.

[56] Hoshina, G., Tsuchimoto, M., and Ohba, S. [*N*,*N*′-Bis(salicylidene)-1,2-diphenyl-(*RS*,*SR*)-1,2-ethanediaminato]nickel(II). *Acta Crystallographica Section C 56*, 4 (Apr 2000), e122.

[57] Hurley, M. M., Pacios, L. F., Christiansen, P. A., Ross, R. B., and Ermler, W. C. Ab initio relativistic effective potentials with spin-orbit operators. II. K through Kr. *Journal of Chemical Physics 84*, 12 (1986), 6840–53.

[58] Iida, Y., Oh, K.-B., Saito, M., Matsuoka, H., Kurata, H., Natsume, M., and Abe, H. Detection of antifungal activity in anemarrhena asphodeloides by sensitive BCT method and isolation of its active compound. *Journal of Agricultural and Food Chemistry 47*, 2 (1999), 584–7.

[59] Iizuka, T., and Morishima, I. NMR studies of hemoproteins. VI. Acid-base transitions of ferric myoglobin and its imidazole complex. *Biochimica et Biophysica Acta 400*, 1 (1975), 143–53.

[60] Ivic, L., Sands, T. T. J., Fishkin, N., Nakanishi, K., Kriegstein, A. R., and Strømgaard, K. Terpene trilactones from ginkgo biloba are antagonists of cortical glycine and $GABA_A$ receptors. *Journal of Biological Chemistry 278*, 49 (2003), 49279–85.

[61] Jeong, S.-J., Higuchi, R., Ono, M., Kuwano, M., Kim, Y.-C., and Miyamoto, T. Cis-hinokiresinol, a norlignan from anemarrhena asphodeloides, inhibits angiogenic response in vitro and in vivo. *Biological & Pharmaceutical Bulletin 26*, 12 (2003), 1721–4.

[62] Jiang, E. Y. *Advanced FTIR Spectroscopy: Principles, Experiments and Applications*. Thermo Electron Corporation, 2003.

[63] Keiderling, T. A. Protein and peptide secondary structure and conformational determination with vibrational circular dichroism. *Current Opinion in Chemical Biology 6*, 5 (2002), 682–8.

[64] Kendall, R. A., Dunning, T. H., J., and Harrison, R. J. Electron affinities of the first-row atoms revisited. Systematic basis sets and wave functions. *Journal of Chemical Physics 96*, 9 (1992), 6796–806.

[65] Koch, W., and Holthausen, M. C. *A Chemist's Guide to Density Functional Theory*, 2nd ed. Wiley-VCH, 2001.

[66] Kohn, W. Nobel lecture: Electronic structure of matter-wave functions and density functionals. *Reviews of Modern Physics 71*, 5 (1999), 1253–66.

[67] Le Bras, J., Jiao, H., Meyer, W. E., Hampel, F., and Gladysz, J. A. Synthesis, crystal structure, and reactions of the 17-valence-electron rhenium methyl complex $[(\eta_5\text{-}C_5Me_5)Re(NO)(P(4\text{-}C_6H_4CH_3)_3)(CH_3)]^{+}$ $B(3,5\text{-}C_6H_3(CF_3)_2)_4^{-}$: experimental and computational bonding comparisons with 18-electron methyl and methylidene complexes. *Journal of Organometallic Chemistry 616*, 1-2 (2000), 54–66.

[68] Liu, S. The role of coordination chemistry in the development of target-specific radiopharmaceuticals. *Chemical Society Reviews 33*, 7 (2004), 445–61.

[69] Maryanoff, B. E., McComsey, D. F., Dukor, R. K., Nafie, L. A., Freedman, T. B., Cao, X., and Day, V. W. Structural studies on McN-5652-X, a high-affinity ligand for the serotonin transporter in mammalian brain. *Bioorganic and Medicinal Chemistry 11*, 11 (2003), 2463–70.

[70] Mason, S. F. From pasteur to parity nonconservation: Theories of the origin of molecular chirality. In *Circular Dichroism: Principles and Applications, Second Edition*, K. Nakanishi, N. Berova, and R. W. Woody, Eds. Wiley, New York, 2000, ch. 2.

[71] Mason, S. F., and Tranter, G. E. The electroweak origin of biomolecular handedness. *Proceedings of the Royal Society of London, Series A (Mathematical and Physical Sciences) 397*, 1812 (1985), 45–65.

[72] Minami, E., Taki, M., Takaishi, S., Iijima, Y., Tsutsumi, S., and Akiyama, T. Stereochemistry of cis- and trans-hinokiresinol and their estrogen-like activity. *Chemical and Pharmaceutical Bulletin 48*, 3 (2000), 389–92.

[73] Mohamadi, F., Richards, N. G. J., Guida, W. C., Liskamp, R., Lipton, M., Caufield, C., Chang, G., Hendrickson, T., and Still, W. C. MacroModel—an integrated software system for modeling organic and bioorganic molecules using molecular mechanics. *Journal of Computational Chemistry 11*, 4 (1990), 440–67.

[74] Nafie, L. A. Velocity-gauge formalism in the theory of vibrational circular dichroism and infrared absorption. *Journal of Chemical Physics 96*, 8 (1992), 5687–702.

[75] Nafie, L. A. Circular polarization spectroscopy of chiral molecules. *Journal of Molecular Structure 347* (1995), 83–100.

[76] Nafie, L. A. Infrared and raman vibrational optical activity: Theoretical and experimental aspects. *Annual Review of Physical Chemistry 48* (1997), 357–86.

[77] Nafie, L. A. Dual polarization modulation: A real-time, spectral-multiplex separation of circular dichroism from linear birefringence spectral intensities. *Applied Spectroscopy 54*, 11 (2000), 1634–45.

[78] Nafie, L. A. Theory of vibrational circular dichroism and infrared absorption: Extension to molecules with low-lying excited electronic states. *Journal of Physical Chemistry A 108*, 35 (2004), 7222–31.

[79] Nafie, L. A., Buijs, H., Rilling, A., Cao, X., and Dukor, R. K. Dual source Fourier transform polarization modulation spectroscopy: An improved method for the measurement of circular and linear dichroism. *Applied Spectroscopy 58*, 6 (2004), 647–54.

[80] Nafie, L. A., Cheng, J. C., and Stephens, P. J. Vibrational circular dichroism of 2,2,2-trifluoro-1-phenylethanol. *Journal of the American Chemical Society 97*, 13 (1975), 3842–3.

[81] Nafie, L. A., Diem, M., and Vidrine, D. W. Fourier transform infrared vibrational circular dichroism. *Journal of the American Chemical Society 101*, 2 (1979), 496–8.

[82] Nafie, L. A., Dukor, R. K., Roy, J.-R., Rilling, A., Cao, X., and Buijs, H. Observation of fourier transform near-infrared vibrational circular dichroism to 6150 cm^{-1}. *Applied Spectroscopy 57*, 10 (2003), 1245–9.

[83] Nafie, L. A., and Freedman, T. B. Vibronic coupling theory of infrared vibrational transitions. *Journal of Chemical Physics 78*, 12 (1983), 7108–16.

[84] Nafie, L. A., and Freedman, T. B. Vibrational optical activity theory. In *Circular Dichroism: Principles and Applications, Second Edition*, K. Nakanishi, N. Berova, and R. W. Woody, Eds. Wiley, New York, 2000, ch. 4.

[85] Nafie, L. A., Freedman, T. B., and Dukor, R. K. Vibrational circular dichroism. In *Handbook of Vibrational Spectroscopy*, J. M. Chalmers and P. R. Griffiths, Eds. John Wiley & Sons, 2002.

[86] Nakanishi, K. Terpene trilactones from Gingko biloba: From ancient times to the 21st century. *Bioorganic & Medicinal Chemistry 13*, 17 (2005), 4987–5000.

[87] Norrby, P.-O., and Brandt, P. Deriving force field parameters for coordination complexes. *Coordination Chemistry Reviews 212*, 1 (2001), 79–109.

[88] O'Connor, M. J., Ernst, R. E., and Holm, R. H. Diastereoisomeric four-coordinate complexes. V. Pseudo-tetrahedral complexes of controlled absolute configuration. Configurational interconversion of nickel(II) complexes without racemization. *Journal of the American Chemical Society 90*, 17 (1968), 4561–8.

[89] Oellerich, S., Bill, E., and Hildebrandt, P. Freeze-quench resonance raman and electron paramagnetic resonance spectroscopy for studying enzyme kinetics: Application to azide binding to myoglobin. *Applied Spectroscopy 54*, 10 (2000), 1480–4.

[90] Oketch-Rabah, H. A., Dossaji, S. F., Christensen, S. B., Frydenvang, K., Lemmich, E., Cornett, C., Olsen, C. E., Chen Ming, Kharazmi, A., and Theander, T. Antiprotozoal compounds from asparagus africanus. *Journal of Natural Products 60*, 10 (1997), 1017–22.

[91] Olsen, L., Antony, J., Ryde, U., Adolph, H.-W., and Hemmingsen, L. Lactam hydrolysis catalyzed by mononuclear metallo-β-lactamases: A density functional study. *Journal of Physical Chemistry B 107*, 10 (2003), 2366–75.

[92] Owens, J. W., Robins, M., and O'Connor, C. J. A comparison of the magnetic and crystal field properties of protoporphyrin-IX, hemeoctapeptide and heme proteins. *Inorganica Chimica Acta 238*, 1-2 (1995), 99–108.

[93] Palmer, M. H., Camp, P. J., Tanjaroon, C., Keck, K. S., and Kukolich, S. G. A theoretical study of the staggered and eclipsed forms of the dinuclear complex Mn $Re(CO)_{10}$. *Journal of Chemical Physics 121*, 15 (2004), 7187–94.

[94] Park, H. J., Lee, J. Y., Moon, S. S., and Hwang, B. K. Isolation and anti-oomycete activity of nyasol from Anemarrhena asphodeloides rhizomes. *Phytochemistry 64*, 5 (2003), 997–1001.

[95] Pavia, D. L., Lampman, G. M., and Kriz, G. S. *Introduction to spectroscopy*, 3rd ed. Thomson Learning, 2001.

[96] Perdew, J. P., Burke, K., and Wang, Y. Generalized gradient approximation for the exchange-correlation hole of a many-electron system. *Physical Review B (Condensed Matter) 54*, 23 (1996), 16533–9.

[97] Perry, C. B., Chick, T., Ntlokwana, A., Davies, G., and Marques, H. M. The co-ordination of ligands by iron porphyrins: A comparison of ligand binding by myoglobin from sperm whale and the haem undecapeptide from cytochrome c. *Journal of the Chemical Society. Dalton Transactions*, 3 (2002), 449–57.

[98] Pople, J. A. Nobel lecture: Quantum chemical models. *Reviews of Modern Physics 71*, 5 (1999), 1267–74.

[99] Quack, M. How important is parity violation for molecular and biomolecular chirality? *Angewandte Chemie-International Edition 41*, 24 (2002), 4618–31.

[100] Rodger, A., and Nordén, B. *Circular Dichroism & Linear Dichroism*. Oxford Chemistry Masters. Oxford University Press, 1997.

[101] Schafer, A., Horn, H., and Ahlrichs, R. Fully optimized contracted Gaussian basis sets for atoms Li to Kr. *Journal of Chemical Physics 97*, 4 (1992), 2571–7.

[102] Schafer, A., Huber, C., and Ahlrichs, R. Fully optimized contracted Gaussian basis sets of triple zeta valence quality for atoms Li to Kr. *Journal of Chemical Physics 100*, 8 (1994), 5829–35.

[103] Schwerdtfeger, P., and Bast, R. Large parity violation effects in the vibrational spectrum of organometallic compounds. *Journal of the American Chemical Society 126*, 6 (2004), 1652–3.

[104] Schwerdtfeger, P., Gierlich, J., and Bollwein, T. Large parity-violation effects in heavy-metal-containing chiral compounds. *Angewandte Chemie-International Edition 42*, 11 (2003), 1293–6.

[105] Shah, R. D., and Nafie, L. A. Spectroscopic methods for determining enantiomeric purity and absolute configuration in chiral pharmaceutical molecules. *Current Opinion in Drug Discovery & Development 4*, 6 (2001), 764–75.

[106] Shelkovnikov, A., Grain, C., Butcher, R. J., Amy-Klein, A., Goncharov, A., and Chardonnet, C. Two-photon Ramsey fringes at 30 THz referenced to an H maser/Cs fountain via an optical-frequency comb at the 1-Hz level. *IEEE Journal of Quantum Electronics 40*, 8 (2004), 1023–9.

[107] Sokolov, V. I. Stereochemistry of optically active compounds. Problems and prospects. *Russian Chemical Bulletin 50*, 8 (2001), 1339–55.

[108] Stephens, P. J. Theory of vibrational circular dichroism. *Journal of Physical Chemistry 89*, 5 (1985), 748–52.

[109] Stephens, P. J. General discussion. *Faraday Discussions 99* (1994), 383–4.

[110] Stephens, P. J., and Devlin, F. J. Determination of the structure of chiral molecules using ab initio vibrational circular dichroism spectroscopy. *Chirality 12* (2000), 172–9.

[111] Stewart, J. P. J. Optimization of parameters for semiempirical methods. I. Method. *Journal of Computational Chemistry 10*, 2 (1989), 209–20.

[112] Strømgaard, K., and Nakanishi, K. Chemistry and biology of terpene trilactones from Ginkgo biloba. *Angewandte Chemie-International Edition 43*, 13 (2004), 1640–58.

[113] Strømgaard, K., Saito, D. R., Shindou, H., Ishii, S., Shimizu, T., and Nakanishi, K. Ginkgolide derivatives for photolabeling studies: Preparation and pharmacological evaluation. *Journal of Medicinal Chemistry 45*, 18 (2002), 4038–46.

[114] Strømgaard, K., Suehiro, M., and Nakanishi, K. Preparation of a tritiated ginkgolide. *Bioorganic and Medicinal Chemistry Letters 14*, 22 (2004), 5673–5.

[115] Suzuki, S., Nakatsubo, T., Umezawa, T., and Shimada, M. First in vitro norlignan formation with asparagus officinalis enzyme preparation. *Chemical Communications 2*, 10 (2002), 1088–9.

[116] Teraoka, J., Nakamura, K., Nakahara, Y., Kyogoku, Y., and Sugeta, H. Extraordinarily intense vibrational circular dichroism of a metmyoglobin cyanide complex. *Journal of the American Chemical Society 114*, 23 (1992), 9211–3.

[117] Teraoka, J., Yamamoto, N., Matsumoto, Y., Kyogoku, Y., and Sugeta, H. What is the crucial factor for vibrational circular dichroism in hemoprotein ligands? *Journal of the American Chemical Society 118*, 37 (1996), 8875–8.

[118] Tsui, W.-Y., and Brown, G. D. (+)-Nyasol from asparagus cochinchinensis. *Phytochemistry 43*, 6 (1996), 1413–5.

[119] van Beek, T. A. Ginkgolides and bilobalide: Their physical, chromatographic and spectroscopic properties. *Bioorganic & Medicinal Chemistry 13*, 17 (2005), 5001–12.

[120] Vogensen, S. B., Strømgaard, K., Shindou, H., Jaracz, S., Suehiro, M., Ishii, S., Shimizu, T., and Nakanishi, K. Preparation of 7-substituted ginkgolide derivatives: Potent platelet activating factor (PAF) receptor antagonists. *Journal of Medicinal Chemistry 46*, 4 (2003), 601–8.

[121] Wadt, W. R., and Hay, P. J. Ab initio effective core potentials for molecular calculations. Potentials for main group elements Na to Bi. *Journal of Chemical Physics 82*, 1 (1985), 284–98.

[122] Wang, X., and Andrews, L. Matrix infrared spectra and density functional theory calculations of manganese and rhenium hydrides. *Journal of Physical Chemistry A 107*, 20 (2003), 4081–91.

[123] Wright, A. E., Pomponi, S., McConnell, O. J., Kohmoto, S., and McCarthy, P. J. (+)-Curcuphenol and (+)-curcudiol, sesquiterpene phenols from shallow and deep water collections of the marine sponge Didiscus flavus. *Journal of Natural Products 50* (1987), 976–8.

[124] Zhang, W., Loebach, J. L., Wilson, S. R., and Jacobsen, E. N. Enantioselective epoxidation of unfunctionalized olefins catalyzed by salen manganese complexes. *Journal of the American Chemical Society 112* (1990), 2801–3.

[125] Zhao, C., and Polavarapu, P. L. Vibrational circular dichroism of gramicidin D in organic solvents. *Biospectroscopy 5* (1999), 276–83.

[126] Zhu, W.-L., Puah, C. M., Tan, X.-J., Jiang, H.-L., Chen, K.-X., and Ji, R.-Y. A density functional theory (DFT) calculation of the geometry and vibrational spectrum of natural product, ginkgolide B. *Journal of Molecular Structure: THEOCHEM 528*, 1-3 (2000), 193–8.

Index

Appendix A

List of Abbreviations

1AZI	Myoglobin-azide crystal structure (PDB ID)
1EBC	Myoglobin-cyanide crystal structure (PDB ID)
AAT	Atomic Axial Tensor
ANO	Atomic Natural Orbital
APT	Atomic Polar Tensor
aug-cc-pVDZ	cc-pVDZ augmented with diffuse functions
BaF_2	Barium fluoride
B3LYP	Becke 3-parameter functional, Lee-Yang-Parr correlation functional
B3PW91	Becke 3-parameter with Perdew-Wang 1991 correlation functional
CADPAC	The Cambridge Analytic Derivatives Package
CaF_2	Calcium fluoride
cc-pVDZ	Dunning's Correlation-Consistent Valence Double Zeta basis set
CCCBDB	Computational Chemistry Comparison and Benchmark DataBase
CD	Circular Dichroism
D95V	Dunning/Huzinaga Valence double zeta
DFT	Density Functional Theory
DFU	Danish University of Pharmaceutical Sciences
DMSO	Dimethylsulfoxide
DNA	DeoxyriboNucleic Acid
DTU	Technical University of Denmark
DZ	Double Zeta
ECD	Electronic Circular Dichroism (often called CD)
ECP	Effective Core Potential
ee	Enantiomeric Excess
ESR	Electron Spin Resonance
FT-IR	Fourier-Transform Infrared
FT-VCD	Fourier-Transform Vibrational Circular Dichroism
GB	Ginkgolide B
GTO	Gaussian-Type Orbital
HF	Hartree-Fock
His	Histidine
HS	High-Spin
HWHM	Half-Width at Half Maximum
Im	Imidazole

IR	Infrared
IUPAC	International Union of Pure and Applied Chemistry
KBr	Potassium bromide
LanL2DZ	Basis set with D95V on H–Ne, Los Alamos ECP plus DZ on Na–Bi
LCP	Left Circularly Polarized
LS	Low-Spin
Mb	Myoglobin
MCT	Mercury Cadmium Telluride (HgCdTe)
Me	Methyl
MePhOx	Methylphenyloxirane
MetMb	Metmyoglobin
MFP	Magnetic Field Perturbation
MIR	Mid-Infrared
MM	Molecular Mechanics
MMFF	Merck Molecular Force Field
MW	Molecular Weight
NIR	Near-Infrared
NMR	Nuclear Magnetic Resonance
NVP	Nuclear Velocity Perturbation
ORD	Optical Rotatory Dispersion
PCM	Polarizable Continuum Model
PDB	Protein Data Bank
PEM	PhotoElastic Modulator
PES	Potential Energy Surface
PM3	Parameterised Model 3, a semi-empirical method
PV	Parity Violation
Py	Pyridine
QM	Quantum Mechanics
QuP	The Quantum Protein Centre
RCP	Right Circularly Polarized
REVCD	Resonance-Enhanced Vibrational Circular Dichroism
ROA	Raman Optical Activity
RSC	Relativistic Small Core
SDD	Stuttgart/Dresden/Dunning basis set
SCF	Self-Consistent Field
SCRF	Self-Consistent Reaction Field
S/N	Signal-to-Noise ratio
STO	Slater-Type Orbital
SU	Syracuse University, Syracuse, NY
SUMM	Systematic Unbounded Multiple Minimum
Tp	Hydrotris(1-pyrazolyl)borate
UV-Vis	Ultraviolet-Visible
VA	Vibrational Absorption
VCD	Vibrational Circular Dichroism
VCT	Vibronic Coupling Theory
VDZ	Valence Double Zeta
VOA	Vibrational Optical Activity
VTZ	Valence Triple Zeta

Appendix B

Unix Scripts

Introduction

Listed on the following pages is a selection of scripts written during this project, which ease the processing of Gaussian calculations, such as generating a plot of spectral data present in a Gaussian output file or comparing calculated energies of different conformers. The present scripts are written in the Bash shell language, which is common on Unix-flavoured platforms. These scripts have been used with Gaussian 03, but should work with Gaussian 98 too. Some of the scripts (`plotCSV.bash` and `annotate*.bash`) are specifically designed to work with GnuPlot, a command-line plotting utility. However, one can plot the tables generated by `g03toCSV.bash` with a number of other programs.

Software requirements

A Bash shell and the Awk text-processing language, and in some cases the GnuPlot program. All of these programs are freely available for several platforms.

B.1 g03energies.bash

```
# Reads SCF energies from named Gaussian files in directory (default is all)
# Prints an array of energies in Ha and kJ/mol relative to the lowest energy
# Also gives Boltzmann fractions
# Version 2 18-11-2004 Peter R. Lassen

if [ $# -lt "1" ]
then
files=*.out
else
files=$*
fi

for file in $files; do grep -H "SCF Done" $file | tail -1;
done | sort -r +5 | awk '
BEGIN {
 OFS="\t";
 print "SCF energies"
 print "Filename","Hartrees","kJ/mol","Fraction"
}{
if (NR==1) min=$6;
name[NR]=$1;
Ha[NR]=$6;
weight[NR]=exp(-($6-min)/0.000950044487);
w+=weight[NR]}
END {for (i=1; i<=NR; i++)
 printf("%s\t%5.9f\t%7.4f\t%.3f\n",
  name[i],Ha[i],(Ha[i]-min)*2625.5,weight[i]/w);
}'
```

B.2 g03toCSV.bash

```
# Generates a table with IR and VCD spectra from a Gaussian output file
# Units are cm^-1 and epsilon (L/(mol*cm))
# Arguments:
# - Gaussian output file,
# - frequency scaling factor (default=1),
# - Lorenzian linewidth (default=5 cm-1),
# - output filename (optional, default is csv-extension)
# Version 2.2 27-10-2005 Peter R. Lassen

# Argument handling
if [ $# -lt "1" ]
then
echo "Usage: ‘basename $0‘ <Gaussian output> <scaling> <linewidth> [<output>]"
exit 65
fi
if [ $# -ge "1" ]
then
input=$1
output=${input%.out}
output=${output%.log}
```

```
output=$output.csv
scaling=1
linewidth=5
if [ $# -ge "2" ]
then
scaling=$2
fi
if [ $# -ge "3" ]
then
linewidth=$3
fi
if [ $# -ge "4" ]
then
output=$4
fi
fi

# Write comment string
echo "# `pwd`/$input scaling=$scaling linewidth=$linewidth" > "$output"

# Get lines that contain frequencies, dipole and rotational strengths
awk 'BEGIN {
 FS="--"
}{
 if($1 ~ /(^ Frequencies)|(^ Dip. str.)|(^ Rot. str.)/) print $2
}' "$input" > _awk_tmp1

# Transpose arrays into sorted columns
awk 'BEGIN {
 n=3;
} {
 r=(NR-1)%n+1;
 for(s=1; s<=NF; ++s) array[r,s]=$s;
 if(r==n) {
  for (i=1; i<s; ++i) {
   for (j=1; j<=r; j++) {
    printf array[j,i];
    printf " ";
   }
   print "";
  };
  r=0;
 }
} END {print "\n"}' _awk_tmp1 > _awk_tmp2

# Generate table of frequencies, IR and VCD intensities
awk -v sc="$scaling" -v D="$linewidth" 'BEGIN{
 OFS=" ";
}
{for (i=1;i<=3;i++) M[NR,i]=$i}
function IR(x) {
 ir=0
 for (i=1; i<=NR; i++)
  ir+=M[i,1]*M[i,2]*sc/(92*D*3.1415927)*D*D/((x-sc*M[i,1])**2+D*D);
 printf ir;
```

```
}
function VCD(x) {
 vcd=0
 for (i=1; i<=NR; i++)
  vcd+=M[i,1]*M[i,3]*sc/(230000*D*3.1415927)*D*D/((x-sc*M[i,1])**2+D*D);
 printf vcd;
}
END{
 for (x=400; x<=4000; x++) print x,IR(x),VCD(x);
}' _awk_tmp2 >> "$output"

# Cleanup
rm -f _awk_tmp1 _awk_tmp2
```

B.3 plotCSV.bash

```
# Returns a GnuPlot script for plotting tables generated by g03toCSV.bash
# Argument: The table file
Version="1.6 26-01-2006 Peter R. Lassen"

echo \#Generated by plotCSV.bash version $Version

if [ $# -lt "1" ]
then
echo "Usage: ‘basename $0‘ <CSV file>"
exit 65
fi
if [ $# -ge "1" ]
then
input=$1
fi

folder=‘pwd‘
folder=${folder##$HOME"/"}"/"

echo set terminal postscript eps 14 enhanced
echo set grid xtics
echo set key noautotitles
echo set lmargin 9
echo set xrange [2000:800] reverse
echo
echo "set xlabel 'Wavenumbers (cm^{-1})'"
echo "set ylabel 'Molar absorptivity {/Symbol e}'"
echo "set output '"${input%.csv}"_IRVCD.eps'"
echo set multiplot
echo set size 1,0.5
echo set origin 0,0
echo set tmargin 0
echo set autoscale yfixmax
echo "#set yrange [0:400]"
echo "plot '$input' u 1:2 w lines lw 2"
echo set xlabel
echo "set ylabel '{/Symbol De} x 10^4'"
```

```
echo set origin 0,0.5
echo "set bmargin 0; set tmargin; set format x ''; set autoscale yfixmin"
echo "#set yrange [-80:80]"
title=${input%.csv}
echo "set title '"$folder${title//_/\\_}"'"
echo "plot '$input' u 1:(""$""3*10000) w lines lw 2"
echo set title
echo unset multiplot
echo set output
```

B.4 g03toFrq.bash

```
# Generates tables of frequencies and properties from Gaussian output
# Adds scaled freq's and IR/VCD intensities derived from Dip./Rot. strength
# Dip./Rot. strength must be column 5-6
# Arguments:
# - Gaussian file,
# - frequency scaling factor (default=0.97),
# - Lorenzian bandwidth (default=5),
# - output filename (optional, default is *.frq)
# Version 1.3 01-09-2005 Peter R. Lassen

if [ $# -lt "1" ]
then
echo "Usage: ‘basename $0‘ <Gaussian output> <scaling> <linewidth> [<output>]"
exit 65
fi
if [ $# -ge "1" ]
then
input=$1
output=${input%.out}
output=${output%.log}
output=$output.frq
scaling=0.97
linewidth=5
if [ $# -ge "2" ]
then
scaling=$2
fi
if [ $# -ge "3" ]
then
linewidth=$3
fi
if [ $# -ge "4" ]
then
output=$4
fi
fi

echo -n "#" > "$output"
grep "#p" "$input" >> "$output"
awk '$1 ~ /^Job/ && $2 ~ /^cpu/ {
 print "#" $0
}' "$input" >> "$output"
```

```
awk 'BEGIN {
 FS="--";
 ORS="\t";
 printf("#")
}
 $1 ~ /^ Frequencies/,$1 ~ /^ Atom AN/ {
  if($1 ~ / Atom AN/) exit;
 print $1
} END {
 printf("\n")
}' "$input" >> "$output"

awk '$1 ~ /^Frequencies/,$1 ~ /^Atom/' "$input" >> "$output"

awk 'BEGIN {
 FS="--"
}{
 if($1 ~ /^#/) print;
 print $2
} END {print
}' "$output" > _awk_tmp_

awk -v sc="$scaling" -v D="$linewidth" 'BEGIN {r=1} {
 if($1 ~ /^#/) print;
 else {
  if(NF>1) {
   for(s=1; s<=NF; ++s) array[r,s]=$s;
  r++}
  else {
   for(i=1; i<s; ++i) {
    for(j=1; j<r; ++j) printf("%s \t ",array[j,i])
    printf("%s \t ",array[1,i]*sc);
    printf("%s \t ",array[5,i]*array[1,i]*sc/(92*D*3.1415927));
    printf("%s \t ",array[6,i]*array[1,i]*sc/(230000*D*3.1415927));
    printf("\n");
   };
   r=1;
  }
 }
}' < _awk_tmp_ > "$output"

rm -f _awk_tmp_
```

B.5 annotateIR.bash

```
# Makes GnuPlot commands for annotating a calculated IR spectrum
# Arguments:
# - Output from g03toFrq.bash,
# - wavenumber range [min,max]
# - minimum epsilon value
# Version 1.1 08-12-2005 Peter R. Lassen

if [ $# -lt "3" ]
then
echo "Usage: ‘basename $0‘ <g03toFrq output> <min> <max> [<epsilon_min>]"
exit 65
fi
input=$1
min=$2
max=$3
eps=1e-5
if [ $# -ge "4" ]
then
eps=$4
fi

awk -v min="$min" -v max="$max" -v eps="$eps" 'BEGIN{
 print "h=0"
}{
if ($1 ~ /^#/) n=0; else {
 n+=1;
 if ($7>min && $7<max && sqrt($8**2)>eps) {
  printf("set label \"^{%d}\" at %d,%d+h c\n",n,$7,$8+5);
 }
}
}' < "$input"
```

B.6 annotateVCD.bash

```
# Makes GnuPlot commands for annotating a calculated VCD spectrum
# Arguments:
# - Output from g03toFrq.bash,
# - wavenumber range [min,max]
# - minimum epsilon value
# Version 1.1 27-10-2005 Peter R. Lassen

if [ $# -lt "3" ]
then
echo "Usage: ‘basename $0‘ <g03toFrq output> <min> <max> [<epsilon_min>]"
exit 65
fi
input=$1
min=$2
max=$3
eps=1e-5
if [ $# -ge "4" ]
then
eps=$4
fi

awk -v min="$min" -v max="$max" -v eps="$eps" 'BEGIN{
 print "h=0"
}{
if ($1 ~ /^#/) n=0; else {
 n+=1;
 if ($7>min && $7<max && sqrt($9**2)>eps) {
  if ($9>0) printf("set label \"^{%d}\" at %d,%d+h c\n",n,$7,$9*10000+5);
  else printf("set label \"_{%d}\" at %d,%d+h c\n",n,$7,$9*10000-5);
 }
}
}' < "$input"
```

Appendix C

Abstract

Structural Characterization of Chiral Molecules Using Vibrational Circular Dichroism Spectroscopy

Chiral molecules, *i.e.*, molecules with handedness, are essential to biology, because most amino acids and sugars are chiral. A pair of molecules which are mirror images of each other have identical physical properties, but they differ in their interaction with other chiral molecules. This is the cornerstone of biological specificity.

Chiral molecules also interact differently with different polarization states of electromagnetic radiation, because the absorption coefficient depends on the state of polarization. This is called *dichroism* and gives rise to several spectroscopic techniques targeting chiral molecules.

This project is about application of one such technique, circular dichroism (CD) spectroscopy, which measures the difference in absorption of left- and right circularly polarized light—hence the name circular dichroism. This study has focused on the infrared (IR) range because there are many vibrational transitions here compared to the number of electronic transitions in the ultraviolet or visible range—hence the term *vibrational* circular dichroism (VCD).

VCD was used to identify the absolute configuration (chirality) and predominant conformers of chiral molecules by direct comparison of experimental and calculated spectra. Theoretical structures of the sample molecules were constructed and optimized using molecular mechanical force fields followed by the quantum mechanical method density functional theory (DFT). Calculations of IR absorption and VCD spectra were then carried out using the same DFT methods. Here, VCD has the advantage over CD that time-independent DFT calculations are sufficient.

During the course of this project, the above methodology has been applied to a range of molecules. Some of them (nyasol, curcuphenol dimers and ginkgolide) are purely organic compounds of pharmaceutical interest. Others are transition metal complexes relevant for the search for parity-violation effects in vibrational spectroscopy (rhenium complexes), for asymmetric catalysis (Schiff-base complexes), or as model systems for metal centres in biology (Schiff-bases and heme). Proteins (primarily myoglobin) have been studied

experimentally by VCD, but are far too large for DFT calculations, in which case one must resort to model systems.

In the case of organic compounds, the absolute configuration has been determined for molecules as large as ginkgolide B with 11 chiral centres or as flexible as the curcuphenol dimer with 11 variable dihedral angles. This illustrates the capabilities of the method, which are primarily limited by the duration of DFT calculations.

In the case of metal complexes, they have only recently become within reach of DFT, which opens new possibilities. Interesting VCD enhancement effects in the vicinity of some transition metal centres have been discovered by a group at Syracuse University, with whom a collaboration was established. A theory for the enhancement has been developed by that group, but is not yet fully implemented in available DFT software. Currently, only part of the enhancement can be reproduced theoretically, as demonstrated for the Schiff-bases. Their conformers and absolute configurations were also identified.

As for proteins, the interpretation of their spectra is different, because the immense number of overlapping vibrational modes makes it difficult to obtain information beyond the predominant secondary structure. However, the discovery of enhanced VCD signals around some metal centres allows for probing of the active site. This has been done for myoglobin with a range of different ligands attached. Corresponding DFT calculations have been carried out for just the heme group and ligands.

Appendix D

Dansk resumé

Strukturel karakterisering af kirale molekyler ved anvendelse af vibrationel cirkulær dikroisme spektroskopi

Kirale molekyler, dvs. molekyler med håndethed, er afgørende for biologien, idet stort set alle aminosyrer og kulhydrater er kirale. To sådanne molekyler vil, hvis de er hinandens spejlbilleder, have identiske fysiske egenskaber men forskellige kemiske egenskaber.

Kirale molekyler vekselvirker ikke blot forskelligt med andre kirale molekyler, men også med forskellige polarisationstilstande af elektromagnetisk stråling, fordi absorptionskoefficienten afhænger af polarisationen. Dette kaldes dikroisme og giver anledning til en række spektroskopiske teknikker målrettet kirale molekyler.

Dette projekt omhandler en af disse teknikker, nemlig cirkulær dikroisme (CD) spektroskopi, som bestemmer forskellen i absorption af venstre- og højredrejende cirkulært polariseret lys—heraf navnet cirkulær dikroisme. Der findes både vibrationel cirkulær dikroisme (VCD) og elektronisk cirkulær dikroisme (ECD), som måler vibrationelle hhv. elektroniske overgange.

VCD blev anvendt til at bestemme den absolutte konfiguration (kiralitet) og fremherskende konformerer af kirale molekyler ved direkte sammenligning af målte og beregnede spektre. Teoretiske strukturer af disse molekyler blev konstrueret og optimiseret ved hjælp af først molekylær mekanik (kraftfelter) efterfulgt af den kvantemekaniske metode tæthedsfunktionalteori (DFT). Beregninger af infrarøde absorptions- og VCD-spektre blev herefter foretaget med de samme DFT metoder.

I løbet af projektet er denne metodik anvendt på en række molekyler, hvoraf nogle er rent organiske stoffer af farmaceutisk interesse (nyasol, curcuphenol-dimerer og ginkgolid). Andre er overgangsmetal-komplekser, som først for-nylig er kommet inden for rækkevidde af de teoretiske metoder: Rhenium-komplekser, som er relevante for jagten på paritetsbrud i vibrationel spektroskopi; Schiff-base-komplekser, som bruges til assymmetrisk katalyse eller som model for biologiske metalcentre. Forskellige hæm-komplekser er også blevet undersøgt teoretisk som model for hæm-proteiner (primært myoglobin). Endelig er myoglobin blevet undersøgt eksperimentelt, men proteiner er alt

for store til DFT-beregninger, hvorfor man er henvist til modelsystemer.

Hvad angår organiske stoffer, så er den absolutte konfiguration blevet bestemt for molekyler så store som ginkgolid B med 11 kirale centre eller så fleksible som curcuphenol-dimeren med 11 variable dihedrale vinkler. Dette illustrerer metodens anvendelighed, som hovedsagelig begrænses af DFT-beregningernes omfang.

Hvad overgangsmetal-komplekser angår, så er nogle interessante forstærkningseffekter omkring metal-centrene blevet opdaget af en gruppe ved Syracuse University, som der blev etableret et samarbejde med. De har udviklet en teori for denne forstærkning, men den er endnu ikke indarbejdet i nogen DFT-software. Derfor kan kun en del af den målte forstærkning reproduceres teoretisk, som det er demonstreret for Schiff-base-komplekserne.

Når det gælder proteiner, så er deres vibrationelle spektre vanskeligere at fortolke pga. det store antal overlappende svingninger, som gør det vanskeligt at bestemme mere end den dominerende sekundære struktur. Men opdagelsen af forstærkede VCD-signaler omkring visse metal-centre åbner mulighed for selektivt at studere disse aktive områder. Dette er gjort for myoglobin med en række ligander bundet, hvoraf nogle giver anledning til forstærkede signaler. Tilhørende beregninger er foretaget på en model bestående af hæm-gruppen med ligander, og de har reproduceret en del af den målte forstærkning.

Appendix E

Included Papers

1 Fristrup, P., Lassen, P. R., Johannessen, C., Tanner, D., Norrby, P.-O., Jalkanen, K. J., and Hemmingsen, L. Direct determination of absolute configuration of methyl-substituted phenyloxiranes: Combined experimental and theoretical approach.
Journal of Physical Chemistry A 110, 29 (2006), 9123–9129.

2 Lassen, P. R., Skytte, D. M., Hemmingsen, L., Nielsen, S. F., Freedman, T. B., Nafie, L. A., and Christensen, S. B. Structure and absolute configuration of nyasol and hinokiresinol via synthesis and vibrational circular dichroism spectroscopy.
Journal of Natural Products 68, 11 (2005), 1603–1609.

3 Cichewicz, R. H., Clifford, L. J., Lassen, P. R., Cao, X., Freedman, T. B., Nafie, L. A., Deschamps, J. D., Kenyon, V. A., Flanary, J. R., Holman, T. R., and Crews, P. Stereochemical determination and bioactivity assessment of (*S*)-(+)-curcuphenol dimers isolated from the marine sponge *Didiscus aceratus* and synthesized through laccase biocatalysis.
Bioorganic & Medicinal Chemistry 13, 19 (2005), 5600–5612.

4 Andersen, N. H., Christensen, N. J., Lassen, P. R., Freedman, T. B., Nafie, L. A., Strømgaard, K., and Hemmingsen, L. Absolute Configuration Determination of Ginkgolides by VCD Spectroscopy.
Journal of Natural Products, in preparation.

5 Lassen, P. R., Guy, L., Karame, I., Roisnel, T., Vanthuyne, N., Roussel, C., Cao, X., Lombardi, R., Crassous, J., Freedman, T. B., and Nafie, L. A. Synthesis and vibrational circular dichroism of enantiopure chiral oxorhenium(V) complexes containing the hydrotris(1-pyrazolyl)borate ligand.
Inorganic Chemistry, submitted.

6 He, Y., Mak, M., Cone, C., Lassen, P. R., Nafie, L. A., and Freedman, T. B. Resonance Enhanced VCD in Chiral Co(II) Schiff-Base Complexes: Experimental Measurement and DFT Calculation.
Manuscript in preparation.

1

Peter Fristrup, Peter R. Lassen, Christian Johannessen, David Tanner, Per-Ola Norrby, Karl J. Jalkanen, and Lars Hemmingsen: Direct Determination of Absolute Configuration of Methyl-Substituted Phenyloxiranes: A Combined Experimental and Theoretical Approach.

Reprinted with permission from *J. Phys. Chem. A* 2006, **110**(29), 9123–9.

1

Direct Determination of Absolute Configuration of Methyl-Substituted Phenyloxiranes: Combined Experimental and Theoretical Approach

Peter Fristrup,*,† Peter R. Lassen,‡ Christian Johannessen,‡ David Tanner,§ Per-Ola Norrby,§ K. J. Jalkanen,‡,⊥ and Lars Hemmingsen‡,||

Center for Sustainable and Green Chemistry, Department of Chemistry, Technical University of Denmark, Building 201 Kemitorvet, DK-2800 Kgs. Lyngby, Denmark, The Quantum Protein Centre, Department of Physics, Technical University of Denmark, Building 309, DK-2800 Kgs. Lyngby, Denmark, Department of Chemistry, Technical University of Denmark, Building 201 Kemitorvet, DK-2800 Kgs. Lyngby, Denmark, Department of Natural Sciences, The Royal Veterinary and Agricultural University, Thorvaldsensvej 40, DK-1871 Frederiksberg C, Denmark, and Nanochemistry Research Institute, Department of Applied Chemistry, Curtin University of Technology, GPO Box U1987, Perth WA 6845, Australia

Received: January 9, 2006; In Final Form: May 15, 2006

Three possible methyl-substituted phenyloxiranes have been synthesized in enantioenriched form (89−99% enantiomeric excess (ee)), and their vibrational absorption (VA) and vibrational circular dichroism (VCD) spectra have been recorded. The experimental spectra are compared to theoretical spectra obtained from quantum mechanical calculations (density functional theory with the B3LYP hybrid exchange correlation functional with 6-31++G**, aug-cc-pVDZ, or aug-cc-pVTZ basis set) and related to the physical structure of the compounds. The absolute configuration could be established directly in each case by comparing experimental and theoretical spectra. In addition, we have been able to document the changes that occur both in structures and in the VA and VCD spectra due to substituent effects on the oxirane ring.

Introduction

Asymmetric synthesis in general, and enantioselective catalysis in particular, is one of the major areas of interest in contemporary organic chemistry.[1] In any research program devoted to the chemical synthesis of chiral compounds in nonracemic form, it is essential to have reliable methods for the determination of absolute configuration. While indirect methods for this (e.g., derivatization and/or degradation followed by chemical correlation) are available, it is highly desirable to develop and refine methods for the direct determination of absolute configuration.[2]

Advanced chiroptical methods such as vibrational circular dichroism (VCD)[3] and Raman optical activity (ROA),[4] along with improved theoretical understanding,[5] have allowed the direct determination of the absolute configuration of an impressive range of small to medium-sized molecules by simple comparison of the calculated and experimental spectra.[6] In addition, for biomolecules, where multiple conformers are the rule rather than the exception, vibrational absorption (VA) and VCD have been used to monitor the conformational changes that occur for these flexible molecules as a function of solvent, pH, and ionic strength (for those molecules that can exist as a mixture of conformers, a Boltzmann-weighted average of the calculated spectra is compared to the experimental data).[3,7] Natural products have recently proved to be useful test cases for theoretical developments,[8] but small synthetic molecules such as phenyloxirane have also been important in the refinement and benchmarking of theory.[9] Oxiranes (three-membered rings containing two carbons and an oxygen) are important intermediates in synthetic organic chemistry, and a number of methods have been developed for the synthesis of chiral oxiranes of high enantiomeric and diastereomeric purity.[10] However, the direct determination of the absolute configuration of even simple chiral oxiranes is often not a trivial task. In this paper we present a comparison between experiment (VCD) and theory (DFT/B3LYP) for the three methyl-substituted phenyloxiranes shown in Figure 1. Our work complements an earlier study by Ashvar et al.,[9] in which the molecular structure of phenyloxirane itself was studied by a combination of vibrational unpolarized absorption and circular dichroism spectroscopies and ab initio theory. Here we also wish to underline the importance of earlier studies using even simpler oxiranes in the development and benchmarking of theoretical methods.[11]

Materials and Methods

Synthesis. The oxiranes were prepared in enantioenriched form (**1**, 95% enantiomeric excess (ee);[12] **2**, 89% ee;[10c] **3**, 99% ee[13]) according to literature procedures. The (1*R*,2*S*)-2-methylphenyloxirane (**2**) sample contained 10% (1*R*,2*R*)-2-methylphenyloxirane (**3**) (73% ee with surplus of (1*S*,2*S*)-2-methylphenyloxirane, the enantiomer of **3**) as a consequence of lack of stereospecificity in the enantioselective Mn(salen)-catalyzed epoxidation. The racemic epoxides were synthesized as reported previously using either *m*-chloroperoxybenzoic acid (MCPBA) in dichloromethane (**2** and **3**) or quinuclidine as achiral ligand in the osmium-catalyzed dihydroxylation (**1**).[12] The enantiomeric excess for each sample was determined by chiral gas chromatography (GC) using either Chrompack CP Chirasil-Dex CB 0.25 mm × 25 m column (90 °C isothermal used for **2** and **3**) or Supelco β-Dex 120 0.25 mm × 30 m column (100 °C isothermal used for **1**).

* Corresponding author. E-mail: pf@kemi.dtu.dk.
† Center for Sustainable and Green Chemistry, Department of Chemistry, Technical University of Denmark.
‡ The Quantum Protein Centre, Department of Physics, Technical University of Denmark.
§ Department of Chemistry, Technical University of Denmark.
|| The Royal Veterinary and Agricultural University.
⊥ Nanochemistry Research Institute, Department of Applied Chemistry, Curtin University of Technology.

10.1021/jp060154m CCC: $33.50
Published on Web 07/06/2006

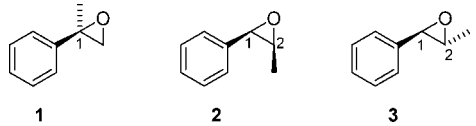

1 **2** **3**

Figure 1. The three methyl-substituted phenyloxiranes under investigation: (1*R*)-1-methylphenyloxirane (**1**), (1*R*,2*S*)-2-methylphenyloxirane (**2**), and (1*R*,2*R*)-2-methylphenyloxirane (**3**). Hydrogen atoms were omitted for clarity.

Vibrational Absorption and VCD Experiments. All VA and VCD experiments were carried out on a Thermo-Nicolet Nexus 870 Fourier transform infrared (FTIR) instrument equipped with a VCD compartment. The following properties were used to convert experimentally determined absorbances to molar extinction coefficients: M_w 134.2 g/mol; densities at 20 °C for (*R*)-1-methylphenyloxirane (**1**), (1*R*,2*S*)-2-methylphenyloxirane (**2**), and (1*R*,2*R*)-2-methylphenyloxirane (**3**), respectively, 1.02, 1.01, and 1.01 g/cm^3.[14] The diastereomeric purity of **2** was taken into account when converting absorbance to molar extinction coefficients.

Experiments on neat samples were carried out using a cell with BaF_2 windows and a 15 μm spacer. Experiments on 1.3 M samples of **1**−**3** in CCl_4 were carried out in a sealed KBr cell with a path length of 100 μm. VA measurements were carried out on samples diluted by a factor of 10 to ensure that no significant solute−solute interactions exist in the concentrated samples. In all cases the VCD spectrum was determined using an optically active sample and the corresponding racemic sample as background, running 8000−30 000 scans with a resolution of 4 cm^{-1}. Collection times ranged from about 2 to 8 h. The photoelastic modulator was set at either 1400 or 1500 cm^{-1}. The standard deviation has been plotted to allow an estimation of the uncertainty in the measurements.

Theoretical Methods. The initial investigations of the potential energy surface for the methyl-substituted phenyloxiranes were carried out using DFT/B3LYP[15] in Jaguar v. 4.2 build 77[16] employing the 6-311++G** basis set.[17] Calculations of vibrational and electronic properties were carried out using the Gaussian03 program package[18] on Linux-based PCs at the Technical University of Denmark. The method employed was DFT/B3LYP with the 6-31++G**, aug-cc-pVDZ, or aug-cc-pVTZ basis set[19] on all atoms for both geometry optimizations, and for calculation of VA and VCD spectra.[20] Lorentzian line shapes were assumed with a half-width of 4 cm^{-1} in the theoretical VA and VCD spectra, and a frequency scaling factor of 0.98 was used throughout to account for the combined error resulting from anharmonicity and basis set. This scaling factor was selected based on our experimental results and lies within the uncertainty of values listed for similar methods in the Computational Chemistry Comparison and Benchmark DataBase.[21] The calculations were all carried out with the (*R*)-configuration at the benzylic position, which is the expected enantiomer for all three compounds with the asymmetric reactions used in this work.[10c,12,13] For the reported VCD spectra, molar extinction coefficients were scaled according to the enantiomeric purity as determined by chiral GC (see Materials and Methods, Synthesis). For sample **2**, which contains a minor amount of **3** having the (*S*)-configuration at the benzylic position, the theoretical VCD spectrum was corrected by subtracting 10% of the calculated VCD spectrum of **3**.

Results and Discussion

Conformational Search. Calculations were performed to explore the potential energy surface of the methyl-substituted phenyloxiranes using DFT/B3LYP with the 6-31++G** basis set in Jaguar. In particular, the rotation of the phenyl ring with respect to the remainder of the molecule was investigated by performing a series of geometry optimizations with different values for the appropriate dihedral angle α in intervals of 10° (Figure 2).

Figure 2. Sign convention used for the dihedral angle α.

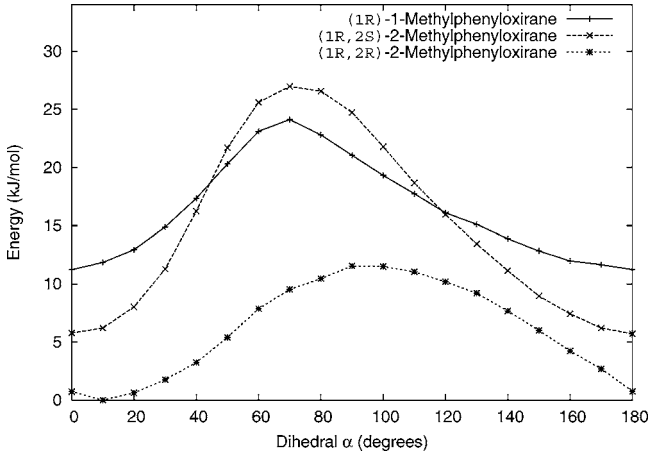

Figure 3. Energy profiles for the rotation of the phenyl group in the three phenyloxiranes. All energies are relative to the minimum for (1*R*,2*R*)-2-methylphenyloxirane (**3**).

For all three compounds there exists only one minimum energy conformation (Figures 3 and 4), which is stabilized by an electrostatic interaction between an ortho-H on the phenyl ring and the oxygen atom (typical Mulliken charges[22] with aug-cc-pVTZ basis: O −0.30 and H +0.16, distance 2.5 Å). In compounds **1** and **2** the steric influence from the proximal methyl causes the phenyl ring to occupy a position coplanar with the closest C−O bond, resulting in an α close to zero. In compound **3** the methyl group is situated at the opposite side of the oxirane ring and cannot obstruct rotation of the phenyl group, thus leading to a minimum energy conformation with α equal to 20°. The use of a polarized continuum (PCM) solvation model does not affect the overall structural features of the minimum energy conformation.

Since the three phenyloxiranes are constitutional isomers, we have plotted the energies obtained by the calculations in the gas phase relative to the most stable conformation of compound **3**, which is the overall energy minimum for all three compounds. In **2** there is additional internal energy due to unfavorable steric interactions between the methyl group and the phenyl ring, which are situated in a cis fashion on the oxirane backbone. In **3** the two groups point in opposite directions and the energy barrier for rotation of the phenyl group is only ca. 12 kJ/mol. In both **1** and **2** the position of equilibrium has the plane of the phenyl ring coplanar with the proximal C−O bond, corresponding to $\alpha = 0°$ or 180°. For these two compounds the minimum energy is higher than for **3**, by 6 kJ/mol for **2** and 11 kJ/mol for **1**.

The validity of the minimum energy structure was verified further by also performing restricted minimizations for the rotation of the methyl group in each of the three compounds. For all three compounds the rotational barriers were symmetrical with heights of 8−10 kJ/mol.

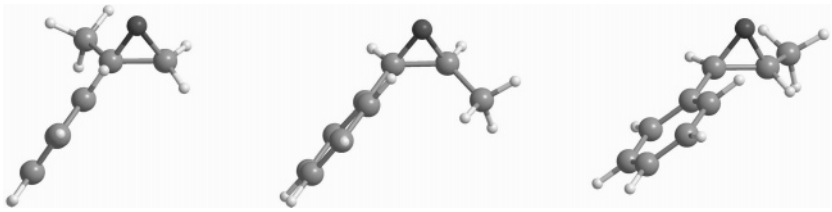

Figure 4. Structures of the three methyl-substituted phenyloxiranes optimized with the aug-cc-pVTZ basis set in Gaussian03.

TABLE 1: Dihedral Angle, α, in the Fully Optimized Structures Used To Calculate Spectroscopic Properties

	α (deg)		
	6-31++G**	aug-cc-pVDZ	aug-cc-pVTZ
(1*R*)-1-methylphenyloxirane (**1**)	0.8	3.3	0.0
(1*R*,2*S*)-2-methylphenyloxirane (**2**)	2.8	1.7	2.0
(1*R*,2*R*)-2-methylphenyloxirane (**3**)	16.6	19.1	18.6

Having established an approximate structure for the minimum energy conformation of each methyl-substituted phenyloxirane, a full energy minimization in Gaussian03 was undertaken followed by calculations of spectroscopic properties. The dihedral angles α in the fully minimized structures are listed in Table 1.

Comparison of Calculated Spectra. To estimate the importance of the basis set on the calculated spectra (in particular VCD), the VA and VCD spectra for all three compounds were calculated using three different basis sets. The smallest basis set was 6-31++G**, which is a split valence double-ζ basis set with an additional diffuse function and a polarization function on all atoms. We have also included Dunning's augmented correlation-consistent double-ζ[23] and triple-ζ basis sets, denoted aug-cc-pVDZ and aug-cc-pVTZ.[24] Inclusion of solvation using a polarized continuum model did not lead to significant changes in the calculated spectra; thus the discussion in the following text has been based on the gas-phase calculations only.

The numbering is based on the calculated fundamentals, starting with the lowest wavenumber mode, and the modes in the mid-IR (800−1800 cm^{-1}) correspond to modes 18−44 out of a total of $3N - 6 = 54$ (with 20 atoms in the molecules). The calculated VA and VCD spectra for (*R*)-1-methylphenyloxirane (**1**) are shown in Figure 5, and a visualization of the most prominent absorptions can be found in the Supporting Information. When examining the calculated VA spectra, it is

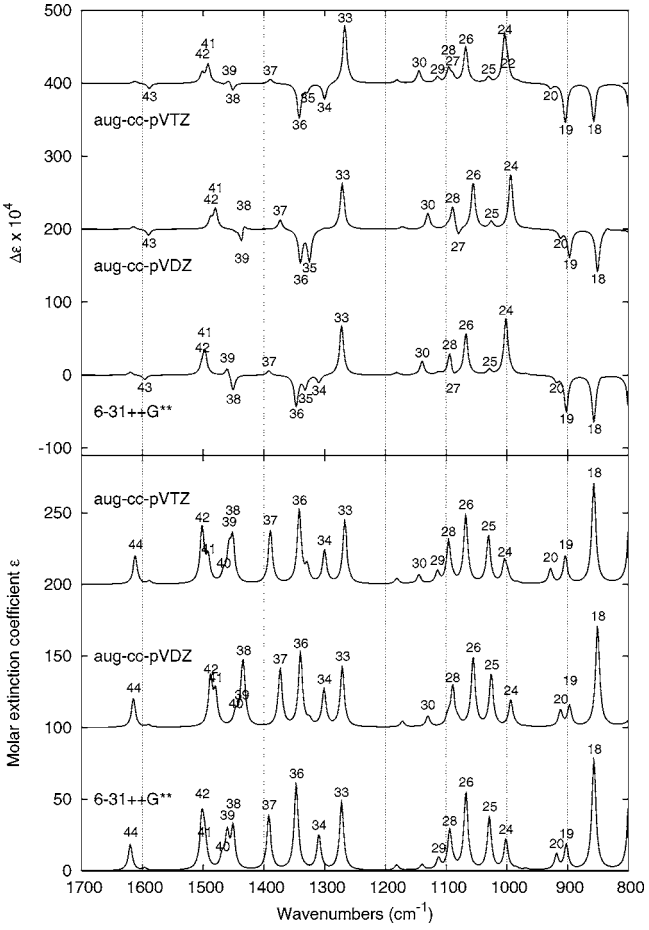

Figure 5. Calculated VA (bottom) and VCD (top) spectra for (*R*)-1-methylphenyloxirane (**1**) with DFT/B3LYP and three different basis sets as indicated. Spectra are offset for clarity, and most fundamentals have been numbered.

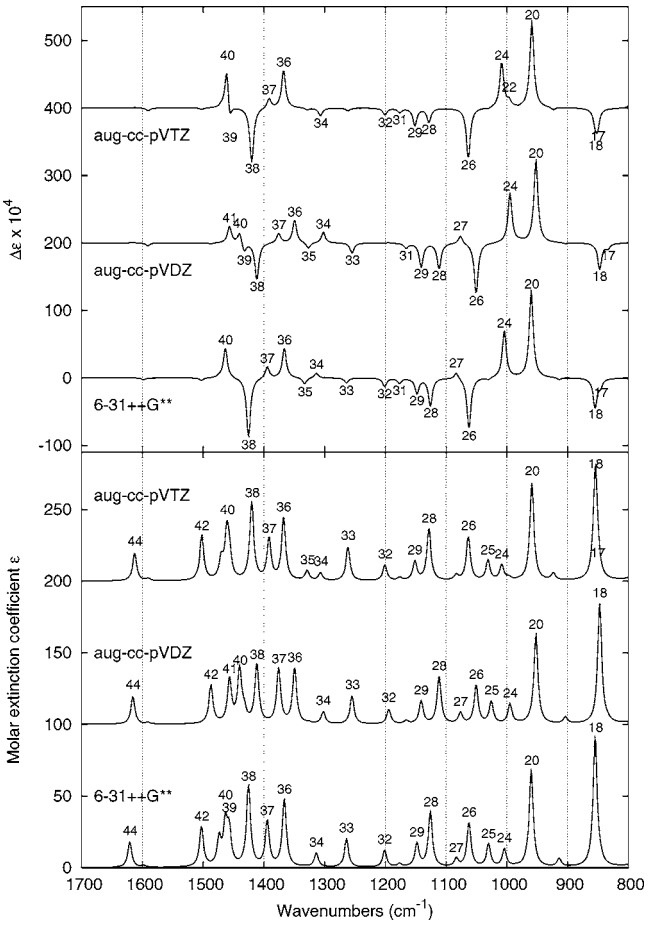

Figure 6. Calculated VA (bottom) and VCD (top) spectra for (1*R*,2*S*)-2-methylphenyloxirane (**2**) using DFT/B3LYP and three different basis sets.

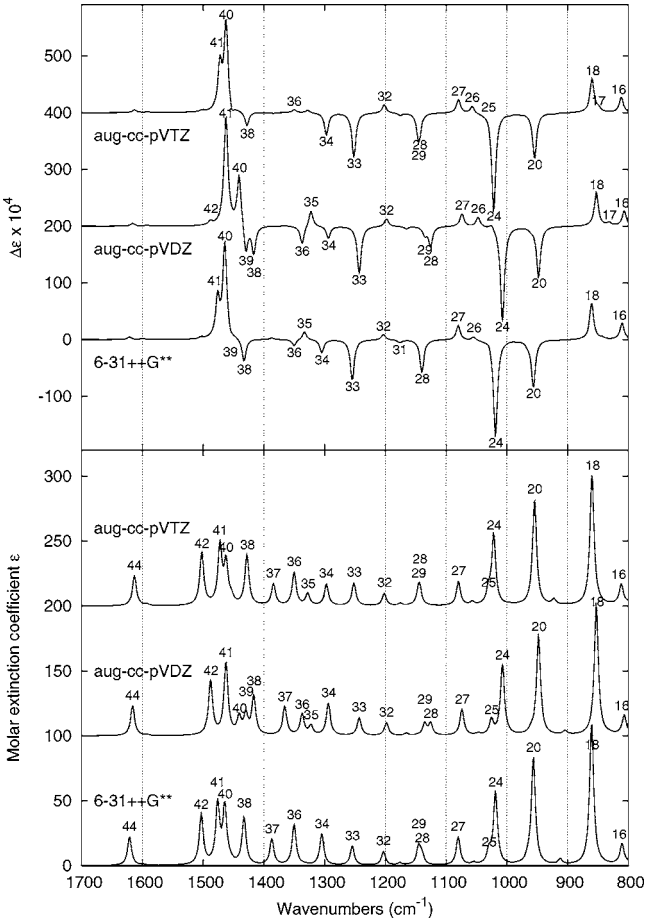

Figure 7. Calculated VA (bottom) and VCD (top) spectra for (1*R*,2*R*)-2-methylphenyloxirane (**3**) using DFT/B3LYP and three different basis sets.

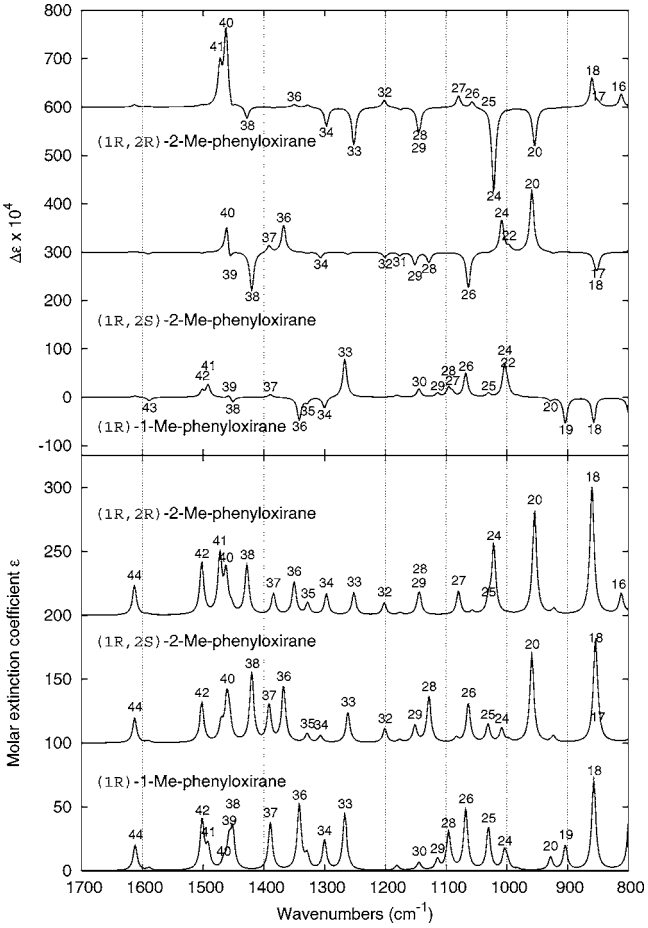

Figure 8. Comparison of calculated VCD spectra (top) and VA spectra (bottom) for **1**, **2**, and **3** using DFT/B3LYP with the augmented cc-pVTZ basis set.

clear that there are only small differences among the three basis sets. Also, for the VCD spectra there are many similarities among the three basis sets, although some differences can also be noted, for example, the relative intensity of the two negative VCD signals arising from fundamentals 18 and 19. With the largest basis set (aug-cc-pVTZ) the two are of equal intensity, whereas for both of the smaller basis sets the intensity of fundamental 18 is predicted to be larger than that of 19. For the two medium-intensity negative signals, 35 and 36, the latter is predicted to be of larger intensity using 6-31++G** and aug-cc-pVTZ basis sets, whereas the prediction from aug-cc-pVDZ is equal intensity for these two fundamentals. For the two very weak signals arising from fundamentals 38 and 39, there is a difference in sign when the aug-cc-pVDZ basis set is used.

The calculated VA and VCD spectra for (1*R*,2*S*)-2-methylphenyloxirane (**2**) are shown in Figure 6, and a visualization of the most prominent absorptions can be found in the Supporting Information. Upon examination of the calculated VA spectra it is clear that there are only small differences among the three basis sets except for the splitting of fundamentals 40 and 41, which is also seen for the spectra calculated with the aug-cc-pVDZ basis set. Also for the VCD spectra, there are many similarities among the three basis sets, although minor differences must be noted. For example, the relative intensity of the absorption arising from the fundamentals 28 and 29 shifts with increasing size of the basis set, with the latter having the strongest absorption with the largest basis set. Also, the sign of fundamental 34 is different with the largest basis set compared to the two smaller basis sets. The pattern around 1350−1450 cm^{-1} is quite different with the aug-cc-pVDZ basis set, compared to the two other basis sets used in this work.

The calculated VA and VCD spectra for (1*R*,2*R*)-2-methylphenyloxirane (**3**) are shown in Figure 7, and a visualization of the most prominent absorptions can be found in the Supporting Information. For the calculated VA spectra it is clear that there are only small differences among the three different basis sets, although it seems that the aug-cc-pVDZ basis set once again gives results different from those obtained using the two other basis sets. When the VCD spectra are compared, there is an overall good agreement in the low wavenumber range (800−1200 cm^{-1}), but for fundamentals 34, 35, and 36 there are relatively large differences. The intensity of the VCD signal arising from fundamental 34 is somewhat larger with the largest basis set when compared to the two smaller ones. Fundamental 35 is predicted to be very small with the largest basis set, whereas the two smaller basis sets predict an absorption of medium intensity. This is also the case for fundamental 36.

The relative intensity and the splitting are very different for fundamentals 40 and 41 when using the aug-cc-pVDZ basis set compared to the two other basis sets.

Comparison between Isomers. The calculated VA and VCD spectra with the largest basis set for all three methyl-substituted phenyloxiranes have been collected in Figure 8. By simple examination of the VA spectra all three compounds can be easily distinguished. For example, the presence of the strong absorption around 960 cm^{-1} (fundamental 20) arising from having an H and a methyl attached to the same carbon in the oxirane ring is present in **2** and **3** but not in **1**. Interestingly, due to the opposite

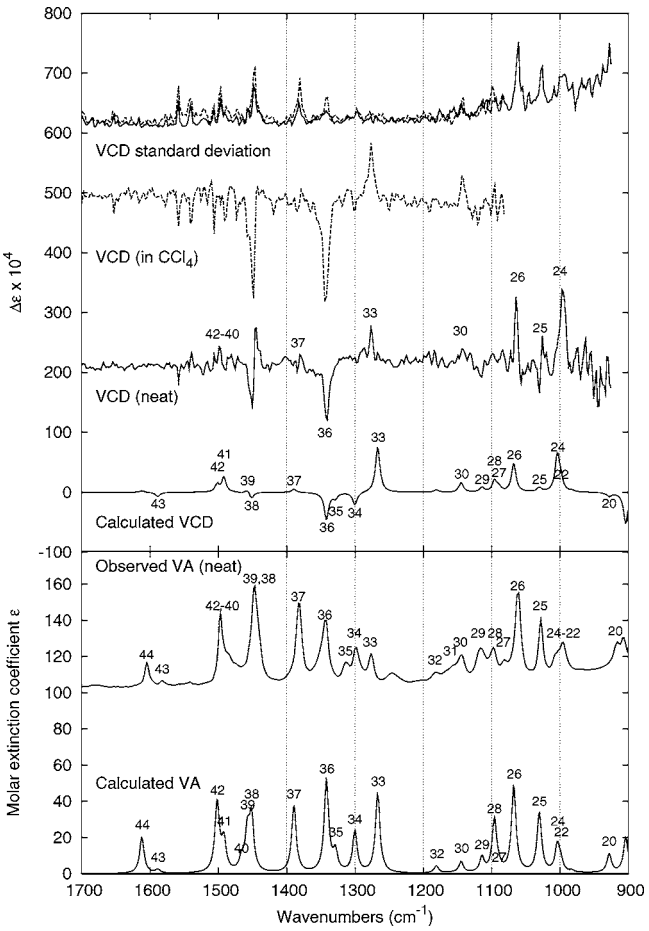

Figure 9. Comparison of experimental and calculated (B3LYP/aug-cc-pVTZ) VCD spectra (top) and VA spectra (bottom) for (*R*)-1-methylphenyloxirane (**1**).

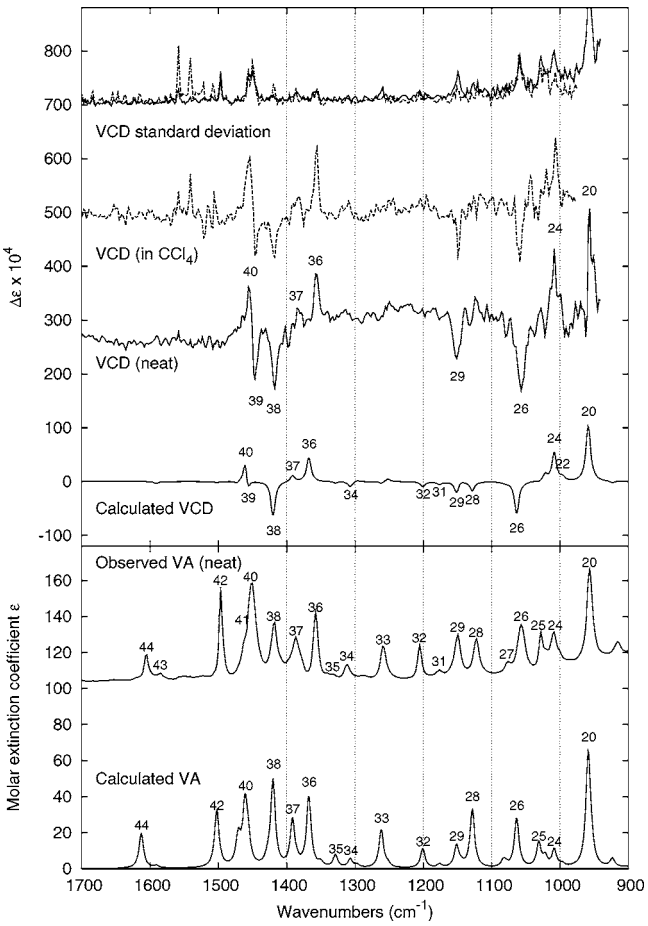

Figure 10. Comparison of experimental and calculated (B3LYP/aug-cc-pVTZ) VCD spectra (top) and VA spectra (bottom) for (1*R*,2*S*)-2-methylphenyloxirane (**2**).

absolute configuration of the carbon atom in the oxirane, the VCD signal from this particular absorption is positive for **2** and negative for **3**, allowing for easy discrimination of these two compounds. This is also the case for fundamental 24 in **2** and **3**, which is the asymmetric pendant to fundamental 20. Fundamental 26 in compounds **1** and **2** can also be used to discriminate efficiently between these two compounds since it gives a positive VCD signal for **1**, a negative VCD signal for **2**, and practically no signal for **3**. Fundamental 33 gives a positive VCD for **1** from a vibration involving the ortho-hydrogens and the oxirane ring. In compounds **2** and **3** fundamental 33 corresponds to a C−C stretching motion within the phenyl ring coupled to the oxirane ring. This vibration results in negative VCD for **3** but does not give any signal for **2**. Fundamental 36 gives negative VCD for **1** from a C−C stretch within the three-membered ring, a motion not responsible for significant VCD in **2** and **3**. The fundamental also numbered 36 in these compounds reflects a symmetric bending motion of the β-hydrogen attached directly to the oxirane ring. This vibration gives a positive VCD for **2**, but almost no signal for **3** despite the structural similarity between the two compounds.

Fundamental 38 is a symmetric stretch/bend motion of the meta- and para-hydrogens on the phenyl ring. This vibration gives a dominant negative VCD for **2**, a much less intense signal for **3**, and no signal for **1**.

The symmetric and asymmetric stretch/bend motion of the methyl group was located as fundamentals 41 and 42 in **1** and 40 and 41 in compounds **2** and **3**. In all three cases these vibrations give rise to VCD absorptions but with different appearances. The absorption is medium intensity for **1** and is located at a higher wavenumber than for **2** and **3**. In **2** only a single absorption is seen, whereas for **3** these vibrations give two dominant positive VCD signals, which are among the strongest ones in the entire spectrum.

Experimental Results

The experimental VA and VCD spectra for **1** obtained neat and in CCl_4 solution are shown in Figure 9, along with calculated spectra using the large aug-cc-pVTZ basis set. The experimental and calculated spectra display a high degree of similarity, allowing for assignment of the individual peaks in the experimental spectra. The similarity of the calculated and experimental VA spectra implies that the theoretically optimized structure lies very close to the real molecular structure. There are, however, minor differences between the calculated and experimental spectra. For **1** the dipole strength of fundamentals 27/28 and 33 seems to be overestimated in the theoretical calculation, whereas modes 37 and 38 seem to be slightly underestimated. In the VCD spectrum obtained using the neat liquid, the fundamentals 24 and 28 give rise to positive signals. The positive VCD signal from fundamental 30 is more clearly seen in CCl_4 solution than in the neat liquid. The signals from fundamentals 33 (positive) and 36 (negative) are easily recognized in both experimental spectra. The strong VA absorption from fundamentals 38 and 39 combined with very small predicted VCD intensity gives rise to artifacts in this region ($\sim$1450 cm^{-1}), which is documented by the higher noise level.

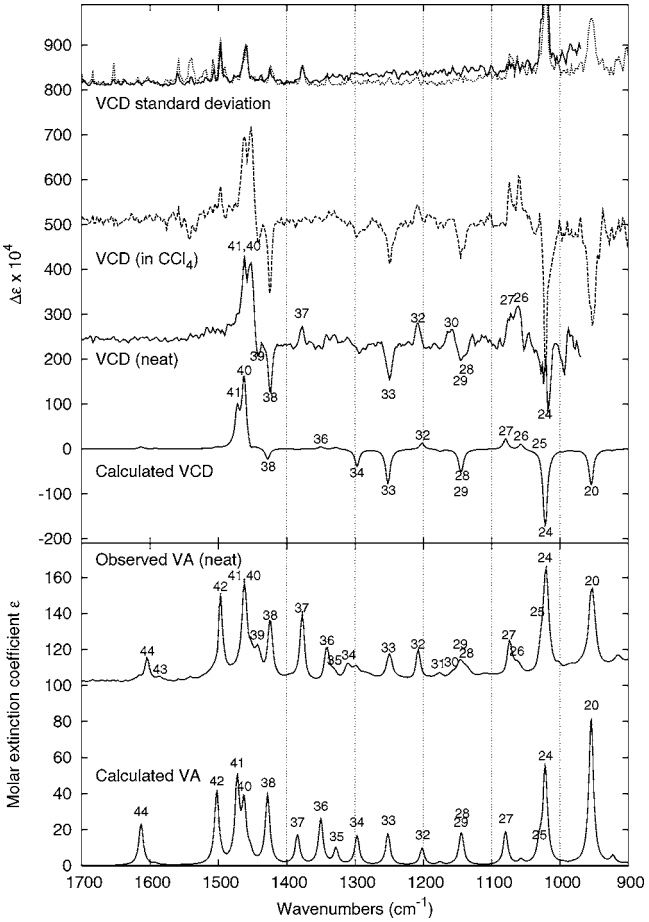

Figure 11. Comparison of experimental and calculated (B3LYP/aug-cc-pVTZ) VCD spectra (top) and VA spectra (bottom) for (1*R*,2*R*)-2-methylphenyloxirane (**3**).

From comparison of theory and experiment, we conclude that the synthesized enantiomer of **1** is the (*R*)-enantiomer at the benzylic position based primarily on the strong VCD absorptions from fundamentals 33 and 36, and further substantiated by the weaker absorptions from fundamentals 24, 26, 30, and 33.

The experimental VA and VCD spectra for **2** obtained neat and in CCl_4 solution are shown in Figure 10 along with calculated spectra using the large aug-cc-pVTZ basis set. Also, for **2** there are small discrepancies between experimental and calculated absorption spectra. In particular, for fundamentals 26 and 28 the calculated dipole strength is too small, whereas for fundamental 38 the calculated dipole strength is too large. When the low wavenumber region of the VCD spectra of the neat liquid is examined, fundamental 20 gives rise to a large positive VCD signal which is in accordance with the calculated spectrum, although the large absorbance gives rise to a relatively high noise level. Fundamentals 24, 26, and 29 are all clearly seen in the experimental spectra; however, it seems that the rotational strength of fundamental 29 is underestimated in the calculation. At higher wavenumbers fundamentals 36, 37, and 38 also give rise to well-defined absorptions in the experimental spectra, thus clearly identifying **2** as having the (*R*)-configuration at the benzylic position. Also, for this compound the intense absorbance at $\sim$1460 cm^{-1} makes the VCD signal there unreliable.

The experimental VA and VCD spectra for **3** obtained neat and in CCl_4 solution are shown in Figure 11 along with calculated spectra using the large aug-cc-pVTZ basis set. Here, the calculated dipole strengths of fundamentals 20 and 38 appear to be overestimated, whereas fundamental 37 seems to be slightly underestimated. The assignment of fundamentals 34−36 was difficult due to overlapping signals and/or insufficient resolution in the experimental spectra.

When the VCD spectra are examined, the agreement between experiment and theory is markedly better for **3** than for **1** and **2**, which is probably a consequence of the fact that the sample consists of essentially a single enantiomer (ee = 99%). In the VCD spectra of the neat liquid the absorption from fundamental 20 was too large to allow for VCD measurements; however, in CCl_4 the VCD signal seems to be reliable. Fundamentals 24, 28/29, 32, 33, 38, 40, and 41 were all easily interpretable in the experimental spectra, and we can confidently assign the synthesized enantiomer as having the (*R*)-configuration at the benzylic position. The weak absorptions arising from fundamentals 26 and 34 could be clearly distinguished from the background noise only in the spectrum of the neat liquid. In this respect the measurements on the neat liquid and in CCl_4 solution complement each other.

Conclusions

Theoretical calculations of dipole strengths and rotational strengths were carried out for the three methyl-substituted phenyloxiranes **1**−**3** having the (*R*)-configuration at the benzylic position using DFT/B3LYP with 6-31++G**, aug-cc-pVDZ, and aug-cc-pVTZ basis sets. Differences among these three basis sets were commented upon, and an overall good agreement between the 6-31++G** basis set and the aug-cc-pVTZ basis set was noted, whereas the aug-cc-pVDZ basis set often yielded markedly different results.

Oxiranes **1**−**3** have been synthesized in enantioenriched form, their VA and VCD spectra were recorded, and the experimental spectra were compared to theoretical spectra obtained using the largest basis set (aug-cc-pVTZ). There was very good agreement between the experimental and calculated VA spectra, allowing for direct assignment of most absorptions to the fundamental vibrations determined by calculation, indicating that the molecules in solution or as neat liquid indeed possess the physical structure obtained by energy minimization in the gas phase, or that the changes which occur at ambient temperature do not affect the overall spectral properties of the molecules. The absolute configuration of all three compounds could be established directly by comparing experimental and theoretical VCD spectra.

Acknowledgment. The Center for Sustainable and Green Chemistry and the Quantum Protein Centre are sponsored by the Danish National Research Foundation. L.H. thanks the Lundbeck Foundation for financial support for the project "Determination of absolute configuration of chiral molecules using VCD spectroscopy". K.J.J. thanks Julian Gale for fruitful discussions and the Government of Western Australia for funding under the Premiers Research Fellow Program. The authors appreciate the many encouraging and constructive suggestions provided by the referees.

Supporting Information Available: *XYZ* coordinates and SCF energies are available for all structures discussed along with tables containing the calculated dipole strengths and rotational strengths. Visual representations of the fundamental vibrational modes are also included. Dipole and rotational strengths have been extracted from the experimental spectra and compared to the calculated values. This material is available free of charge via the Internet at http://pubs.acs.org.

References and Notes

(1) See, e.g.: *Comprehensive Asymmetric Catalysis*; Jacobsen, E. N., Pfaltz, A., Yamamoto, H., Eds.; Springer-Verlag: New York, 1999.

(2) For a discussion, see: Eliel, E. L.; Wilen, S. H.; Mander, L. N. *Stereochemistry of Organic Compounds*; Wiley: New York, 1994: Chapter 6.

(3) For a review, see: Freedman, T. B.; Cao, X. L.; Dukor, R. K.; Nafie, L. A. *Chirality* **2003**, *15*, 743.

(4) (a) Barron, L. D.; Hecht, L.; Mccoll, I. H.; Blanch, E. W. *Mol. Phys.* **2004**, *102*, 731. (b) Nafie, L. A. *Annu. Rev. Phys. Chem.* **1997**, *48*, 357.

(5) (a) Cheeseman, J. R.; Frisch, M. J.; Devlin, F. J.; Stephens, P. J. *Chem. Phys. Lett.* **1996**, *252*, 211. (b) Stephens, P. J.; Ashvar, C. S.; Devlin, F. J.; Cheeseman, J. R.; Frisch, M. J. *Mol. Phys.* **1996**, *89*, 579. (c) Johnson, B. G.; Frisch, M. J. *J. Chem. Phys.* **1994**, *100*, 7429. (d) Johnson, B. G.; Frisch, M. J. *J. Chem. Phys. Lett.* **1993**, *216*, 133.

(6) (a) Cere, V.; Peri, F.; Pollicino, S.; Ricci, A.; Devlin, F. J.; Stephens, P. J.; Gasparrini, F.; Rompietti, R.; Villani, C. *J. Org. Chem.* **2005**, *70*, 664. (b) Roda, G.; Conti, P.; De Amici, M.; He, J. T.; Polavarapu, P. L.; De Micheli, C. *Tetrahedron: Asymmetry* **2004**, *15*, 3079. (c) Freedman, T. B.; Cao, X.; Nafie, L. A.; Solladie-Cavallo, A.; Jierry, L.; Bouerat, L. *Chirality* **2004**, *16*, 467. (d) Burgi, T.; Urakawa, A.; Behzadi, B.; Ernst, K. H.; Baiker, A. *New J. Chem.* **2004**, *28*, 332. (e) Donnoli, M. I.; Giorgio, E.; Superchi, S.; Rosini, C. *Org. Biomol. Chem.* **2003**, *1*, 3444. (f) Freedman, T. B.; Cao, X. L.; Rajca, A.; Wang, H.; Nafie, L. A. *J. Phys. Chem. A* **2003**, *107*, 7692. (g) Solladie-Cavallo, A.; Marsol, C.; Yaakoub, M.; Azyat, K.; Klein, A.; Roje, M.; Suteu, C.; Freedman, T. B.; Cao, X.; Nafie, L. A. *J. Org. Chem.* **2003**, *68*, 7308. (h) Holmen, A.; Oxelbark, J.; Allenmark, S. *Tetrahedron: Asymmetry* **2003**, *14*, 2267. (i) Monde, K.; Taniguchi, T.; Miura, N.; Nishimura, S. I.; Harada, N.; Dukor, R. K.; Nafie, L. A. *Tetrahedron Lett.* **2003**, *44*, 6017. (j) Kuppens, T.; Langenaeker, W.; Tollenaere, J. P.; Bultinck, P. *J. Phys. Chem. A* **2003**, *107*, 542. (k) Devlin, F. J.; Stephens, P. J.; Osterle, C.; Wiberg, K. B.; Cheeseman, J. R.; Frisch, M. J. *J. Org. Chem.* **2002**, *67*, 8090. (l) Devlin, F. J.; Stephens, P. J. *J. Phys. Chem. A* **2002**, *106*, 10510. (m) Wang, F.; Polavarapu, P. L. *J. Phys. Chem. A* **2001**, *105*, 6991. (n) Wang, F.; Wang, H.; Polavarapu, P. L.; Rizzo, C. J. *J. Org. Chem.* **2001**, *66*, 3507. (o) Drabowicz, J.; Dudzinski, B.; Mikolajczyk, M.; Wang, F.; Dehlavi, A.; Goring, J.; Park, M.; Rizzo, C. J.; Polavarapu, P. L.; Biscarini, P.; Wieczorek, M. W.; Majzner, W. R. *J. Org. Chem.* **2001**, *66*, 1122. (p) Wang, F.; Polavarapu, P. L.; Drabowicz, J.; Mikolajczyk, M. *J. Org. Chem.* **2000**, *65*, 7561. (q) Aamouche, A.; Devlin, F. J.; Stephens, P. J. *J. Am. Chem. Soc.* **2000**, *122*, 7358. (r) Aamouche, A.; Devlin, F. J.; Stephens, P. J. *J. Am. Chem. Soc.* **2000**, *122*, 2346.

(7) (a) Freedman, T. B.; Cao, X. L.; Oliveira, R. V.; Cass, Q. B.; Nafie, L. A. *Chirality* **2003**, *15*, 196. (b) He, J. T.; Petrovic, A. G.; Polavarapu, P. L. *J. Phys. Chem. B* **2004**, *108*, 20451. (c) He, J. T.; Petrovich, A.; Polavarapu, P. L. *J. Phys. Chem. A* **2004**, *108*, 1671. (d) Wang, F.; Polavarapu, P. L.; Lebon, F.; Longhi, G.; Abbate, S.; Catellani, M. *J. Phys. Chem. A* **2002**, *106*, 12365. (e) Wang, P.; Polavarapu, P. L. *J. Phys. Chem. A* **2000**, *104*, 6189.

(8) (a) Devlin, F. J.; Stephens, P. J.; Cheeseman, J. R.; Frisch, M. J. *J. Phys. Chem. A* **1997**, *101*, 9912. (b) Devlin, F. J.; Stephens, P. J.; Cheeseman, J. R.; Frisch, M. J. *J. Phys. Chem. A* **1997**, *101*, 6322.

(9) Ashvar, C. S.; Devlin, F. J.; Stephens, P. J. *J. Am. Chem. Soc.* **1999**, *121*, 2836.

(10) For example, Sharpless Asymmetric Epoxidation: (a) Katsuki, T.; Sharpless, K. B. *J. Am. Chem. Soc.* **1980**, *102*, 5974. (b) For a review, see: Johnson, R. A.; Sharpless, K. B. In *Catalytic Asymmetric Synthesis*, 2nd ed.; Ojima, I., Ed.; Wiley-VCH: New York, 2000; Chapter 6A. Jacobsen-Katsuki Epoxidation: (c) Zhang, W.; Loebach, J. L.; Wilson, S. R.; Jacobsen, E. N. *J. Am. Chem. Soc.* **1990**, *112*, 2801. (d) Irie, R.; Noda, K.; Ito, Y.; Matsumoto, N.; Katsuki, T. *Tetrahedron Lett.* **1990**, *31*, 7345. (e) Katsuki, T. In *Catalytic Asymmetric Synthesis*, 2nd Ed., Ojima, I., Ed.; Wiley-VCH: New York, 2000, Chapter 6B. (f) Jacobsen, E. N.; Wu, M. H. In *Comprehensive Asymmetric Catalysis*; Jacobsen, E. N., Pfaltz, A., Yamamoto, H., Eds.; Springer-Verlag: New York, 1999; Chapter 18.2. Shi Epoxidation: (g) Shi, Y. *Acc. Chem. Res.* **2004**, *37*, 488. (h) Adam, W.; Saha-Möller, C. R.; Zhao, C.-G. *Org. React.* **2002**, *61*, Chapter 2.

(11) (a) Cheeseman, J. R.; Frisch, M. J.; Devlin, F. J.; Stephens, P. J. *Chem. Phys. Lett.* **1996**, *252*, 211. (b) Devlin, F. J.; Finley, J. W.; Stephens, P. J.; Frisch, M. J. *J. Phys. Chem.* **1995**, *99*, 16883. (c) Bak, K. L.; Devlin, F. J.; Ashvar, C. S.; Taylor, P. R.; Frisch, M. J.; Stephens, P. J. *J. Phys. Chem.* **1995**, *99*, 14918. (d) Kawiecki, R. W.; Devlin, F. J.; Stephens, P. J.; Amos, R. D. *J. Phys. Chem.* **1991**, *95*, 9817.

(12) Fristrup, P.; Dideriksen, B. D.; Tanner D.; Norrby. P.-O. *J. Am. Chem. Soc.* **2005**, *127*, 13672.

(13) Kolb, H. C.; Sharpless, K. B. *Tetrahedron* **1992**, *48*, 10515.

(14) (a) Somerville, W. T.; Spoerri, P. E. *J. Am. Chem. Soc.* **1951**, *73*, 697. (b) Fischer, F. *Chem. Ber.* **1956**, *89*, 2438.

(15) (a) Becke, A. D. *J. Chem. Phys.* **1993**, *98*, 1372−1377. (b) Becke, A. D. *J. Chem. Phys.* **1993**, *98*, 5648−5652. (c) Lee, C.; Yang, W.; Parr, R. G. *Phys. Rev. B* **1988**, *37*, 785−789.

(16) *Jaguar 4.2*; Schrödinger, Inc.: Portland, OR, 1991−2000; see http://schrodinger.com.

(17) (a) McLean, A. D.; Chandler, G. S. *J. Chem. Phys.* **1980**, *72*, 5639. (b) Krishnan, R.; Binkley, J. S.; Seeger, R.; Pople, J. A. *J. Chem. Phys.* **1980**, *72*, 650.

(18) Frisch, M. J.; et al. *Gaussian03*, revision B.04; Gaussian, Inc.: Pittsburgh, PA, 2003. The full reference is in the Supporting Information.

(19) (a) Petersson, G. A.; Bennett, A.; Tensfeldt, T. G.; Al-Laham, M. A.; Shirley, W. A.; Mantzaris, J. *J. Chem. Phys.* **1988**, *89*, 2193. (b) Petersson, G. A.; Al-Laham, M. A. *J. Chem. Phys.* **1991**, *94*, 6081. (c) Dunning, T. H., Jr. *J. Chem. Phys.* **1989**, *90*, 1007.

(20) For a comparison of the performance of different basis sets in the calculation of optical rotation using GIAOs, see: Cheeseman, J. R., Frisch, M. J.; Devlin, F. J.; Stephens, P. J. *J. Phys. Chem. A* **2000**, *104*, 1039.

(21) http://srdata.nist.gov/cccbdb/vibrations.asp.

(22) Mulliken, R. S. *J. Chem. Phys.* **1955**, *23*, 1833.

(23) Woon, D. E.; Dunning, T. H., Jr. *J. Chem. Phys.* **1993**, *98*, 1358.

(24) Kendall, R. A.; Dunning, T. H., Jr.; Harrison, R. J. *J. Chem. Phys.* **1992**, *96*, 6796.

Peter R. Lassen, Dorthe M. Skytte, Lars Hemmingsen, Simon F. Nielsen, Teresa B. Freedman, Laurence A. Nafie, and Søren B. Christensen: Structure and Absolute Configuration of Nyasol and Hinokiresinol via Synthesis and Vibrational Circular Dichroism Spectroscopy.

Reprinted with permission from *J. Nat. Prod.* 2005, **68**, 1603–9.

2

2

Structure and Absolute Configuration of Nyasol and Hinokiresinol via Synthesis and Vibrational Circular Dichroism Spectroscopy

Peter R. Lassen,[†,#] Dorthe Mondrup Skytte,[‡,#] Lars Hemmingsen,[§] Simon Feldbæk Nielsen,[∥] Teresa B. Freedman,[⊥] Laurence A. Nafie,[⊥] and S. Brøgger Christensen*[,‡]

The Quantum Protein Centre, Department of Physics, Technical University of Denmark, DK 2800 Lyngby, Denmark, Department of Medicinal Chemistry, The Danish University of Pharmaceutical Sciences, Universitetsparken 2, DK-2100 Copenhagen, Denmark, Department of Natural Sciences, Royal Veterinary and Agricultural University, Thorvaldsensvej 40, DK-1871 Frederiksberg C, Denmark, Lica Pharmaceuticals, Fruebjergvej 3, DK-2100 Copenhagen Ø, Denmark, and Department of Chemistry, Syracuse University, Syracuse, New York 13244

Received August 16, 2005

The absolute configuration of the norlignan (+)-nyasol was determined to be *S* by comparison of the experimental vibrational circular dichroism data with first-principle calculations taking into account the eight lowest energy conformations. The established absolute configuration of (+)-nyasol enables establishment of the absolute configuration of (−)-hinokiresinol, which is concluded to be *S*. A total synthesis and resolution of hinokiresinol has been performed to resolve the conflicting reports of the coupling constant of the vinylic protons of the disubstituted double bond in this molecule. Racemic hinokiresinol was resolved. Both enantiomers possess the same antiplasmodial activity.

Nyasol (**1**) and the *E*-isomer hinokiresinol (**2**) (Chart 1) possessing the skeleton $C_6C_5C_6$ are typical examples of naturally occurring norlignans. The confusion concerning the nomenclature of these two compounds should have been settled by Minami et al.[1] and Oketch-Rabah et al.,[2] who agreed that the *Z*-isomer should be named nyasol and the *E*-isomer hinokiresinol. Unfortunately, confusion concerning the magnitude of the coupling constant of the vinylic protons of the disubstituted double bond in **2** has still not been settled.[3−5]

The first report on the isolation of hinokiresinol from *Chamaecyparis obtusa* did not specify the optical rotation,[6] but a later report established that this plant forms (−)-(**2**).[1] Similarly, no rotation was reported for hinokiresinol isolated from *Libocedrus yateensis*[7] or from *Agathis australis*.[8] Both antipodes of nyasol are naturally occurring. (+)-Nyasol has been isolated from *Asparagus africanus*[2] and *A. cochinchinensis*,[9] and (−)-nyasol has been obtained from *Anemarrhena asphodeloides*.[10,11] A chiral analysis revealed that the nyasol with a specific rotation of $[\alpha]_D$ −67° consisted of 77% of the levorotatory enantiomer and 23% of the dextrorotatory enantiomer, corresponding to a specific rotation of −124° for enantiomeric pure (−)-nyasol.[1]

The absolute configuration of hinokiresinol (**2**) isolated from *Agathis australis* has been assigned as *S* on the basis of correlation with **3** and **4** (Chart 2).[8] However, no specific rotation for the isolated hinokiresinol (**2**) was reported, which makes the determined absolute configuration less authoritative.[8] The correlation is based on comparison of the ORD curve of the dimethyl ether of **2**, formed by thermal conversion of an orthoformate of the dimethyl ether of agatharesinol (**4**), with the ORD curve of the free phenol **2**.[8] The specific rotation of the phenol **2** isolated from *Chamaecyparis obtusa* is −3,[1] whereas the dimethyl ether

Chart 1

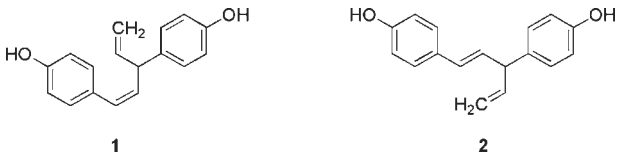

1 **2**

Chart 2

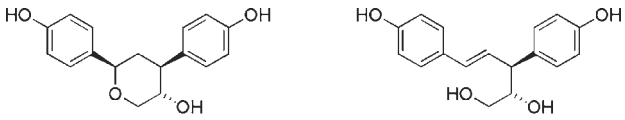

3 **4**

is reported to have a specific rotation of +8.4.[12] Comparison of the ORD curves of these two compounds, thus, should take this shift of sign of the rotation into consideration. The thermal conversion of the orthoformate apparently isomerizes the disubstituted double bond into the *Z*-isomer, since later studies showed that the ^3J coupling of the two vinylic protons at the disubstituted double bond is 12 Hz.[4,5] Such a coupling constant is similar to that reported for nyasol,[2,9] whereas the coupling constant in **2** is 15.9 Hz.[1] This isomerization further questions the conclusion concerning the configuration.

The poor basis for the suggested absolute configuration of hinokiresinol (**2**) and nyasol (**1**) has encouraged us to reinvestigate the absolute configuration of (+)-**2**, isolated from *Asparagus africanus*, by vibrational circular dichroism spectroscopy (VCD). This technique permits comparison of a recorded spectrum with a spectrum calculated from first-principle quantum mechanical methods, i.e., in a nonempirical way.[13] A total synthesis of **2** and comparison of the ^{1}H NMR spectra of **1** and **2** should finally settle the confusion of the magnitude of the coupling constant. Finally advantage was taken of access to the two optical antipodes of **2** to reveal if the antiplasmodial activity was related to the configurational variations. (+)-Nyasol is a modest antiplasmodial agent,[2] but a possible relationship between configuration and antiplasmodial activity has not been investigated.

* To whom correspondence should be addressed. Tel: +45 3530 6253. Fax: +45 3530 6041. E-mail: sbc@dfuni.dk.
† The Quantum Protein Centre.
‡ The Danish University of Pharmaceutical Sciences.
§ Royal Veterinary and Agricultural University.
∥ Lica Pharmaceuticals. Present address: Leo Pharma, Industriparken 55, DK-2710 Ballerup, Denmark.
⊥ Syracuse University.
# These two authors have contributed equally to the article.

10.1021/np0502995 CCC: $30.25
Published on Web 10/21/2005

Table 1. Calculated Energies of Gas-Phase Nyasol Conformers (kJ/mol), Relative to the Lowest Energy Structure, as Found Using the MMFF Force Field and Two DFT Methods, B3LYP/6-31G** and B3LYP/AUG-cc-pVDZ[a]

no.	MMFF	B3LYP/6-31G**	B3LYP/AUG-cc-pVDZ
1	0.330200	0.0000	0.0567
2	0.000000	0.0105	0.0000
3	0.402573	0.1444	0.2133
4	0.729980	0.1864	0.1895
5	2.226303	0.2547	1.5526
6	3.039871	0.9321	1.8797
7	2.559570	1.0502	1.9229
8	2.368820	1.2025	2.1405
9	5.528778	4.3426	
10	5.008957	4.4450	
11	6.133102	4.5631	
12	5.669357	4.9753	
13	14.325104	5.4190	
14	14.631180	5.4715	
15	15.171234	5.6002	
16	14.964020	5.6632	
17	19.457092	19.1898	
18	16.850830	19.2134	
19	19.126968	20.7913	
20	19.592728	21.0276	
21	18.936859	21.3007	
22	19.799881	21.5002	
23	19.873138	24.8189	
24	14.858643	24.9974	
25	16.962799	25.3807	
26	17.427505	25.6984	

[a] The conformations are numbered according to the B3LYP/6-31G** energies. The DFT results include thermal free energy contributions calculated using B3LYP/6-31G**.

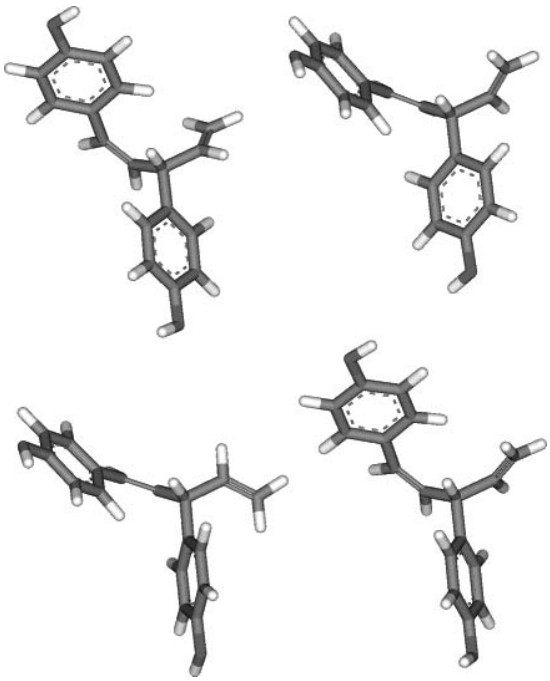

Figure 1. DFT-optimized structures of four (*S*)-nyasol conformers (top left: 1, top right: 5, bottom left: 9, bottom right: 13; numbered according to relative energies, see Table 1), representing the 16 lowest energy conformers. Each structure represents a group of four conformers, which differ only in the relative orientation of the hydroxy groups.

Results and Discussion

Despite the moderate size of **1**, a considerable number of conformers exist at room temperature (Table 1 and Figure 1), with the eight lowest energy structures within 2.1 kJ/mol at the B3LYP/AUG-cc-pVDZ level of theory.

Thus, **1** is among the most flexible small organic molecules studied by VCD spectroscopy. Spectral assignments of theoretical VCD signals are given in Table 2 and Figure 2.

The challenge arises from the fact that the VCD signals from the various conformers tend to extinguish one another, putting high demands on the signal-to-noise ratio of the instrument. There are, however, spectral regions where the first-principle calculations predict that most conformers give similar VCD signals, allowing determination of the absolute configuration of nyasol (Figure 3).

In particular the strong positive signal at 1510 cm^{-1} observed for nyasol dissolved in DMSO-d_6 (Figure 4) and the spectral signatures at 800−1000 and 1590−1650 cm^{-1} observed for nyasol in a KBr pellet (Figure 5) are such regions.

The pronounced similarities between the recorded spectrum of (+)-nyasol and the calculated spectrum for (*S*)-nyasol in these regions therefore show that (+)-nyasol possesses the *S*-configuration. There are discrepancies between experimental and calculated spectra, particularly in the region from 1100 to 1300 cm^{-1}, for both the IR absorption and VCD signals. The most intense signals in this region originate from vibrations involving the two hydroxy groups of nyasol, indicating that the broadening and changes in frequencies and relative intensities of the signals are due to nyasol−solvent and/or nyasol−nyasol interactions. These intermolecular interactions tend to broaden the signal from the C−O stretching vibration at 1270 cm^{-1} and almost extinguish the O−H bending at 1170 cm^{-1}. Their combined vibration at 1620 cm^{-1} is less affected. The quenched O−H bending has been reproduced theoretically by calculating spectra with one explicit DMSO molecule next to each of the two hydroxy groups, putting the qualitative interpretation on more firm theoretical grounds. UV−vis absorption and conventional (electronic) CD spectra were also recorded for nyasol from *A. africanus* (see Figure 6), and given the assignment derived from the VCD experiments, we conclude that the CD spectrum corresponds to (*S*)-nyasol.

Minami et al.[1] have similarly utilized CD data in the assignment of absolute configuration of nyasol and hinokiresinol, in agreement with the data presented in Figure 6. Their findings prove that (−)-nyasol is hydrogenated to the antipode of the tetrahydro derivative of (−)-hinokiresinol. Consequently the parent compounds (−)-nyasol and (−)-hinokiresinol must possess opposite absolute configurations as well. Since (+)-nyasol is *S*-configured, (−)-nyasol must possess the *R*-configuration. (−)-Hinokiresinol has the opposite configuration, that is, *S*, and consequently (+)-hinokiresinol possesses the *R*-configuration as previously concluded.[8]

Synthesis of Hinokiresinol (2). Some synthetic methods for the dimethyl ether of **2** have been published.[6,14] The synthesis of the dimethyl ether of hinokiresinol is initiated by an addition of a Grignard reagent to an oxo compound, preventing the direct synthesis of hinokiresinol with free phenolic groups.

In the only reported synthesis of the free diphenol **2**[15] the phenolic hydroxyl groups were protected as *tert*-butyldimethylsilyl ethers (TBDMS). The TBDMS group was cleaved during the initial Claisen−Schmidt condensation and had to be reintroduced in a modest yield. This problem was overcome by protecting the phenolic groups as tetrahydropyranyl ethers. This protecting group survived the condensation of the ketone and the aldehyde to give **5**, which smoothly reacted with vinylmagnesium bromide to give **6**. Addition of copper(I) iodide ensured 1,4-addition of the Grignard reagent. Sodium borohydride

Table 2. Assignment of Selected Peaks in the B3LYP/AUG-cc-pVDZ-Calculated IR and VCD Spectra for the Lowest Energy Conformer[a]

ν (cm^{-1})	ϵ ($M^{-1}\,cm^{-1}$)	$10^4\Delta\epsilon$ ($M^{-1}\,cm^{-1}$)	assignment
846	43.267	−263.076	phenol C−H oop bend
849	96.499	323.353	phenol C−H oop bend
859	54.035	−49.5495	phenol C−H oop bend
888	79.521	−42.1694	methine C−H bend
949	23.575	26.0106	vinyl C−H oop bend
959	55.749	−4.53252	vinyl C−H oop bend
1005	22.618	−4.70156	vinyl C−H oop bend
1025	36.633	13.4051	vinyl C−H ip bend
1120	33.284	−75.0412	phenol C−H ip bend
1127	33.226	−7.48434	phenol C−H ip bend
1184	482.469	96.6739	O−H bend
1186	161.730	−92.2848	O−H bend
1189	253.009	−23.8879	O−H bend
1269	124.863	78.9772	C−O stretch, methine C−H bend
1273	207.496	−39.1544	C−O stretch, methine C−H bend
1279	197.746	−84.5487	C−O stretch, methine C−H bend
1322	15.465	97.8881	vinyl C−H ip bend
1367	87.202	−40.1792	phenol C−C stretch, C−H and O−H ip bend
1369	73.435	33.0594	Phenol C−C stretch, C−H and O−H ip bend
1423	57.911	−27.8639	vinyl C−H ip bend
1434	35.367	−19.088	vinyl C−H ip bend
1464	37.615	111.113	phenol C−H, O−H ip bend
1535	276.918	22.9206	phenol C−O stretch, C−H ip bend
1539	257.528	146.532	phenol C−O stretch, C−H ip bend
1625	42.569	−55.4286	phenol C−C stretch
1634	48.017	−5.691	phenol C−C stretch
1653	186.086	2.0246	phenol C−C stretch
1654	94.705	−5.97896	phenol C−C stretch
1689	7.045	−25.3217	vinyl C−C stretch
1693	38.819	−76.3316	vinyl C−C stretch

[a] Columns are wavenumbers ν, molar absorptivities ϵ, differential absorptivities $\Delta\epsilon$, and assignments. Abbreviations: ip = in-plane, oop = out-of-plane.

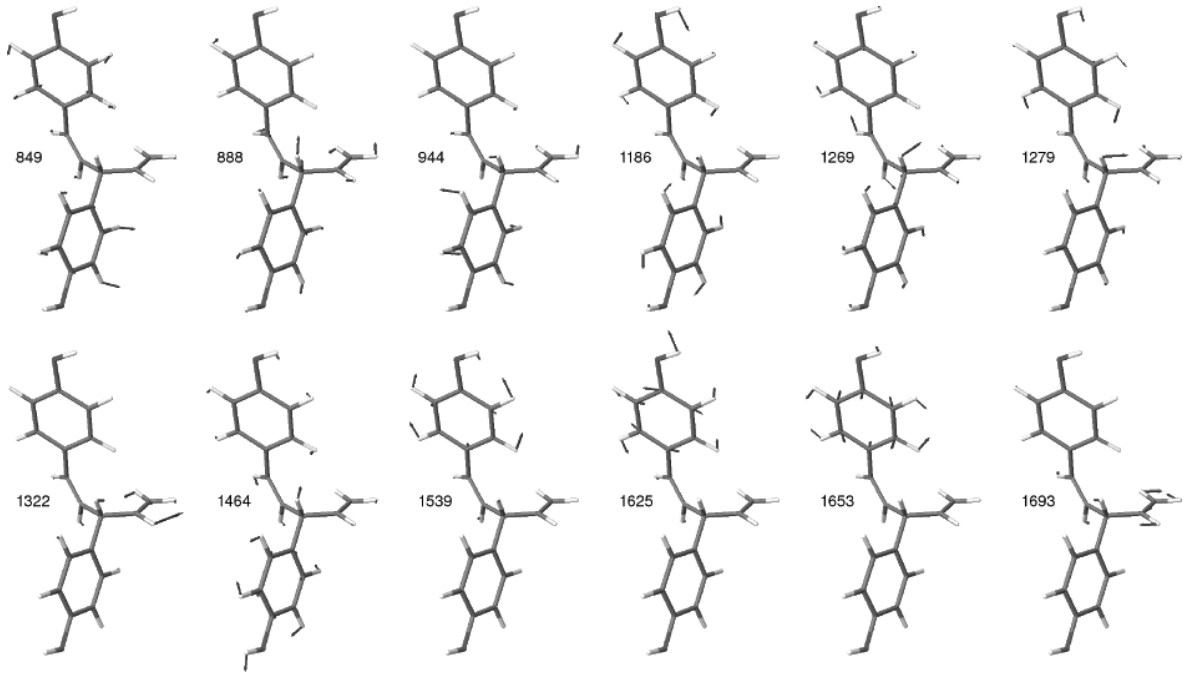

Figure 2. Relative amplitudes of selected vibrational modes assigned in Table 2 for the lowest energy conformer, calculated using B3LYP/AUG-cc-pVDZ. Each mode is labeled with the corresponding wavenumber (cm^{-1}).

reduction of the ketone yielded a mixture of the diastereomeric alcohols **7**. A further advantage of the tetrahydropyranyl group was that a hydrochloric acid-catalyzed elimination of water from **7** simultaneously cleaved the protecting groups. In addition all the steps in the reaction sequence in Scheme 1 afforded better yields than the reaction sequence using the TBDMS protecting group. No nyasol was detected in the reaction mixture. The vinylic coupling constant was found to be 15.9 Hz, as expected for a *trans* coupling.

Optical resolution was performed by chiral HPLC to give the two enantiomers having identical ^{1}H NMR spectra.

The antiplasmodial effect of the two enantiomers of **2** was determined. Surprisingly, the enantiomers were equi-

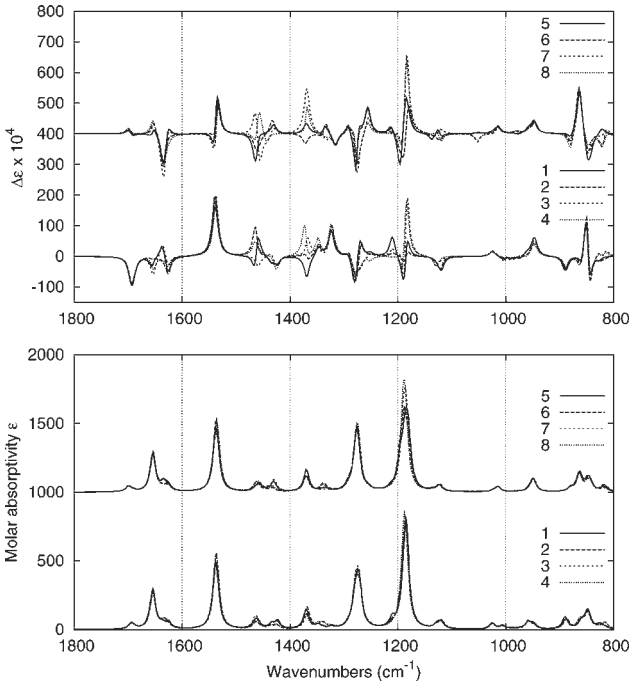

Figure 3. Calculated IR absorption (lower half) and VCD spectra (upper half) for the eight lowest energy conformers of (*S*)-nyasol, at the B3LYP/AUG-cc-pVDZ level of theory. Frequencies are not scaled. The bands are plotted as Lorentzians with half-widths of 6 cm^{-1}. Half of the spectra are offset for clarity.

potent [IC_{50} values: *rac*-**2**, 51 ± 10 μM; (+)-**2**, 55 ± 14 μM; (−)-**2**, 80 ± 25 μM]. The antiplasmodial activity, thus, is not dependent on the absolute configuration.

Experimental Section

General Experimental Procedures. IR and VCD spectra were obtained on a Chiral*IR* FT-VCD spectrometer (BioTools, Inc., Wauconda, IL), equipped with two sources[16] and two photoelastic modulators[17] optimized at 1400 cm^{-1}. An optical band-pass filter was used to allow only the spectral region 800−2000 cm^{-1} to reach the detector. Spectra were calibrated automatically, using the standard calibration files.

VCD spectra were recorded both in DMSO-d_6 solution (5 mg of nyasol in 100 μL of DMSO-d_6 in a BaF_2 cell with 100 μm path length) and in KBr pellets (250 mg KBr, ϕ 13 mm × 1 mm). The resolution was 8 cm^{-1}, and the acquisition time was 9 h for DMSO-d_6 solution and 31 h for the KBr pellet. In the latter case, spectra from two different orientations of the KBr pellet were averaged to reduce the baseline offset. ^{1}H NMR spectra were recorded on a Varian Mercury spectrometer or Varian Gemini 2000 spectrometer at 300 MHz using tetramethylsilane as internal standard. Splitting patterns are described as singlet (s), doublet (d), triplet (t), doublet of doublets (dd), doublet of double doublets (ddd), and multiplet (m). Uncorrected melting points were determined on a Büchi SMP-20 apparatus, and optical rotation was measured on a Perkin-Elmer 241 polarimeter. Column chromatography was performed on silica gel 60 (Merck 107734). For HPLC a Waters 6000A pump and a Shimadzu SPD 6A detector was used. THF was distilled from LAH and kept over molecular sieves. UV−vis absorption spectra were recorded on a Cary 5 spectrometer, and conventional (electronic) CD spectra were recorded on a JASCO-720 CD instrument using a cylindrical quartz cuvette with a light path of 5 μm and a 61 mg/mL solution of nyasol in MeCN. Using MeOH as solvent does not change the spectra significantly. The instrument was purged with N_2. All spectra were baseline corrected using a baseline recorded with no cell in the instrument and collected at room temperature.

Computational Methods. Conformational searches and geometry optimizations of (*S*)-nyasol were performed with

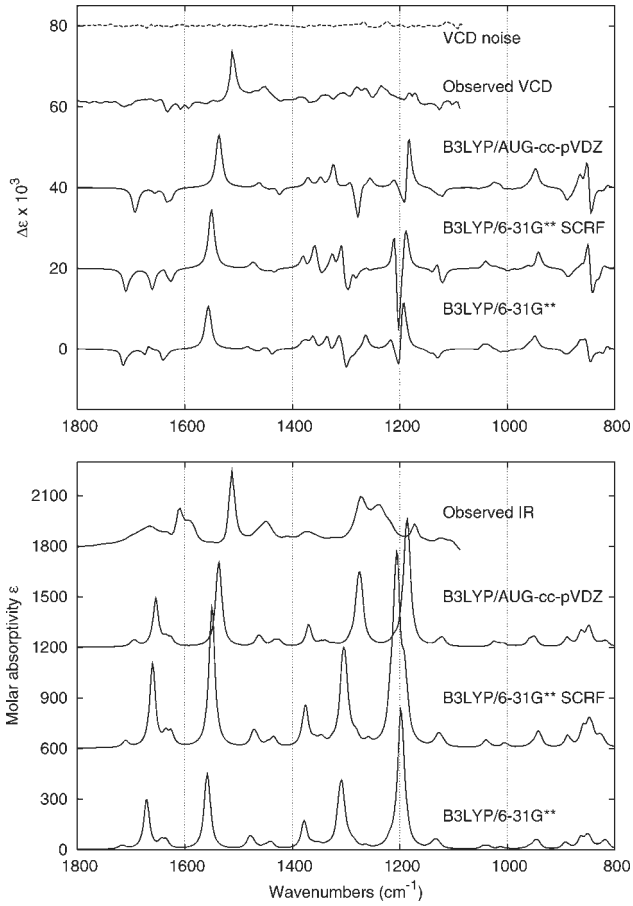

Figure 4. Comparison of observed and calculated IR absorption (lower half) and VCD (upper half) spectra of nyasol. Experimental spectra are measured in DMSO-d_6, using a resolution of 8 cm^{-1} and 9 h acquisition time, with the instrument optimized at 1400 cm^{-1}. VCD noise is shown in the uppermost (dashed) trace. Experimental IR absorption spectra are corrected for the presence of solvent, and spectra are offset for clarity. Calculated spectra are Boltzmann-weighted averages of the eight lowest energy conformers of the *S*-enantiomer, with three different DFT methods as indicated. The B3LYP/6-31G** SCRF uses a continuum solvent model for DMSO.

MacroModel (Schrödinger, Portland, OR).[18] Conformational searches were made in the gas phase using systematic torsional search (SUMM) and an energy window of 20 kJ/mol. For each structure the structure was optimized using the MMFF force field, with 500 steps, 1000 iterations, and a threshold of 0.05. The (unique) structures from the conformational search were subsequently geometry optimized using density functional theory (DFT) as implemented in Gaussian 03,[19] using the B3LYP functional[20] with the 6-31G** and AUG-cc-pVDZ basis sets and default convergence criteria.[21,22] Vibrational spectra were calculated with the same methods. Dipole and rotational strengths from Gaussian were converted into molar absorptivities[13] (M^{-1} cm^{-1}), and each spectrum was plotted as a sum of Lorentzian bands with half-widths of 6 cm^{-1} for comparison with experiments. The relative energies presented include free energy corrections from molecular vibrations.

Nyasol Conformers. In both the gas phase and solvent, the conformational searches of (*S*)-nyasol yielded 26−29 structures within the energy window. A few of these structures converged to the same local minimum at the B3LYP/6-31G** level of theory. All energies from gas-phase geometry optimizations in MacroModel and Gaussian 03 are shown in Table 1, where the conformations are numbered in order of the B3LYP/6-31G** energies. In most cases the MMFF force field performs very well, but there are cases where the relative energy deviates by up to 8 kJ/mol from the first-principle calculations.

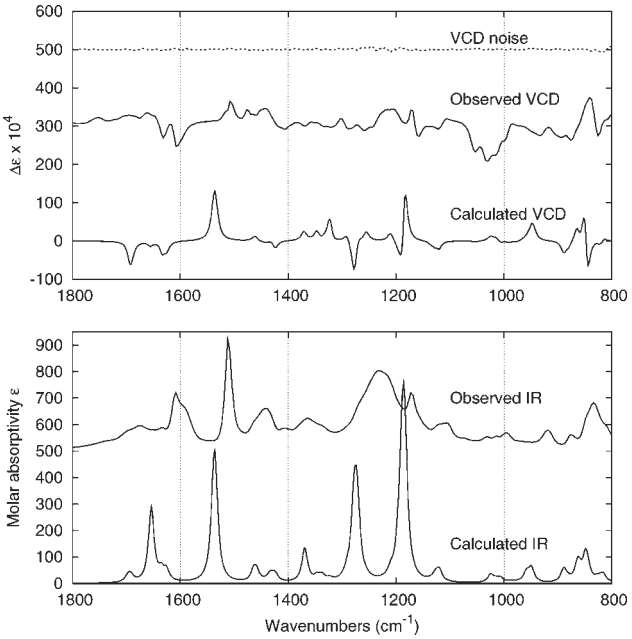

Figure 5. Observed IR absorption (lower half) and VCD (upper half) spectra of nyasol in a KBr pellet, compared to the DFT calculation for (*S*)-nyasol using B3LYP/AUG-cc-pVDZ. The experimental resolution is 8 cm^{-1}, with the instrument optimized at 1400 cm^{-1}. The total acquisition time is 31 h, and spectra from two different orientations of the KBr pellet were averaged to reduce the baseline offset. VCD noise is shown in the uppermost (dashed) trace.

A representative selection of the gas-phase structures are shown in Figure 1, arranged in order of increasing energy. The conformational energy displays gaps of about 3 kJ/mol between conformers 8 and 9 and of about 14 kJ/mol between conformers 16 and 17. In the analysis of the VCD spectra we have therefore included only the eight lowest energy conformers. Furthermore, the conformational energies of the 16 lowest energy conformers fall into groups of four having rather similar energies, because both hydroxy groups can point in two almost equally favorable orientations. Within each group of four conformers, the carbon skeleton is basically fixed, and only the hydroxy group orientations differ. No considerable geometry changes in the gas-phase structures occur when DFT optimization includes a self-consistent reaction field (SCRF) solvent model (polarizable continuum model)[23] for DMSO.

Infrared and VCD Spectra. Figure 3 depicts the calculated IR and VCD spectra for the eight lowest energy structures, calculated using the B3LYP functional and AUG-cc-pVDZ basis set. The spectra of conformers 5−8 are offset for clarity. All of the conformations have very similar IR spectra, differing mostly in frequency and intensity of some minor peaks. However, in the calculated VCD spectra, considerable differences arise between the conformers To determine the absolute configuration, we identified the spectral regions in Figure 3 with the least variability. These regions will be optimal for determinations of the absolute configurations of nyasol, as the signals from different conformers do not extinguish each other to any significant extent. These regions are 800−1000, 1250−1350, and 1510 cm^{-1}, and the negative amplitude signals around 1650−1700 cm^{-1}. To distinguish conformers in the observed spectra, we note that the band around 1530 cm^{-1} has a different shape for the two groups of conformers (1−4 and 5−8). Additionally, around 1300 and 1650 cm^{-1}, there seem to be consistent differences between these two groups.

Assignments for the lowest energy conformer are shown in Table 2.

In Figure 4 the recorded spectrum (DMSO-d_6 solution) of (+)-nyasol isolated from *A. africanus* as previously reported[8] is compared to the Boltzmann weighted average of the calculated spectra for the eight lowest energy conformers,

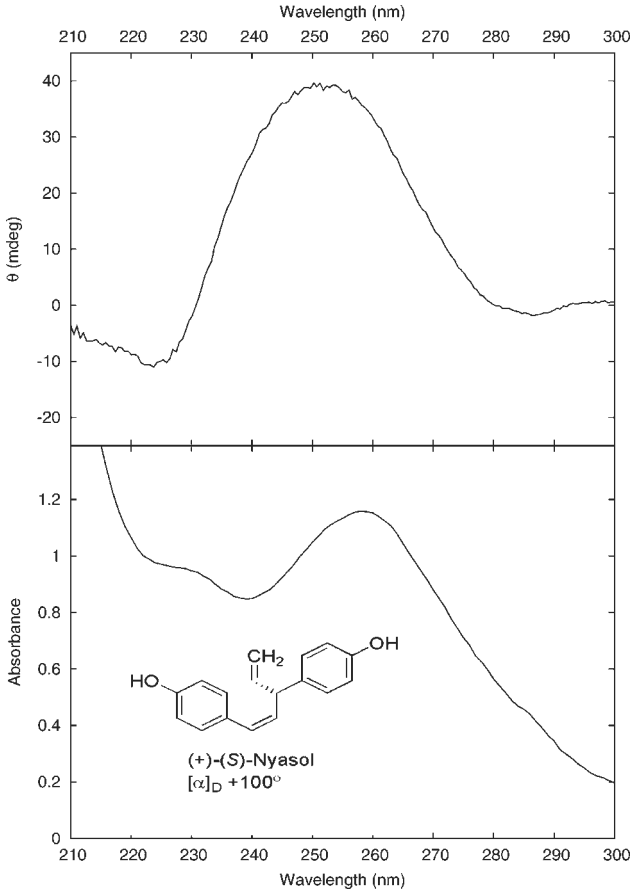

Figure 6. UV−vis absorption (bottom) and CD (top) of (+)-(*S*)-nyasol in MeCN (61 mg/mL), path length of 5 μm. Based on the assignment derived from the VCD spectra, the CD spectrum represents (*S*)-nyasol.

using B3LYP/6-31G**, B3LYP/6-31G** with an SCRF continuum solvent model for DMSO, and B3LYP/AUG-cc-pVDZ, respectively. The solvent DMSO-d_6 obscures the spectrum below 1100 cm^{-1}. In the 1250−1350 cm^{-1} region the VCD signals are too weak to reliably determine the absolute configuration, but above 1400 cm^{-1} the experimental spectrum of (+)-nyasol and the calculated spectrum for *S*-nyasol compare well. Similarly, there are considerable differences between the calculated and observed IR absorption signals in the 1180−1300 cm^{-1} region. In Figure 5 the (+)-nyasol containing a KBr pellet measurement is compared to the B3LYP/AUG-cc-pVDZ calculation for *S*-nyasol, which shows very good agreement in the region 800−1000 cm^{-1} and reasonable agreement above 1300 cm^{-1}. The nyasol concentration differs between the DMSO-d_6 solution and KBr pellet experiments, and consequently different spectral regions have optimal IR absorption for VCD measurements. Thus the two measurements complement each other by probing different spectral regions, and consequently, VCD signal intensities should not be compared between the two observed spectra. KBr pellets can easily show birefringence artifacts, which is probably the case in the 1000−1100 cm^{-1} region, and possibly other spectral regions as well. The noise level does not identify such artifacts.

Synthesis of Hinokiresinol. (*E*)-1,3-Bis(4-[(tetrahydro-2*H*-pyran-2-yl)methyl]phenyl)pent-4-en-1-one (6). A solution of vinylmagnesium bromide (1.0 M solution in THF, 60.0 mmol, 60.0 mL), in an inert nitrogen atmosphere, was added to a suspension of cuprous iodide (2.7 mmol, 0.520 g) in THF (60 mL) and cooled to 0 °C. After stirring for 15 min at 0 °C a solution of (*E*)-1,3-bis(4-[tetrahydro-2*H*-pyran-2-yloxy]phenyl)-prop-2-en-1-one (**5**)[24] (11.13 g, 27.3 mmol) in THF (30 mL) was added to the reaction mixture, and the mixture was stirred for an additional 2 h at 0 °C. After quenching with an aqueous saturated NH_4Cl solution the mixture was diluted with Et_2O (400 mL) and successively washed twice with water (400 mL)

Scheme 1

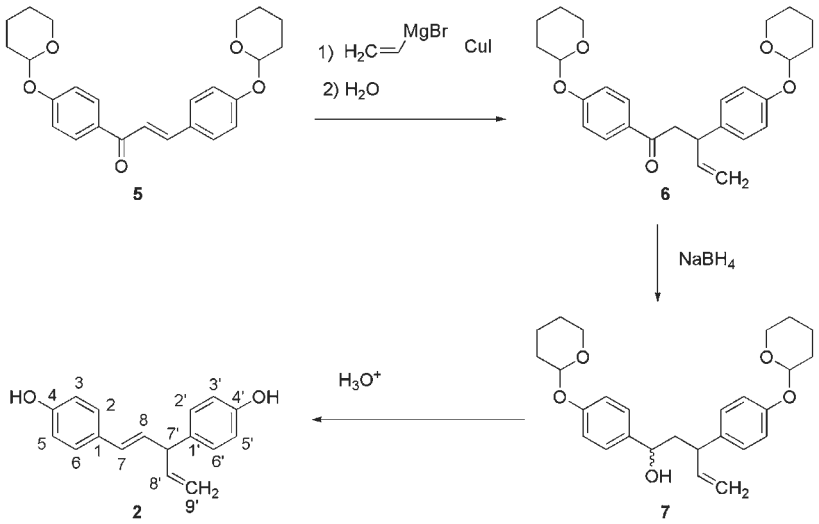

and once with brine (200 mL). The organic layer was dried over Na_2SO_4, filtered, and concentrated in vacuo. The product was purified by column chromatography using toluene−EtOAc (20:1) as an eluent to give **6** (7.47 g, 75%) as pale yellow crystals, mp 92−94 °C (MeOH): ^{1}H NMR ($CDCl_3$, 300 MHz) δ 1.55−2.05 (12H, m, CH_2 groups from THP); 3.26 (1H, dd, J = 6.6, 16.8 Hz, H-8); 3.35 (1H, dd, J = 7.8, 16.8 Hz, H-8); 3.56−3.64 (2H, m, OCH_2 groups from THP); 3.81−3.94 (2H, m, OCH_2 groups from THP); 4.07 (1H, ddd, J = 7.2 Hz, H-7′); 4.99 (1H, d, J = 17.4 Hz, H-9′); 5.03 (1H, d, J = 10.2 Hz, H-9′); 5.37 (1H, ddd, J = 3.0 Hz, O_2CH group from THP); 5.51 (1H, ddd, J = 3.0 Hz, O_2CH group from THP); 6.01 (1H, ddd, J = 6.6, 10.8, 17.4 Hz, H-8′); 6.98 (2H, d, J = 8.7 Hz, H-3′, H-5′); 7.06 (2H, d, J = 8.7 Hz, H-3, H-5); 7.16 (2H, d, J = 8.4 Hz, H-2′, H-6′); 7.90 (2H, d, J = 8.4 Hz, H-2, H-6).

***(E)*-1,3-Bis(4-[(tetrahydro-2*H*-pyran-2-yl)methyl]phenyl)pent-4-en-1-ol (7).** $NaBH_4$ (3.24 g, 85.6 mmol) was added to a solution of **6** (7.47 g, 17.1 mmol) in EtOH (150 mL), and the solution was stirred overnight at room temperature. The reaction mixture was quenched with an aqueous solution of NaOH (5%, 300 mL), and the mixture was extracted twice with Et_2O (150 mL). The combined organic layers were dried over Na_2SO_4, filtered, and concentrated in vacuo. The product was purified by column chromatography using toluene−EtOAc (9:1) as an eluent to give a mixture of the diastereomers as a yellow syrup (7.20 g, 96%): ^{1}H NMR ($CDCl_3$, 300 MHz) δ 1.56−2.34 (14H, m, H-8 + CH_2 groups from THP); 3.32 (ddd, J = 7.5 Hz); 3.44 (ddd, J = 8.1 Hz) (1H all together, H7′); 3.56−3.60 (2H, m, OCH_2 groups from THP); 3.84−3.93 (2H, m, OCH_2 groups from THP); 4.43 (dd, J = 6.0 Hz); 4.54 (dd, J = 6.0 Hz) (1H all together, H-7); 4.96−5.06 (2H, m, H-9′); 5.36−5.40 (2H, m, O_2CH groups from THP); 5.89 (ddd, J = 7.5, 9.9, 17.4 Hz); 5.96 (ddd, J = 7.5, 9.9, 17.4 Hz) (1H all together, H-8′); 6.95−7.23 (8H, m, H-2, H-3, H-5, H-6, H-2′, H-3′, H-5′, H-6′).

Hinokiresinol (2) (racemic). To a solution of the alcohol **7** (7.19 g, 16.4 mmol) in MeOH (150 mL) was added a 7% aqueous solution of HCl (85 mL), and the mixture was refluxed for 1 h. After cooling it was poured into a saturated aqueous $NaHCO_3$ solution (500 mL). The mixture was extracted twice with CH_2Cl_2 (200 mL). The combined organic layers were washed with brine (200 mL), dried over Na_2SO_4, filtered, and concentrated in vacuo. The product was purified by column chromatography using toluene−EtOAc (9:1) to give racemic **2** as colorless crystals, which over time turned red (1.93 g, 47%), mp 69−71 °C ($CHCl_3$): ^{1}H NMR (acetone-d_6, 300 MHz) δ 4.12 (1H, t, J = 6.9 Hz, H-7′); 5.09 (2H, m, H-9′); 6.09 (1H, ddd, J = 6.9, 9.9, 17.7 Hz, H-8′); 6.26 (1H, dd, J = 6.9, 15.9 Hz, H-8); 6.36 (1H, d, J = 16.2 Hz, H-7); 6.78 (2H, d, J = 8.7 Hz, H-3′, H-5′); 6.80 (2H, d, J = 9.0 Hz, H-3, H-5); 7.10 (2H, d, J = 8.7 Hz, H-2′, H-6′); 7.27 (2H, d, J = 9.0 Hz, H-2, H-6); 8.24 (1H, s, br, OH); 8.41 (1H, s, br, OH)

Optical Resolution of Hinokiresinol (2). Racemic hinokiresinol was resolved over a Daicel Chiralcel OD 0.46 × 25 cm chiral column using petroleum ether−2-propanol (94:6) with added HOAc (0.4%) as an eluent and a flow of 1 mL/min. The two enantiomers eluted with retention times of 64.2 min ($[\alpha]_D^{25}$ −1.7° (*c* 0.27, acetone)), lit.[25] −3°) and 71 min ($[\alpha]_D^{25}$ +4.4° (*c* 0.38, acetone)).

Antiplasmodial Assay. The antiplasmodial activity toward the chloroquine-sensitive 3D7 *Plasmodium falciparum* strain (IC_{50} 24 nM) was determined as previously described.[26] The experiments were performed three times, each time in triplicate.

Acknowledgment. This work was supported by the Danish Ministry of Science Technology and Innovation and by the Lundbeck Foundation. P.-O. Norrby from the Technical University of Denmark is acknowledged for assistance with MacroModel. P. W. Thulstrup, The Royal Veterinary and Agricultural University, is acknowledged for help with the electronic CD measurements. The Jmol development team (http://jmol.sourceforge.net) is acknowledged for their molecular visualization software.

References and Notes

(1) Minami, E.; Taki, M.; Takaishi, S.; Iijima, Y.; Tsutsumi, S.; Akiyama, T. *Chem. Pharm. Bull.* **2000**, *48*, 389−392.
(2) Oketch-Rabah, H. A.; Dossaji, S. F.; Christensen, S. B.; Frydenvang, K.; Lemmich, E.; Cornett, C.; Olsen, C. E.; Chen, M.; Kharazmi, A.; Theander, T. *J. Nat. Prod.* **1997**, *60*, 1017−1022.
(3) Ameer, F.; Drewes, S. E.; Drewes, M. W.; Roos, G. H. P.; Watson, M. C. *J. Chem. Soc., Perkin Trans. 1* **1988**, 1425−1430.
(4) Beracierta, A.; Whiting, D. *J. Chem. Soc., Perkin Trans. 1* **1978**, 1257−1263.
(5) Beracierta, A.; Whiting, D. A. *Tetrahedron Lett.* **1976**, 2367−2370.
(6) Hirose, Y.; Oishi, N.; Nagaki, H.; Nakatsuka, T. *Tetrahedron Lett.* **1965**, 3665−3668.
(7) Erdtman, H.; Harmatha, J. *Phytochemistry* **1979**, *18*, 1495−1500.
(8) Enzell, C. R.; Hirose, Y.; Thomas, B. R. *Tetrahedron Lett.* **1967**, 793−798.
(9) Tsui, W.; Brown, G. D. *Phytochemistry* **1996**, *43*, 1413−1415.
(10) Jeong, S.-J.; Higuchi, R.; Ono, M.; Kuwano, M.; Kim, Y. C.; Miyamoto, T. *Biol. Pharm. Bull.* **2003**, *26*, 1721−1724.
(11) Iida, Y.; Oh, K.-B.; Saito, M.; Matsuoka, H.; Kurata, H.; Natsume, M.; Abe, H. *J. Agric. Food Chem.* **1999**, *47*, 584−587.
(12) Hirose, T.; Oishi, N.; Nagaki, H.; Nakatsuka, T. *Tetrahedron Lett.* **1965**, 3665−3668.
(13) Freedman, T. B.; Cao, X. L.; Dukor, R. K.; Nafie, L. A. *Chirality* **2003**, *15*, 743−758.
(14) Hirose, Y.; Ishikawa, K.; Nakatsuka, T. *Agric. Biol. Chem.* **1968**, *32*, 1283−1286.
(15) Hishiyama, S.; Kato, A.; Lee, S. S. *Tennen Yuki Kagobutsu Toronkai Koen Yoshishu* **1998**, *40*, 625−630.
(16) Nafie, L. A.; Buijs, H.; Rilling, A.; Cao, X. L.; Dukor, R. K. *Appl. Spectrosc.* **2004**, *58*, 647−654.
(17) Nafie, L. A. *Appl. Spectrosc.* **2000**, *54*, 1634−1645.

(18) Mohamadi, F.; Richards, N. G. J.; Guida, W. C.; Liskamp, R.; Lipton, M.; Caufield, C.; Chang, G.; Hendrickson, T.; Still, W. C. *J. Comput. Chem.* **1990**, *11*, 440−467.
(19) Frisch, M. J.; Trucks, G. W.; Schlegel, H. B.; Scuseria, G. E.; Robb, M. A.; Cheeseman, J. R.; Montgomery, J. A., Jr.; Vreven, T.; Kudin, K. N.; Burant, J. C.; Millam, J. M.; Iyengar, S. S.; Tomasi, J.; Barone, V.; Mennucci, B.; Cossi, M.; Scalmani, G.; Rega, N.; Petersson, G. A.; Nakatsuji, H.; Hada, M.; Ehara, M.; Toyota, K.; Fukuda, R.; Hasegawa, J.; Ishida, M.; Nakajima, T.; Honda, Y.; Kitao, O.; Nakai, H.; Klene, M.; Li, X.; Knox, J. E.; Hratchian, H. P.; Cross, J. B.; Adamo, C.; Jaramillo, J.; Gomperts, R.; Stratmann, R. E.; Yazyev, O.; Austin, A. J.; Cammi, R.; Pomelli, C.; Ochterski, J. W.; Ayala, P. Y.; Morokuma, K.; Voth, G. A.; Salvador, P.; Dannenberg, J. J.; Zakrzewski, V. G.; Dapprich, S.; Daniels, A. D.; Strain, M. C.; Farkas, O.; Malick, D. K.; Rabuck, A. D.; Raghavachari, K.; Foresman, J. B.; Ortiz, J. V.; Cui, Q.; Baboul, A. G.; Clifford, S.; Cioslowski, J.; Stefanov, B. B.; Liu, G.; Liashenko, A.; Piskorz, P.; Komaromi, I.; Martin, R. L.; Fox, D. J.; Keith, T.; Al-Laham, M. A.; Peng, C. Y.; Nanayakkara, A.; Challacombe, M.; Gill, P. M. W.; Johnson, B.; Chen, W.; Wong, M. W.; Gonzalez, C.; Pople, J. A. *Gaussian 03, Revision B.04*; Gaussian, Inc.: Wallingford, CT, 2004.
(20) Becke, A. D. *J. Chem. Phys.* **1993**, *98*, 5648−5652.
(21) Hariharan, P.; Pople, J. A. *Theor. Chim. Acta* **1973**, *28*, 213−222.
(22) Kendall, R. A.; Dunning, T. H.; Harrison, R. J. *J. Chem. Phys.* **1992**, *96*, 6796−6806.
(23) Cossi, M.; Scalmani, G.; Rega, N.; Barone, V. *J. Chem. Phys.* **2002**, *117*, 43−54.
(24) Severi, F.; Costantino, L.; Benvenuti, S.; Vampa, G.; Mucci, A. *Med. Chem. Res.* **1996**, *6*, 128−136.
(25) Minami, E.; Taki, M.; Takaishi, S.; Ijima, Y.; Tsutsumi, S.; Akiyama, T. *Chem. Pharm. Bull.* **2000**, *48*, 389−392.
(26) Ziegler, H.; Stærk, D.; Christensen, J.; Hviid, L.; Hägerstrand, H.; Jaroszewski, J. W. *Antimicrob. Agents Chemother.* **2002**, *46*, 1441−1446.

NP0502995

Robert H. Cichewicz, Laura J. Clifford, Peter R. Lassen, Xiaolin Cao, Teresa B. Freedman, Laurence A. Nafie, Joshua D. Deschamps, Victor A. Kenyon, Jocelyn R. Flanary, Theodore R. Holman, and Phillip Crews: Stereochemical determination and bioactivity assessment of (*S*)-(+)-curcuphenol dimers isolated from the marine sponge *Didiscus aceratus* and synthesized through laccase biocatalysis.

Reprinted from *Bioorg. Med. Chem.* **13**(19), 5600–12, Copyright 2005, with permission from Elsevier.

3

3

Available online at www.sciencedirect.com
SCIENCE DIRECT®
Bioorganic & Medicinal Chemistry
ELSEVIER
Bioorganic & Medicinal Chemistry 13 (2005) 5600–5612

Stereochemical determination and bioactivity assessment of (*S*)-(+)-curcuphenol dimers isolated from the marine sponge *Didiscus aceratus* and synthesized through laccase biocatalysis

Robert H. Cichewicz,[a,b] Laura J. Clifford,[a,b] Peter R. Lassen,[c,†] Xiaolin Cao,[c] Teresa B. Freedman,[c] Laurence A. Nafie,[c] Joshua D. Deschamps,[a] Victor A. Kenyon,[a] Jocelyn R. Flanary,[a,b] Theodore R. Holman[a,*] and Phillip Crews[a,b,*]

[a]*Department of Chemistry and Biochemistry, University of California, Santa Cruz, CA 95064, USA*
[b]*Institute for Marine Sciences, University of California, Santa Cruz, CA 95064, USA*
[c]*Department of Chemistry, Syracuse University, Syracuse, NY 13244, USA*

Received 15 March 2005; revised 2 June 2005; accepted 2 June 2005
Available online 20 July 2005

Abstract—Electrospray ionization mass spectrometry-guided isolation of extracts from *Didiscus aceratus* led to the discovery of several new derivatives of the bioactive bisabolene-type sponge metabolite (*S*)-(+)-curcuphenol (**1**). The compounds obtained by this method included a mixture of known (**2**) and new (**3**) dihydroxylated analogs as well as a novel family of dimeric derivatives, dicurcuphenols A–E (**4**–**8**), and dicurcuphenol ether F (**9**). Dimers **4**–**9** were also subsequently obtained through a hemisynthetic method in which **1** was incubated with the enzyme laccase. Atropisomeric dimers **5** and **6** were subjected to vibrational circular dichroism analysis thereby establishing their absolute biaryl axial chirality as *P* and *M*, respectively. In contrast to **1**, metabolites **2**–**9** exhibited weak or no cytotoxic or lipoxygenase inhibitory effects.

1. Introduction

Bisabolene-type sesquiterpenoids constitute a class of broadly active natural products biosynthesized by a diverse range of organisms from both terrestrial and marine habitats. Within the marine environment alone, numerous bisabolene sesquiterpenoids have been reported from sponges (*Acanthella*,[1] *Arenochalina*,[2] *Axinyssa*,[3] *Ciocalypta*,[4] *Didiscus*,[5,6] *Epipolasis*,[7,8] *Halichondria*,[9] *Haliclona*,[10] *Myrmekioderma*,[11] and *Theonella*[12,13]), a nudibranch,[14] gorgonians,[15–18] a sea hare,[19] and red algae.[20,21] Included among these discoveries are a number of uniquely functionalized bisabolene species such as heterocyclic,[10] nitrogenous,[3,4,9,13] halogenated,[19] polyhydroxylated quinone,[15] and acetylated[20] derivatives that have significantly broadened the biosynthetic scope of this distinct chemical family. It is of particular interest to note that two unique classes of bisabolene-type metabolites are recognized based on their C-7 absolute stereochemistry. As previously described,[10] all known sponge-derived bisabolenes possess a 7*S* configuration while the remaining marine and terrestrial metabolites exhibit a 7*R* configuration.

The lead compound of this family, (*S*)-(+)-curcuphenol (**1**) ($C_{15}H_{22}O$), has attracted much attention due to its distribution among marine sponges and biological activities. This compound has been encountered as a major sesquiterpene metabolite (yield > 1 % dry weight) in four sponge genera (*Arenochalina*,[2] *Didiscus*,[5,6] *Epipolasis*,[7,8] and *Myrmekioderma*[11]) from the Caribbean,[5,6,8,11] western Australia,[2] and Japan.[11] In contrast, the marine occurrences of the optical antipode of **1**, (*R*)-(−)-curcuphenol, have been limited to several New World gorgonians from the genus *Pseudopterogorgia*.[15,16,18] These compounds are reported to possess numerous biological effects including antimicrobial,[5,6,18] H/K-ATPase

Keywords: Atropisomer; Curcuphenol; Dicurcuphenol; *Didiscus aceratus*; Dimer; Laccase; Lipoxygenase; Vibrational circular dichroism (VCD).
* Corresponding authors. Tel.: +1 831 459 2603; fax: +1 831 459 2935 (P.C.); tel.: +1 831 459 5884; fax: +1 831 459 2935 (T.R.H.); e-mail addresses: holman@chemistry.ucsc.edu; phil@chemistry.ucsc.edu
† Visiting from Quantum Protein Center, Department of Physics, Technical University of Denmark, DK-2800 Lyngby, Denmark.

0968-0896/$ - see front matter © 2005 Elsevier Ltd. All rights reserved.
doi:10.1016/j.bmc.2005.06.020

inhibitory,[7] antiplasmodial,[5] and cytotoxic activities.[22] In light of these promising findings, we believed that the search for novel derivatives of **1** would be rewarding. It could provide opportunities to explore new structural themes and further probe the pharmacological activities in this family of bioactive metabolites.

Herein, we report on the discovery of a unique branch in this family of sponge-derived curcuphenol metabolites based on ESIMS screening of extracts. The goal of the project was to engage in the structure elucidation, absolute configuration analysis, cytotoxicity, lipoxygenase inhibition, and active site modeling of the new compounds encountered. Further insights addressing the biogenic origin of the curcuphenol-derivatives are also addressed. Additionally, we highlight the first application of vibrational circular dichroism (VCD)[23] to the stereochemical analysis of marine natural products. Traditional UV–circular dichroism (CD) studies, as exemplified by numerous scholarly studies performed by Prof. Koji Nakanishi and colleagues,[24,25] have greatly enhanced the field of stereochemical analysis in organic chemistry. Our studies serve as an extension of these insightful efforts via the application of contemporary VCD analysis methodologies that should serve to compliment traditional UV–CD techniques.

2. Results and discussion

2.1. Summary of compounds studied

Sponges from the western Indo-Pacific region have continued to serve as a source of unique and bioactive secondary metabolites. Many of the specimens in our extensive collection have been subjected to preliminary bioactivity screening with a simple brine shrimp assay.[26] Partitioning of the total crude organic extract of *Didiscus aceratus* (Ridley and Dendy)[27] yielded a CH_2Cl_2 soluble fraction that exhibited potent toxicity against brine shrimp (100% lethality in ~20 min, 10 μg/mL). Bioassay-guided isolation of the active fraction provided (*S*)-(+)-curcuphenol (**1**) (Fig. 1) identified by its HRESIMS (*m/z* 219.1746 $[MH]^+$, calcd for $C_{15}H_{23}O$, 219.1749), NMR data, and optical rotation value.[6,7] Studies of the cancer cell cytotoxicity of compound **1** were performed as previously described.[28] These data revealed that **1** possessed moderate, but nonspecific toxicity against human bone marrow, leukemia, and colon solid tumor cell lines as observed earlier for similar curcuphenol analogs[22] and therefore was not pursued for subsequent in vivo evaluation.

Interestingly, further consideration of the planar structure of **1** revealed that it shared several key features with other marine biomolecules previously isolated by our laboratory that exhibited potent inhibition against human lipoxygenases.[29–32] These attributes included (i) a polar phenolic head group, (ii) a lipophilic tail, (iii) moderate c Log *P* value (4.9), and (iv) probable redox activity. In view of these features, compound **1** was tested and determined to be a potent, but nonselective inhibitor of human lipoxygenases (human 12-lipoxygenase (12-hLo): IC_{50} 2.9 ± 0.4 μM and human 15-lipoxygenase (15-hLo): IC_{50} 1.6 ± 0.3 μM).

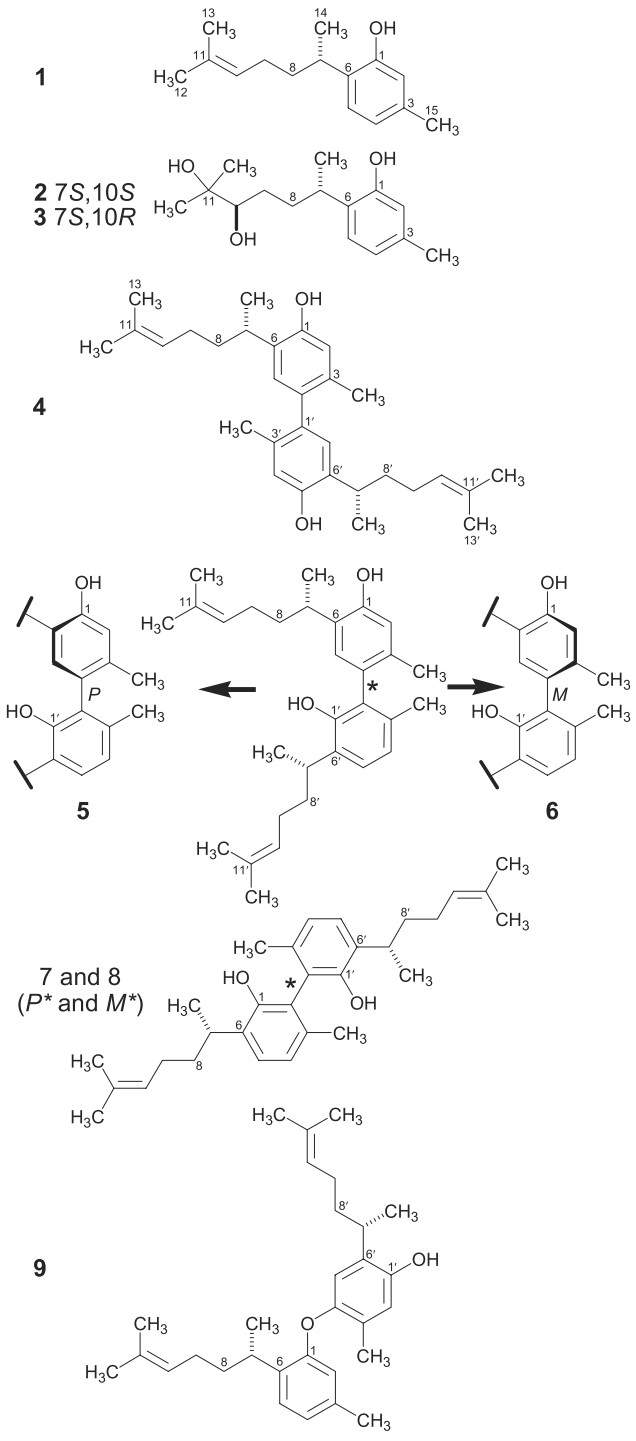

Figure 1. Structures of the bisabolene sesquiterpene (*S*)-(+)-curcuphenol (**1**) and derivatives (**2**–**9**) obtained from *Didicus aceratus* in this study.

The overwhelming presence of **1** in the *D. aceratus* extracts (>8% of total crude extract) precluded the direct bioassay-guided isolation of related analogs from the remaining fractions due to the masking effects of **1**. Another approach based on ESIMS analysis of the sponge extracts was utilized to systematically screen

for the presence of analogs of compound **1**. It was anticipated that these compounds would help compliment our growing library of marine-derived human lipoxygenase inhibitors and shed further light on key structure–activity relationships of these biomolecules. Consequently, two fractions were identified that exhibited *m/z* 253 $[MH]^+$ ($C_{15}H_{25}O_3$) and 435 $[MH]^+$ ($C_{30}H_{43}O_2$) representing dihydroxylated and dimeric curcuphenol species, respectively. Subsequent ESIMS-guided isolation led to the purification of a mixture of the known 10β-hydroxycurcudiol[5] (**2**) and new 10α-hydroxycurcudiol (**3**) as well as six curcuphenol dimers, dicurcuphenols A–E (**4**–**8**) and dicurcuphenol ether F (**9**) (Fig. 1).

2.2. Structure determination of compounds 2–9

Compounds **2** and **3**, obtained as a mixture, were not further separated because their characterization as 10-hydroxycurcudiol (*syn* 10,11-dihydroxycurcuphenol) diastereomers was straightforward. The HRESIMS (obsd *m/z* 253.1800; calcd for $C_{15}H_{25}O_3$, 253.1804) of the single HPLC peak containing **2** and **3** indicated that two OH groups have been added to the curcuphenol (**1**) skeleton. Further attempts on separating **2** and **3** by HPLC provided inadequate resolution of the metabolites; therefore, structure determination proceeded with the mixture. Inspection of the ^1H, ^{13}C, and DEPT NMR spectra of the mixture confirmed the presence of 10β-hydroxycurcudiol (**2**) that was previously reported as a microbial biotransformation product of **1**.[5] A second set of closely aligned peaks of equivalent intensity was also noted in the NMR spectra. Careful examination of these proton and carbon spins indicated that they were derived from the C-10 epimer of **2**, 10α-hydroxycurcudiol (**3**).

The remaining compounds, **4**–**9**, were isomeric dimers that each exhibited *m/z* 435 $[MH]^+$ by low-resolution MS. Their molecular formulas were subsequently established as $C_{30}H_{42}O_2$ by HRESIMS. Compared to curcuphenol (**1**), this represented nearly double the number of carbon ($2 \times 15C$), hydrogen ($2 \times 22H$–$2H$), and oxygen ($2 \times 2O$) atoms expected for two units of monomeric **1**. The loss of 2H atoms was determined to arise from the formation of a new covalent bond indicating that **4**–**9** were dimeric metabolites of **1**. An initial assessment of the ^1H NMR spectra of **4**–**9** confirmed that these metabolites exhibited analogous spectral features to **1** thereby establishing their common curcuphenol-derived skeleton. Most of the upfield ^1H NMR peaks appeared doubled in **4**–**9** compared to **1**; however, the downfield aromatic resonances of the dimers differed significantly both in the absence of key proton spins and/or divergent chemical shifts indicating that dimerization had occurred through the aryl portion of **1**. The structure elucidation of **4**–**9** was greatly supported via utilization of the comparative ^1H NMR spectra as illustrated in Figure 2. Further confirmation of these assignments was achieved by ^{13}C NMR and HMQC/HMBC experiments focusing on the downfield spectral region in order to discern the unique aryl linkages of these six dimers.

The benzenoid protons of dicurcuphenol A (**4**) appeared as singlets (δ 6.90, 6.87, 6.68, and 6.67) versus the doublets observed in the aromatic region for **1** (H-4 to H-5 coupling). This indicated that the two possible dimerization sites were either at the C-4 or C-5 positions of **1**. Thus, three possible dimers were envisioned with the aryl linkages being between positions C-4 to C-4′, C-5 to C-5′, C-4 to C-5′/C-4′ to C-5. All of the nonaromatic ring NMR signals of **4** could be correlated to resonances of **1** including C-7 to C-15. Subsequent detailed analysis of selected elements from 1D- and 2D-NMR data were required to distinguish among the three alternatives for the dimer skeleton.

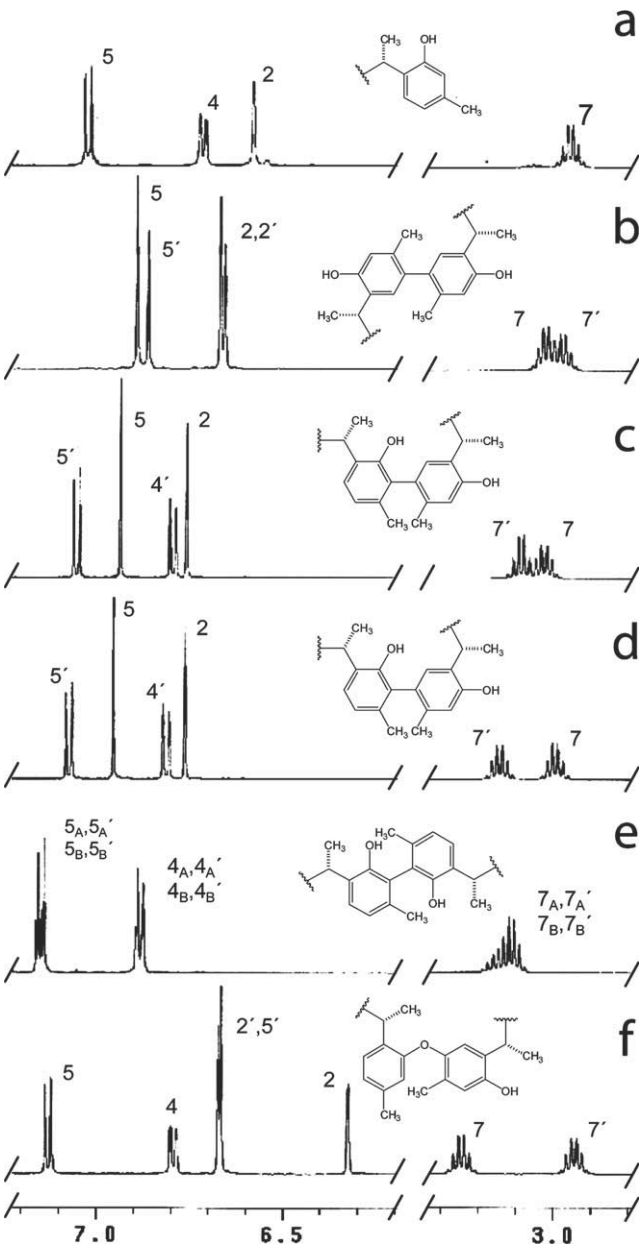

Figure 2. Comparative partial ^1H NMR spectra of compounds **1** (panel 'a'), **4** (panel 'b'), **5** (panel 'c'), **6** (panel 'd'), **7** and **8** (panel 'e'), and **9** (panel 'f').

The choice in favor of C-4 to C4′ dimerization in **4** was made as outlined below. The ^{13}C resonances assigned to C-4 and C-4′ (δ 134.8, two quaternary C's) were

significantly shifted downfield ($\Delta\delta \sim 12$) relative to C-4 of **1**, and protons H-5 and H-5′ (both singlets) in **4** were shifted upfield relative to that of the H-5 doublet in **1** as illustrated in Figures 2a and b, respectively. The most important $^{2,3}J_{H-C}$ data shown in Figure 3 consisted of distinct three-bond HMBC correlations observed between H-7/C-5, H-15/C-4, H-7′/C-5′, and H-15′/C-4′. Both of the alternate dimeric structures considered at the outset were ruled out because several of these HMBC correlations would span across four bonds. Further HMBC correlations were ambiguous due to the coincidental overlap of carbon resonances.

Once separated, it was clear that subtle structural features were responsible for the diastereomeric differences between dicurcuphenols B (**5**) and C (**6**). For example, the downfield resonances in the ^{1}H NMR spectra for **5** and **6** exhibited identical multiplet patterns with very similar chemical shifts as shown in Figures 2c and d, respectively. However, this pair exhibited unique optical rotatory properties with $[\alpha]_D^{25}$ +103.0 for **5** and $[\alpha]_D^{25}$ +2.87 for **6**. The downfield ^{1}H NMR data in Figure 2c and d revealed that **5** and **6** possessed biaryl linkages quite different from that of **4**. Two connectivity arrangements were possible for **5** and **6** based on the multiplet patterns observed for the aryl protons. For example in **5** this consisted of one set of *ortho*-coupled aromatic protons (δ 6.80 and 7.06, each 1H, d, J = 8.0 Hz, H-4′ and H-5′, respectively) and two singlets (δ 6.76 and 6.94, each 1H, H-2 and H-5, respectively). Similar NMR spectral data were observed for **6**. Between the two possibilities for dimerization, C-4 to C-2′ and C-5 to C-2′, only the former was consistent with three-bond HMBC correlations observed in both **5** and **6** between

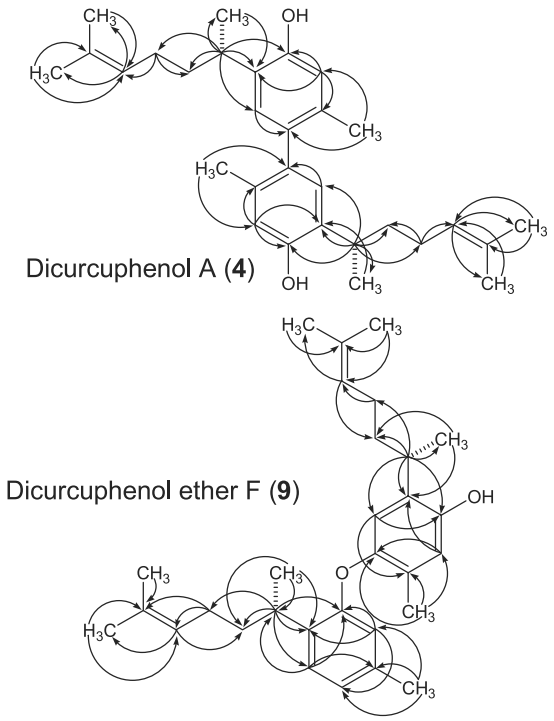

Figure 3. Significant HMBC correlations (→) observed for dicurcuphenol A (**4**) and dicurcuphenol ether F (**9**).

H-7/C-5 and H-2/C-4. The very subtle differences between **5** and **6** could be attributed to the existence of stable atropisomers arising from hindered rotation at the biaryl bond due to the *ortho* substituents consisting of one hydroxyl and two methyl groups.

An additional set of closely related diastereomers, dicurcuphenols D (**7**) and E (**8**), were co-eluted from C_{18} HPLC as an inseparable mixture. As compared with the downfield ^{1}H NMR spectra for **5** and **6** described above, the aryl resonances for **7** and **8** in Figure 2e were comprised of two sets of overlapping doublets. Furthermore, **7** and **8** were distinguished by the lack of singlet aromatic resonances characteristic of H-2 in **1** (Fig. 1a). This unequivocally indicated the presence of a biaryl bond connectivity from C-2 to C-2′ in **7** and **8**. In analogy to the situation above, it was further concluded that each compound could exist as atropisomers, as there were now four *ortho* substituents present in the vicinity of the biaryl bond. Finally, the resonances for H-7and H-7′ (Fig. 2e), as well as other upfield signals, provided insight as to the relative ratio of **7** to **8** in the mixture (~1:2.3, major isomer not defined here).

It was immediately evident that the final dimer isolated, dicurcuphenol ether F (**9**) was different than **4**–**8**. Dimer **9** exhibited five aromatic protons (Fig. 2f), whereas all the former five compounds had four such protons. The aryl resonances in **9** consisted of two *ortho*-coupled protons, H-4 and H-5 (each d, J = 7.5 Hz) in addition to three singlet resonances. These data indicated the presence of tri- and tetra-substituted aryl rings connected in two possible ways: C-1 to C-4′, or C-1 to C-5′. The singlet at δ 6.32 (H-2) exhibited HMBC correlations to C-4, which with the above information, was key in defining the tri-substituted ring. Similarly, the tetra-substituted ring was delineated by the correlations between H-7′/C-5′, H-7′/C-1′, and H-15′/C-4′. The other two nearly overlapping singlets ($\delta \sim 6.67$) were assigned by HMBC as H-2′ and H-5′. The three sets of data supporting the conclusion that **9** possessed the C-1 to C-4′ linkage were as follows. The similar shifts of **1** H-2 (δ 6.62) versus **9** H-2′ (δ 6.67) were consistent with an additional oxygen added to the *meta* and not *ortho* position in contrast to the large *ortho* effect differences in **1** H-5 (δ 7.05) versus **9** H-5′ (δ 6.67). Also, the nearly identical shifts of C-2′ (δ 118.0) and C-5′ (δ 118.8) meant that these carbons were *ortho* and *para* relative to both oxygen substituents. Finally, the three-bond HMBC correlations observed between H-5′/C-7′, H-15′/C-4′, and H-7′/C-1′ fixed H-5′ as being between C-6′ and C-4′.

2.3. Absolute configuration analysis and laccase-mediated formation of dicurcuphenols 4–9

With the planar structures of the dicurcuphenols established, the next challenge was to elucidate their absolute configurations. A key benchmark was the 7*S* absolute stereochemistry of (*S*)-(+)-curcuphenol (**1**), previously determined via total synthesis,[33–35] and the 7*R* stereoisomer, (*R*)-(−)-curcuphenol, also established by synthesis.[34,36,37] From a biosynthetic perspective, it seemed reasonable to assume that **4**–**9** also possessed

7*S*, 7′*S* stereochemistry based on the co-occurrence of **1** with **4**–**9**.

As a logical extension of this observation, it can be hypothesized that the radical-mediated coupling of **1** would lead to the formation of dimers **4**–**9**. The steps in this process beginning with loss of H**.** followed by reassembly of the various possible radical species are shown in Figure 4. Numerous organisms, particularly fungi, are known to possess phenol oxidase-type enzymes that are capable of catalyzing the polymerization of phenolic substrates under both natural and laboratory conditions.[38,39] The laccases, which are blue-copper oxidases, constitute one prominent class of phenol oxidases that have received widespread attention for their industrial applications.[40] Polyphenol oxidase (tyrosinase)[38] and horseradish peroxidase[41] represent other notable enzymes that carry out similar transformations.

To test the above hypothesis, an experiment was undertaken with the goal of using **1** as a substrate for generating dimers. Accordingly, laccase, polyphenol oxidase, and horseradish peroxidase were surveyed in a set of preliminary experiments. The catalysis products were assessed by ESIMS analysis with success achieved in 13 out of 78 different experimental conditions employing laccase while the other enzymes proved ineffective. Summarized in Table 1 (and Table S1, Supplementary data) are the conditions producing the desired $[MH]^+$ peak at *m*/*z* 435 ($C_{30}H_{43}O_2$). Not shown here are data demonstrating that similar results were obtained using a polyphenol oxidase-mimetic periodate oxidation system[42] and Fenton peroxidation.[43]

Scale-up biocatalysis accompanied by isolation of the target *m*/*z* 435 products afforded the series of compounds illustrated in Figure 4. All six dimers, **4**–**9**, were formed in varying relative amounts. Also tabulated are the relative percentages of these compounds isolated in this study from the sponge source. Each enzyme reaction product was identified by comparisons of their ^{1}H NMR and optical rotation data to that obtained for the sponge-derived compounds. We were amazed to note that: (i) all of the sponge-derived dicurcuphenols **4**–**9** were also produced by the laccase transformation of **1**, (ii) no other dimers of **1** were detected, and (iii) the relative yield of the dimers obtained from laccase incubation were, with the exception of that for **4**, parallel to that from the sponge source (Fig. 4). These data intimate that **4**–**9** may also be produced in the sponge by a radical-mediated coupling mechanism. Another important outcome of the results of Table in Figure 4 is the implications for bolstering the 7*S* stereochemical assignment proposed herein for the dicurcuphenols. The biocatalysis results clearly show that the 7*S* stereochemistry of **1** is maintained among dimeric products **4**–**9**.

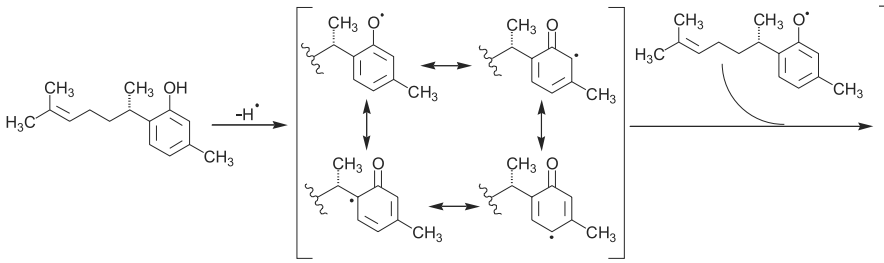

compound	sponge		laccase	
	total yield (%)	relative yield	total yield (%)	relative yield
dicurcuphenol A (4)	2.2· 10^{-4}	3.3	2.9	14.2
dicurcuphenol B (5)	5.6· 10^{-4}	8.7	1.4	6.8
dicurcuphenol C (6)	5.6· 10^{-4}	8.7	1.1	5.2
dicurcuphenol D (7)	1.5· 10^{-4}	2.3	0.5	2.2
dicurcuphenol E (8)	6.5· 10^{-5}	1	0.2	1
dicurcuphenol ether F (9)	4.3· 10^{-4}	6.7	0.7	3.2

Figure 4. Yields and proposed mechanism for the formation of dicurcuphenols A–F (**4**–**9**) from the sponge *Didicus aceratus* and laccase-mediated biocatalysis of (*S*)-(+)-curcuphenol (**1**).

Table 1. Summary of mediators, buffers, and co-solvents tested in the laccase-mediated biocatalysis of curcuphenol (**1**) to dimers (ESIMS *m*/*z* 435).

Mediators	Buffers	Co-solvents
Benzoic acid*	Citrate (0.1 M, pH 5.0)*	Acetone
Catechol	Potassium phosphate (0.1 M, pH 7.0)	Acetonitrile*
Hydroquinone*		Butanol
4-Methoxybenzoic acid*		Benzene
4-Methoxybenzoic acid polymer*		Dimethylforamide*
Phloroglucinol		Dioxane*
Tempo		Ether
		Ethanol*
		Isopropanol*
		Methanol*
		Toluene
		Triton X*

Items marked with an asterisk (*) were found to promote the transformation of compound **1**. See Table S1 in Supplementary data for complete experimental details of 78 combinations tested.

Somewhat surprising is that despite numerous repeated reisolations of compound **1** from sponges, it has not been previously reported to be accompanied by dimerized sesquiterpenes. Furthermore, a comprehensive study[5] on the microbial biotransformation products of curcuphenol and curcudiol resulted in the formation of a large number of functionalized analogs but no dimers were observed. Surprisingly, these experiments employed several fungi that are likely to be competent for the production of laccase or other phenol oxidases. By ESIMS, we detected dimers of **1** in the sponge crude extracts and also observed the long-term bench-top stability of compound **1** in a variety of solvents (MeOH, CH_2Cl_2, $CHCl_3$, and DMF) suggesting that **4**–**9** are not artifacts of our isolation procedures.

It is interesting to note that a similar oxidative coupling process has been proposed in the formation of the acylphenol dimers, giganteones A and B from the fruits of the Malaysian plant *Myristica gigantea* (Myristicaceae).[44] Further biosynthetic parallels can also be drawn to the formation of the biphenyl lichen metabolite, contortin, from *Psoroma contortum*[45] and cuparane-type sesquiterpene dimers, mastigophorenes, from the liverwort *Mastigophora diclados*.[46] The formation of complex polymeric tyrosine metabolites such as bastadins from *Ianthella* spp. sponges[47–49] and pulcherosine from sea urchin embryos[50] represent pertinent parallels to the metabolites observed in this study.

Up to this point, the absolute configuration of the biaryl axial chirality of atropisomers **5** and **6**, as well as **7** and **8**, still remained undefined. The former two compounds, and their acetyl and benzyl ester derivatives were oils that precluded X-ray analysis, while the latter two resisted all of our attempts at chromatographic separation. The chiroptical data we obtained on the purified isomers could not be further evaluated because of a lack of appropriate reference compounds or applicable sets of empirical rules. Therefore, a sensitive and reference-independent spectroscopic technique was sought that could fulfill these required needs. Vibrational circular dichroism (VCD)[51] has developed in recent years as a powerful, but underutilized method and it seemed relevant to address the difficult assignment of the axial chirality for **5** and **6**. In fact, important proof-of-concept illustrations of the power of this technique to solve our problem reside in the absolute configuration determination by VCD of the cotton atropisomers (+)- and (−)-gossypol as *P* and *M*, respectively,[52] and in a VCD study of an unexpected atropisomerically stable 1,1-biphenyl.[53]

The superimposed IR and VCD spectra of atropisomers **5** and **6** shown in Figure 5 provides the key data to be applied in the stereochemical determination. As expected, the IR spectra for both atropisomers, are virtually identical except for the negligible contributions of minor impurities at ~1700 and 1025 cm^{-1}. In contrast, their VCD spectra contains important diagnostic bands between 1600 and 1425 cm^{-1}, which are of opposite inflection, arising from the axial chirality differences of this pair. Some of the remaining VCD bands are nearly

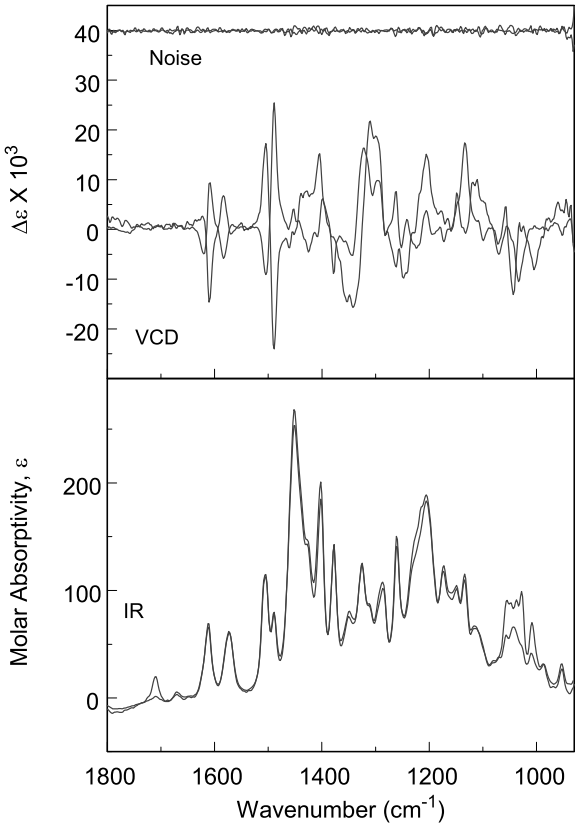

Figure 5. IR (lower traces) and VCD (upper traces, with VCD noise level shown above) spectra of **5** (red) and **6** (blue), in $CDCl_3$ solution. The IR spectra look quite similar with the exception of minor discrepancies around 1000–1050 cm^{-1} and 1700 cm^{-1} arising from impurities. Spectra are solvent subtracted.

superimposible due to the identical chiral alkyl side chains present in both compounds. Consistent with this trend are the appearance of the IR and VCD spectra for **1** shown in Figure 6. As expected, the IR spectra of **1**, **5**, and **6** are similar while the VCD spectra of **1** is rather featureless between 1600 and 1425 cm^{-1}. This latter point strengthens observation that this region contained peaks diagnostic of the *P*/*M* axial chirality. The region between 1400 and 1000 cm^{-1} includes features arising from both the *P*/*M* and 7*S* chiralities. The strong positive VCD intensity near 1300 cm^{-1} in **1**, **5**, and **6** is consistent with 7*S* chirality for this trio of compounds.

The next step in completing the stereochemical analysis involved generating theoretical VCD spectra expected for the two configurational possibilities. However, the flexible nature of the biaryl alkyl side chains presented a complication because a large set of nearly isoenergetic solution phase conformations would need to be considered. As a simplification, the truncated atropisomer (*P*)-**10** (Fig. 7) was selected for theoretical analysis since it eliminates conformational flexibility, thus permitting the singular visualization of VCD effects arising from axial chirality. Calculations of VCD intensity at the DFT level were needed for the (*P*)-atropisomer only since the opposite (*M*)-**10** structure must exhibit a mirror image VCD spectrum of (*P*)-**10**.

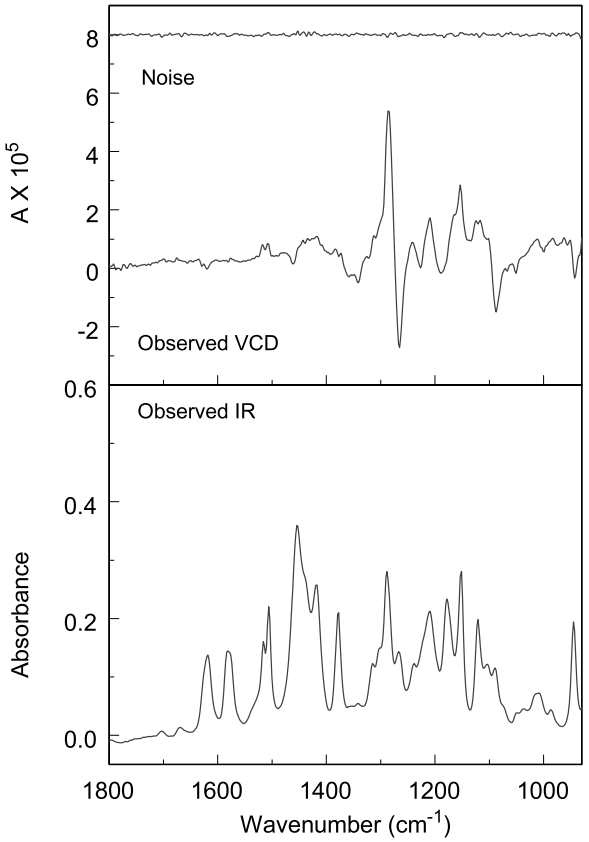

Figure 6. IR (lower trace) and VCD (upper trace, with the VCD noise level shown above in red) spectra of monomer **1**, in $CDCl_3$ solution. Both spectra are solvent subtracted.

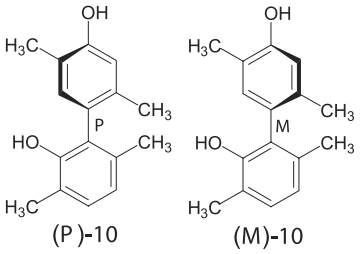

Figure 7. Model phenol atropisomers (*P*)-**10** and (*M*)-**10** used for theoretical VCD calculations.

An additional step was needed in order to directly apply the calculated VCD spectra of model compound (*P*)-**10**, shown as the lower trace in Figure 8, to the stereochemical determination under consideration. Reanalysis of the VCD spectra for atropisomers **5** and **6** was carried out to isolate the spectral effects arising from axial chirality. This consisted of subtraction of the VCD spectrum of **6** from that of **5** and dividing by 2, and the resultant difference spectrum is shown in the upper trace of Figure 8. Focusing on the VCD spectral region between 1600 and 1400 cm^{-1} in Figure 8, a comparison of the calculated spectrum for (*P*)-**10** to the difference spectrum [$(VCD_5 - VCD_6)/2 = VCD_{difference}$] revealed striking similarities among their prominent features. The close correlation between these spectra is quite outstanding in view of the simplicity of the model system

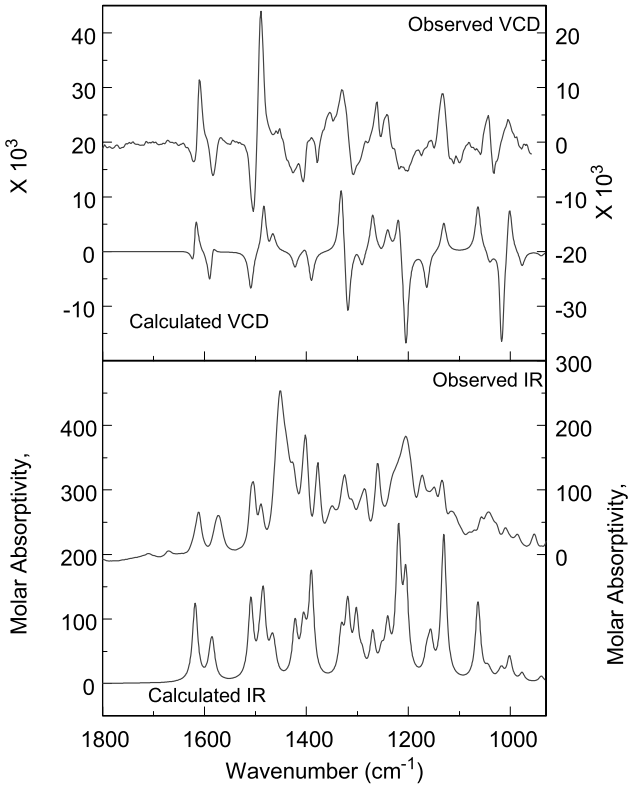

Figure 8. Observed (red, right axes) IR spectrum of **5** and difference VCD [(**5**–**6**)/2] versus calculated (blue, left axes) spectra for the truncated model compound (*P*)-**10**. The observed spectra have been converted to molar absorptivities for direct comparison with the calculated spectrum.

employed for this purpose. Therefore, it was unambiguously determined that **5** and **6** exhibit *P* and *M* axial chirality, respectively.

2.4. Biological activity and modeling studies of curcuphenol metabolites

Studies on the cytotoxic effects of **1**, using our standard disk-diffusion assay,[28] revealed that it possessed potent, but nonspecific activity against several murine and human cell lines including colon and breast. This was in accordance with previous bioactivity observations for analogs of **1**.[22] Compounds **2**–**9** were subsequently examined in this screen against the same cell lines, but were found to be completely inactive. In addition, all compounds were also examined in a bench-top brine shrimp assay[26] similar to that performed for **1**. Only **1** displayed potent activity, killing all brine shrimp within ~20 min (LC_{50} = 0.63 ± 0.04 μg/mL), while **2**–**9** exhibited no lethality even after 24 h at 100 μg/mL.

Curcuphenol (**1**) was examined for its lipoxygenase inhibitory activity against both human 12-lipoxygenase (12-hLO) and 15-lipoxygenase (15-hLO). These enzymes represent important therapeutic targets for the development of novel pharmaceuticals for the treatment of cancer (12-hLO) and atherosclerosis (15-hLO).[54] Compound **1** exhibited potent, but nonselective inhibitory activity against both 12-hLO (IC_{50} 2.9 ± 0.4 μM)

and 15-hLO (IC_{50} 1.6 ± 0.3 μM). All of the other six compounds isolated herein were tested against both lipoxygenases, but only dimer **4** tested positive in this assay as it possessed modest and equipotent activity against both 12-hLO (IC_{50} 11.6 ± 1.8 μM) and 15-hLO (IC_{50} 11.4 ± 2.5 μM). Not clear at this juncture are the structural features responsible for the inactivity of compounds **2**, **3**, and **5**–**9** as compared to **1** and **4**.

In further examining the lipoxygenase activity data and structures for **1** and **4**, we suspected that both functioned as redox-type inhibitors. In our past experience, the structural signature for such activity was the presence of a phenolic head group.[31] Using a fluorescence-based assay, it was determined that **4** did not reduce the active site ferric iron species while **1** exhibited a more modest reducing effect over a relatively extended timeframe. This suggested that **1** functioned through both competitive- and redox-based inhibition mechanisms while **4** was not redox active.

These concepts were further explored by means of molecular modeling analysis of the active site binding of **1** and **4**. A homology model of 15-hLO from rabbit 15-lipoxygenase (15-rLO) has recently been developed by which the docking behavior of inhibitors can be visualized.[55] This model system has been effectively employed for the in silico selection and experimental validation of potent (low mM) inhibitors of 15-hLO. Shown in Figure 9 are docking results for **1** calculated with GLIDE in the 15-hLO active site. As seen in the upper panel (Fig. 9a), the hydroxyl moiety was predicted to adopt a preferred orientation >4.0 Å away from the active site iron atom and therefore would not be able to reduce the iron atom. In this model, hydrogen bonding was observed to occur between the OH group and active site residues Glu355 and Gln546. Since the active site iron can change the pK_a of nearby ligands, deprotonated-**1** was also docked in the same manner using GLIDE (Fig. 9b). These conditions showed that the hydroxide anion resided within 2.1 Å of the iron atom and should be capable of redox inactivation. These two supporting models help to explain the 15-hLO inhibitory properties and weak redox activity observed for **1**. Further modeling studies (data not shown) performed with the weak, nonreductive inhibitor **4** suggested that this compound is too sterically restrained within the active site to function in a redox fashion.

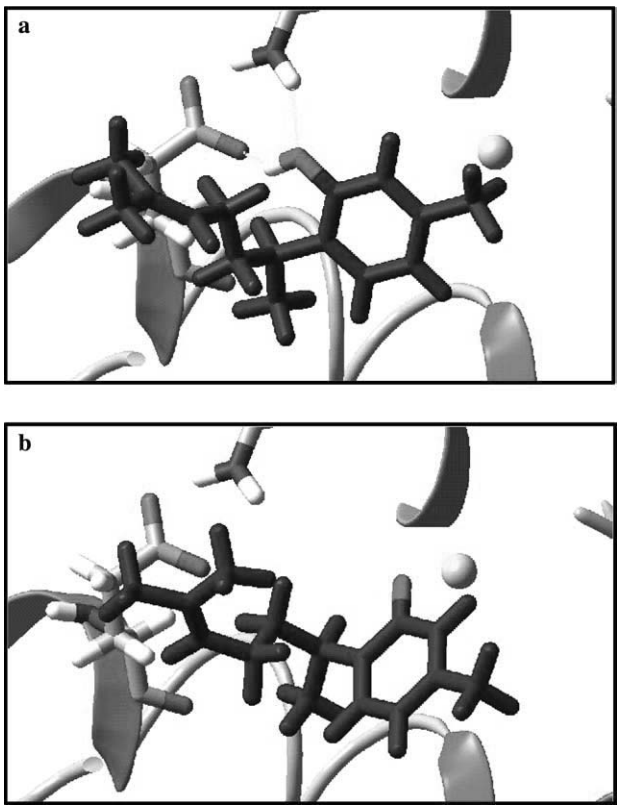

Figure 9. Docking results for **1** (panel 'a') and deprotonated-**1** (panel 'b') in the active site of 15-hLO. Compound **1** is shown in blue with the active site iron identified as a yellow sphere.

3. Conclusions

Bisabolene-type sesquiterpenes constitute a diverse assemblage of terrestrial- and marine-derived metabolites. These compounds have demonstrated promising biological effects in a variety of assay systems, but none appear to be under current consideration for preclinical development. In an effort to further probe the structural and biological relationships of these metabolites, ESIMS-guided isolation was used to obtain several new dimeric curcuphenol (**1**) derivatives that were examined for their cell cytotoxicity and lipoxygenase inhibitory activities. Dimerization of **1**, both in the sponge and through laccase biocatalysis, resulted in the general loss of activity across all assay systems examined in this study. Molecular modeling studies of **1** and **4** with 15-hLO provided intriguing evidence for the existence of multiple active site conformations of this compound resulting in a mixed inhibition profile.

The biogenic origin of dimers **4**–**9** is likely due to the oxidative coupling of **1** which can take place at more than one site. Atropisomeric dimers **5** and **6** provided an opportunity to explore the application of VCD spectroscopy in the absolute configuration determination of marine-derived metabolites. This study offered compelling evidence that VCD is a powerful technique that should find broad application in modern structure determination studies. We are currently engaged in a wider survey of bisabolene structural variants including higher molecular weight congeners. This should lead to further opportunities to discover novel structural themes and biological activities within this chemical family. The application of methodologies such as ESIMS in the structure discovery process will be crucial in making this assertion a reality.

4. Experimental

4.1. General methods

All 1D- and 2D-NMR spectra were recorded in $CDCl_3$ (Cambridge Isotope Laboratories, Inc. Andover, MA)

on Varian UNITY INOVA 500 instruments. Multiplicities of carbon resonances were confirmed by DEPT experiments. Low- and high-resolution ESIMS data were obtained on an Applied Biosystems Mariner Biospectrometry Workstation. Optical rotations were determined on a Jasco DIP 370 polarimeter using a 130 μL microcuvett. VCD measurements were performed using a Chiralir FT-VCD/IR spectrometer (BioTools, Wauconda, IL) with a liquid nitrogen-cooled MCT detector, which has been modified with two photoelastic modulators optimized at 1400 cm^{-1}.[56]

Chromatography materials and supplies were used as previously described.[31] Buffers and other chemicals for biocatalysis studies were obtained from Sigma-Aldrich and used without further purification. Laccase was a gift from L. T. Holst Jr. (Dexter Chemical L.L.C.) and used without further purification. Horseradish peroxidase and polyphenol oxidase were purchased from Research Organics and Worthington, respectively.

4.2. Animal material

The sponge (UCSC collection number 00372) was collected by SCUBA from the region of New Britton, Papua New Guinea in 2000 and examined by R. W. N. Van Soest (Zoological Museum, University of Amsterdam, Amsterdam, The Netherlands) for taxonomic identification. The sponge (~2.3 kg wet weight) exhibited a massive, lobate morphology with a light pink to tan exterior and light yellow interior. The surface morphology of the organism was characterized as composed of convoluted grooves with a membraneous surface. The interior was fibrous featuring spicules in a chaotic composition. These features support that UCSC 00372 is a relatively rare specimen of *Didiscus aceratus* (Ridley and Dendy) (Halichondrida, Desmoxyidae)[27] (see Supplementary data for underwater photo of the sponge). Immediately following collection, the sponge was soaked in EtOH/sea H_2O (1:1) for 24 h after which the liquid was decanted and the sponge transported to UCSC. Upon arrival, the sponge was immediately immersed in MeOH and placed in cold storage at 4 °C until extracted. Voucher specimens have been retained at UCSC and the Amsterdam Zoological Museum (ZMAPOR 17712) for reference.

4.3. Extraction and isolation

The sponge (UCSC 00372, 2.3 kg wet weight) was extracted with MeOH (1 L, 3×) and MeOH/CH_2Cl_2 (1 L, 3×). These extracts were combined yielding 29.5 g of brown oily residue. The total organic extract was dissolved in 800 mL MeOH/H_2O (9:1) and partitioned against hexane (800 mL, 3×). The aqueous MeOH extract was further diluted with H_2O (final 1:1, vol:vol) and partitioned against CH_2Cl_2 (800 mL, 3×). The CH_2Cl_2 extract (10.1 g) exhibited brine shrimp toxicity (100% lethality at 10 μg/mL) and as a result was chromatographed over silica gel (gradient 100% hexane to 100% acetone) providing fractions S1 (31 mg), S2 (7.83 g) S3 (1.22 g), S4 (370 mg), and S5 (331 mg). Brine shrimp toxic fraction S2 (100% lethality at 10 μg/mL) was purified by C_{18} LPLC (50–100% acetonitrile) yielding fractions B1 (1.73 g), B2 (5.02 g), B3 (105 mg), B4 (109 mg), and B5 (59 mg). All the biological activity was associated with fraction B2 (100% lethality at 10 μg/mL) which was subsequently analyzed by MS and HPLC and found to contain a single major (~50% by mass) component that upon further HPLC purification (semipreperative C_{18} HPLC, 80–100% acetonitrile) was identified as (*S*)-(+)-curcuphenol (**1**) ($[\alpha]_D^{25}$ +30.7, *c* 4.3, $CHCl_3$) by comparison to literature data.[6,7] Compound **1** was responsible for all of the observed brine shrimp toxicity (LC_{50} = 0.63 ± 0.04 μg/mL).

Based on a different bioassay lead for compound **1** (hLO inhibition, see Section 2), all other fractions were examined by MS analysis to determine the presence of potential related chemical species for further biological evaluation. Fraction B1 exhibited an ion of *m*/*z* 253 $[MH]^+$ suggesting the presence of a dihydroxylated derivative. Further purification of B1 by C_{18} preparative HPLC (40–60% acetonitrile) and semipreparative HPLC (isocratic 30% acetonitrile) yielded a 40 mg 1:1 mixture of 10β-hydroxycurcudiol (**2**) and its C-10 epimer, 10α-hydroxycurcudiol (**3**).

Further evaluation of fraction B2 provided evidence for the presence of several putative dimeric derivatives (*m*/*z* 435 $[MH]^+$) that were targeted for purification. Accordingly, fraction B2 was subjected to C_{18} preparative HPLC affording fractions P1 (86 mg), P2 (58 mg), P3 (2.89 g), P4 (18 mg), P5 (60 mg), P6 (31 mg), and P7 (18 mg). Fraction P3 was found to comprise mainly of compound **1** (purity >95%). Fraction P5 was applied to a PTLC plate and developed with toluene/ethyl acetate (95:5). A band (27 mg) possessing a molecular weight of *m*/*z* 435 was further purified by C_{18} semipreparative HPLC (isocratic 85% acetonitrile) yielding dicurcuphenol A (**4**). Similarly, fraction P6 was applied to PTLC (100% toluene) providing fractions T1 (17 mg) and T2 (15 mg) each possessing *m*/*z* 435. Both fractions T1 and T2 were purified by C_{18} semipreparative HPLC (isocratic 90% acetonitrile) affording 13 mg each of dicurcuphenols B (**5**) and C (**6**), respectively.

Fraction P8 was chromatographed by C_{18} semipreparative HPLC (isocratic 90% acetonitrile) yielding H1 (6 mg) and H2 (11 mg). Fraction H1 was further purified by C_{18} semipreparative HPLC (isocratic 90% acetonitrile) affording 5 mg of a 1:2.3 mixture of dicurcuphenols D (**7**) and E (**8**), respectively. Fraction H2 was also purified by C_{18} semipreparative HPLC (isocratic 90% acetonitrile) yielding 10 mg of dicurcuphenol ether F (**9**).

4.3.1. 10α-Hydroxycurcudiol (3). Clear oil; ^1H NMR ($CDCl_3$, 500 MHz) δ 7.04 (1H, d, J = 8.0 Hz, H-5), 6.73 (1H, d, J = 8.0 Hz, H-4), 6.67 (1H, s, H-2), 3.53 (1H, br d, J = 9.5 Hz, H-10), 3.23 (1H, sextet, J = 7.0 Hz, H-7), 3.26 (3H, s, H-15), 1.70, (2H, m, H-8 and/or H-9), 1.46 (1H, m, H-8 and/or H-9), 1.24 (1H, m, H-8 and/or H-9), 1.24 (3H, d, J = 6.5 Hz, H-14), 1.18 and 1.11 (each 3H, s, H-12 and H-13); ^{13}C NMR ($CDCl_3$, 125 MHz) δ 153.3 (C-1), 136.6 (C-3), 130.1 (C-6), 126.4 (C-5), 121.7 (C-4), 117.1 (C-2), 79.6 (C-

10), 73.7 (C-11), 36.5 (C-8), 30.2 (C-7), 28.0 (C-9), 26.7 (C-12), 22.7 (C-13), 21.0 (C-14 and C-15); HRESIMS *m/z* 253.1800 $[MH]^+$ (calcd for $C_{15}H_{25}O_3$, 253.1804).

4.3.2. Dicurcuphenol A (4). Clear oil; $[\alpha]_D^{25}$ +61.5 (*c* 4.7, $CHCl_3$); ^1H NMR ($CDCl_3$, 500 MHz) δ 6.90 (1H, s, H-5), 6.87 (1H, s, H-5′), 6.68 and 6.67 (each 1H, s, H-2 and H-2′), 5.13 (2H, t, J = 7.0 Hz, H-10 and H-10′), 4.70 (2H, br s, OH), 3.03 (1H, sextet, J = 7.0 Hz, H-7), 3.00 (1H, sextet, J = 7.0 Hz, H-7′), 1.97 (6H, s, H-15 and H-15′), 1.94 (4H, m, H-9 and H-9′), 1.68 and 1.67 (each 3H, s, H-12 and H-12′), 1.67 (2H, m, H-8_a and H-$8'_a$), 1.59 (2H, m, H-8_b and H-$8'_b$), 1.56 and 1.51 (each 3H, s, H-13 and H-13′), 1.23 (6H, d, J = 7.0 Hz, H-14 and H-14′); ^{13}C NMR ($CDCl_3$, 125 MHz) δ 151.9 and 151.8 (C-1 and C-1′), 134.8 (C-4 and C-4′), 134.3 (C-3, C-3′), 132.1 and 132.0 (C-11 and C-11′), 130.1 (C-6′), 130.0 (C-6), 128.8 (C-5′), 128.5 (C-5), 124.7 (C-10 and C-10′), 116.6 (C-2 and C-2′), 37.4 and 37.3 (C-8 and C-8′), 31.8 (C-7′), 31.3 (C-7), 26.3 and 26.1 (C-9′, C-15, and C-15′), 25.8 (C-9, C-12, and C-12′), 21.4 (C-14′), 21.1 (C-14), 17.8 (C-13 and C-13′); HRESIMS *m/z* 435.3262 $[MH]^+$ (calcd for $C_{30}H_{43}O_2$, 435.3263).

4.3.3. Dicurcuphenol B (5). Clear oil; $[\alpha]_D^{25}$ +103.0 (*c* 1.0, $CHCl_3$); ^1H NMR ($CDCl_3$, 500 MHz) δ 7.06 (1H, d, J = 8.0 Hz, H-5′), 6.94 (1H, s, H-5), 6.80 (1H, d, J = 8.0 Hz, H-4′), 6.76 (1H, s, H-2), 5.15 (1H, t, J = 7.0 Hz, H-10′), 5.11 (1H, t, J = 7.0 Hz, H-10), 4.80 and 4.67 (each 1H, br s, OH), 3.09 (1H, sextet, J = 7.0 Hz, H-7′), 3.03 (1H, sextet, J = 7.0 Hz, H-7), 1.96 (3H, s, H-15′), 1.93 (3H, s, H-15), 1.93 (4H, m, H-9 and H-9′), 1.76 (2H, m, H-8_a and H-$8'_a$), 1.67 (6H, s, H-12 and H-12′), 1.65–1.58 (2H, m, H-8_b and H-$8'_b$), 1.56 and 1.52 (each 3H, s, H-13 and H-13′), 1.24 (3H, d, J = 7.0 Hz, H-14′), 1.22 (3H, d, J = 7.0 Hz, H-14′); ^{13}C NMR ($CDCl_3$, 125 MHz) δ 153.2 (C-1), 150.5 (C-1′), 136.5 (C-3), 134.6 (C-3′), 132.2 and 131.3 (C-11 and C-11′), 131.6 (C-6), 130.5 (C-6′), 129.5 (C-5), 127.1 (C-2′), 126.9 (C-4), 126.0 (C-5′), 125.0 (C-10′), 124.5 (C-10), 121.3 (C-4′), 117.7 (C-2), 37.2 (C-8), 36.9 (C-8′), 32.7 (C-7′), 31.3 (C-7), 26.5 (C-9′), 26.0 (C-9), 25.8 (C-12 and C-12′), 21.4 (C-14), 21.0 (C-14′), 19.9 (C-15′), 19.1 (C-15), 17.8 (C-13 and C-13′); HRESIMS *m/z* 435.3261 $[MH]^+$ (calcd for $C_{30}H_{43}O_2$, 435.3263).

4.3.4. Dicurcuphenol C (6). Clear oil; $[\alpha]_D^{25}$ +2.87 (*c* 1.6, $CHCl_3$); ^1H NMR ($CDCl_3$, 500 MHz) δ 7.08 (1H, d, J = 8.0 Hz, H-5′), 6.96 (1H, s, H-5), 6.82 (1H, d, J = 8.0 Hz, H-4′), 6.77 (1H, s, H-2), 5.13 and 5.12 (each 1H, t, J = 7.0 Hz, H-10 and H-10′), 4.85 and 4.65 (each 2H, br s, OH), 3.14 (1H, sextet, J = 7.0 Hz, H-7′), 3.00 (1H, sextet, J = 7.0 Hz, H-7), 1.96 (3H, s, H-15), 1.94 (4H, m, H-9 and H-9′), 1.93 (3H, s, H-15′), 1.68 and 1.66 (each 3H, s, H-12 and H-12′), 1.68 (2H, m, H-8_a and H-$8'_a$), 1.56 (2H, m, H-8_b and H-$8'_b$), 1.54 and 1.53 (each 3H, s, H-13 and H-13′), 1.26 (3H, d, J = 7.0 Hz, H-14′), 1.24 (3H, d, J = 7.0 Hz, H-14); ^{13}C NMR ($CDCl_3$, 125 MHz) δ 153.2 (C-1), 150.5 (C-1′), 136.6 (C-3), 134.6 (C-3′), 132.2 and 131.3 (C-11 and C-11′), 131.7 (C-6), 130.5 (C-6′), 129.6 (C-5), 126.9 (C-4 and C-2′), 125.7 (C-5′), 125.0 (C-10′), 124.5 (C-10), 121.4 (C-4′), 117.8 (C-2), 37.7 (C-8′), 37.3 (C-8), 31.9 (C-7′), 31.7 (C-7), 26.3 (C-9′), 26.2 (C-9), 25.8 (C-12 and C-12′), 21.1 (C-14), 21.0 (C-14′), 19.9 (C-15′), 19.0 (C-15), 17.8 and 17.7 (C-13 and C-13′); HRESIMS *m/z* 435.3262 $[MH]^+$ (calcd for $C_{30}H_{43}O_2$, 435.3263).

4.3.5. Mixture of dicurcuphenols D and E (7 and 8). Clear oil; $[\alpha]_D^{25}$ −10.0 (*c* 0.3, $CHCl_3$); ^1H NMR ($CDCl_3$, 500 MHz) δ 7.16 (d, J = 7.5 Hz, H-5_E and H-$5'_E$), 7.15 (d, J = 7.5 Hz, H-5_D and H-$5'_D$), 6.89 (d, J = 7.5 Hz, H-4_E and H-$4'_E$), 6.88 (d, J = 7.5 Hz, H-4_D, H-$4'_D$), 5.13 (m, H-10_D, H-$10'_D$, H-10_E and H-$10'_E$), 4.75 and 4.74 (br s, OH), 3.13 (t, J = 7.0 Hz, H-7_E and H-$7'_E$), 3.12 (t, J = 7.0 Hz, H-7_D and H-$7'_D$), 1.954 (s, H-15_D and H-$15'_D$), 1.946 (s, H-15_E and H-$15'_E$), 2.02–1.98 (m, H-9_D, H-$9'_D$, H-9_E and H-$9'_E$), 1.76–1.53 (m, H-8_D, H-$8'_D$, H-8_E and H-$8'_E$), 1.67 (s, H-12_D, H-$12'_D$, H-12_E and H-$12'_E$), 1.54 (s, H-13_D and H-$13'_D$), 1.53 (s, H-13_E and H-$13'_E$), 1.243 (d, J = 6.5 Hz, H-14_E and H-$14'_E$), 1.240 (d, J = 6.5 Hz, H-14_D and H-$14'_D$); ^{13}C NMR ($CDCl_3$, 125 MHz) δ 151.4 (C-1_D, C-$1'_D$, C-1_E, and C-$1'_E$), 135.7 (C-3_D, C-$3'_D$, C-3_E, and C-$3'_E$), 131.4 (C-6_D, C-$6'_D$, C-6_E, C-$6'_E$, C-11_D, C-$11'_D$, C-11_E, and C-$11'_E$), 127.8 (C-5_D and C-$5'_D$), 127.6 (C-5_E and C-$5'_E$), 124.8 (C-10_D, C-$10'_D$, C-10_E, and C-$10'_E$), 122.3 (C-4_D, C-$4'_D$, C-4_E, and C-$4'_E$), 119.6 (C-2_D, C-$2'_D$, C-2_E, and C-$2'_E$), 37.6 (C-8_E and C-$8'_E$), 36.9 (C-8_D and C-$8'_D$), 32.6 (C-7_D and C-$7'_D$), 32.0 (C-7_E and C-$7'_E$), 26.4 (C-9_D and C-$9'_D$), 26.2 (C-9_E and C-$9'_E$), 25.8 (C-12_D and C-$12'_D$, C-12_E and C-$12'_E$), 20.9 (C-14_D, C-$14'_D$, C-14_E, and C-$14'_E$), 19.4 (C-15_D, C-$15'_D$, C-15_E, and C-$15'_E$), 17.7 (C-13_D, C-$13'_D$, C-13_E, and C-$13'_E$); HRESIMS *m/z* 435.3260 $[MH]^+$ (calcd for $C_{30}H_{43}O_2$, 435.3263).

4.3.6. Dicurcuphenol ether F (9). Clear oil; $[\alpha]_D^{25}$ +67.5 (*c* 0.7, $CHCl_3$); ^1H NMR ($CDCl_3$, 500 MHz) δ 7.13 (1H, d, J = 7.5 Hz, H-5), 6.79 (1H, d, J = 7.5 Hz, H-4), 6.673 and 6.666 (each 1H, s, H-2′ and H-5′), 6.32 (1H, s, H-2), 5.11 (2H, m, H-10 and H-10′), 4.55 (1H, br s, OH), 3.24 (1H, sextet, J = 7.0 Hz, H-7), 2.94 (1H, sextet, J = 7.0 Hz, H-7′), 2.19 (3H, s, H-15), 2.12 (3H, s, H-15′), 1.89 (4H, m, H-9 and H-9′), 1.74 (1H, m, H-8_a), 1.67 and 1.66 (each 3H, s, H-12 and H-12′), 1.59 (3H, m, H-8_b and H-8′), 1.54 and 1.52 (each 3H, s, H-13 and H-13′), 1.25 (3H, d, J = 7.0 Hz, H-14), 1.17 (3H, d, J = 7.0 Hz, H-14′); ^{13}C NMR ($CDCl_3$, 125 MHz) δ 155.8 (C-1), 149.1 (C-1′), 148.2 (C-4′), 136.4 (C-3), 133.4 (C-6), 132.2 (C-6′), 131.8 and 131.3 (C-11 and C-11′), 128.3 (C-3′), 127.2 (C-5), 124.9 and 124.6 (C-10 and C-10′), 122.7 (C-4), 118.8 (C-5′), 118.0 (C-2′), 115.6 (C-2), 37.3 (C-8), 37.2 (C-8′), 32.0 (C-7), 31.7 (C-7′), 26.5 (C-9), 26.0 (C-9′), 25.8 (C-12 and C-12′), 21.4 (C-14), 21.2 (C-15 and C-14′), 17.8 (C-13 and C-13′), 16.0 (C-15′); HRESIMS *m/z* 435.3262 $[MH]^+$ (calcd for $C_{30}H_{43}O_2$, 435.3263).

4.4. Enzyme-mediated synthesis of dicurcuphenols

Three enzymes, horseradish peroxidase, polyphenol oxidase, and laccase, were screened for their ability to catalyze the production of the dimeric dicurcuphenols from the monomeric **1**. Very little transformation to the

desired dimeric species was observed among the horseradish peroxidase and polyphenol oxidase preparations. However, several laccase preparations (13 of 78 combinations of buffers, co-solvents, and mediators) were identified as capable of catalyzing this transformation (see Supplementary data) and therefore this enzyme was selected for further scale-up studies.

Three, 1 L Erlenmeyer flasks were prepared each containing 150 mL of 100 mM citrate buffer (pH 5) and 50 mL of MeOH. The crude enzyme preparation (4 g) was gently stirred for 30 min in 50 mL of citrate buffer and allowed to settle for 2 min before use. The cloudy suspension was decanted to remove the insoluble solid residue and the supernatant divided equally among the three flasks. Compound **1** (1.5 g) was dissolved in 3 mL DMF and 500 mg of **1** distributed to each of the three flasks. The flasks were loosely capped with aluminum foil and placed on a rotary shaker at 150 rpm for 24 h.

The flasks were removed and their contents pooled before extraction by partitioning with a mixture of ethyl acetate/*sec*-butanol (95:5) (200 mL, 3×). The organic layer was removed and dried over $MgSO_4$ yielding 1.6 g of crude extract. Analysis by ESIMS of this extract was performed giving evidence for the presence of dimers (*m*/*z* 435) of **1**. The extract was subjected to repeated C_{18} HPLC and silica gel PTLC as outlined above yielding 608 mg of untransformed **1** and dicurcuphenols **4** (46 mg), **5** (22 mg), **6** (18 mg), 1:2.3 mixture of **7** and **8** (11 mg), and **9** (11 mg).

4.5. Periodate oxidation of 1

A periodate oxidative catalytic resin was prepared as described[57] with minor modifications. Briefly, 2.5 g of Amberlite IRA-900 ion exchange resin was combined with 2 g $NaIO_4$ in 20 mL deionized H_2O and stirred overnight. The liquid was decanted and an additional 2 g $NaIO_4$ in 20 mL deionized H_2O was added. This was stirred for 6 h at room temperature. The resin was filtered and washed with H_2O, THF, and ethyl acetate before being dried in a desiccator. Dimerization of **1** was performed as described.[42,57,58]

4.6. Fenton peroxidation of 1

Compound **1** was incubated with Fenton-type reagents as described.[43,59] Briefly, 5 mM of metal (Fe^{2+}, Cu^{2+}, and Mn^{2+}) salts were combined with 5 mM EDTA, 5 mg of **1**, and 1 mM H_2O_2 in a mixture of 0.1 M potassium phosphate buffer (pH 7.0) with acetonitrile (1:1, vol:vol). Reactions proceeded at 37 °C for 60 min at which time cold H_2O was added and the mixture extracted with diethyl ether.

4.7. Vibrational circular dichroism (VCD) studies

Compounds **5** (0.23 M) and **6** (0.11 M) were dissolved in $CDCl_3$ and placed in CaF_2 cells (path length 98 μm) for analysis. Spectra were acquired over 10 h at a resolution of 4 cm^{-1}.

Calculations were performed on the model atropisomer (*P*)-**10** using Gaussian 03[60] at the DTF level (B3LYP functional and 6-31G(d) basis set). Vibrational frequencies were scaled by 0.97 and converted to Lorentzian bands with 6 cm^{-1} half-widths for comparison to experimental data. The truncated (*P*)-**10** lacking the alkyl tails was chosen for analysis due to its limited conformational flexibility and so as to eliminate the contribution of the C-7 chiral center, thereby providing a spectrum whose features were dependant solely on the C-2/C-4′ axial chirality. The scaled VCD spectra for **5** and **6** were subtracted from one another and the resultant difference spectrum aligned and visually compared with that generated for (*P*)-**10**.

4.8. Lipoxygenase inhibition assay

Human reticulocyte 15-lipoxygenase (15-hLO) and human platelet 12-lipoxygenase (12-hLO) were expressed and purified as previously described.[29,61] The IC_{50} values for compounds **1**–**9** against these enzymes were determined as previously described with minor modifications.[29,62] Briefly, all inhibitors and enzyme substrates were dissolved in MeOH (1 mg/mL) and added to 2 mL buffer with 0.1% Triton-X under constant stirring. After a brief equilibration, 15-hLO (25 mM HEPES, pH 7.5) or 12-hLO (25 mM HEPES, pH 8) was added and the enzyme activity monitored based on the rate of diene product formation at 234 nm at room temperature. Multiple data points inclusive of the 50% inhibitory concentration were acquired and the data were fit to a simple saturation curve.

4.9. Redox inhibition studies

Characterization of a redox mode of inhibition of compounds against lipoxygenase was performed as previously described.[31] Briefly, the iron atom in the model lipoxygenase, soybean 15-lipoxygenase (15-sLO), was activated to the ferric species with 13-hydroperoxy-9(*Z*),11(*E*)-octadecadienoic acid (HPOD). The oxidation status of the 15-sLO was monitored by fluorescence (excitation: 280 nm; emission: 328 nm) while test compounds were added to the reaction cell containing 2 mL borate buffer (pH 9.2) at room temperature with constant stirring. A relative increase in the fluorescence signal intensity indicated a reduction of the 15-sLO active site iron.

4.10. Molecular modeling studies

The 15-hLO homology model was created using the Protein local optimization program (PLOP, University of California, San Francisco) whereby conserved residues were aligned with the rabbit 15-lipoxygenase (15-rLO) template. Docking of **1** and deprotonated-**1** into the active site was performed using GLIDE. Active site van der Waals forces were reduced and the ligand inserted. The protein was then relaxed about the ligand using PLOP. The resultant Ramachandran maps generated from the STRIDE database indicated that all residues were within acceptable phi psi spaces. Compound **1** and its ion form were then redocked into the minimized protein active site and found to adopt chemically

reasonable poses. Full details of these methods and creation of the 15-hLO homology model can be found in Chorny and co-workers.[55]

Acknowledgments

We thank R. W. N. Van Soest (University of Amsterdam) for sponge taxonomic identification and L. T. Holst Jr. (Dexter Chemical L.L.C.) for the laccase used in this study. The human 15-lipoxygenase computer model was developed in collaboration with I. Chorny and M. Jacobson (Department of Pharmaceutical Chemistry, University of California, San Francisco). Financial support for this work came from NIH-CA47135 (P.C.), NIH/NIGMS-R25GM51765 (P.C.), NIH-GM56062-06 (T.R.H.), and ACS RPG-00-219-01-CDD (T.R.H.).

Supplementary data

Supplementary material associated with this article can be found, in the online version, at doi:10.1016/j.bmc.2005.06.020.

References and notes

1. Fusetani, N.; Wolstenholme, H. J.; Shinoda, K.; Asai, N.; Matsunaga, S.; Onuki, H.; Hirota, H. *Tetrahedron Lett.* **1992**, *33*, 6823.
2. Butler, M. S.; Capon, R. J.; Nadeson, R.; Beveridge, A. A. *J. Nat. Prod.* **1991**, *54*, 619.
3. Li, C.-J.; Schmitz, F. J.; Kelly, M. *J. Nat. Prod.* **1999**, *62*, 1330.
4. Gulavita, N. K.; De Silva, E. D.; Hagadone, M. R.; Karuso, P.; Scheuer, P. J.; Van Duyne, G. D.; Clardy, J. *J. Org. Chem.* **1986**, *51*, 5136.
5. El Sayed, K. A.; Yousaf, M.; Hamann, M. T.; Avery, M. A.; Kelly, M.; Wipf, P. *J. Nat. Prod.* **2002**, *65*, 1547.
6. Wright, A. E.; Pomponi, S. A.; McConnell, O. J.; Kohmoto, S.; McCarthy, P. J. *J. Nat. Prod.* **1987**, *50*, 976.
7. Fusetani, N.; Sugano, M.; Matsunaga, S.; Hashimoto, K. *Experientia* **1987**, *43*, 1234.
8. Rodríguez, A. D.; Vera, B. *J. Org. Chem.* **2001**, *66*, 6364.
9. Sullivan, B. W.; Faulkner, D. J.; Okamoto, K. T.; Chen, M. H. M.; Clardy, J. *J. Org. Chem.* **1986**, *51*, 5134.
10. Harrison, B.; Crews, P. *J. Org. Chem.* **1997**, *62*, 2646.
11. Peng, J.; Franzblau, S. G.; Zhang, F.; Hamann, M. T. *Tetrahedron Lett.* **2002**, *43*, 9699.
12. Kitagawa, I.; Yoshioka, N.; Kamba, C.; Yoshikawa, M.; Hamamoto, Y. *Chem. Pharm. Bull.* **1987**, *35*, 928.
13. Nakamura, H.; Kobayashi, J.; Ohizumi, Y.; Hirata, Y. *Tetrahedron Lett.* **1984**, *25*, 5401.
14. Kassulke, K. E.; Potts, B. C. M.; Faulkner, D. J. *J. Org. Chem.* **1991**, *56*, 3747.
15. D'Armas, H. T.; Mootoo, B. S.; Reynolds, W. F. *J. Nat. Prod.* **2000**, *63*, 1593.
16. Freyer, A. J.; Patil, A. D.; Killmer, L.; Zuber, G.; Myers, C.; Johnson, R. K. *J. Nat. Prod.* **1997**, *60*, 309.
17. Miller, S. L.; Tinto, W. F.; McLean, S.; Reynolds, W. F.; Yu, M. *J. Nat. Prod.* **1995**, *58*, 1116.
18. McEnroe, F.; Fenical, W. *Tetrahedron* **1978**, *34*, 1661.
19. Schmitz, F. J.; Michaud, D. P.; Hollenbeak, K. H. *J. Org. Chem.* **1980**, *45*, 1525.
20. König, G. M.; Wright, A. D. *J. Nat. Prod.* **1997**, *60*, 967.
21. Suzuki, T.; Kikuchi, H.; Kurosawa, E. *Chem. Lett.* **1980**, *10*, 1267.
22. Valeriote, F.; Corbett, T.; LoRusso, P.; Moore, R. E.; Scheuer, P. J.; Patterson, G.; Paul, V.; Grindely, G.; Bonjouklian, R.; Pearce, H.; Stuffness, M. *Int. J. Pharmacog.* **1995**, *33*(Suppl.), 59.
23. Nafie, L. A.; Freedman, T. B. In *Circular Dichroism*; 2nd ed.; Berova, N., Nakanishi, K., Woody, R. W., Eds.; Wiley-VCH: New York, 2000, pp 97–131.
24. Berova, N., Nakanishi, K., Woody, R. W., Eds., *Circular Dichroism* 2nd ed.; Wiley-VCH: New York, 2000.
25. Berova, N.; Borhan, B.; Dong, J. G.; Guo, J.; Huang, X.; Karnaukhova, E.; Kawamura, A.; Lou, J.; Matile, S.; Nakanishi, K.; Rickman, B.; Su, J.; Tan, Q.; Zanze, I. **1998**, *70*, , p 377.
26. Sam, T. W. In *Bioactive Natural Products: Detection Isolation and Structure Elucidation*; Colgate, S. M., Molyneux, R. J., Eds.; CRC Press: Boca Raton, 1993, pp 441–456.
27. Hooper, J. N. A. In *JNA Systema Porifera: A Guide to the Classification of Sponges*; Hooper, J. N. A., Van Soest, R. W. M., Eds.; Kluwer Academic: New York, 2002; Vol. 1, pp 755–772.
28. Valeriote, F.; Grieshaber, C. K.; Media, J.; Pietraszkewicz, H.; Hoffmann, J.; Pan, M.; McLaughlin, S. *J. Exp. Ther. Oncol.* **2002**, *2*, 228.
29. Amagata, T.; Whitman, S.; Johnson, T. A.; Stessman, C. C.; Loo, C. P.; Lobkovsky, E.; Clardy, J.; Crews, P.; Holman, T. R. *J. Nat. Prod.* **2003**, *66*, 230.
30. Carroll, J.; Jonsson, E. N.; Ebel, R.; Hartman, M. S.; Holman, T. R.; Crews, P. *J. Org. Chem.* **2001**, *66*, 6847.
31. Cichewicz, R. H.; Kenyon, V. A.; Whitman, S.; Morales, N. M.; Arguello, J. F.; Holman, T. R.; Crews, P. *J. Am. Chem. Soc.* **2004**, *126*, 14910.
32. Segraves, E. N.; Shah, R. R.; Segraves, N. L.; Johnson, T. A.; Whitman, S.; Sui, J. K.; Kenyon, V.; Cichewicz, R. H.; Crews, P.; Holman, T. R. *J. Med. Chem.* **2004**, *47*, 4060.
33. Fuganti, C.; Serra, S. *J. Chem. Soc., Perkin Trans. 1* **2000**, 3758.
34. Kimachi, T.; Takemoto, Y. *J. Org. Chem.* **2001**, *66*, 2700.
35. Hagiwara, H.; Okabe, T.; Ono, H.; Kamat, V. P.; Hoshi, T.; Suzuki, T.; Ando, M. *J. Chem. Soc., Perkin Trans. 1* **2002**, 895.
36. Ono, M.; Ogura, Y.; Hatogai, K.; Akita, H. *Tetrahedron: Asymmetry* **1995**, *6*, 1829.
37. Ono, M.; Ogura, Y.; Hatogai, K.; Akita, H. *Chem. Pharm. Bull.* **2001**, *49*, 1581.
38. Burton, S. G. *Curr. Org. Chem.* **2003**, *7*, 1317.
39. Kobayashi, S.; Uyama, H.; Kimura, S. *Chem. Rev.* **2001**, *101*, 3793.
40. Mayer, A. M.; Staples, R. C. *Phytochemistry* **2002**, *60*, 551.
41. Veitch, N. C. *Phytochemistry* **2004**, *65*, 249.
42. Antolovich, M.; Bedgood, D. R., Jr.; Bishop, A. G.; Jardine, D.; Prenzler, P. D.; Robards, K. *J. Agric. Food Chem.* **2004**, *52*, 962.
43. Goldstein, S.; Meyerstein, D.; Czapski, G. *Free Radical Biol. Med.* **1993**, *15*, 435.
44. Pham, V. C.; Jossang, A.; Sévenet, T.; Bodo, B. *Tetrahedron* **2002**, *58*, 5709.
45. Elix, J. A.; Jayanthi, V. K.; Jones, A. J.; Lennard, C. J. *Aust. J. Chem.* **1984**, *37*, 1531.
46. Fukuyama, Y.; Asakawa, Y. *J. Chem. Soc., Perkin Trans. 1* **1991**, 2737.
47. Jaspars, M.; Rali, T.; Laney, M.; Schatzman, R. C.; Diaz, M. C.; Schmitz, F.; Pordesimo, E. O.; Crews, P. *Tetrahedron* **1994**, *50*, 7367.

48. Miao, S.; Andersen, R. J.; Allen, T. M. *J. Nat. Prod.* **1990**, *53*, 1441.
49. Pordesimo, E. O.; Schmitz, F. J. *J. Org. Chem.* **1990**, *55*, 4704.
50. Nomura, K.; Suzuki, N.; Matsumoto, S. *Biochemistry* **1990**, *29*, 4525.
51. Freedman, T. B.; Cao, X.; Dukor, R. K.; Nafie, L. A. *Chirality* **2003**, *15*, 743.
52. Freedman, T. B.; Cao, X.; Oliveira, R. V.; Cass, Q. B.; Nafie, L. A. *Chirality* **2003**, *15*, 196.
53. Freedman, T. B.; Cao, X.; Nafie, L. A.; Kalbermatter, M.; Linden, A.; Rippert, A. J. *Helv. Chim. Acta* **2003**, *86*, 3141.
54. Dailey, L. A.; Imming, P. *Curr. Med. Chem.* **1999**, *6*, 389.
55. Kenyon, V.; Chorny, I.; Holman, T.; Jacobson, M. *J. Med. Chem.*, submitted.
56. Nafie, L. A. *Appl. Spectrosc.* **2000**, *54*, 1634.
57. Harrison, C. R.; Hodge, P. *J. Chem. Soc., Perkin Trans. 1* **1982**, 509.
58. Fulcrand, H.; Cheminat, A.; Brouillard, R.; Cheynier, V. *Phytochemistry* **1994**, *35*, 499.
59. Foppoli, C.; Coccia, R.; Blarzino, C.; Rosei, M. A. *Int. J. Biochem. Cell Biol.* **2000**, *32*, 657.
60. Frisch, M. J.; Trucks, G. W.; Schlegel, H. B.; Scuseria, G. E.; Robb, M. A.; Cheeseman, J. R.; Montgomery, J. A., Jr.; Vreven, T.; Kudin, K. N.; Burant, J. C.; Millam, J. M.; Iyengar, S. S.; Tomasi, J.; Barone, V.; Mennucci, B.; Cossi, M.; Scalmani, G.; Rega, N.; Petersson, G. A.; Nakatsuji, H.; Hada, M.; Ehara, M.; Toyota, K.; Fukuda, R.; Hasegawa, J.; Ishida, M.; Nakajima, T.; Honda, Y.; Kitao, O.; Nakai, H.; Klene, M.; Li, X.; Knox, J. E.; Hratchian, H. P.; Cross, J. B.; Adamo, C.; Jaramillo, J.; Gomperts, R.; Stratmann, R. E.; Yazyev, O.; Austin, A. J.; Cammi, R.; Pomelli, C.; Ochterski, J. W.; Ayala, P. Y.; Morokuma, K.; Voth, G. A.; Salvador, P.; Dannenberg, J. J.; Zakrzewski, V. G.; Dapprich, S.; Daniels, A. D.; Strain, M. C.; Farkas, O.; Malick, D. K.; Rabuck, A. D.; Raghavachari, K.; Foresman, J. B.; Ortiz, J. V.; Cui, Q.; Baboul, A. G.; Clifford, S.; Cioslowski, J.; Stefanov, B. B.; Liu, G.; Liashenko, A.; Piskorz, P.; Komaromi, I.; Martin, R. L.; Fox, D. J.; Keith, T.; Al-Laham, M. A.; Peng, C. Y.; Nanayakkara, A.; Challacombe, M.; Gill, P. M. W.; Johnson, B.; Chen, W.; Wong, M. W.; Gonzalez, C.; Pople, J. A. Gaussian 03, Revision B.04, Gaussian, Pittsburgh PA, 2003.
61. Holman, T. R.; Zhou, J.; Solomon, E. I. *J. Am. Chem. Soc.* **1998**, *120*, 12564.
62. Finazzi-Agro, A.; Avigliano, L.; Veldink, G. A.; Vliegenthart, J. F. G.; Boldingh, J. *Biochim. Biophys. Acta* **1973**, *326*, 462.

Niels H. Andersen, Niels J. Christensen, Peter R. Lassen, Teresa B. Freedman, Laurence A. Nafie, Kristian Strømgaard, and Lars Hemmingsen: Absolute Configuration Determination of Ginkgolides by VCD Spectroscopy.

Journal of Natural Products, in preparation.

4

4

Absolute Configuration Determination of Ginkgolides by VCD Spectroscopy

Niels H. Andersen,[*,†] Niels J. Christensen,[$] Peter R Lassen,[†] Teresa B. Freedman,[‡] Laurence A. Nafie,[‡] Kristian Strømgaard,[*] Lars Hemmingsen [$]

Department of Physics, Quantum Protein (QuP) Center, Technical University of Denmark, Building 309, 2800 Kgs. Lyngby, Denmark, Department of Natural Sciences, The Royal Veterinary and Agricultural University of Denmark, Thorvaldsensvej 40, 1871 Frederiksberg C, Denmark, Department of Chemistry, Syracuse University, New York 13244-4100, USA, Department of Medical Chemistry, The Danish University of Pharmaceutical Sciences, Universitetsparken 2, 2100 Copenhagen, Denmark

Abstract. Vibrational Circular Dichroism (VCD) and IR spectroscopy combined with DFT (B3LYP/6-31G(d)) calculations have successfully been applied to determine the absolute configuration of Ginkgolide B (GB) from *Ginkgo Biloba*. In addition, the calculated spectra indicate that it is possible to distinguish GB from stereoisomers with inversion at a single chiral center (C_1 or C_{10}) and from the other Ginkgolides A, C, J, and M (GA, GC, GJ and GM) by VCD and IR spectroscopy. The VCD and IR spectra of GB were recorded using two different solvents (DMSO-d_6 and CD_3CN) and a KBr pellet and two different VCD instruments. The elucidation of vibrational spectral bands of GB has been improved compared to previous assignments in the literature.[1-3]

Introduction. The interest in the medical effects of the Ginkgo-tree has persisted since ancient time in Eastern Asia. Extracts from the Ginkgo-tree comprise GA, GB, GC, GJ and GM. The latter is only found the root bark and GJ only in the leaves while the others can be isolated from all parts of the tree.[4] The ginkgo tree itself is very remarkable in being a specimen that has survived since the Jurassic era.[2,4] In 1932 Ginkgolides were discovered to be terpene trilactones, but the elucidation of their structure and their ability to interact with the platelet activating factor (PAF) receptor in 1985 markedly increased the attention. Among the ginkgolides, GB is found to be the most potent PAF antagonist.[4]

The overall IR spectral features of ginkgolides comprise characteristics of alcohols, ethers, esters and aliphatic hydrocarbons, which are all strongly entangled by sharing of many atoms among the rings.[1] The fingerprint spectral region is therefore highly complex, and spectral bands should rather be assigned to the vibrational character of the whole molecular frame than to specific molecular bonds as for simpler organic compounds. Addition and removal of OH-groups as well as chiral inversion should therefore have a dramatic effect on both the IR and VCD spectra. There are 10-12 chiral centres in ginkgolides depending on the type as shown in table 1. However, 3 of these (C_4, C_5 and C_9) cannot contribute to the number of possible diastereomers without rupture of the 6-ring structure, and 4 (C_2, C_3, C_6 and C_{12}) will severely alter the shape of molecular frame. Inversion of C_8 and C_{14} implies change of the *t*-butyl and methyl group orientations, respectively. Thus, we have limited our investigations for GB to inversions at the positions 1 and 10 (denoted GB-C_1i and GB-C_{10}i, respectively). These isomers are also relevant for total synthesis of GB where stereospecific addition to double bonds at C_1 and C_{10} occurs. The strength of VCD together with IR is not limited only to distinguish between enantiomers, but also enables vibrational assignment of diastereomers that occur on inversion of one or several chiral centres. In the case of ginkgolides, in particular, discrimination between stereoisomers with inversion at just one chiral center is essential, with reference to both synthesis and isolation.[5]

In this work we wish to demonstrate that VCD spectroscopy combined with DFT calculations is a powerful tool for absolute configuration determination of even relatively large organic molecules with many chiral centres such as GB and to test the reliability when distinguishing GB from selected diastereomers and other types of ginkgolides. Molecular mechanics force field calculations, two types of DFT calculations and three different sample preparations which implied use of two different VCD instruments have been examined and compared. The DFT calculations were done with GAUSSIAN 03 ™.[6] GB ($C_{20}H_{24}O_{10}$) has 224 electrons and no symmetry and is among the larger molecules studied by this combination of experimental and theoretical methods, albeit similar works on even larger molecular systems have been published.[7-9]

Results and Discussion. The Boltzmann weighting of the conformers with relevance of GB, GC and GM shown in table 2 illustrates that the IR and VCD spectra at room temperature are dominated by main contributions from the lowest energy conformer by 95.8%, 96.8% and 97.8%, respectively. Only minor changes in the calculated spectra could be seen when incorporating the weighted data from the second conformers that in the same order are 7.8, 8.5 and 9.4 kJ/mol higher in energy. The geometry optimized structure of GB at B3LYP/6-31G(d)-level is identical to that of earlier work.[10] The overall agreement between the calculated and experimental VCD spectra of GB is striking, see Figure 2, and thus indicates that VCD spectroscopy can be applied in determination of absolute configuration of ginkgolides. The absolute configuration determined in this work agrees with the crystal structure of GB.[10,11] However, it is also necessary to demonstrate that the calculated spectra of other stereoisomers of GB differ significantly from the recorded spectrum, in order to validate that the assignment is unambiguous, see below.

The IR spectrum of GB in KBr and/or Nujol has previously been assigned.[1,2,3] As seen in figure 2, VCD improves the spectral assignment: In the 1000 to 1200 cm^{-1} region, five broad and intense IR bands are observed at 1168, 1130, 1098, 1065 and 1044 cm^{-1}. The last two of these are obscured by solvent absorption in the DMSO-d_6 experiment. Overarchingly, these bands are accompanied by negative VCD at 1168, 1134 and 1046 cm^{-1} and positive VCD at 1098 and 1068 cm^{-1}. There is nonetheless a significant discrepancy for the band at 1168 cm^{-1} where the intensity calculation fails for both IR and VCD. For this mode, C-O-H bending is prominent and the discrepancy may be caused by changes in the hydrogen bonding pattern on exposure to solvent. Here the bands at 1065 and 1044 cm^{-1} are assigned to C-O-H bending. This is in excellent agreement with both the observed KBr spectrum in figure 2 and the scaled frequencies from the DFT calculations. By visualization of the Gaussian results, $C_{10}OH$ and C_3OH bending could be assigned to the band at 1168 cm^{-1} while C_1OH shows bending motion at 1134 cm^{-1}.

The IR and VCD spectrum for GB differs markedly from those of GB-C_1i and GB-C_{10}i and the other Ginkgolides, figure 3. At 872, 926, 986, 1031, 1082, 1157 and 1282 cm^{-1} the VCD spectra display distinct differences. However, at other spectral regions great care should be taken as several IR and VCD patterns appears quite alike. The highly distinguishable C=O stretching bands and the striking differences at 950, 1030, 1120, 1140, 1170 and 1230 cm^{-1} should be remarked.

The differences between the different ginkgolide spectra in figure 4 are puzzling, but at certain wavenumbers the deviations are clear. At 1425 cm^{-1} GC, GJ and GM has IR peaks that is also accompanied with a positive-negative VCD feature for GC and GM. Around 1340 cm^{-1} GA and GJ shows similar VCD patterns, but this appears to be inverted in case of GM. At 1300, 1320 and 1360 cm^{-1} GB have a characteristic pattern consisting of three positive VCD peaks that seems to occur also for GC. The negative VCD features for GB between 1300 and 1260 cm^{-1} looks like those for GC that also has

a negative VCD shoulder at 1250, whereas GA and GJ have positive VCD peaks at 1270 cm^{-1}. For GM this negative VCD pattern is limited to the range from 1280 to 1250 cm^{-1}. The strong negative VCD band at 1170 $cm^{-}1$ is observed for all the ginkgolides but GM where the peak is shifted to 1160 cm^{-1}. As the only one, GA lacks a negative VCD peak near 1140 cm^{-1}.

Thus IR and VCD can be used to discriminate between the various ginkgolides. Similarly, and perhaps most importantly, the calculated spectra for GB with inversion of chirality at the C_1 or C_{10} positions are clearly different from the GB spectrum, indicating that IR and VCD spectroscopy may be applied to discriminate between stereoisomers where only one chiral center is inverted. That is, the technique may be applied to investigate the stereochemistry at individual chiral centers in molecules with many such centers.

Experimental Section

Sample Preparation and VCD Spectroscopy. Ginkgolides are very soluble in highly polar and hydrogen bonding solvents as water/acetone mixtures, methanol or DMSO but they are insoluble in low dielectric constant solvents as CCl_4 and $CHCl_3$.[2] DMSO-d_6, CD_3CN and KBr were chosen as media for sample preparation. DMSO-d_6 dissolves GB most efficiently, evaporates slowly but suffers from a limited transparency range (1100 to 2100 cm^{-1}). CD_3CN has a much better transparency range (500 to 2500 cm^{-1}) but dissolves less GB and evaporates faster while KBr pellets might cause artifacts in VCD spectra due to mechanical stress that is difficult to reproduce. In all cases care should be taken to avoid water because of hygroscopicity, and the risk of lactone ring opening which occurs at pH over 6.[12]

Both instruments used were of the FT-type with PEM modulation of the IR light. The first instrument at QuP, is a Thermo Nicolet Nexus 870 infrared spectrometer equipped with a single PEM and improved with a filter that only allowed light in the range between 1000 and 1750 cm^{-1} to pass.

The second is a modified Chiral/IR FT-VCD instrument at Syracuse University, New York. Here, an extra PEM is added after the sample, which eliminates most of the LD artifacts that often occur. As a consequence this instrument produces a much flatter baseline but background spectra still have to be recorded.[13]

3.9 mg GB (424 g/mol) was dissolved in 20 µl DMSO-d_6 and placed in a 48 µm CaF_2 sandwich-cell in the Thermo Nicolet instrument with the PEM set to 1500 cm^{-1}. Assuming volume-additivity of solvent and GB (ρ = 1.377 g cm^{-3},[11]) the concentration was c = 0.40 M. Sample and solvent were scanned for 57 h and the latter spectrum was subtracted. The cell was solvent-tight for several days. A calibration of the instrument was performed immediately after scanning of the sample. In the narrow spectral range 1000-1750 cm^{-1} the effectivity of the PEM is approximately constant, and the raw VCD data were calibrated by multiplication with the constant 0.565.

The next two measurements were made with the modified ChiralIR instrument in Syracuse. 1.8 mg GB was dissolved in 50 µl CD_3CN and transferred to a 54 µm BaF_2 cell. The concentration was c = 85 mM. ~½ mg GB recovered from the CD_3CN experiment was ground with 250 mg KBr (ρ = 2.75 g cm^{-3}, *CRC*) and pressed to a 13 mm diameter disk for 4 min at 13000 lbs. The GB concentration and disk path-length was calculated to be c = 13 mM and l = 0.69 mm, respectively. In both cases the PEMs were set to 1400 cm^{-1}. Here the VCD spectra were corrected automatically by the software using previous calibration measurements.

Theoretical Calculations. Structures of all ginkgolides and two stereoisomers of GB were subjected to conformational analysis using MacroModel prior to DFT calculations. An energy window of 50 kJ/mol was applied and the input files were generated from published crystal structures of GA, GB and GC or modifications of these.[11,14] The relative energies of the relevant conformer outcome are shown in table 2. The DFT calculations were run at Qup and at HPC, the University of Oslo. Sets of conformers with energies within a 20 kJ/mol from the lowest level for each ginkgolide type were geometry optimized with B3LYP/6-31G(d). In case of GA, GJ, GBC_1i and $GBC_{10}i$, there was at least 17 kJ/mol to the conformer with next lowest energy, leaving back one conformer of each for further calculations. In case of GB, GC and GM, at least two conformers of each were subjected to VCD calculations. To be able to perform a more precise Boltzmann weighting analysis for the actual sets of conformers, a single point energy calculation was undertaken for each geometry optimized conformer with a larger basis set (6-311+G(2d,2p)). The Gibbs free energies were calculated by addition of the electronic energies from the higher quality single point calculations to thermal correction to the corresponding 6-31G(d) frequency calculations. However, the thermal energy corrections should be used with care due to larger deviations from harmonic behavior of the vibrational modes with lowest frequencies that are heavily populated at room temperature. The VCD and IR spectra were extracted from the Gaussian output files, and a Lorentzian band profile of 5 cm^{-1} bandwidth was applied. A scaling factor of 0.982 were multiplied with the calculated frequencies and band intensities. This ensured the best fit to the data in the fingerprint region.

Acknowledgement. We are grateful for financial support from The Lundbeck Foundation for the funding allocated to this project. We also wish to thank the University of Oslo, Norway, for providing the superdome calculation facility at HPC and for collaboration with IMBV and the Department of Chemistry.

References

(1) Broquet, C.; Braquet, P. In Ginkgolides – Chemistry, Biology, Pharmacology and Clinical Perspectives. P. Braquet (Ed.) J.R. Prous Science Publishers, S.A. (1988).

(2) van Beek, T. A. *Bioorganic & Medicinal Chemistry* **13** (2005) 5001–5012.

(3) Okabe, K.; Yamada, K.; Yamamura, S.; Takeda, S. *J. chem. Soc. C* (1967) 2201-2206.

(4) Strømgaard, K; Nakanishi, K. *Angewandte Chemie - International Edition* **43**, 13 (2004), 1640–1658.

(5) Corey, E.J.; Gavai, A.V., *Tetrahedron Lett.* **1988**, 29, 3201-??

(6) Frisch, M. J.;Trucks, G.W.; Schlegel, H.B.; Scuseria, G. E.;Robb,M.A.;Cheeseman, J.R.; Montgomery, J. A.; J., Vreven, T.;Kudin, K. N.;Burant, J. C.;Millam, J.M.; Iyengar, S. S.; Tomasi, J.; Barone, V.;Mennucci, B.;Cossi, M.; Scalmani, G.; Rega, N.; Petersson, G. A.; Nakatsuji, H.; Hada, M.; Ehara, M.; Toyota, K.; Fukuda, R.; Hasegawa, J.; Ishida, M.; Nakajima, T.;Honda, Y.; Kitao, O.;Nakai, H.; Klene, M.; Li, X.; Knox, J. E.; Hratchian, H. P.; Cross, J. B.; Adamo, C.; Jaramillo, J.; Gomperts, R.; Stratmann, R. E.; Yazyev, O.; Austin, A. J.;Cammi, R.; Pomelli, C.;Ochterski, J.

W.;Ayala, P. Y.; Morokuma, K.;Voth, G. A.; Salvador, P.; Dannenberg, J. J.; Zakrzewski, V. G.; Dapprich, S.; Daniels, A. D.; Strain, M. C.; Farkas, O.; Malick, D. K.; Rabuck, A. D.; Raghavachari, K.; Foresman, J. B.; Ortiz, J. V.; Cui, Q.; Baboul, A. G.; Clifford, S.; Cioslowski, J.; Stefanov, B. B.; Liu, G.; Liashenko, A.; Piskorz, P.; Komaromi, I.;Martin, R. L.; Fox, D. J.; Keith, T.; Al-Laham, M.A.; Peng, C. Y.;Nanayakkara, A.; Challacombe, M.;Gill, P. M.W.; Johnson, B.; Chen, W.; Wong, M. W.; Gonzalez, C.; Pople, J. A. Gaussian 03, Revision B.04. Gaussian, Inc., Pittsburgh PA, 2003.

(7) Freedman, T. B.; Cao, X.; Rajca, A.; Wang, H.; Nafie L. A. *J. Phys. Chem. A* **107** (2003) 7692-7696.

(8) Brotin, T; Cavagnat, D; Dutasta, J.-P.; Buffeteau, T. *J. Am. Chem. Soc.* **128** (2006) 5533-5540.

(9) Bürgi, T.; Urakawa, A.; Behzadi, B.; Ernst, K.H.; Baiker, A. *New J. Chem.* **3** (2004) 332-334.

(10) Zhu, W.-L.; Puah, C. M.; Tan, X.-J.; Jiang, H.-L.; Chen, K.-X.; Ji, R.-Y. *Journal of Molecular Structure (Theochem)* **528** (2000) 193-198.

(11) Dupont, L.; Dideberg, O.; Germain, G.; Braquet, P. *Acta Cryst.* **C42** (1986) 1759-1762.

(12) Zekri, O.; Boudeville P.; Genay, P.; Perly, B.; Braquet, P.; Jouenne, P.; Burgot, J.-L., *Anal. chem.* **1996**, 68, 2598-2604.

(13) Nafie, L. A. *Applied Spectroscopy* **54** (2000) 1634-1645.

(14) Sbit, M.; Dupont, L; Dideberg, O; Braquet, P. *Acta Cryst.* **C43** (1987) 2377-2381

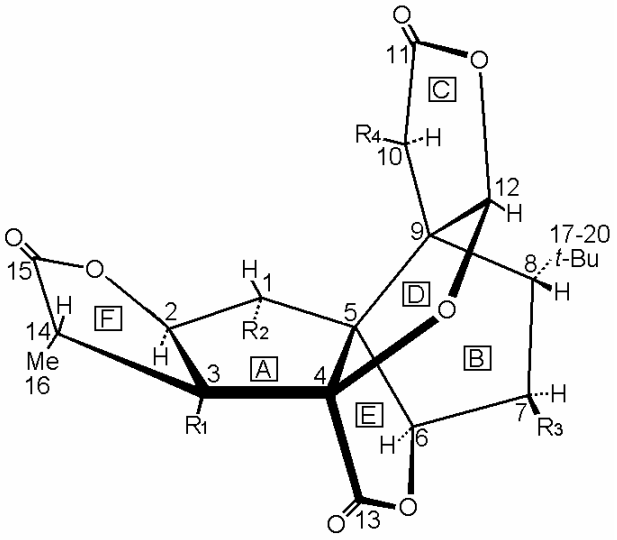

Figure 1
Sketch of the Ginkgolide skeleton showing the relative orientation of the 6 five-rings. Rings A & B are aliphatic while rings C, E & F are γ-lactone rings and ring D an ether ring. The numbering of the Carbon atoms grossly follows the order of the letters for the rings.

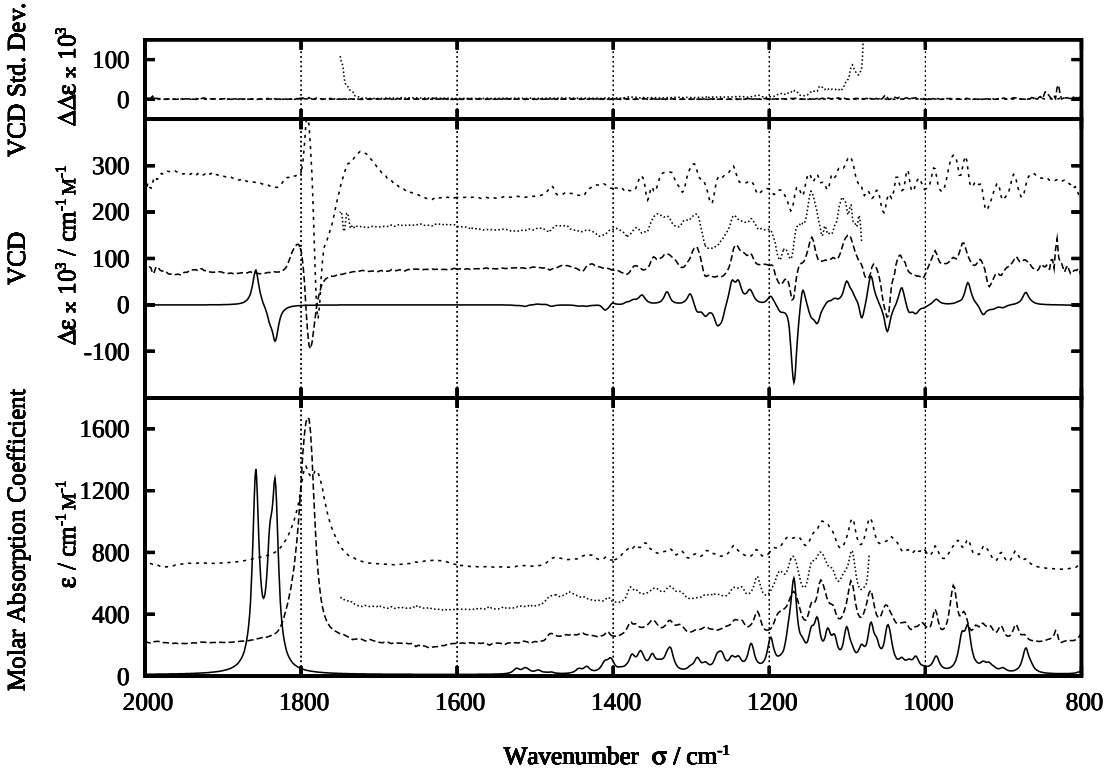

Figure 2
Calculated and measured IR- (lower panel), VCD-spectra (middle panel) and VCD-noise (upper panel) of pure GB. From bottom to top: Calculated spectrum at B3LYP/6-31G(d) level scaled by a factor 0.982, spectrum of GB in a pressed KBr pellet, GB dissolved in DMSO-d_6 and in CD_3CN.

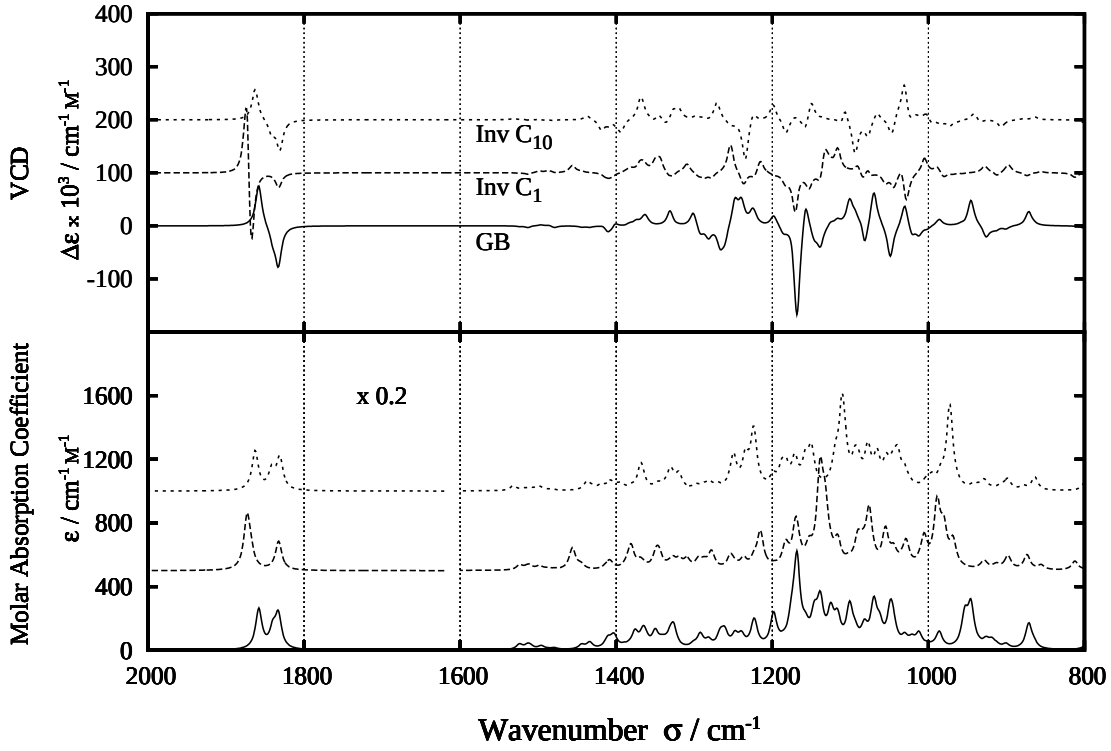

Figure 3
Calculated IR and VCD spectra (upper panel) of GB, GB-C_1i and GB-C_{10}i scaled with a factor 0.982. The IR bands between 1600 and 2000 cm^{-1} have been multiplied with 0.2.

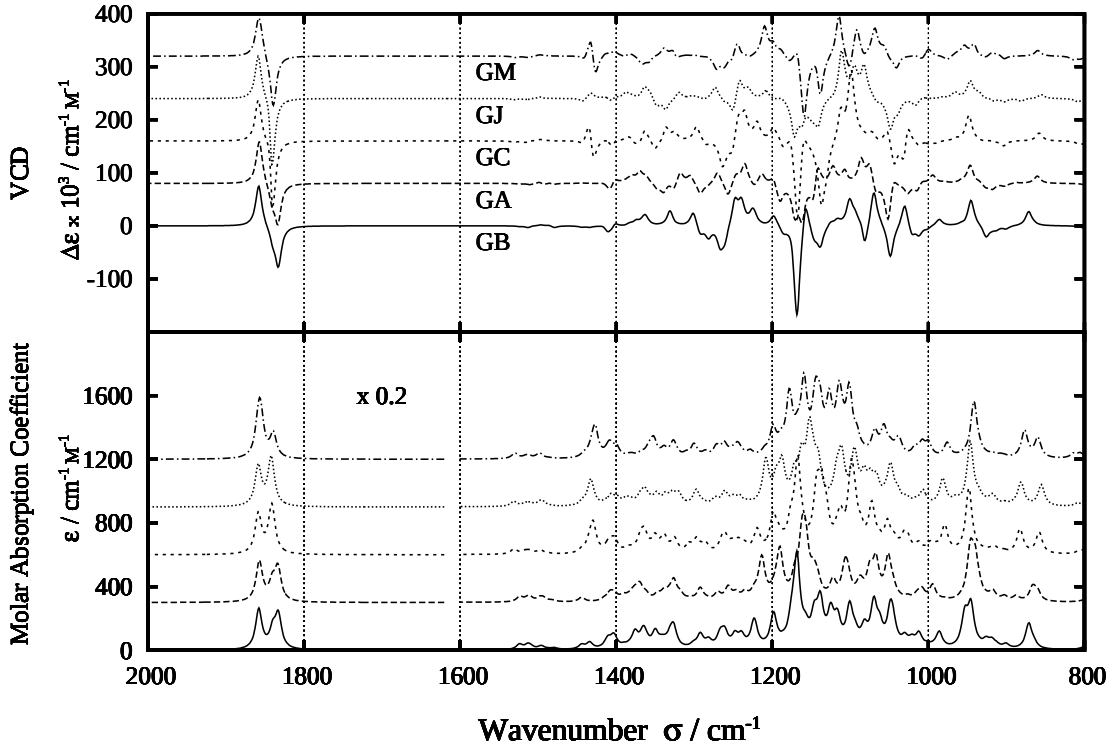

Figure 4
Calculated IR and VCD spectra for GB, GA, GC, GJ and GM scaled with a factor 0.982. The IR spectra were multiplied with a factor 0.2 in the 1600 to 2000 cm cm^{-1} region.

Ginkgolide	R_1 on C_3 ring A	R_2 on C_1 ring A	R_3 on C_7 ring B	R_4 on C_{10} ring C	N° of chiral centers
A	OH	H	H	OH	10
B	OH	OH	H	OH	11
C	OH	OH	OH	OH	12
J	OH	H	OH	OH	11
M	H	OH	OH	OH	12

Table 1

		Energies in kJ/mol			
	Macro-Model	Gaussian 03			
Ginkgolide type & Conformer number		B3LYP 6-31G(d)	B3LYP 6-311+G(2d,2p)	Sum of electronic and thermal Free Energies	Thermal correction to Gibbs Free Energy
GB		-1528.81188050	-1529.30880065	-1528.92409965	0.384701
1	0.0	0.0	0.0	0.0	1010.0
3	7.6	7.3	7.3	7.8	1010.5
2	5.8	16.4			
4	11.7	18.7			
GA		-1453.59918521	-1454.06370226	-1453.68326226	0.38044
1	0.0	0.0	0.0	0.0	998.8
2	13.8	19.6			
GC		-1604.02098315	-1604.55046206	-1604.16204506	0.388417
1	0.0	0.0	0.0	0.0	1019.8
3	8.9	7.3	7.5	8.5	1020.8
4	10.3	16.5			
2	3.0	17.2			
GJ		-1528.80830905	-1529.30545244	-1528.92116144	0.384291
1	0.0	0.0	0.0	0.0	1009.0
2	12.2	17.3			
3	17.0	19.1			
GM		-1528.80929453	-1529.30642498	-1528.92131598	0.385109
1	0.0	0.0	0.0	0.0	1011.1
3	9.5	8.2	7.9	9.4	1012.6
2	5.2	17.5			
GB-C_1i		-1528.80861698	-1529.30348050	-1528.91806450	0.385416
1	0.0	0.0	0.0	0.0	1011.9
2	16.3	22.7			
GB-C_{10}i		-1528.80018326	-1529.29802106	-1528.91404606	0.383975
1	0.0	0.0	0.0	0.0	1008.1
2	13.2	18.2			

Table 2

Relative energies of ginkgolide conformers from MacroModel and DFT calculations on GA, GB, GC, GJ, GM and GB with the atoms C_1 and C_{10} inverted. The energies in the ginkgolide name containing rows are in atomic units, while relative energies referring to each column are given in kJ/mol.

Peter R. Lassen, Laure Guy, Iyad Karame, Thierry Roisnel, Nicolas Vanthuyne, Christian Roussel, Xiaolin Cao, Rosina Lombardi, Jeanne Crassous, Teresa B. Freedman, and Laurence A. Nafie: Synthesis and vibrational circular dichroism of enantiopure chiral oxorhenium(V) complexes containing the hydrotris(1-pyrazolyl)borate ligand.

Inorganic Chemistry, accepted.

5

5

Synthesis and vibrational circular dichroism of enantiopure chiral oxorhenium(V) complexes containing the hydrotris(1-pyrazolyl)borate ligand

Peter R. Lassen,[a,†] Laure Guy,[b] Iyad Karame,[b] Thierry Roisnel ,[c] Nicolas Vanthuyne,[d] Christian Roussel,[d] Xiaolin Cao [a], Rosina Lombardi,[a] Jeanne Crassous,[c], Teresa B. Freedman,*[a] and Laurence A. Nafie[a]*

[a] Department of Chemistry, Syracuse University, Syracuse NY 13244, USA

[b] Laboratoire de Chimie, École Normale Supérieure de Lyon, UMR CNRS 5182, 46, Allée d'Italie, F-69364, Lyon 07, France

[c]Sciences chimiques de Rennes, UMR CNRS 6226,Université de Rennes 1, Campus de Beaulieu, 35042 Rennes cedex, France

[d] UMR Chirotechnologies : Catalyse et Biocatalyse, Université Paul Cézanne, 13397 Marseille Cedex 20, France

†Syracuse University (Visiting from Quantum Protein Centre, Department of Physics, Technical University of Denmark, DK-2800 Lyngby, Denmark).

RECEIVED DATE

TITLE RUNNING HEAD Vibrational circular dichroism of chiral Re(V) complexes

* Authors to whom correspondence should be addressed. Dr. Jeanne Crassous. Phone : +33 02 23 23 63 70. Fax: +33 02 23 23 69 39. E-mail: jeanne.crassous@univ-rennes1.fr. Prof. Teresa Freedman. Phone: (315) 443-1134. Fax: (315) 443-4070. E-mail: tbfreedm@syr.edu.

Abstract

The infrared (IR) and vibrational circular dichroism (VCD) spectra of six chiral oxorhenium(V) complexes, bearing a hydrotris(1-pyrazolyl)borate (Tp) ligand have been investigated. These complexes are promising candidates for observation of parity violation (PV) (symmetry breaking due to the weak nuclear force). New chiral oxorhenium complexes have been synthesized, namely [TpReO(η^2-O(CH_3)CH_2CH_2O-*O*,*O*)] **4a** and **4b** diastereomers, [TpReO(η^2-N(CH_3)CH_2CH_2O-*N*,*O*)] **5** and [TpReO(η^2-N(*t*Bu)CH_2CH_2O-*N*,*O*)] **6** enantiomers. All compounds could be obtained in enantiomerically pure forms by using either column chromatography or HPLC over chiral columns. Vibrational circular dichroism (VCD) spectroscopy of these compounds and of [TpReO(η^2-N(CH_3)CH(CH_3)CH(Ph)O-*N*,*O*)] **2** and [TpReO(η^2-N$(CH_2)_3CHCO_2$-*N*,*O*)] **3** (with chiral bidentate ligands derived respectively from ephedrine and proline) were studied. It allowed the absolute configuration determinations of all compounds together with their conformational analysis, by comparing calculated and experimental spectra. This is the first VCD study of rhenium complexes which further demonstrates the applicability of VCD spectroscopy in determining chirality of inorganic complexes, both in solution and in KBr pellets.

Introduction

Oxorhenium complexes have proven useful in catalysis[1] and in radiopharmaceutical chemistry[2]. Moreover, chiral oxorhenium complexes have revealed to be good candidates for the observation of parity violation (PV) effects in chiral molecules.[3] Parity violation is a fundamental effect which breaks the space symmetry and which is due to weak interaction between elementary particles.[4] It has been experimentally observed in atoms and in nuclear physics.[5] At the molecular level, PV is known to induce a very tiny energy difference (PVED) between the two enantiomers of a chiral molecule. However, observing such a tiny energy difference ΔE_{PV} (ΔE_{PV} *c.a.* 10^{-17} kT) is still a scientific challenge and requires very accurate spectroscopy methods together with a good chiral model molecule.[6] For example, parity violation (PV) may be observed by unpolarized IR spectroscopy, *i.e.*, by measuring slightly different absorption frequencies for opposite enantiomers. PVED measurements have already been searched on simple chiral hetero-halogenomethanes such as CHFClBr, resulting in the determination of an experimental upper limit of 10 Hz for this effect.[7] Meanwhile, theoreticians have shown that transition metal complexes such as rhenium compounds, *i.e.* bearing a heavy metal[3,8] nearby the chirality center, are very promising compounds. Indeed, they display much higher PV effects than organic compounds, thanks to the dependence of ΔE_{PV} on the number of electrons and neutrons in the nucleus; this difference (ΔE_{PV}) scales approximately like Z^5.[9]

Finding the ideal chiral candidate molecule for the first observation of parity violation at the molecular level is a real challenge. The design of the best candidate is related to the ultra-high resolution spectroscopy technique involved for the measurement. The experimental and theoretical aspects[10,6] of the PV measurement imposes several requirements such as: i) a very simple molecule with a total number of atoms as few as possible, ii) a heavy atom like rhenium nearby the chirality center, iii) a rigid molecule for good spectroscopic properties, and iv) an isolated absorption peak with a frequency lying in the domain 1000±100 cm^{-1} which is imposed by the use of ultrastable CO_2 laser in the case of the ultrahigh resolution IR spectroscopy.[7] Oxorhenium complexes usually display a sharp Re=O stretching mode around 950 cm^{-1}. We have found a number of chiral oxorhenium complexes in the literature[11] and have focused our attention on enantiomerically pure Faller's oxorhenium complexes containing a hydrotris(1-pyrazolyl)borate (Tp) ligand because they are readily available, robust and "chiral at the rhenium".[11b] In this context, we show in this paper that VCD spectroscopy is a valuable tool for finding the best candidate molecule which displays all the features discussed above. The VCD spectrum of the bulk solution provides important

information on whether the Re=O stretching absorption band is active or not, on the absolute configuration of the sample, and on the conformations present in solution.

Vibrational circular dichroism (VCD) spectroscopy is an advanced form of infrared (IR) absorption spectroscopy, in which information about the chirality of a sample is obtained by the differential absorption of left and right circularly polarized IR radiation.[12] Compared to electronic circular dichroism, VCD spectra are more detailed because of the many bands contained in the mid-IR "fingerprint" region. Since the discovery of VCD three decades ago,[13] the technique has been applied mostly to small organic molecules. Commercial software for calculations of VCD spectra has been introduced in 1998, allowing direct comparison with experimental data. Recently, VCD has been calculated for several transition metal complexes and successfully compared to experiments.[14]

This paper presents the synthesis and the separation of enantiomerically pure new compounds (R_{Re}*,R_C*) and (R_{Re}*,S_C*)-[TpReO(η^2-O(CH_3)CH_2CH_2O-*O*,*O*)] **4a** and **4b** respectively (four stereoisomers), together with R_{Re} and S_{Re}-[TpReO(η^2-N(CH_3)CH_2CH_2O-*N*,*O*)] **5** and R_{Re} and S_{Re}-[TpReO(η^2-N(*t*Bu)CH_2CH_2O-*N*,*O*)] **6**, where Tp = hydrotris(1-pyrazolyl)borate (See Schemes 1 and 2). Analytical and semi-preparative HPLC over chiral columns of **5** and **6** enantiomers have been performed. A benchmark analysis of chiral oxorhenium complexes is presented in detail, which includes IR and VCD spectra of the compounds along with the density functional theory (DFT) calculated ones. In a first step, the calculation methods (choice of the basis sets and of the density functional) have been determined on already known complexes R_{Re},$R_{O\text{-}C}$,$S_{C\text{-}N}$-(+)-**2** and R_{Re},R_C-(-)-**3**. In a second step, the comparison of experimental and calculated VCD spectra allowed the determination of the R_{Re},R_C-(+)-**4a**, R_{Re},S_C-(-)-**4b**, R_{Re}-(-)-**5** and R_{Re}-(-)-**6** absolute configurations. X-ray crystallography enabled to confirm absolute configurations for **4a** and **4b** (see Figure 1). In the case of compounds **3**, **4b** and **5**, VCD studies showed the presence of several conformers in solution. These are important features for the choice of the best candidate for future PV measurements by IR spectroscopy.

Results and discussion

Synthesis and separation of compounds

The samples studied first were the two enantiomeric pairs S_{Re},$S_{O\text{-}C}$,$R_{C\text{-}N}$- and R_{Re},$R_{O\text{-}C}$,$S_{C\text{-}N}$-[TpReO(η^2-N(CH_3)CH(CH_3)CH(Ph)O-*N*,*O*)] **2**, and S_{Re},S_C- and R_{Re},R_C-[TpReO(η^2-N(CH_2)$_3$$CHCO_2$-*N*,*O*)] **3** because they were readily synthesized according to literature procedures[11b] from the precursor $TpReOCl_2$. For both cases, only one diastereomer was obtained among the two possible ones, due to steric interactions. The absolute configurations of these two compounds have already been determined by Faller and Lavoie by X-ray crystallography[11b] and they could be confirmed by our VCD spectroscopy studies (see below). Following the same synthetic strategy, diastereomeric compounds S_{Re},S_C-**4a** and R_{Re},S_C-**4b** were obtained from *S*-1,2-propanediol as described in Scheme 1, together with their enantiomers R_{Re},R_C-**4a** and S_{Re},R_C-**4b** when using *R*-1,2-propanediol. No diastereoselectivity was observed with these less hindered chiral diols: the two possible diastereomers corresponding to the both *R* and *S* configurations at the rhenium chiral center were obtained in equal proportions. These diastereomers could however be separated by regular column chromatography over silical gel and no epimerization was observed. S_{Re},S_C-(-)-**4a** and R_{Re},S_C-(-)-**4b** could therefore be obtained with *ee*'s better than 99% from *S*-1,2-propanediol. Their enantiomers R_{Re},R_C-(+)-**4a** and S_{Re},R_C-(+)-**4b** could also be prepared in the same way by using *R*-1,2-propanediol. The absolute configurations S_{Re},S_C-(-) and R_{Re},R_C-(+) for **4a** and R_{Re},S_C-(-) and S_{Re},R_C-(+) for **4b** were first determined by VCD spectroscopy as explained in detail below. Later on, they were confirmed by X-ray crystallography analysis of R_{Re},R_C-(+)-**4a** and R_{Re},S_C-(-)-**4b** samples which gave monocrystals and whose absolute structures are displayed in Figure 1. Their detailed crystallographic data are given in Table 1.

In order to simplify one step further the molecules for PV experiments, enantiomerically pure pairs R_{Re}- and S_{Re}-**5** and R_{Re}- and S_{Re}-**6** were prepared by using achiral aminoalcohols, namely N-methylaminoethanol and N-*tert*-butylaminoethanol. These compounds were prepared in their racemic form by reacting $TpReOCl_2$ with the achiral aminoalcohols with good yields (Scheme 2). Monocrystals of (±)-**5** were obtained and their X-ray structure analysis revealed a centrosymmetric space group which means that the R_{Re} and S_{Re} enantiomers are found in the same asymmetric unit *i.e.* (±)-**5** is a racemic compound (see Figure 1 and Table 1). The separation, impossible by direct crystallization, was therefore investigated by HPLC over chiral stationnary phases. The screening of ChirBase[15] revealed that a few chiral rhenium complexes have already been separated by this method.[16] Eleven chiral stationary phases were tested in order to find the best separation conditions to resolve the two enantiomers at a semi-preparative scale (see supplementary). For both racemates, Chiralcel OD-H (250x4.6 mm, cellulose tris-3,5-dimethylphenyl-carbamate) gave excellent baseline separation, good enantioselectivity and resolution (see Figure 2). So, the semi-preparative chiral separations were performed on Chiralcel OD (250x10 mm) to give 22 mg of each enantiomer of **5** and 9 mg of each enantiomer of **6**, with enantiomeric excesses higher than 99.5% (see supplementary for details). The separated enantiomers were characterized by their optical rotation: $[\alpha]_D^{25}$ = +935 ($CHCl_3$, *c* 0.04) for the first eluted enantiomer of **5** and –930 ($CHCl_3$, *c* 0.04) for the second eluted, $[\alpha]_D^{25}$ = +1240 ($CHCl_3$, *c* 0.03) for the first eluted enantiomer of **6** and –1235 ($CHCl_3$, *c* 0.03) for the second eluted. Those specific rotation values are the highest related for such chiral rhenium compounds. Interestingly, samples of resolved **5** were heated at 50°C in chloroform for 24 hours and no racemization could be observed. Furthermore, we have shown that compound **2** sublimates under mild conditions without alteration of its chemical composition and optical rotation. These features provide evidence for the robustness of these oxorhenium(V) compounds and let consider confidently the possibility to generate a molecular beam for high resolution spectroscopy.

Oxorhenium complexes bearing a Cp* of the type $LReO_3$ have been extensively studied by Herrmann *et al*..[17] Replacement of the Tp ligand by a Cp* have been considered in order to simplify the structure of our complexes, and we have therefore synthesized [Cp*ReO(η^2-N(CH_3)CH(CH_3)CH(Ph)O-*N*,*O*)] from Cp^*ReOCl_2 and ephedrine but we observed that such a complex was not stable at all and that epimerization at the rhenium center occurred spontaneously. We therefore did not pursue this direction further.

VCD spectroscopy studies

[TpReO(η^2-N(CH_3)CH(CH_3)CH(Ph)O-*N*,*O*)] (2)

Conformational analysis revealed only one conformer of R_{Re},$R_{O\text{-}C}$,$S_{C\text{-}N}$-**2** (**2-I**), shown in Figure 3, optimized at the DFT/B3LYP level with the basis sets 6-31G* [H, B, C, N, O] and Stuttgart RSC 1997 ECP [Re][18] (abbreviated as 6-31G*/Stuttgart). Very little variation is seen in the optimized structure when different basis sets are used. Geometry optimization of the S_{Re},$R_{O\text{-}C}$,$S_{C\text{-}N}$-**2** diastereomer gave an energy 3.01 kcal/mol higher, suggesting a population fraction of 0.6%, consistent with the results from the synthesis.

IR and VCD spectra of **2** are shown in Figure 4, where the IR and raw VCD spectra of both enantiomers in $CDCl_3$ are shown. The VCD intensities are very close to opposite in sign for the enantiomers. To eliminate minor absorption artifacts and increase the signal-to-noise ratio, the average VCD spectrum of the enantiomers (corresponding to a racemic sample) was used as the VCD baseline in subsequent figures.

In Figure 5, the observed IR and VCD spectra are compared to the array of calculated ones with the B3LYP function and the basis set LanL2DZ for all elements[19,20,21], or a combination of 6-31G(d) for elements H through O and a larger basis set for Re (Hay-Wadt VDZ (n+1) ECP[22] or Stuttgart RSC 1997 ECP.[18] Experimental spectra using both $CHCl_3$ and $CDCl_3$ solutions have been combined to cover a wider spectral range to 880 cm^{-1}. A progressively better fit to the experimental spectra can be seen when increasing the basis set size. The results for the SDD basis set for all

elements (not shown) are almost identical to the B3LYP/LanL2DZ calculation. In general, the comparison of observed and calculated VCD spectral patterns is quite good and allows for an unambiguous verification of absolute configuration. However, the relative intensities of VCD peaks differ somewhat between the observed and calculated spectra. We find the best agreement using the combination of the Stuttgart basis set for rhenium and 6-31G* for the other elements.

Most of the observed vibrational bands can be assigned based on the Gaussian 03 calculations. The Re=O stretching band at ~930 cm^{-1} is the most interesting vibration in this study because of the ongoing search for PV effects. The two large basis sets for rhenium yield slightly different results in the Re=O stretching region. With the Hay-Wadt basis set for Re, the Re=O stretch couples more strongly with a phenyl ring deformation than with the Stuttgart basis set (which has an additional 15 basis functions). In addition to large Re=O stretching motion, the normal mode generating positive VCD intensity for **2** at ~930 cm^{-1} has contributions from deformations of the entire ephedrine ligand, as well as Tp deformation.

Closer inspection of the observed Re=O stretching band reveals a non-Lorentzian shape due to shoulders at lower frequencies, which are not readily assigned by the calculations. Similarly, the B-H stretching band at 2500 cm^{-1} has shoulders at higher frequencies. Figure 6 displays higher resolution (0.25 cm^{-1}) IR spectra in these regions, recorded for samples both in $CHCl_3$ solution and as a KBr pellet. The shoulders cannot be readily assigned to other normal modes, since there is only one additional calculated normal mode near the Re=O stretch, and its calculated IR intensity is 2 orders of magnitude smaller. The B-H stretching band is completely isolated between the fingerprint and C-H stretching regions.

Several explanations can be invoked in order to explain the observed shoulders. Both rhenium and boron have naturally occurring isotopes, i.e., 37% ^{185}Re and 20% ^{10}B, which would generate minor peaks at shifted frequencies. The size of these frequency shifts can be estimated from the reduced masses or calculated for the isotope with Gaussian 03 to be 0.37 cm^{-1} for Re=O and 11 cm^{-1} for B-H, making only the B-H shift observable experimentally. Additional shoulders in the BH stretching region may arise from Fermi resonance with overtones of B-H deformations, which indeed are found in the calculation at around half the stretching frequency. The shoulders to the Re=O stretch may also arise due to Fermi resonance, since the calculated Re=O stretching at 970 cm^{-1} (unscaled) matches combination bands for modes calculated at 146 and 823 cm^{-1} (involving the N-Re=O angle deformation), as well as 301 and 669 cm^{-1} (involving ephedrine chelate ring deformation).

IR spectra at a roughly 13 times lower concentration were recorded, and they reveal practically no difference in band shape beyond the scaling factor (data not shown). This evidence supports the possibility of solvent interaction or intramolecular effects like Fermi resonance and precludes solute-solute interactions as sources for the additional weak features in the BH and Re=O stretching regions.

[TpReO(η^2-N$(CH_2)_3$CHCO$_2$-*N*,*O*)] (3)

Two conformers of the R_{Re},R_C-[TpReO(η^2-N$(CH_2)_3$CHCO$_2$-*N*,*O*)] sample (**3**) have been identified, with different puckering of the five-membered proline ring, referred to as **3-I** and **3-II**, shown in Figure 7. In the gas phase, the calculated energies for the two conformers differ by 0.11 kcal/mol according to the B3LYP/LanL2DZ calculation, corresponding to Boltzmann populations of 55% **3-I** vs. 45% **3-II**. With the 6-31G(d)/Stuttgart basis set, the energy difference is smaller and opposite, with **3-I** lying 0.013 kcal/mol higher in energy, suggesting almost equal populations. Interestingly, the presence of two conformers is also suggested by the published crystal structure,[11b] where the relevant 50% probability ellipsoids in the ORTEP representation appear prolate. At the B3LYP/LanL2DZ level, the S_{Re},R_C-**3** diastereomer is calculated to lie 5.1 kcal/mol higher in energy than R_{Re},R_C-**3**, consistent with the presence of only the R_{Re},R_C-diastereomer in the experimental sample.

IR and VCD spectra were calculated for both conformers **3-I** and **3-II**, and the average spectra for the two conformers (B3LYP/6-31G(d)/Stuttgart) is compared to experiment in Figure 8. The overall agreement in VCD patterns between observed and calculated spectra again provides an unambiguous assignment of absolute configuration, but the agreement is not as good as for **2**.

Positive VCD intensity near 1200 cm^{-1} correlates with modes involving the proline ligand. The carbonyl stretching mode is calculated to exhibit fairly intense, positive VCD intensity, but with a frequency 100 cm^{-1} too high with 6-31G(d)/Stuttgart and 100 cm^{-1} too low with LanL2DZ and SDD basis sets (not shown). The observed C=O stretching band also has two separate peaks observed at 1691 and 1704 cm^{-1}, but the calculated carbonyl stretching frequencies for the two conformers differ only by 2 cm^{-1}. The Re=O and B-H bands also reveal shoulders in the 0.25 cm^{-1} resolution IR spectra (data not shown), which can be explained in the same way as for **2**.

[TpReO(η^2-O(CH_3)CH_2CH_2O-*O*,*O*)] (4a and 4b)

For the diastereomer R_{Re},R_C-**4a**, two diolate conformers were identified at the B3LYP/6-31G(d)/Stuttgart level that differ by 2.2 Kcal/mol, suggesting only a 3% population of the minor conformer R_{Re},R_C-**4a-II** (Figure 9). The comparison between the composite calculated spectra and the observed spectrum for (+)-**4a**, shown in Figure 10, provides an unambiguous assignment of absolute configuration for this experimental diastereomer sample fraction as (R_{Re},R_C)-(+)-**4a**, consistent with the X-ray crystallography analysis presented above. The Re=O stretch, calculated at 965 cm^{-1} (scaled by 0.97) correlates with positive VCD at 966 cm^{-1}.

Two optimized conformations that differ in conformation of the chelated diolate ring were identified for the diastereomer R_{Re},S_C-**4b** at the B3LYP/6-31G(d)/Stuttgart level, shown in Figure 11. Conformer **4b-II** is higher in energy by 1.1 Kcal/mol, yielding a population of 87% **4b-I** and 13% **4b-II** at room temperature. The calculated conformer spectra and their Boltzmann-population-weighted composite are compared to experiment for (-)-**4b** in Figure 12, demonstrating very good agreement in VCD pattern and identifying the absolute configuration of this sample as R_{Re},S_C(-)-**4b**. In this case, the band with predominant Re=O stretch at 965 cm^{-1} (scaled frequency) has opposite sign for the two conformers, and correlates with the negative VCD at 968 cm^{-1}, consistent with the larger population of **4b-I**. The comparison between observed and calculated spectra for the two conformations provides evidence for the presence of both conformations in solution, where, for example, the negative feature at 1050 cm^{-1} is characteristic of the minor conformer and the positive VCD feature at 1000 cm^{-1} is characteristic of the major conformer.

[TpReO(η^2-N(CH_3)CH_2CH_2O-*N*,*O*)] (5)

The chelated bidentate ligand can assume two conformations, calculated to differ in energy by 0.30 Kcal/mol, with populations 62% **5-I** and 38% **5-II** (Figure 13). From the Boltzmann-population-weighted sum of the calculated spectra, shown in Figure 14, sufficient agreement with experiment is found for assignment of the absolute configuration as R_{Re}-(-)-[TpReO(η^2-N(CH_3)CH_2CH_2O-*N*,*O*)]. In regions where the two conformations exhibit VCD bands opposite in sign, the agreement between the composite calculated spectra and experiment is not quite as good. The Re=O stretches for the two conformers are opposite in sign, with rather weak negative VCD intensity calculated for the dominant conformation at 945 cm^{-1} (scaled frequency). An absorption band near this frequency appears at the cut-off for the $CDCl_3$ solvent measurements, but no distinct VCD feature is observed for **5** in this region.

[TpReO(η^2-N(*t*Bu)CH_2CH_2O-*N*,*O*)] (6)

The two optimized conformers for **6**, shown in Figure 13, differ by 2.5 Kcal/mol, indicating a population of less than 2% for conformer **6-II**. The comparison of the experimental VCD spectrum for (-)-**6** with the calculated spectrum for **6-I** (Figure 14) identifies the absolute configuration as R_{Re}-(-)- [TpReO(η^2-N(*t*Bu)CH_2CH_2O-*N*,*O*)]. The Re=O stretch generates the positive VCD band at ~940 cm^{-1}.

Summary

We have recorded good quality IR and VCD spectra of six enantiomeric pairs of rhenium complexes and successfully verified their absolute configuration by comparison to spectra calculated at the DFT level for one of each enantiomeric pair. Several basis sets have been investigated, and the best fit to experiments has been obtained using the B3LYP functional and a custom basis set for rhenium, Stuttgart RSC 1997 ECP, along with 6-31G(d) for the remaining elements.

Only one conformation of **2** was found during the calculations, but the remaining samples exist in solution as two chelate ring conformers with different populations. For **3**, **4b**, and **5**, both conformers contribute to the observed spectra in solution at room temperature. The Re=O stretch is identified by a distinct VCD band in the 930 to 965 cm^{-1} region in **2**, **3**, **4a**, **4b**, and **6**. For **5**, the opposite signs for the VCD of the two populated conformers results in little or no VCD intensity for the Re=O stretch.

All samples investigated reveal bands with several components, both in solution and in a solid-state matrix. This is apparent from the fine structure of the Re=O stretch and B-H stretching absorption bands, which consist of several peaks, and most prominently in the C=O vibration of **3**, which has two distinct peaks. Both inter- and intramolecular effects have been considered to explain these effects. In solution, we expect negligible solvent interaction. We attribute the splitting of the B-H and Re=O stretching bands to Fermi resonance and isotope shifts by ^{10}B. The key results for all the samples have been summarized in Table 2.

Conclusion

New chiral oxorhenium(V) complexes have been synthesized from $TpReOCl_2$ and suitable chiral diols or achiral aminoalcohols. Regular column chromatography could be used to prepare diastereomerically pure complexes [TpReO(η^2-O(CH_3)CH_2CH_2O-*O*,*O*)] [(S_{Re},S_C)-(-)-**4a** and (R_{Re},S_C)-(-)-**4b** and their mirror-images]. On the other hand, semi-preparative HPLC over chiral stationary phases has proven very efficient to obtain enantiomerically pure complexes [TpReO(η^2-N(CH_3)CH_2CH_2O-*N*,*O*)] [S_{Re}-(+) and R_{Re}-(-)-**5**] and [TpReO(η^2-N(*t*Bu)CH_2CH_2O-*N*,*O*)] [S_{Re}-(+) and R_{Re}-(-)-**6**]. Absolute configurations were determined by VCD studies and some were confirmed by X-ray crystallography. The advantages *vs.* drawbacks towards using such chiral complexes for parity violation experiments have been considered. The main advantages are their ease of synthesis, their robustness and their enantiomeric stability, which is not straightforward in inorganic chemistry. These complexes all display a sharp Re=O stretching mode that may be carefully studied by using an ultrastable CO_2 laser in the case of the ultrahigh resolution IR spectroscopy.[7] The main drawbacks are the total number of atoms (especially because of the Tp ligand) and the presence of several conformational isomers in solution as evidenced by VCD. Indeed, in addition to identification of absolute configuration of the complexes without the need for X-ray studies, the VCD study has characterized the solution conformations of the complexes and identified complexes that may not be suitable for further study because of opposite VCD intensities (and presumably other chiral properties) for the Re=O stretch for two populated conformers (**4b** and **5**). The Re=O stretches are identified by distinct vibrational bands in the region 930 to 965 cm^{-1}, with dominant Re=O stretching motion accompanied by motion of the ligand rings. The sign and intensity of the Re=O stretching VCD is influenced by the chirality at the rhenium, the chirality of the ligand chelating TpReO and by the conformation of the chelating ligand.

Aknowledgment. The Agence Nationale pour la Recherche (ANR) is warmly thanked for fundings (NCPMOL project).

"**Supporting Information Available**": listings of experimental procedures, HPLC separations, crystallographic data, VCD measurements and theoretical calculations. This material is free of charge via the Internet at http://pubs.acs.org.

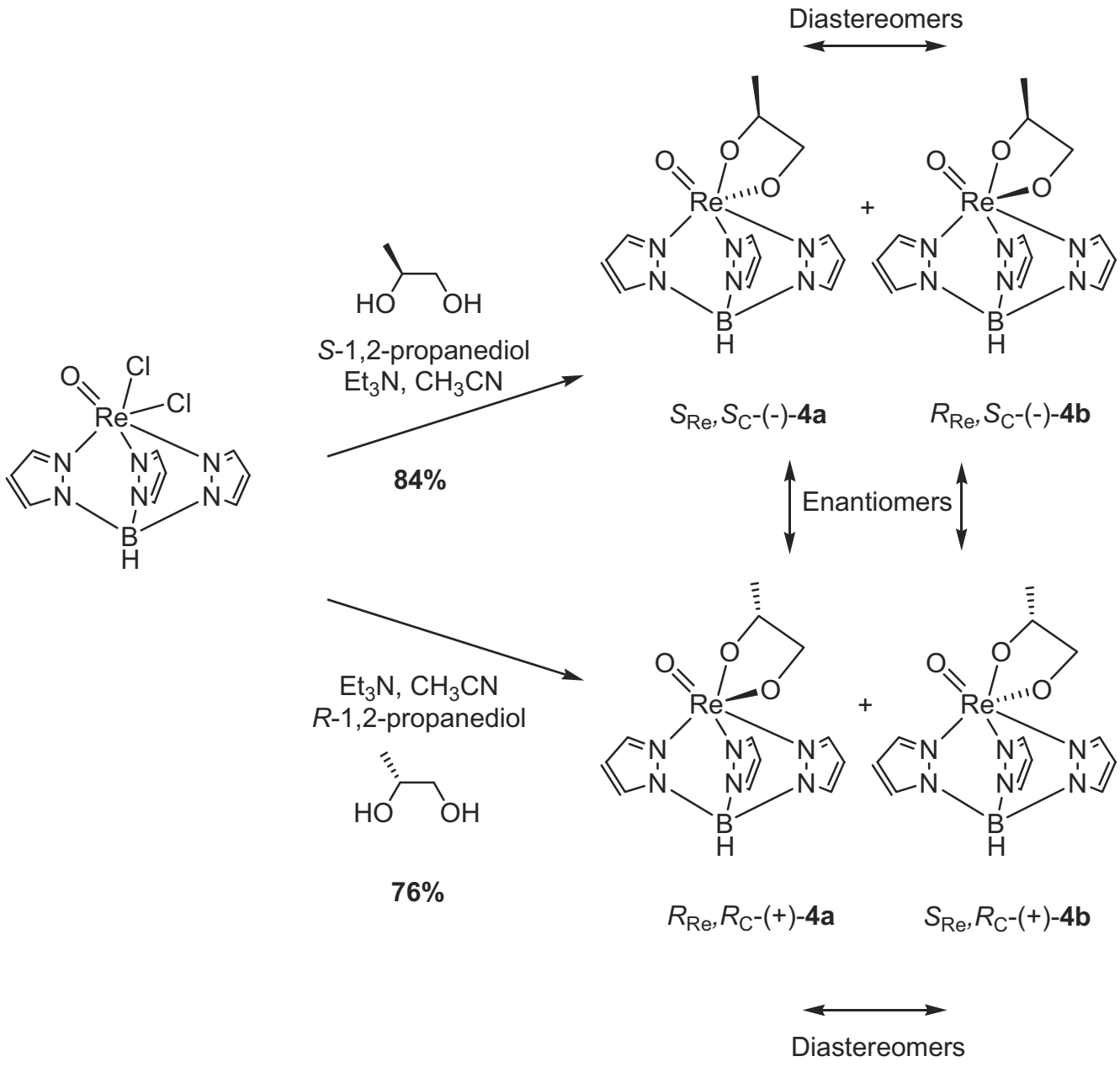

Scheme 1. Synthetic route to the four oxorhenium(V) complexes **4a** and **4b** stereoisomers, which were separated by column chromatography.

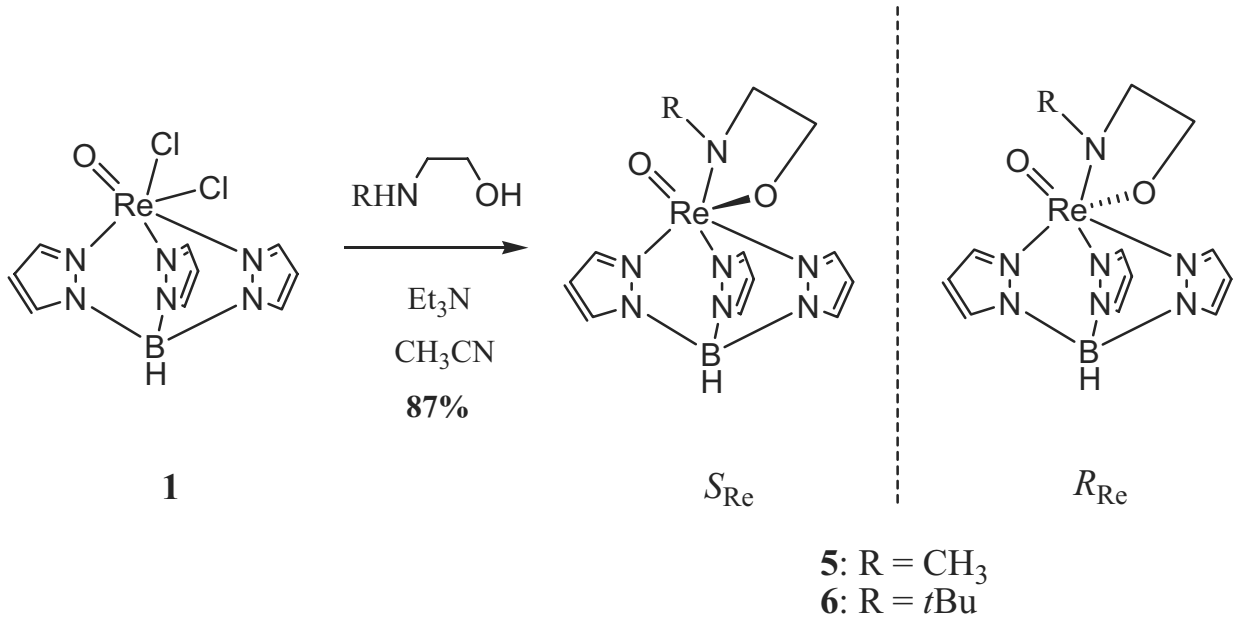

Scheme 2. Synthesis of enantiomeric oxorhenium complexes **5** and **6** with the use of achiral aminoalcohols.

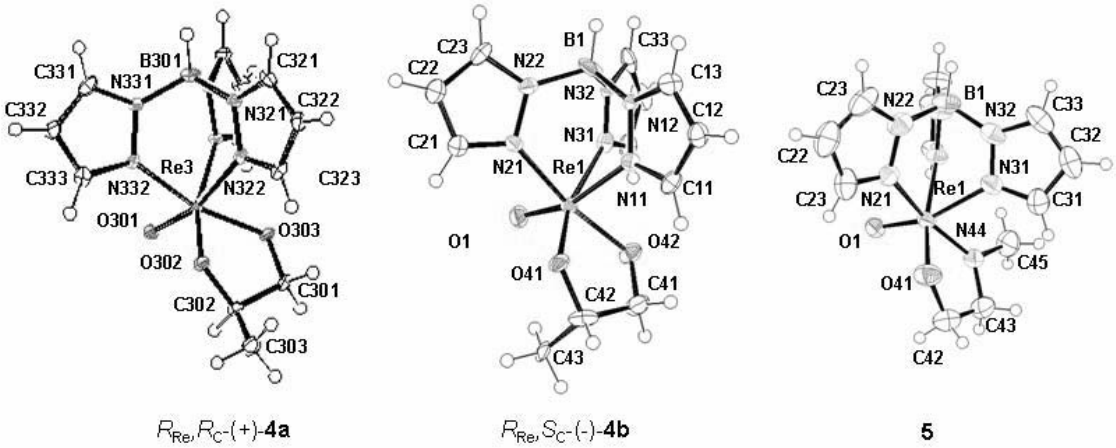

Figure 1. ORTEP diagrams (50% probability) of molecules R_{Re},R_C-(+)-**4a** and R_{Re},S_C-(-)-**4b** (only one out of three molecules in the asymmetric unit shown) and (±)-**5** (only one out of the two enantiomeric molecules in the asymmetric unit shown).

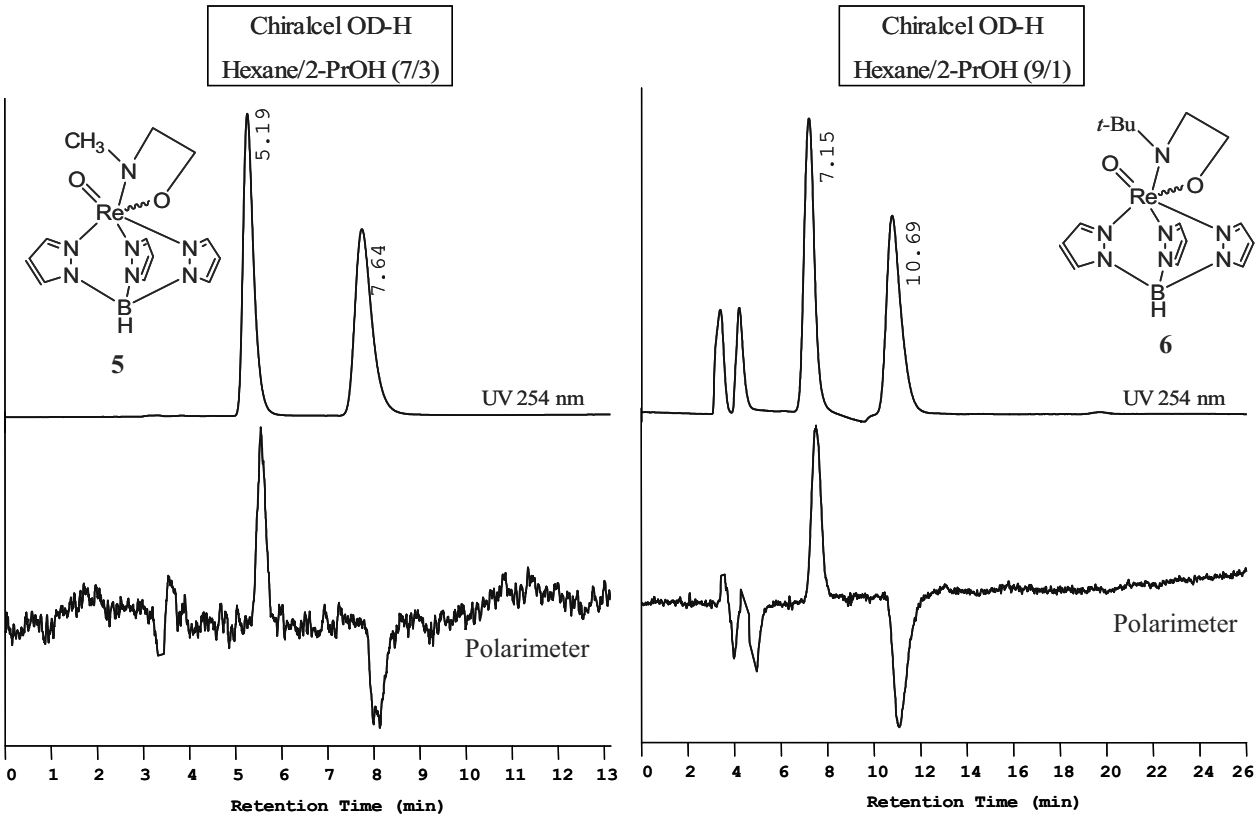

Figure 2. Analytical chiral HPLC chromatograms for the separations of compounds **5** and **6** on Chiralcel OD-H, with hexane/2-PrOH (7/3) as mobile phase at 1 ml/min for **5**, and hexane/2-PrOH (9/1) for **6**, and with UV (254 nm) and polarimetric detectors.

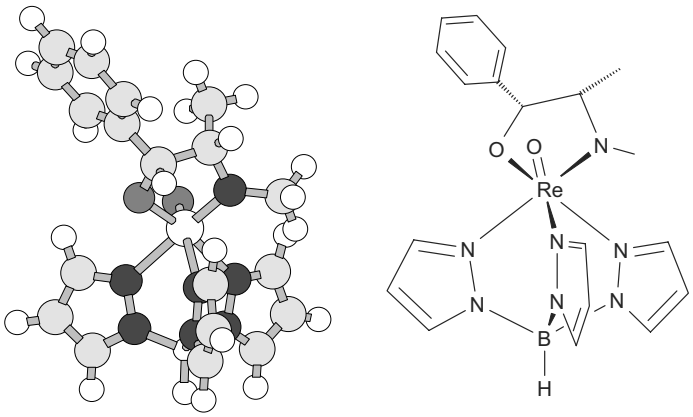

Figure 3. Optimized structure of the single conformation of R_{Re},$R_{O\text{-}C}$,$S_{C\text{-}N}$-**2**, **2-I** (B3LYP/6-31G*/Stuttgart calculation).

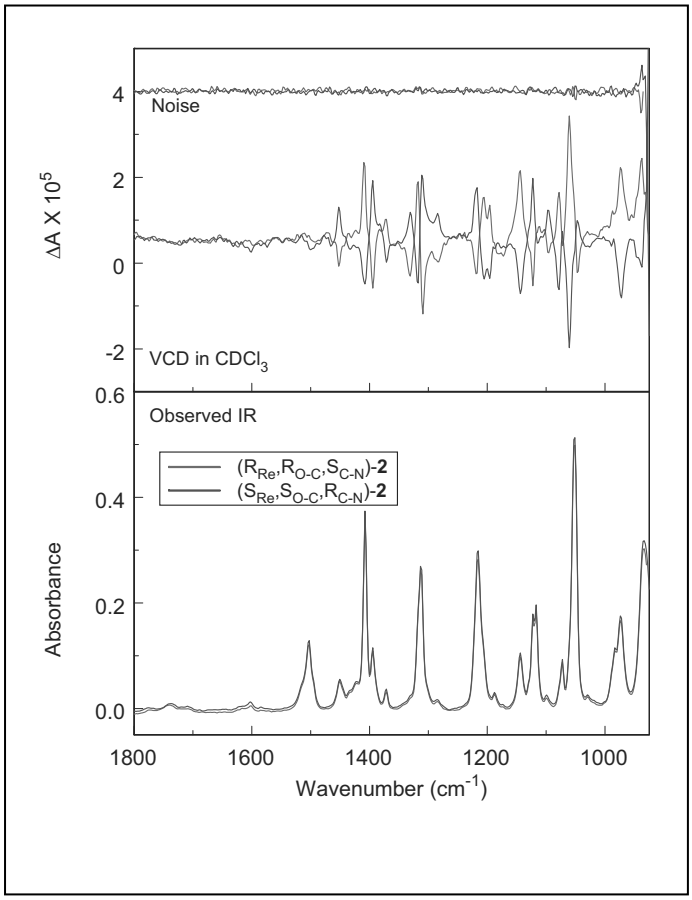

Figure 4. Observed IR (lower frame) and VCD (upper frame) of the two enantiomers of **2** in $CDCl_3$, 10 mg sample in 300 μL solvent (58 mM); 4 cm^{-1} resolution; instrument optimized at 1400 cm^{-1}; collection time 12 h. IR spectra are solvent subtracted.

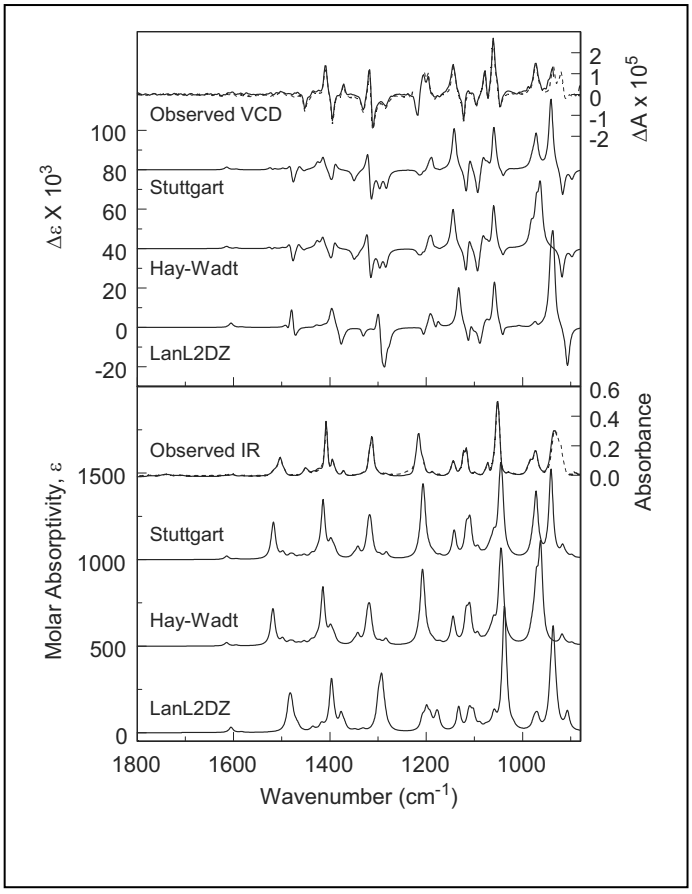

Figure 5. Observed IR (lower frame) and VCD (upper frame) spectra for R_{Re},$R_{O\text{-}C}$,$S_{C\text{-}N}$-**2** (right axes) compared to DFT calculations for **2-I** with the B3LYP functional and three basis sets (left axes, shown offset for clarity): LanL2DZ for all elements and Stuttgart or Hay-Wadt for Re with 6-31G(d) for elements H through O. Observed IR spectra are solvent subtracted and VCD is baseline corrected using the average of the two enantiomers. Experimental data presented for $CHCl_3$ solvent (dashed line) and $CDCl_3$ solvent (solid line). Experimental conditions as in Figure 2.

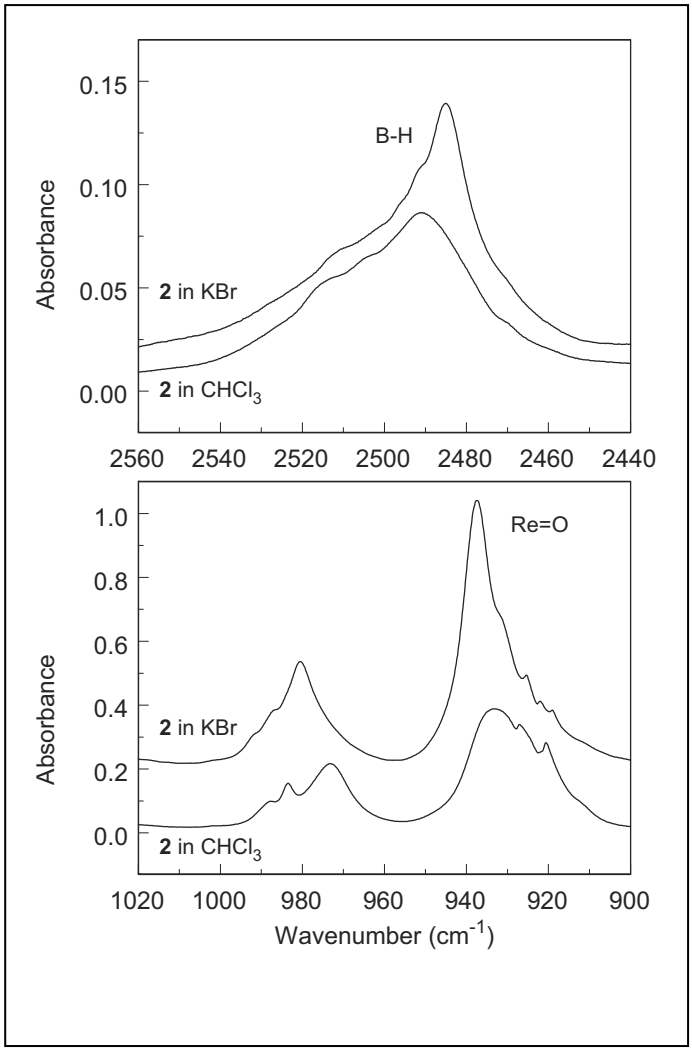

Figure 6. Higher resolution IR spectra of **2** in $CHCl_3$ solution and in a KBr pellet, showing the B-H stretching (top) and Re=O stretching regions (bottom). Resolution 0.25 cm^{-1}; collection time 90 min. KBr spectra are offset for clarity.

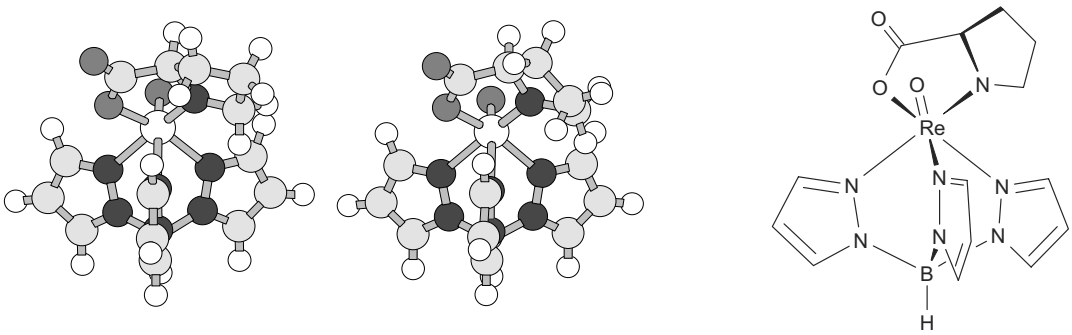

Figure 7. The two optimized conformers of R_{Re},R_C-**3**, **3-I** (left, 51%) and **3-II** (center, 49%). Geometries optimized using B3LYP/6-31G*/Stuttgart.

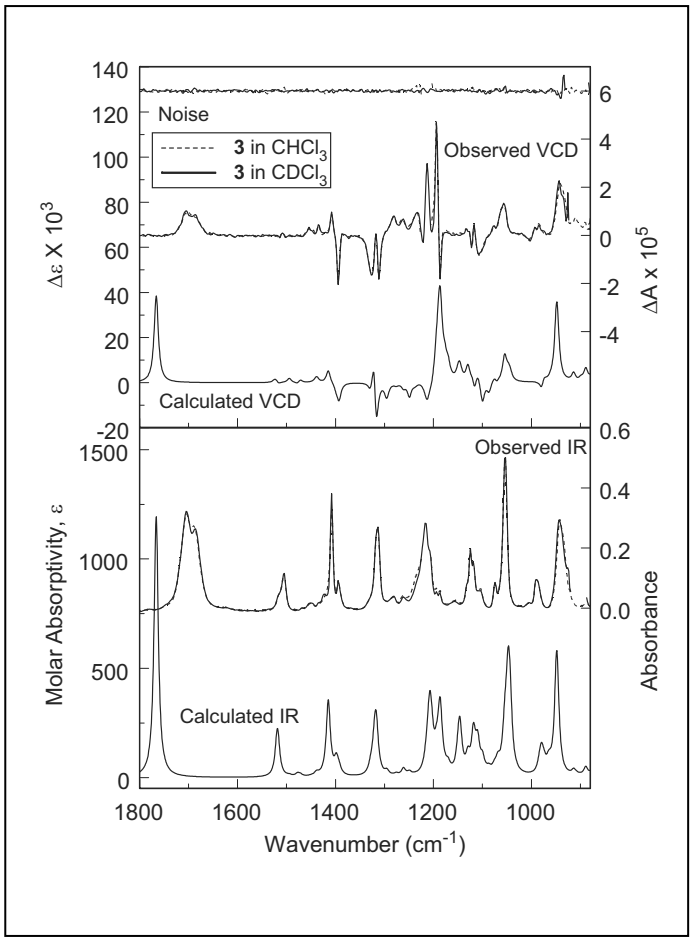

Figure 8. Expeimental IR (bottom) and VCD (top) spectra for (-)-**3**, with VCD noise as the uppermost trace (right axes, both chloroform and deuterated chloroform solutions; 5 mg/150 μL solvent (63 mM); IR spectra solvent subtracted; VCD spectra enantiomer subtracted; 4 cm^{-1} resolution; instrument optimized at 1400 cm^{-1}; collection time 12 h) compared to calculated spectra for R_{Re},R_C-**3** (left axes, B3LYP/6-31G*/Stuttgart; frequencies scaled by 0.97; bandwidth to 5 cm^{-1}) averaged for the two conformers **3-I** and **3-II**.

Figure 9. The two conformers of R_C,R_{Re}-**4a**, **4a-I** (left, 97%) and **4a-II** (center, 3%), optimized using B3LYP/6-31G*/Stuttgart.

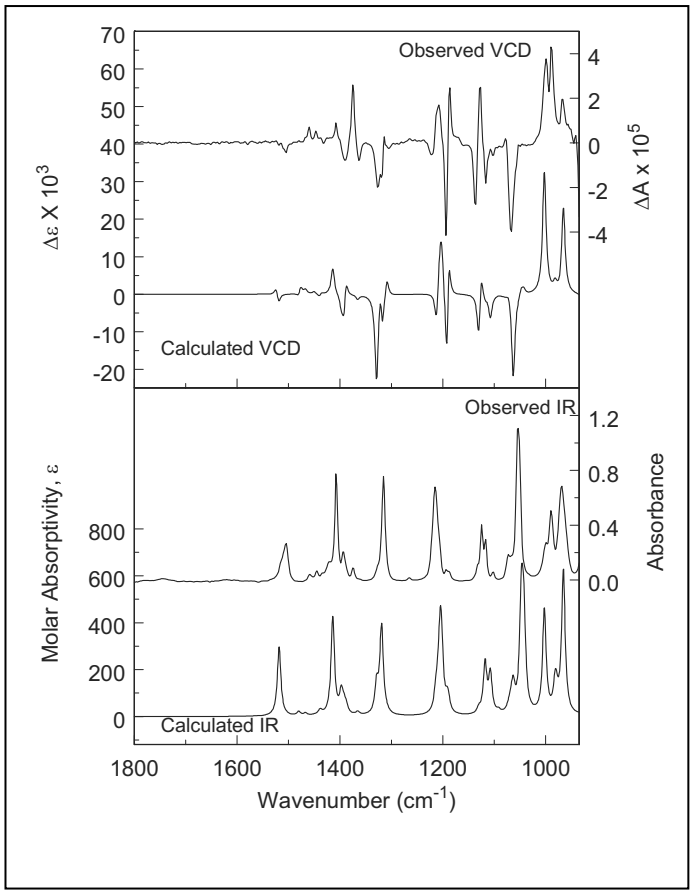

Figure 10. IR (bottom) and VCD (top) spectra for R_C,R_{Re}-**4a**. Calculated spectra (left axis) are weighted averages of the two conformers 87% **4a-I** + 13% **4a-II** determined using B3LYP/6-31G*/Stuttgart. Frequencies are scaled by 0.97, and the bandwidth is set to 4 cm^{-1}. Observed spectra for (-)-**4b** (right axis, 4 mg/100 μL $CDCl_3$ (81 mM)) are solvent subtracted, resolution 4 cm^{-1}; instrument optimized at 1400 cm^{-1}; collection time 9 h.

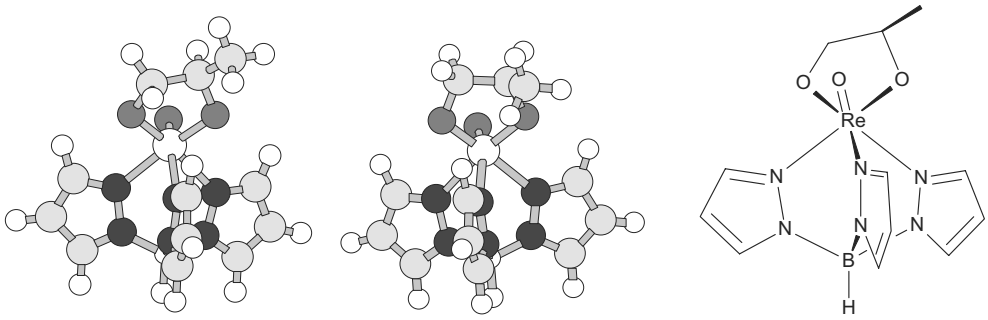

Figure 11. The two conformers of S_C,R_{Re}-**4b**, **4b-I** (left, 87%) and **4b-II** (center, 13%), optimized using B3LYP/6-31G*/Stuttgart.

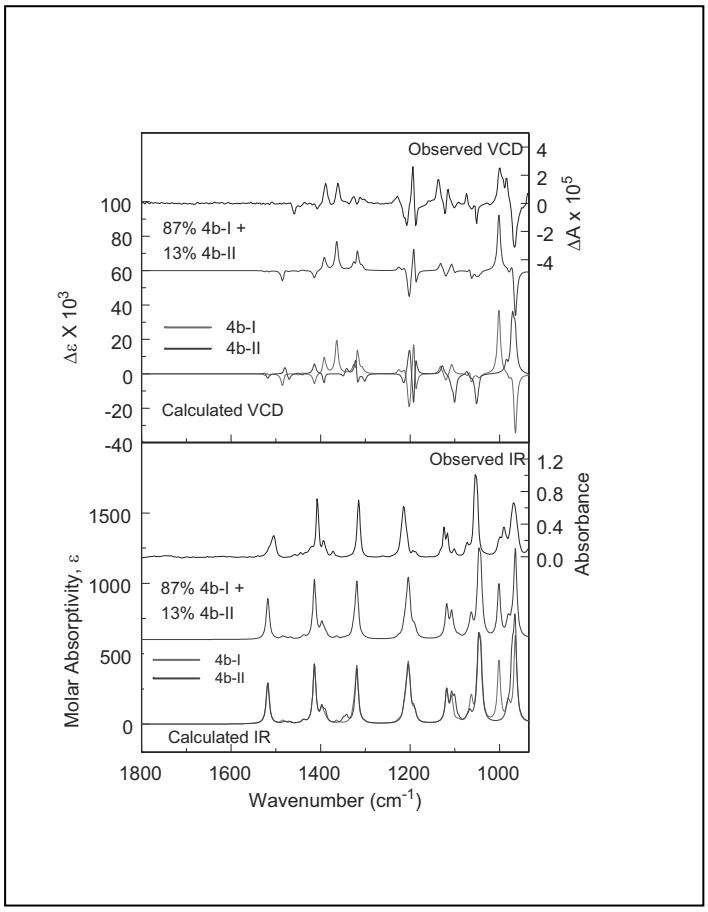

Figure 12. IR (bottom) and VCD (top) spectra for S_C,R_{Re}-**4b**. Calculated spectra (left axis) are weighted averages of the two conformers **4b-I** and **4b-II** determined using B3LYP/6-31G*/Stuttgart. Frequencies scaled by 0.97, bandwidth 4 cm^{-1}. Observed spectra for (-)-4b (right axes, 4 mg/100 μL $CDCl_3$ (81 mM)) are solvent subtracted; resolution 4 cm^{-1}; instrument optimized at 1400 cm^{-1}; collection time 9 h.

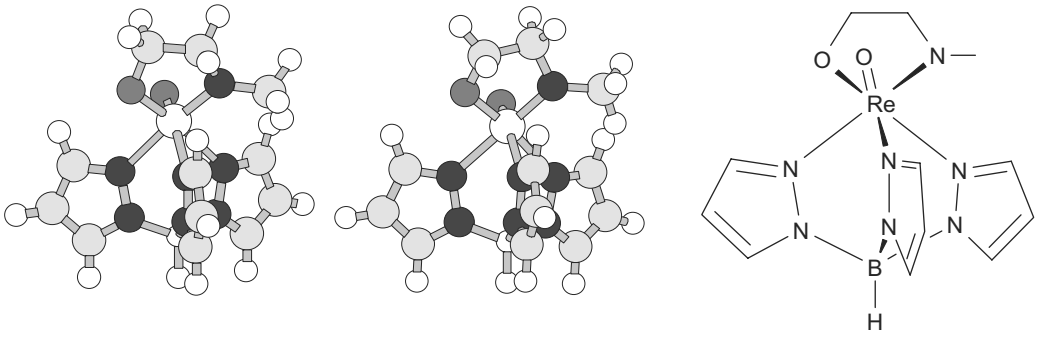

Figure 13. The two conformers of R_{Re}-**5**, **5-I** (left, 62%) and **5-II** (right, 38%), optimized using B3LYP/6-31G*/Stuttgart.

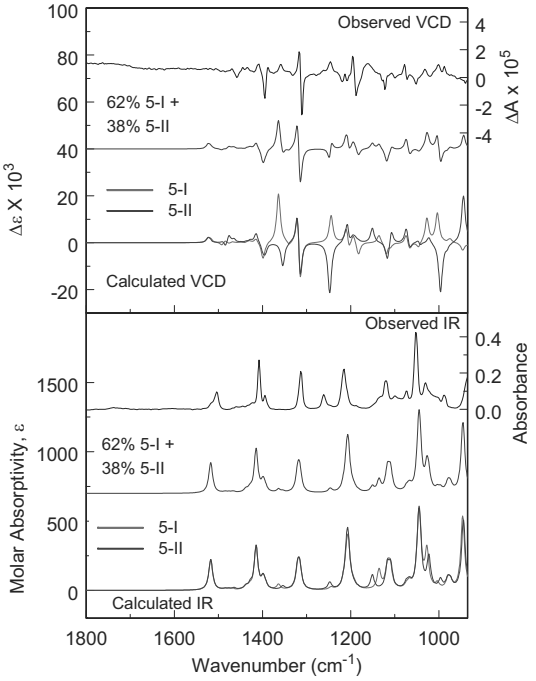

Figure 14. IR (bottom) and VCD (top) spectra for R_{Re}-**5**. Calculated spectra of the two conformers **5-I** and **5-II** and their Boltzmann-population weighted sum (left axes, B3LYP/6-31G*/Stuttgart; frequencies scaled by 0.97; bandwidth 5 cm^{-1}) compared to observed spectra for (-)-**5** (right axes, 3 mg/100 μL $CDCl_3$ (61 mM); solvent subtracted; resolution 4 cm^{-1}; instrument optimized at 1400 cm^{-1}; collection time 12 h).

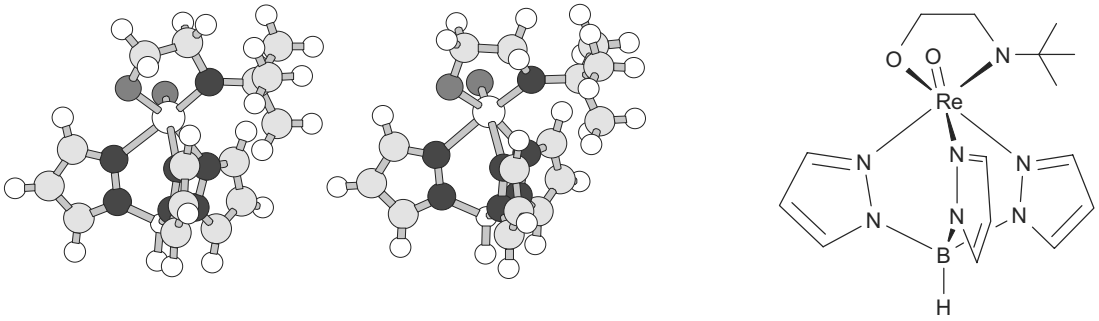

Figure 15. The two conformers of R_{Re}-**6, 6-I** (left, 98%) and **6-II** (center, 2%), optimized using B3LYP/6-31G*/Stuttgart.

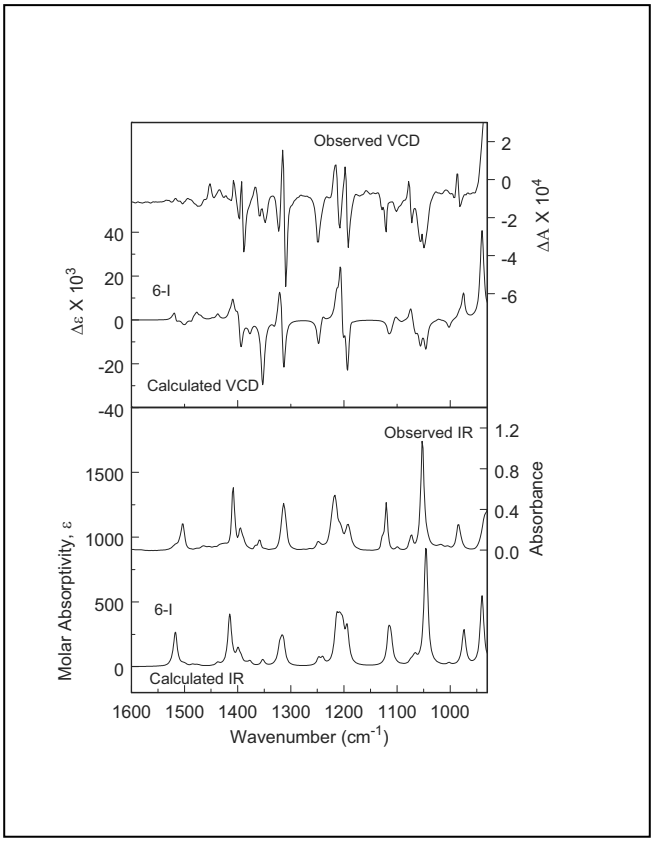

Figure 16. IR (bottom) and VCD (top) spectra for R_{Re}-**6**. Calculated spectra of the predominant conformer **6-I** (left axis; B3LYP/6-31G*/Stuttgart; frequencies scaled by 0.97; bandwidth 4 cm^{-1}) compared to observed spectra for (-)-**6** (right axis; 4.8 mg/100 μL $CDCl_3$; solvent subtracted; resolution 4 cm^{-1}; instrument optimized at 1400 cm^{-1}; collection time is 12 h).

Table 1. Crystallographic data for compounds **4a**, **4b** and **5**.

	R_{Re},R_C-(+)-**4a**	R_{Re},S_C-(-)-**4b**	**5**
Empirical formula	C12 H16 B N6 O3 Re	C12 H16 B N6 O3 Re	C12 H17 B N7 O2 Re
Formula weight	489.32	489.32	488.34
Crystal system	monoclinic	orthorhombic	monoclinic
Space group	P 2_1	P 2_1 2_1 2_1	P 2_1/n
Unit cell dimensions	a = 8.3663(5) Å b = 8.3379(5) Å c = 11.3364(8) Å β = 101.869(3)°	a = 7.7937(4) Å b = 18.9861(10) Å c = 31.4245(17)Å	a = 10.4580(2) Å b = 10.6516(3) c = 14.5438(4) Å β = 96.703(1)
Unit cell volume (Å^3)	773.89(9)	4649.9(4)	1609.02(7)
Z	2	12	4
Calculated density	2.100	2.097	2.016
Absorption coef. (mm^{-1})	7.874	7.863	7.572
F000	468	2808	936
Crystal size (mm^3)	0.25 x 0.25 x 0.20	0.30 x 0.02 x 0.02	0.38 x 0.35 x 0.32
θ range for data collection	2.77 – 27.62	1.68 – 27.61	2.74 – 27.58
Limiting indices	-10 ≤ h ≤ 10 -10 ≤ k ≤ 9 -14 ≤ l ≤ 14	-10 ≤ h ≤ 9 -24 ≤ k ≤ 24 -40 ≤ l ≤ 40	-13 ≤ h ≤ 13 -13 ≤ k ≤ 13 -18 ≤ l ≤18
Reflections collected / unique	5310 / 3344	58695 / 10698	28509 / 3691
Rint	0.034	0.045	0.040
Completeness to θ_{max}	96.7%	99.3%	99.1%
Transmission coef. max / min	0.207 / 0.140	0.854 / 0.095	0.151 / 0.056
Data / restraints / parameters	3344 / 1 / 028	10698 / 0 / 622	3691 / 0 / 208
Goodness of fit on F^2	1.105	0.995	1.058
Final R indices [I>2sig(I)]: R1 / wR2	0.0352 / 0.0891	0.0207 / 0.0340	0.0276 / 0.0685
Final R indices [all data]: R1 / wR2	0.0392 / 0.0905	0.0261 / 0.0349	0.0335 / 0.073
Absolute structure parameter	0.081(18)	-0.014(4)	
Largest diff. peak and hole (e.Å^{-3})	4.58 / -2.41	0.68 / -0.59	1.46 / -1.90

Table 2. Summary of Results for VCD Analysis

Sample	**2**	**3**	**4a**	**4b**	**5**	**6**
Absolute Configuration	R_{Re},$R_{O\text{-}C}$,$S_{C\text{-}N}$-(+)	R_{Re},R_{C}-(-)	R_{Re},R_{C}-(+)	R_{Re},S_{C}-(-)	R_{Re}-(-)	R_{Re}-(-)
Molecular weight (g/mol)	578.452	528.349	489.312	489.312	488.327	530.408
Calculated conformer populations (23°C)	100 % (**2-I**)	51% (**3-I**) 49% (**3-II**)	97% (**4a-I**) 3% (**4a-II**)	89% (**4b-I**) 13% (**4b-II**)	62% (**5-I**) 38% (**5-II**)	98% (**6-I**) 2% (**6-II**)
Calculated Re=O stretch (cm^{-1}) scaled by 0.97 and VCD rotational strengths[a]	941 (+141)	949 (**3-I**) (+120) 946 (**3-II**) (+158)	965 (**4a-I**) (+68) 963 (**4a-II**) (-129)	965 (**4b-I**) (-107) 965 (**4b-II**) (+64)	946 (**5-I**) (-11) 944 (**5-II**) (+75)	940 (**6-I**) (+124) 942 (**6-II**) (+48)
Observed Re=O stretch (cm^{-1}) and VCD sign	934 (+)	943 (+)	966 (+)	965 (-)	not observed	940 (+)

[a]Calculated rotational strength for Re=O stretch, $10^{-44}esu^2cm^2$.

Reference section

[1] a) Morris, L. J.; Downs, A. J.; Greene, T. M.; McGrady, G. S.; Herrmann, W. A.; Sirsch, P.; Scherer, W.; Gropen, O. *Organometallics* **2001**, *20*, 2344-2352 and references therein. b) Kennedy-Smith, J. J.; Nolin, K. A.; Gunterman, H. P.; Toste, F. D. *J. Am. Chem. Soc.* **2003**, *125*, 4056-4057. c) Morrill, C.; Grubbs, R. H. *J. Am. Chem. Soc.* **2005**, *127*, 2842-2843. d) Rudolph, J.; Reddy, K. L.; Chiang, J. P.; Sharpless, K. B. *J. Am. Chem. Soc.* **1997**, *119*, 6189-6190. e) Cai, Y.; Espenson, J. H. *Inorg. Chem*. **2005**, *44*, 2560-2565. f) Ison, E. A. ; Trivedi, E. R. ; Corbin, R. A.; Abu-Omar, M. M. *J. Am. Chem. Soc.* **2005**, *127*, 15374-15375.

[2] a) Nicolini, A.; Bandoli, G.; Mazzi, U. *Technetium, Rhenium and Other Metals in Chemistry and Nuclear Medicine, 5*; Raven Press: New York, 2000. b) Liu, S. *Chem. Soc. Rev.* **2004**, *33*, 445-461. c) Jurisson, S. S.; Lydon, J. D. *Chem. Rev.* **1999**, *99*, 2205-2218.

[3] Schwerdtfeger, P.; Bast, R. *J. Am. Chem. Soc.* **2004**, *126*, 1652-1653.

[4] Quack, M. *Angew. Chem. Int. Ed.* **2002**, *41*, 4618-4630 and references therein.

[5] a) Bouchiat M. A.; Bouchiat, C. C. *Phys. Lett.* **1974**, *48B*, 111-114. b) Barkov, L. M.; Zolotorev, M. S. *JETP* **1980**, *52*, 360-376. c) Bouchiat, M. A.; Bouchiat, C. C. *Rep. Prog. Phys*. **1997**, *60*, 1351-1396. d) Wood, C. S.; Bennett, S. C.; Cho, D.; Masterson, B. P.; Roberts, J. L.; Tanner, C. E.; Wieman, C. E. *Science* **1997**, *275(5307),* 1759-1763. e) Wu, C. S.; Ambler, E.; Hayward, R.; Hoppes, W. D. D.; Hudson, R. P. *Phys. Rev.* **1957**, *105*, 1413-1415.

[6] a) Crassous, J.; Chardonnet, C.; Saue, T.; Schwerdtfeger, P. *Org. Biomol. Chem*. **2005**, *3*, 2218-2224. b) Crassous, J.; Monier, F.; Dutasta, J. P.; Ziskind, M.; Daussy, C.; Grain, C.; Chardonnet, C. *ChemPhysChem* **2003**, *4*, 541-548.

[7] a) Daussy, C.; Marrel, T.; Amy-Klein,A.; Nguyen, C. T.; Bordé, C. J.; Chardonnet, C. *Phys. Rev. Lett.* **1999**, *83*, 1554-1557. b) Chardonnet, C.; Daussy, C.; Marrel, T.; Amy-Klein, A.; Nguyen, C. T.; Bordé, C. J. in Parity *violation in atomic physics and electron scattering,* B. Frois and M.A. Bouchiat (eds.), World Scientific, New-York, 1999, 325-355. c) Chardonnet, C.; Marrel, T.; Ziskind, M.; Daussy, C.; Amy-Klein, A.; Bordé, C. J. *J. Phys. IV (France)* **2000**, *10-Pr8*, 45-54.

[8] a) Schwerdtfeger, P.; Gierlich, J.; Bollwein, T. *Angew. Chem., Int. Ed.* **2003**, 42, 1293-1296. b) Laerdahl, J. K.; Schwerdtfeger, P.; Quiney, H. M. *Phys. Rev. Lett.* **2000**, *84*, 3811-3814.

[9] Schwerdtfeger, P.; Saue, T.; van Stralen, J. N. P.; Visscher, L. *Phys. Rev. A* **2005**, *71*, 012103-1-7.

[10] Shelkovnikov, A.; Grain, C.; Butcher, R.J.; Amy-Klein, A.; Goncharov, A.; Chardonnet, C. *IEEE-J. of Quant. Electron* **2004**, *40*, 1023-1029.

[11] a) Nolin, K. A. ; Ahn, R. W. ; Toste, F. D. *J. Am. Chem. Soc.* **2005**, *127*, 12462-12463. b) Faller, J. W.; Lavoie, A. R. *Organometallics* **2000**, *19*,3957-3962. c) Parr, M. L.; Perez-Acosta, C.; Faller. J. W. *New. J. Chem.* **2005**, *29*, 613-619. d) Rybak, W. K.; Sharzynska, A.; Glowiak, T. *Angew. Chem. Int. Ed.* **2003**, *42*, 1725-1727. e) Rybak, W. K.; Sharzynska, A.; Szterenberg, L.; Ciunik, Z.; Glowiak, T. *Eur. J. Inorg. Chem.* **2005**, 4964-4975. f) Hansen, L.; Yue, K. T.; Xu, X.; Lipowska, M.; Taylor, A.; Jr.; Marzilli, L. G. *J. Am. Chem. Soc.* **1997**, *119*, 8965-8972. g) Herrmann, W. A.; Marz, D. W.; Herdtweck, E. *J. Organomet. Chem.* **1990**, *394*, 285-303. h) Tessier, C.; Rochon, F. D.; Beauchamp, A. L. *Inorg. Chem.* **2002**, *41*, 6527-6536. i) Melian, C.;

Kremer, C.; Suescun, L.; Mombru, A.; Mariezcurrena, R.; Kremer, E. *Inorg. Chim. Acta* **2000**, *306*, 70-77. j) Gable, K. P.; Khownium, K.; Chuawong, P.; *Organometallics* **2004**, *23*, 5268-5274.

[12] Freedman, T. B.; Cao, X.; Dukor, R. K.; Nafie, L. A. *Chirality* **2003**, *15*, 743-758.

[13] (a) Holzwarth, G.; Hsu, E.; Mosher, H.; Faulkner, T.; Moscowitz, A. *J. Am. Chem. Soc*. **1974**, *96*, 251-2. (b) Nafie, L. A.; Cheng, J.; Stephens, P. *J. Am. Chem. Soc*. **1975**, *97*, 3842-3.

[14] (a) He, Y.; Cao, X.; Nafie, L. A.; Freedman, T. B. *J. Am. Chem. Soc*. **2001**, *123*, 11320-11321. (b) Freedman, T. B.; Cao, X.; Young, D. A.; Nafie, L. A. *J. Phys. Chem. A* **2002**, *106*, 3560-3565.

[15] Roussel, C. ; Piras, P. CHIRBASE http://chirbase.u-3mrs.fr. CHIRBASE, Database current status and derived research applications using molecular similarity, decision tree and 3D « enantiophore » search. pp. 95-125. Roussel, C.; Pierrot-Sanders, J.; Heitmann, I.; Piras, P. In: *Chiral Separation Techniques - A Practical Approach*, Second, completely revised and updated edition, Edited by G. Subramanian, Wiley-VCH, Weinheim, 2001.

[16] a) Ramsden, J. A.; Garner, C. M.; Gladysz, J. A. *Organometallics* **1991**, *10*, 1631-1633. b) Green, J. M.; Jones, R.; Harrison, R. D.; Edwards, D. S.; Glajch, J. L. *J. Chromatogr.* **1993**, *635*, 203-209. c) Ciruelos, S.; Englert, U.; Salzer, A.; Bolm, C.; Maischak, A. *Organometallics* **2000**, *19*, 2240-2242.

[17] Romao, C. C. ; Kuhn, F. E. ; Herrmann, W. A. *Chem. Rev.* **1997**, *97*, 3197-3246.

[18] Andrae, D.; Haussermann, U.; Dolg, M.; Stoll, H.; Preuss, H. *Theor. Chim. Acta* **1990**, *77*, 123-41.

[19] T. H., Jr. Dunning and P. J. Hay, in *Modern Theoretical Chemistry,* Schaefer, H. F., III, Ed.; Plenum: New York, 1976; Vol. 3, pp 1-28.

[20] Hay, P. J.; Wadt, W. R. *J. Chem. Phys.* **1985**, *82*, 299-310.

[21] Wadt, W. R.; Hay, P. J. *J. Chem. Phys.* **1985**, *82*, 284-98.

[22] Hay, P.; Wadt, W. *J. Chem. Phys*. **1985**, *82*, 299-310.

Yanan He, Mimi Mak, Craig Cone, Peter R. Lassen, Laurence A. Nafie, and Teresa B. Freedman: Resonance Enhanced VCD in Chiral Co(II) Schiff-Base Complexes: Experimental Measurement and DFT Calculation.

Manuscript in preparation.

6

6

Resonance Enhanced VCD in Chiral Co(II) Schiff-Base Complexes: Experimental Measurement and DFT Calculation

Yanan He, Mimi Mak, Craig Cone, Peter Lassen, Laurence A. Nafie and Teresa B. Freedman
Department of Chemistry, Syracuse University, Syracuse, New York 13244-4100

Abstract

A ten to 30-fold increase in vibrational circular dichroism (VCD) intensity is observed for several chiral Co(II) Schiff base complexes compared to corresponding Ni(II), Zn(II) or Mn(III) complexes. The effect, termed resonance enhanced VCD (REVCD), is attributed to the occurrence of low-lying, magnetic-dipole-allowed, electronic d-d transitions, in the infrared region with energies comparable to the vibrational frequencies, that enhance the vibrational magnetic dipole transition moment. Calculations at the DFT level with Ahlrich VTZ basis set for cobalt reproduce the magnitudes of the REVCD for the low-spin, approximately square-planar chiral Co(II) salen (CoSA, (*R,R*)-(+)-N,N'-Bis(3,5-di-tert-butylsalicylidene)-1,2-cyclohexanediaminocobalt(II)) and Co(II) saldiphenyl ((*R,R*)-[N,N'-Bis(salicylidene)-1,2-diphenyl-1,2-ethanediaminenato]-Co(II)) Schiff-base complexes and some of the enhancement for the high-spin pseudotetrahedral Co(II) salbinaphthyl complex ((*R,R*)-[[2,2'-[[1,1'-binaphthalene]-2,2'-diylbis(nitrilomethylidyne)]-bis(phenolato)](2-)-N,N',O,O']-Co(II)). DFT calculations with the smaller LanL2DZ basis set are sufficient to reproduce the non-enhanced VCD intensities for the Mn(III) salen-Cl and Ni(II) saldiphenyl complexes. Formation of a μ-peroxo bridged dimer through oxidative addition to Co(III) is demonstrated by loss of REVCD intensity as CoSA is titrated with 1-methylimidazole in the presence of oxygen.

Introduction. Vibrational circular dichroism (VCD) intensities are typically associated with anisotropy ratios ($\Delta A/A$) on the order of 10^{-4} to 10^{-5} and molar absorptivity differences ($\Delta\varepsilon$) in the 10^{-1} to 10^{-3} range, and these intensities are reproduced with DFT calculations.[1,2] However, anisotropy ratios and VCD intensities ten to 100 times larger have been observed for stretches of ligands bound to certain metalloproteins and for vibrations of metal complexes when the metal has magnetic-dipole allowed electronic d-d transitions in the infrared region (below 4000 cm^{-1}). Such systems include tetrahedral high-spin Ni(II) and Co(II) complexes with (-)-sparteine,[3,4] and azide and cyanide bound to low-spin Fe(III) in metmyoglobin.[5,6] We examine here chiral Schiff-base complexes (Scheme 1) with both pseudoplanar and pseudotetrahedral coordination and high- and low-spin states for the metal ion, identifying a new class of metal center geometry and spin-state for which VCD intensity enhancement is generated, which we term resonance-enhanced VCD (REVCD). The Schiff-base complexes are important catalysts for asymmetric synthesis including enantioselective hydrogenation and epoxidation of alkenes and other reactions.[7-9] Some of the complexes bind oxygen reversibly,[10-16] and we also examine the effect of oxygen-binding on the REVCD spectra. Whereas our previous attempts to calculate REVCD for high-spin pseudotetrahedral complexes of Co(II) and Ni(II) with (-)-sparteine, using commericial DFT implementations[17,18] for VCD intensity calculations, were not successful,[3] we demonstrate here calculations that reproduce the intensity enhancement for chiral low-spin pseudoplanar Co(II) complexes and verify the mechanism of enhancement.

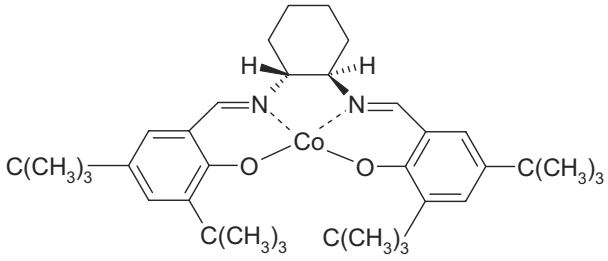

(*R,R*)-CoSA **1**

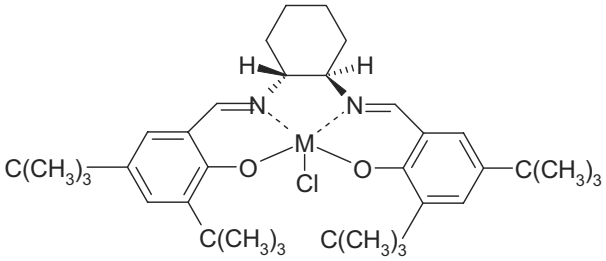

(*R,R*)-MClSA (M = Al(III), Cr(III) and Mn(III)) **2**

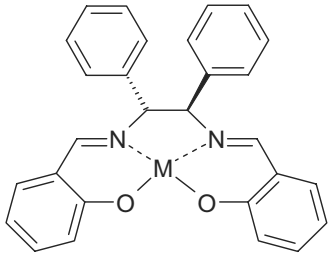

(*R,R*)-MSaldiphenyl (M = Co(II) and Ni(II)) **3**

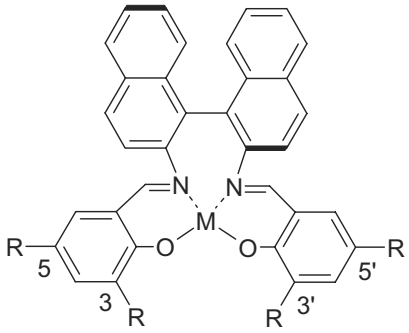

(*R*)-MR$_4$Salbinapht
(R = H or Cl, M = Co(II), Ni(II) and Zn(II)) **4**

Scheme 1 Schiff-base Metal Complexes

Experimental: (*R,R*)-(-)- and (*S,S*)-(+)-N,N'-Bis(3,5-di-tert-butylsalicylidene)-1,2-cyclohexanediaminocobalt(II) (**1**, abbreviated as (*R,R*)- and (*S,S*)-CoSA), and (*R,R*)-(-)-N,N'-Bis(3,5-di-tert-butylsalicylidene)-1,2-cyclohexanediaminoM(III) chloride (**2**, M = Al(III), Cr(III), Mn(III); abbreviated as (*R,R*)-AlClSA, (*R,R*)-CrClSA) and (*R,R*)-MnClSA) were purchased from Aldrich and used without further purification. (*R,R*)- and (*S,S*)-[N,N'-Bis(salicylidene)-1,2-diphenyl-1,2-ethanediaminenato]-M(II) (**3**, abbreviated as (*R,R*)- and (*S,S*)-MSaldiphenyl; M = Co(II), Ni(II)) and (*R,R*)- and (*S,S*)-[[2,2'-[[1,1'-binaphthalene]-2,2'-diylbis(nitrilomethylidyne)]bis[4,6-dichlorophenolato]](2-)-N,N',O,O']-M(II) (**4**, abbreviated as (*R,R*)- and (*S,S*)-MCl$_4$Salbinapht; M = Co(II), Ni(II), Zn(II)) and (*R,R*)- and (*S,S*)-[[2,2'-[[1,1'-binaphthalene]-2,2'-diylbis(nitrilomethylidyne)]-bis(phenolato)](2-)-N,N',O,O']-Co(II) (abbreviated as (*R,R*)- and (*S,S*)-CoH$_4$Salbinapht) complexes were synthesized following literature procedures from the appropriate diamine and salicylaldehyde by refluxing in ethanol to produce the Schiff-base, followed by reluxing in methanol with the appropriate metal acetate and sodium methoxide to generate the metal complex.[9,19]

For VCD measurement, the metal complexes were dissolved in $CDCl_3$ at an appropriate concentration and placed cell with BaF_2 windows at a suitable pathlength to obtain IR intensity for bands of interest in the range 0.2 to 1 to obtain a good signal to noise ratio. For the mid-IR region (800-2000 cm^{-1}) the VCD spectra were measured for 1 hour with 4 or 8 cm^{-1} resolution on a modified Chiral*IR* VCD spectrometer (BioTools, Inc., Wauconda, IL) configured with two photoelastic modulators (PEMs).[1,20,21] Some measurements on this instrument were also obtained for the larger 4000 -800 cm^{-1} region. For the C-H stretching region (2000-4000 cm^{-1}) and near-IR region (4000-6000 cm^{-1}) the VCD spectra were measured for 4 hours with 8 or 16 cm^{-1} resolution on modified Chiral*IR* VCD spectrometers equipped for higher vibrational frequency coverage with two tungsten

halogen sources, two CaF_2 PEMs and either a thermoelectrically-cooled MCT detector with coverage from 2000 to 4000 cm^{-1}, or a room-temperature InGaAs detector with coverage from 4000 to 7000 cm^{-1}.[22,23] The VCD and IR baselines were corrected by subtracting the VCD or IR spectrum of the solvent from that of the sample.

Calculation: The VCD and IR spectra were calculated with Gaussian 03[18] at the DFT level (B3LYP functional) with 6-31G(d) basis set for the ligand and Ahlrich VTZ basis set[24] for Co(II) or Ni(II) for (*R,R*)-CoSA, (*R*,*R*)-CoSaldiphenyl, (*R*,*R*)-NiSaldiphenyl and (*R*)-CoSalbinapht, and with the LanL2DZ basis set[25,26] for a model for (*R*,*R*)-MnClSA without the *t*-butyl groups. The magnetic field perturbation (MFP) method[17,27] for VCD intensities is incorporated into Gaussian 03, utilizing gauge-invariant atomic orbitals.[2,28,29]

Theoretical Background

VCD intensity is proportional to the rotational strength, the scalar product of electric and magnetic dipole transition moments for ground electronic state *g* and 0→1 transition of vibrational mode *a*, Eq. (1),[30]

$$R_{10}^{a} = \mathrm{Im}\left\langle \Psi_{g1}^{a} \middle| \hat{\mu}_{\beta} \middle| \Psi_{g0}^{a} \right\rangle \cdot \left\langle \Psi_{g1}^{a} \middle| \hat{m}_{\beta} \middle| \Psi_{g0}^{a} \right\rangle \tag{1}$$

Calculation of the rotational strength *R* requires the electronic contribution to the atomic axial tensor for atom *A*, $I_{\alpha\beta}^{A}$, derived from the second derivative of the electronic energy (E_{el}) with respect to magnetic field (***H***) and nuclear velocity ($\dot{\boldsymbol{R}}$), a non-Born-Oppenheimer quantity.[30] The magnetic dipole transition moment is expanded as

$$\left\langle \Psi_{g1}^{a} \middle| \hat{m}_{\beta}^{E} \middle| \Psi_{g0}^{a} \right\rangle = \sum_{A,\alpha} \left(\frac{\partial m_{\beta}^{E}}{\partial \dot{R}_{A,\alpha}} \right)_{0} s_{A\alpha,a} \left\langle \phi_{g1}^{a} \middle| P_{a} \middle| \phi_{g0}^{a} \right\rangle \tag{2}$$

where $R_{A,\alpha}$ gives the position of atom *A* (α = x, y, z), P_a is the conjugate momentum for mode Q_a with angular frequency ω_a, $s_{A\alpha,a} = \left(\partial \dot{R}_{A\alpha} / \partial P_a\right)_0 = \left(\partial R_{A\alpha} / \partial Q_a\right)_0$ is the displacement of atom A in the α-direction for normal mode *a*, and ϕ_{gi}^{a} are the vibrational wavefunctions. We then introduce equivalent expressions for the atomic axial tensor $I_{\alpha\beta}^{A}$:

$$\left(\frac{\partial m_{\boldsymbol{\beta}}^{E}}{\partial \dot{R}_{A\boldsymbol{\alpha}}} \right)_{0} = I_{\alpha\beta}^{A} = -\left(\frac{\partial E_{\mathrm{el}}}{\partial H_{\beta} \partial \dot{R}_{\mathrm{A}\alpha}} \right)_{0} = -2\mathrm{i}\hbar \left(\left\langle \frac{\partial \tilde{\psi}_{g}}{\partial R_{A\alpha}} \middle| \frac{\partial \tilde{\psi}_{g}}{\partial H_{\beta}} \right\rangle \right)_{0} = 2\mathrm{i}\hbar \sum_{\mathrm{e} \neq \mathrm{g}} \frac{\left\langle \psi_{\mathrm{g}}^{0} \middle| \hat{m}_{\beta} \middle| \psi_{\mathrm{e}}^{0} \right\rangle \left\langle \psi_{\mathrm{e}}^{0} \middle| \left(\partial \psi_{\mathrm{g}} / \partial R_{A\alpha} \right)_{0} \right\rangle}{E_{e}^{0} - E_{g}^{0}} \tag{3}$$

MFP VCT

The third equality in Eq. (3) is the magnetic field perturbation (MFP) expression[27] incorporated into Gaussian 03 for VCD calculations, which depends on derivatives of the ground-state electronic complex wavefunction $\tilde{\psi}_g$. The implementation of the MFP formalism in Gaussian employs gauge-invariant atomic orbitals (GIAOs) for the magnetic-field derivatives and hence achieves an origin-independent rotational strength.[2,28,29] The last equality in Eq. (3) is the formally equivalent, vibronic coupling theory (VCT) sum-over-states expression,[31] where $\hat{\mathbf{m}}$ is the magnetic-dipole moment operator and the sum is over all excited electronic states *e*. The VCT expression shows how a low-lying electronic state (LLES) that is strongly magnetic-dipole allowed and vibrationally coupled to the ground state can lead to enhancement of the VCD intensity. When the electronic transition energies are comparable to vibrational frequencies, the VCT expression must be modified as shown below (Eq. (6)), but direct dependence on the VCT expression in Eq. (3) remains. One goal of the present study is to evaluate to what extent the current implementation of the MFP expression in Eq. (3) in Gaussian 03 can be applied to calculate REVCD in chiral Schiff-base complexes with LLES.

The neglect of vibronic detail in excited electronic states of the VCD formalism is an approximation that fails in the case of low-lying electronic states where the electronic state energy is comparable to that of the vibrational transition energy, and a theoretical correction to the standard formalism has recently been developed.[32] The standard sum-over-states expression for the electronic contribution to the magnetic-dipole transition moment (Eq. 2) is given by[31,33]

$$\left\langle \Psi^a_{g1} \middle| \hat{m}^E_\beta \middle| \Psi^a_{g0} \right\rangle = \left[2i\hbar \sum_{e\neq g} \sum_{A,\alpha} \frac{\left\langle \psi^0_g \middle| \hat{m}^E_\beta \middle| \psi^0_e \right\rangle \left\langle \psi^0_e \middle| (\partial \psi_g / \partial R_{A,\alpha})_0 \right\rangle}{E^0_e - E^0_g} \right] s_{A\alpha,a} \left\langle \phi^a_{g1} \middle| P_a \middle| \phi^a_{g0} \right\rangle \quad (4)$$

If this expression is generalized to include vibronic detail for the excited electronic states, one has[32]

$$\left\langle \Psi^a_{g1} \middle| \hat{m}^E_\beta \middle| \Psi^a_{g0} \right\rangle = i\hbar \sum_{ev\neq g0} \sum_{A,\alpha} \left[\frac{\left\langle \psi^0_g \middle| \hat{m}^E_\beta \middle| \psi^0_e \right\rangle \left\langle \psi^0_e \middle| (\partial \psi_g / \partial R_{A,\alpha})_0 \right\rangle \left\langle \phi^a_{g1} \middle| \phi_{ev} \right\rangle \left\langle \phi_{ev} \middle| P_a \middle| \phi^a_{g0} \right\rangle}{E^0_{ev} - E^0_{g0}} \right.$$

$$\left. + \frac{\left\langle \psi^0_g \middle| (\partial \psi_e / \partial R_{A,\alpha})_0 \right\rangle \left\langle \psi^0_e \middle| \hat{m}^E_\beta \middle| \psi^0_g \right\rangle \left\langle \phi^a_{g1} \middle| P_a \middle| \phi_{ev} \right\rangle \left\langle \phi_{ev} \middle| \phi^a_{g0} \right\rangle}{E^0_{ev} - E^0_{g1}} \right] s_{A\alpha,a} \quad (5)$$

Removal of vibronic detail in Eq. (5) allows reduction to Eq. (4). Under the assumption that the vibrational sublevels of the low-lying excited states are the same as those of the ground electronic state, the expression for Eq. (5) can be written as

$$\left\langle \Psi^a_{g1} \middle| \hat{m}^E_\beta \middle| \Psi^a_{g0} \right\rangle = 2i\hbar \sum_{e\neq g} \sum_{A,\alpha} \frac{\left\langle \psi^0_g \middle| \hat{m}^E_\beta \middle| \psi^0_e \right\rangle \left\langle \psi^0_e \middle| (\partial \psi_g / \partial R_{A,\alpha})_0 \right\rangle s_{A\alpha,a}}{E^0_{eg}} \left(1 + \frac{{\omega_a}^2}{{\omega^0_{eg}}^2 - {\omega_a}^2} \right) \left\langle \phi^a_{g1} \middle| P_a \middle| \phi^a_{g0} \right\rangle \quad (6)$$

The expression in brackets is written as the sum of a term representing the standard magnetic-dipole transition moment in Eq. (4) plus a correction term that becomes significant only for electronic states with energy less than an order of magnitude above the vibrational energy levels. One can see a significant new source of intensity enhancement in the limit that the excited state energy and the vibrational energy are the same. The infinity in the resonance energy denominator can be avoided with appropriate damping terms representing the natural electronic and vibrational bandwidths. For most systems of interest, the VCD enhancement is approximately 10-fold, and the non-enhanced VCD contributions can be ignored or subtracted. REVCD could then be calculated by considering Eqs. (3) and (6) for only the low-lying electronic states *e'*:

$$I^A_{\alpha\beta}(\mathrm{e}', \omega_a) = 2i\hbar \sum_{\mathrm{e}'\neq \mathrm{g}} \frac{\left\langle \psi^0_{\mathrm{g}} \middle| \hat{m}_\beta \middle| \psi^0_{\mathrm{e}'} \right\rangle \left\langle \psi^0_{\mathrm{e}'} \middle| \left(\partial \psi_{\mathrm{g}} / \partial R_{A\alpha} \right)_0 \right\rangle}{E^0_{e'} - E^0_g} \left(1 + \frac{{\omega_a}^2}{{\omega^0_{\mathrm{e}'\mathrm{g}}}^2 - {\omega_a}^2} \right) \quad (7)$$

This is analogous to the approximations made for calculating resonance Raman intensities where only the resonant electronic state is needed in the formal sum over excited states.[34] The correction term is calculated individually for each LLES and for each normal mode of vibration, and imaginary damping terms can be incorporated to represent the finite spectral width of the LLES and the vibrational bandshape. We are initiating implemention of this expression, but the calculations included in the current study ignore the correction terms.

Results

Metal salen complexes (1 and 2). The IR and VCD spectra of (*R*,*R*)- and (*S*,*S*)-CoSA (**1**) measured on three VCD instruments, covering the spectral ranges in the fingerprint region (2000-930 cm^{-1}), hydrogen stretching (4000-2500 cm^{-1}) and CH-stretch/bend combination and CH-stretch overtone regions (6000-3900 cm^{-1}) are compared in Fig. 1, demonstrating the mirror-image nature of the VCD spectra for the two enantiomers and the occurrence of broad electronic circular dichroism (ECD) features centered ~4200 cm^{-1} and

~2200 cm^{-1}, both positive for (*R*,*R*)-CoSA. A weak negative ECD feature for (*R*,*R*)-CoSA occurs at 3700 cm^{-1}, and an additional positive ECD feature is evident above 6000 cm^{-1}. Hydrogen-stretching REVCD features occur superimposed on the ECD near 3000 cm^{-1}, and intense REVCD features are observed between 1650 and 1000 cm^{-1}, beyond the region of ECD. For (*R*,*R*)-CoSA, these latter REVCD features are primarily positive. The largest VCD anisotropy ratios for (*R*,*R*)-CoSA are +4.3 x 10^{-3} at 1528 cm^{-1} in the mid-IR region and -5.1 x 10^{-3} at 3020 cm^{-1} in the hydrogen-stretching region, an order of magnitude larger than for closed-shell metal complexes.[35] Shown in Fig. 2 are the mid-IR region IR and VCD spectra for the pentacoordinate (*R*,*R*)-MnClSA, (*R*,*R*)-CrClSA and (*R*,*R*)-AlClSA complexes, all of which do not have low-lying electronic states and for which the VCD intensity is not enhanced. The dramatic increase in intensity for REVCD is seen in the overlay of spectra for (*R*,*R*)-CoSA and (*R*,*R*)-MnClSA in Fig. 3, showing similar IR intensities, but a factor of 20-30 increase in VCD intensity for (*R*,*R*)-CoSA.

The optimized structures of (*R*,*R*)-CoSA and the model (*R*,*R*)-MnClSA' (without *t*-butyl groups) are shown in Fig. 4. (*R*,*R*)-CoSA has C_2 symmetry with a distorted square-planar coordination at the cobalt. (*R*,*R*)-MnClSA' has distorted square-pyramidal coordination at manganese. The intensity enhancement and most REVCD features are reproduced for (*R*,*R*)-CoSA at this level of DFT calculation with the Ahlrich VTZ basis set for low-spin Co(II)[24] (Fig. 5). Calculations were also carried out for (*R*,*R*)-CoSA with the LanL2DZ basis set[25,26] for both the high and low-spin Co(II) cases, demonstrating some intensity enhancement in each case, but with a poorer fit to experiment (Fig. 6). For the intense band observed near 1600 cm^{-1}, for example, the VCD intensity ($\Delta\varepsilon$) is ~+2.5 for the observed and Ahlrich VTZ calculation (low spin), ~+1.0 for the LanL2DZ calculation (low-spin) and ~+0.3 for LanL2DZ (high-spin). Intensities (LanL2DZ basis set) calculated for the low-spin case approximately three times larger than for high-spin. EPR data indicate that (*R*,*R*)-CoSA is low-spin.[Deeth, 1987 #56][Hitchman, 1977 #4] In contrast, the LanL2DZ basis set calculation for the model (*R*,*R*)-MnClSA' shows very good agreement in both magnitude and sign pattern with the experimental spectra for high-spin (*R*,*R*)-MnClSA (Fig. 7).

A comparison IR and VCD spectra of (*R*,*R*)-CoSA in $CDCl_3$ solution and in the solid as a mull in mineral oil is shown in Fig. 8, where the IR intensity of the mull has been scaled to that of the solution, with the same scale factor for the mull VCD, to estimate molar absorptivities for the mull for a better intensity comparison, since the concentration in the mull is not known. The VCD intensity in the solid is decreased by a factor of ~5 compared to solution, and the features, while still enhanced 5-fold relative to MnClSA, exhibit some similarities in pattern to the VCD of the trivalent metal complexes (see Fig. 2). The crystal structure of (*R*,*R*)-CoSA reveals that a dimer is formed in the solid[36] (Fig. 9), which can alter the low-lying electronic states.[Hitchman, 1977 #4] The coordination geometry at the cobalt center in the dimer resembles that of the trivalent metals in the MClSA complexes.

Metal saldiphenyl complexes (3). The IR and VCD spectra of (*R*,*R*)-CoSaldiphenyl and (*R*,*R*)-NiSaldiphenyl in $CDCl_3$ solution are compared in Fig. 10. The low-spin Co(II) complex exhibits a broad low-lying electronic CD feature centered at 2100 cm^{-1}, with intense, primarily negative REVCD features extending to lower frequencies beyond the electronic band envelope. The VCD anisotropy ratios are on the order of 10^{-3}, with the highest value ~6.7x10^{-3} at 1390 cm^{-1}. In contrast, low-spin (*R*,*R*)-NiSaldiphenyl, with no low-lying electronic states, generates VCD intensities an order of magnitude smaller than the (*R*,*R*)-CoSaldiphenyl VCD intensities. The calculated optimized geometries for the (*R*,*R*)-CoSaldiphenyl conformer with axial phenyl groups, the (*S*,*S*)-CoSaldiphenyl conformer with equatorial phenyl groups and the (*R*,*R*)-NiSaldiphenyl conformer with axial phenyl groups are compared in Fig. 11, and the ring puckering for the Co(II) diamine rings for the

saldiphenyl complexes are shown in Fig. 12, compared to that calculated for (*R*,*R*)-CoSA. In Fig. 13, the observed spectra for (*R*,*R*)-CoSaldiphenyl are compared with DFT calculations for the (*R*,*R*)-enantiomer conformer with axial phenyl groups and the (*S*,*S*)-enantiomer conformer with equatorial phenyl groups. The calculated VCD intensites for the (*S*,*S*)-equatorial and (*R*,*R*)-axial conformers are quite similar, and for the most intense bands, above 1550 cm^{-1}, show good agreement with experiment, allowing correlation of the VCD spectra in this region with the puckering of the Co(II) diamine ring (Fig. 12). The calculated energies place the equatorial conformer 1.2 kcal/mol higher in energy (12% population). Thus, the comparison of observed and calculated VCD spectra confirm the absolute configuration of the sample synthesized as (*R*,*R*), and identify a dominant axial phenyl group conformation in solution for CoSaldiphenyl.

The electronic CD for (*R*,*R*)-CoSA and (*R*,*R*)-CoSaldiphenyl near 2200 cm^{-1} have opposite sign, and the REVCD features for (*R*,*R*)-CoSaldiphenyl are predominantly negative, whereas those for (*R*,*R*)-CoSA are predominantly positive. We note that the Co(II) diamine ring puckering is opposite for the two complexes (Fig. 12), and both the electronic CD and REVCD correlate with these opposite chiral environments at the Co(II), rather than with the (*R*,*R*) absolute configuration designation.

The observed and calculated IR and VCD spectra for low-spin (*R*,*R*)-NiSaldiphenyl are compared in Fig. 14. The non-enhanced VCD intensity magnitudes and overall sign pattern are reproduced in the calculation. The calculated geometry (Fig. 11) shows a slightly more planar metal-N_2O_2 coordination for the Ni(II) complex compared to the Co(II) complex, but a similar diamine ring puckering.

Metal salbinaphthyl complexes (4). The IR and VCD spectra for metal complexes with the binaphthyl Schiff-base ligand (*R,R*)-MCl_4Salbinapht are compared for M = Co(II), Ni(II) and Zn(II) in Figure 15. The low-lying electronic transition for (*R*)-$CoCl_4$Salbinapht is observed at 2240 cm^{-1}, with positive ECD intensity. The mid-IR REVCD occurs on the low-frequency tail of the ECD, with VCD anisotropy ratios for $CoCl_4$Salbinapht on the order of 10^{-3} with the highest value of ~–5 $x10^{-3}$ at 1380 cm^{-1}. The Ni(II) and Zn(II)-Cl_4Salbinapht complexes do not have low-lying electronic transitions, and exhibit similar non-enhanced VCD intensities a factor of 10 lower than those of the Co(II) complex.

In Figure 16, the REVCD for four chiral Co(II) Schiff-base complexes are compared. Focusing on the two Salbinapht complexes, we can compare the effects of the H vs. Cl substituents at the 3-, 5-, 3'- and 5'-positions of the Schiff-base phenyl rings. For (*R*)-CoH_4Salbinapht, positive ECD is observed centered at 2540 cm^{-1}, 300 cm^{-1} higher than for $CoCl_4$Salbinapht, and the maximum REVCD anisotropy ratio is ~–5.7$x10^{-3}$ at 1318 cm^{-1}. The differences in the IR and VCD patterns for the two Salbinapht complexes reflect the different vibrational contributions from the disubstituted and tetrasubstituted phenyl rings.

Geometry and VCD calculations were carried out for CoSalbinapht in both the low-spin (doublet) and high-spin (quartet) states. The calculated optimized geometries are quite different, with the CoN_2O_2 coordination distorted planar for low-spin, and distorted tetrahedral for high-spin (Figure 17). Comparison of the observed and calculated spectra for the two spin states (Figure 18) shows better agreement with experiment for both IR and VCD for the high-spin state. Although some of the VCD sign pattern agrees with experiment, the fit is not as good as for the low-spin, approximately square planar coordination in CoSA and CoSaldiphenyl complexes shown above in Figures 5 and 13.

Effects of O_2 Binding on the REVCD for (*R*,*R*)- CoSA. Cobalt(II) salen complexes have been shown to bind oxygen reversibly in the presence of a base such as 1-methylimidazole (1-MeIm) or pyridine.[13-16] Two types of addition complexes have been considered, oxidative additions to form a monomeric species[13,16,37] with O_2^- and a dimeric species[11,12,38] with O_2^{2-} (dimer shown schematically in Scheme 2).

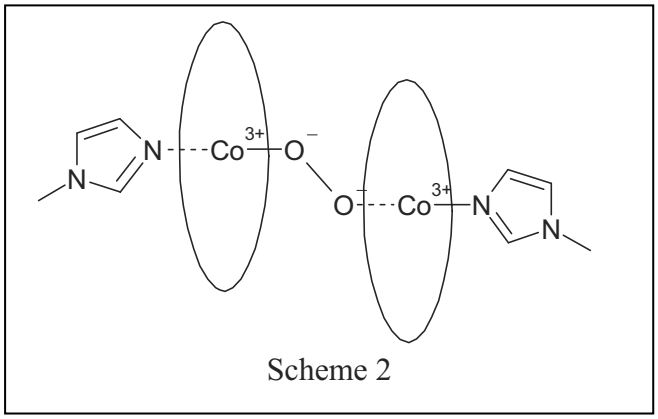

Scheme 2

In Figure 18, we show spectra for several points in the titration of (*R*,*R*)-CoSA, **1**, with 1-methyl imidazole (0 to 2 molar equivalents) in the presence of oxygen. A striking decrease in REVCD intensity is observed, concurrent with growth of IR features at 1629, 1437 and 1100 cm^{-1} and decrease in IR intensity for bands near 1600 cm^{-1}. As seen from the comparisons with and without O_2 in Figure 19, the VCD spectral changes occur only in the presence of oxygen, and with a 2-fold molar equivalent of base, the VCD intensity is reduced to a non-enhanced level. We show plots of the IR intensity at 1629 cm^{-1} and VCD intensity at 1600 cm^{-1} as a function of 1-MeIm concentration in the presence of O_2 in Figure 20. The monomer and dimer equilibria with O_2 in the presence of base and their associated equilibrium constants are

$$\mathrm{CoSA} + \text{1-MeIm} + \mathrm{O_2} \rightleftarrows \mathrm{CoSA}\cdot\text{1-MeIm}\cdot\mathrm{O_2} \tag{8}$$

$$K_1 = \frac{\left[\mathrm{CoSA}\cdot\text{1-MeIm}\cdot\mathrm{O_2}\right]}{\left[\mathrm{CoSA}\right]\cdot\left[\text{1-MeIm}\right]\cdot \mathrm{P_{O_2}}} \tag{9}$$

$$2\mathrm{CoSA} + 2(\text{1-MeIm}) + \mathrm{O_2} \rightleftarrows \left(\mathrm{CoSA}\cdot\text{1-MeIm}\right)_2\cdot\mathrm{O_2} \tag{10}$$

$$K_2 = \frac{\left[\left(\mathrm{CoSA}\bullet\text{1-MeIm}\right)_2\,\mathrm{O_2}\right]}{\left[\mathrm{CoSA}\right]^2\left[\text{1-MeIm}\right]^2 P_{\mathrm{O_2}}} \tag{11}$$

The concentration of CoSA in the solution at each point in the titration is proportional to the REVCD intensity at 1600 cm^{-1}, because the VCD of the oxygen-bound complex is not enhanced and is thus very weak at that frequency. The equilibrium constants can therefore be calculated at each point in the titration from the initial concentrations of CoSA and 1-MeIm and the CoSA concentration deduced from the VCD spectrum. For up to a 1-fold equivalent of 1-MeIm, a constant value is obtained for K_2, but not for K_1, confirming that the oxidative addition of O_2 to CoSA in the presence of base generates a μ-peroxide dimer (Scheme 2, Eq. 10) in $CDCl_3$ solution at room temperature. Above 1-fold molar equivalent base, competing equilibria, such as axial binding of two 1-MeIm molecules with the metal center, limit the formation of additional peroxide dimer. Our data suggest that at room temperature and ambient oxygen pressure, the base only binds when oxygen is present, since the VCD spectrum with two-fold molar equivalent 1-MeIm without oxygen is identical to that in the absence of 1-MeIm. The dramatic decrease in REVCD intensity during the titration is readily interpreted in terms of the oxidative addition producing a Co(III) center with no low-lying electronic states.

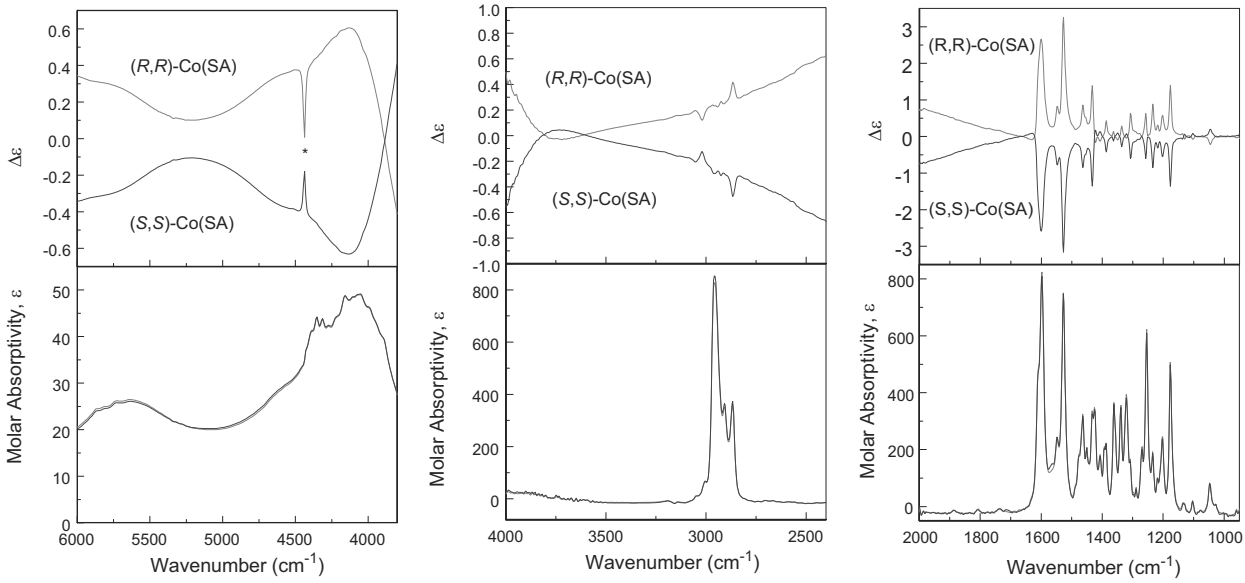

Fig. 1. Observed VCD (upper frames) and IR (lower frames) spectra of (*R,R*)-CoSA (red) and (*S,S*)-CoSA (blue) in $CDCl_3$ solution, in near-IR (left), C-H stretching (middle) and mid-IR (right) regions. Near-IR region: 31.1mg/700μL (*R,R*)- and 20.5mg/500μL (*S,S*)- in $CDCl_3$, 1 mm pathlength BaF_2 cell, 16 cm^{-1} resolution, 2 h collection, PEM optimized at 4700 cm^{-1}. C-H stretching region: 8.5mg/200μL (*R,R*)- and 9.1mg/200μL (*S,S*)- in $CDCl_3$, 92 μm pathlength BaF_2 cell, 8 cm^{-1} resolution, 4 h collection, instrument optimized at 3000 cm^{-1}. Mid-IR region: 5.4mg/154μL (*R,R*)- and 6.4mg/200μL (S,S)- in $CDCl_3$, 92 μm pathlength BaF_2 cell, 4 cm^{-1} resolution, 1 h collection, instrument optimized at 3000 cm^{-1}. Baselines corrected by subtraction of solvent spectra. VCD artifact from intense $CDCl_3$ absorbance indicated by *.

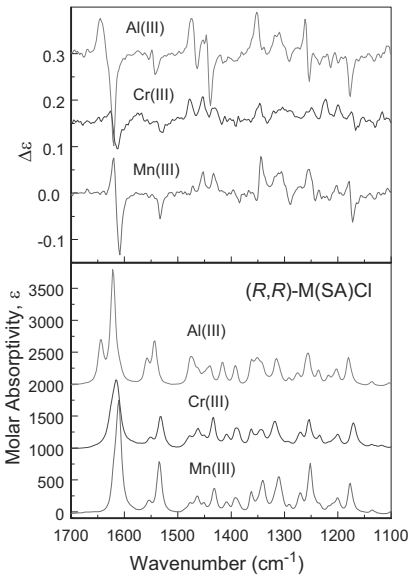

Fig. 2. Observed VCD (upper frame) and IR (lower frame) spectra of (*R,R*)-AlClSA (6.2mg/180µL, 57 mM), (*R,R*)-MnClSA (5.4mg/150µL, 54 mM) and (*R,R*)-CrClSA (6.7mg/180µL, 57 mM) in $CDCl_3$; 92 µm pathlength BaF_2 cell, instrument optimized at 1400 cm^{-1}, 4 cm^{-1} resolution and 1 h collection. Spectral baselines were corrected by subtraction of $CDCl_3$ spectra from sample spectra. Baselines corrected by subtraction of solvent spectra. Spectra of CrClSA and AlClSA are offset on molar absorptivity axis for clarity.

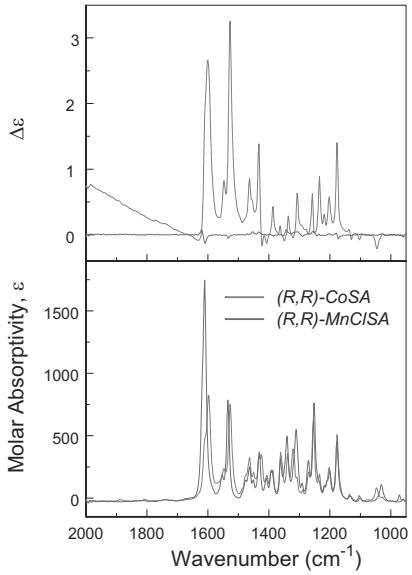

Fig. 3. Observed VCD (upper frames) and IR (lower frames) spectra of (*R,R*)-CoSA (5.4mg/154µL, 58 mM in $CDCl_3$) and (*R,R*)-MnClSA (5.4mg/150µL, 57 mM in $CDCl_3$); 92 µm pathlength BaF_2 cell, instrument optimized at 1400 cm^{-1}, 4 cm^{-1} resolution and 1 h collection. scanning. Baselines corrected by subtraction of solvent spectra.

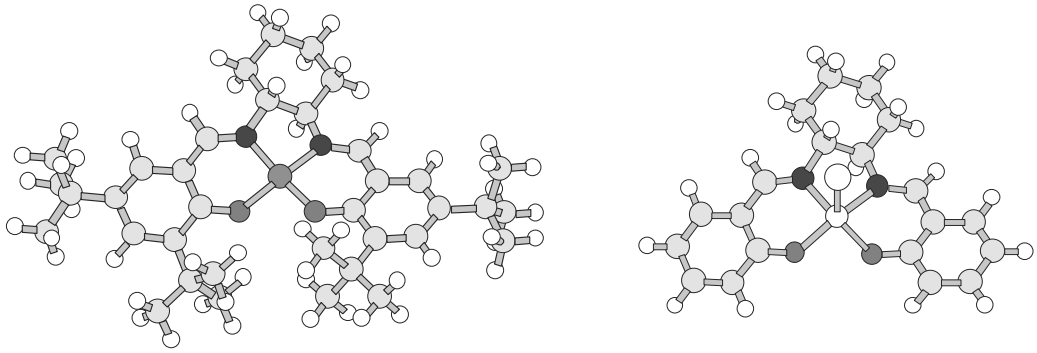

Fig. 4. Optimized structures of (*R*,*R*)-CoSA (left, B3LYP functional, Ahlrich VTZ (Co) and 6-31G(d) (ligand) basis sets) and model for (*R*,*R*)-MnClSA without *t*-butyl groups (right, B3LYP functional, LanL2DZ basis set).

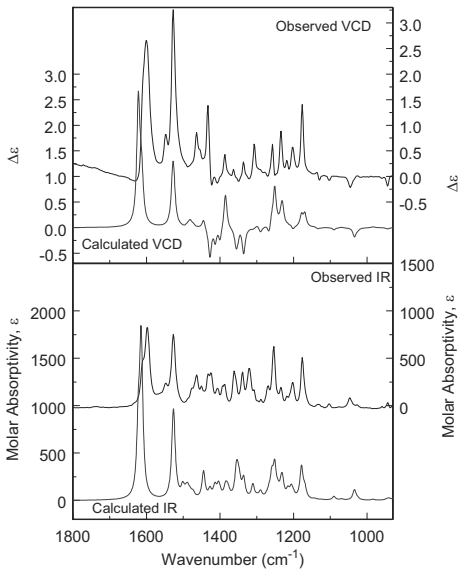

Fig. 5. Comparison of observed (right axes) and calculated (left axes) IR and VCD spectra of (*R*,*R*)-CoSA. Sample measured with a concentration of 5.4mg/154μL (58mM) in $CDCl_3$, 92 μm pathlength BaF_2 cell, 1 hour collection, 4 cm^{-1} resolution, PEM optimized at 1400 cm^{-1}. Calculation with Gaussian 03 at DFT level with B3LYP functional and 6-31G(d) basis set for the ligand and Ahlrich VTZ[24] basis set for low-spin Co(II), 5 cm^{-1} half-width, frequency scaled by 0.97.

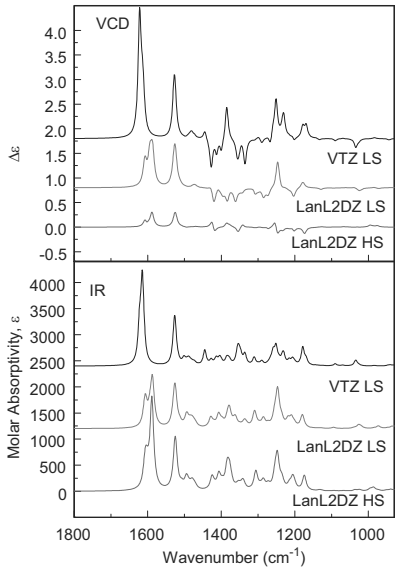

Fig. 6. Comparison of calculated IR (lower frame) and VCD (upper frame) for (*R*,*R*)-CoSA, DFT with B3LYP functional and LanL2DZ (high-spin and low-spin Co(II) and Ahlrich VTZ (Co)/6-31G(d) (ligand) basis sets, 5 cm^{-1} half-widths, frequencies scaled by 0.97.

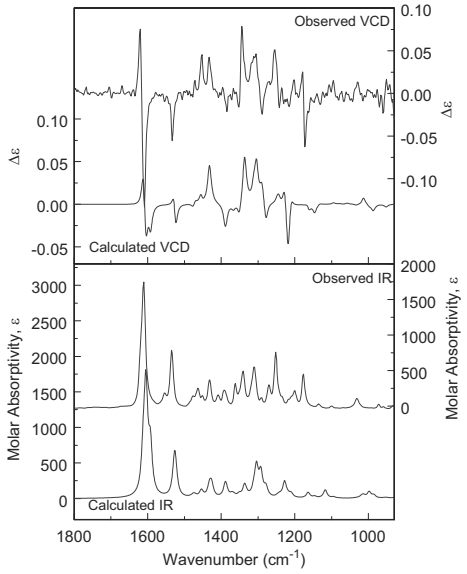

Fig. 7. Comparison of observed (right axes) and calculated (left axes) IR and VCD spectra of (*R*,*R*)-MnClSA. Sample measured with concentration 5.4mg/150μL (57 mM) in $CDCl_3$, 92 μm pathlength BaF_2 cell, instrument optimized at 1400 cm^{-1}, 4 cm^{-1} resolution and 1 h collection. Calculation with Gaussian 03 at DFT level with B3LYP functional and LanL2DZ basis set for complex without t-butyl groups.

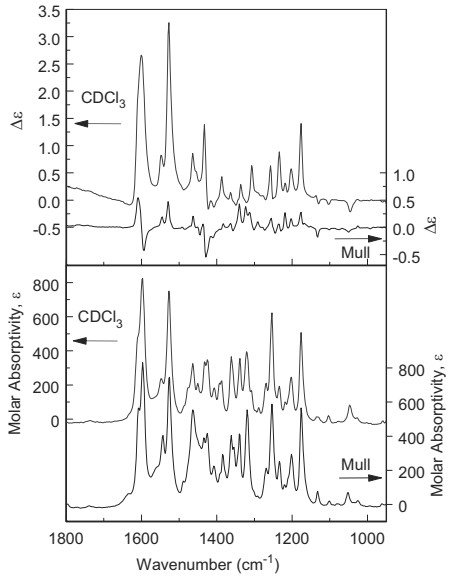

Fig. 8. IR (lower frame) and VCD (upper frame) spectra of (*R*,*R*)-CoSA in $CDCl_3$ solution (conditions as in Fig. 4, left axes) compared to mull in mineral oil (right axes, 1 h collection, 4 cm^{-1} resolution, instrument optimized at 1400 cm^{-1}, IR intensity scaled to solution and same scale factor used for mull VCD). Baselines corrected by subtraction of corresponding spectra of $CDCl_3$ or mineral oil.

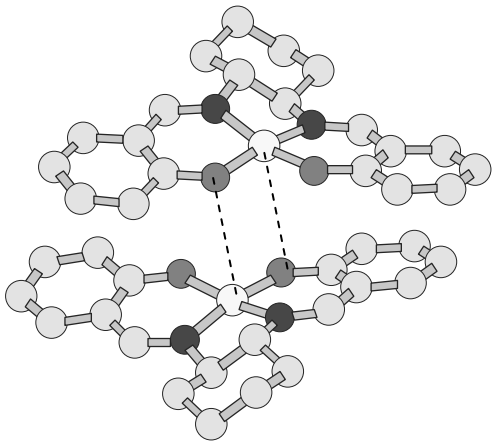

Fig. 9. Dimer of (*R*,*R*)-CoSA, from crystal structure. Hydrogens and *t*-butyl groups omitted for clarity.

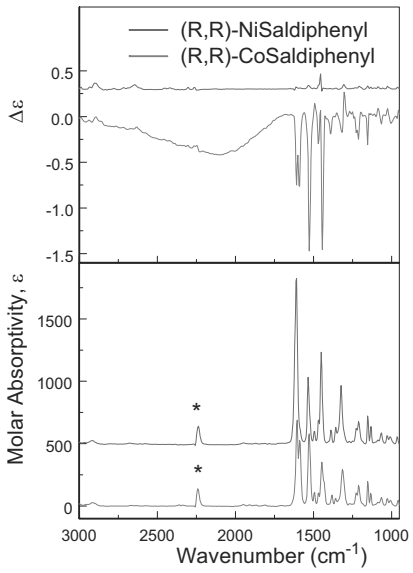

Fig. 10. Comparison of observed VCD (upper frames) and IR (lower frames) spectra of (*R,R*)-MSaldiphenyl (M = Co(II) and Ni(II), sample concentrations are ~ 0.12 M in $CDCl_3$). Spectra collected with 6 1-h blocks at 8 cm^{-1} resolution using a 54 μm pathlength cell with BaF_2 windows, and the PEM optimized at 2000 cm^{-1}. Baselines corrected by subtraction of solvent spectra. Spectra of Ni(II) complex are offset in molar absorptivity for clarity. Artifacts from intense $CDCl_3$ absorbance are indicated by *.

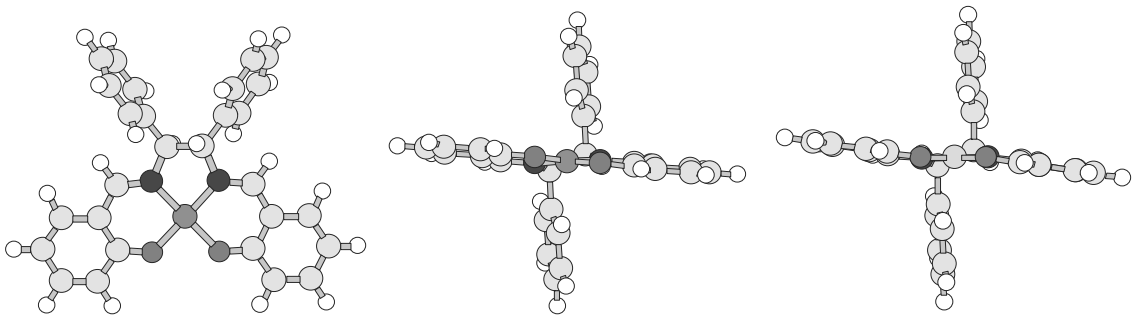

(a) (*S*,*S*)-CoSaldiphenyl equatorial (b) (*R*,*R*)-CoSaldiphenyl axial (c) (*R*,*R*)-NiSaldiphenyl axial

Fig. 11. Optimized geometries of (a) (*S*,*S*)-CoSaldiphenyl with equatorial phenyl substituents, viewed along inertial axis perpendicular to C_2-axis, and (b) (*R*,*R*)-CoSaldiphenyl and (c) (*R*,*R*)-NiSaldiphenyl with axial phenyl substituents, viewed along C_2-axis.

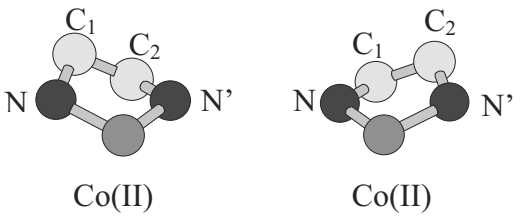

(*R*,*R*)-CoSA (*S*,*S*)-CoSaldiphenyl (equatorial) and (*R*,*R*)-CoSaldiphenyl (axial)

Fig. 12. Comparison of ring puckering in (*R*,*R*)-CoSA with that in either (*S*,*S*)-CoSaldiphenyl (equatorial phenyl conformer) or (*R*,*R*)-CoSaldiphenyl (axial phenyl conformer); structures taken from optimized DFT geometries.

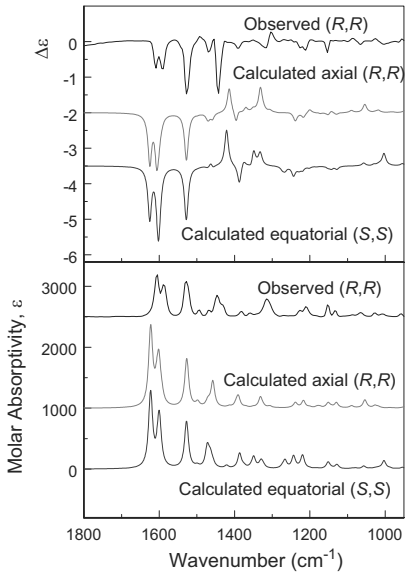

Fig. 13. Observed VCD (upper frame) and IR (lower frame) spectra of (*R,R*)-CoSaldiphenyl compared with calculated spectra of the axial conformer of (*R,R*)-CoSaldiphenyl and the equatorial conformer of (*S,S*)-CoSaldiphenyl. The observed spectra were obtained under the same conditions as in Figure 10. Calculations of the VCD and IR spectra carried out with Gaussian 03 at DFT level with B3LYP functional and 6-31G(d) basis set for C, N, O, H and Ahlrich VTZ basis set for low-spin Co(II).

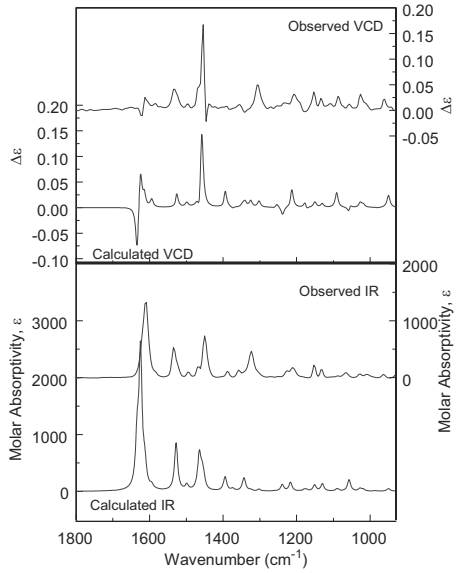

Fig. 14. Observed VCD (upper frame) and IR (lower frame) spectra of (*R,R*)-NiSaldiphenyl compared with calculated spectra of the axial conformer. The observed spectra were obtained under the same conditions as in Figure 10. Calculations of the VCD and IR spectra carried out with Gaussian 03 at DFT level with B3LYP functional and 6-31G(d) basis set for C, N, O, H and Ahlrich VTZ basis set for low-spin Ni(II).

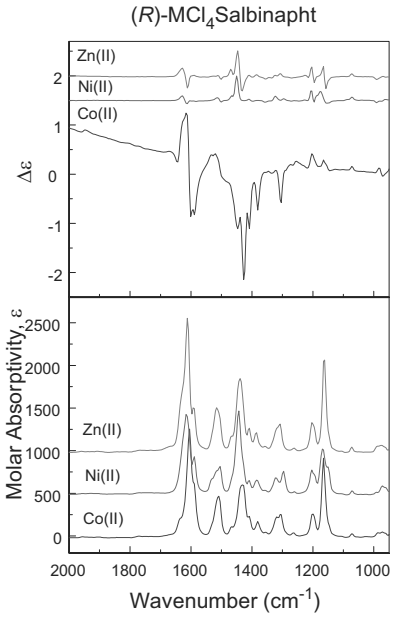

Fig. 15. Comparison of observed VCD (upper frame) and IR (lower frame) spectra of (*R,R*)-MCl_4Salbinapht (M = Co(II), Ni(II) and Zn(II), sample concentrations ~75mM in $CDCl_3$). Spectra were collected with six 1-h blocks at 8 cm^{-1} resolution using a 54 μm pathlength cell with BaF_2 windows, PEM optimized at 2000 cm^{-1}. Baselines corrected by subtraction of solvent spectra. Molar absorptivities of Zn(II) and Ni(II) complexes offset for clarity.

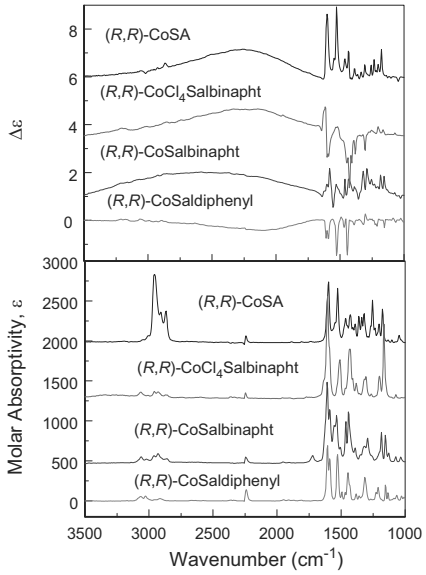

Fig. 16. Comparison of observed VCD (upper frames) and IR (lower frames) spectra of (*R,R*)-CoSaldiphenyl (0.12M), (*R*)-CoSalbinapht (95 mM), (*R*)-$CoCl_4$Salbinapht (77 mM) and (*R,R*)-CoSA (58mM) in $CDCl_3$. Spectra were collected with six 1-h blocks scanning at 8 cm^{-1} resolution using a 54 μm pathlength cell with BaF_2 windows, and the PEM optimized at 2000 cm^{-1}. Baselines corrected by subtraction of solvent spectra. Molar absorptivities offset for clarity. IR absorbance near 2250 cm^{-1} due to intense $CDCl_3$ solvent band.

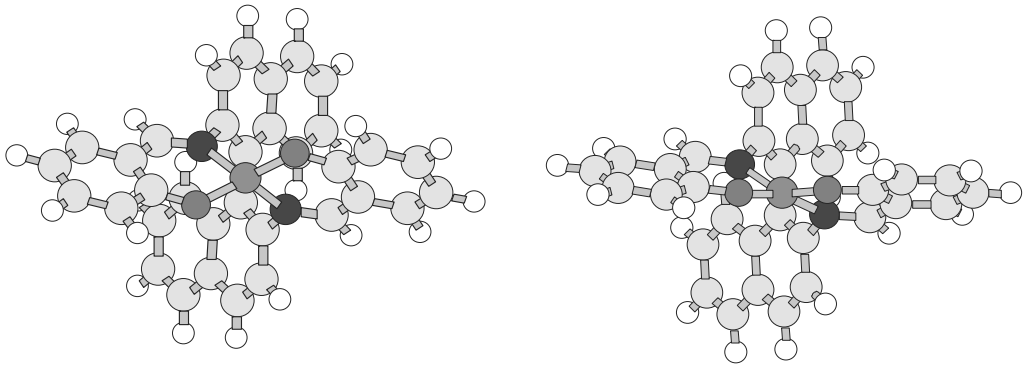

CoSalbinapht

High-spin Low-spin

Figure 17. Optimized structures of CoSalbinapht, in high- and low-spin states (Gaussian 03, DFT with B3LYP functional, 6-31G(d) basis for ligand, Ahlrichs VTZ basis for Co(II)).

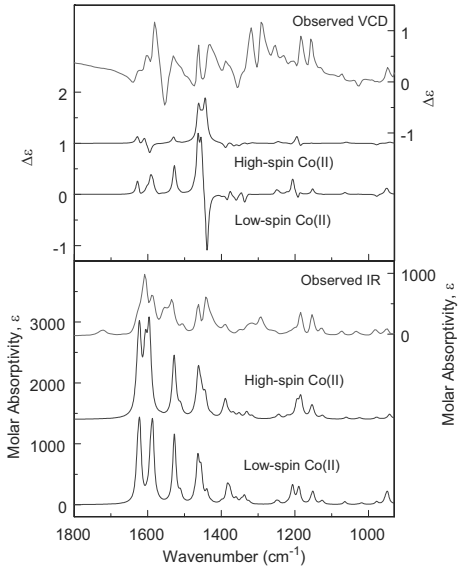

Fig. 18. Comparison of VCD (upper frame) and IR (lower frame) spectra observed for (*R*)-CoSalbinapht (right axes) with calculated spectra for the high- and low-spin Co(II) complexes (left axes). Observed spectra were obtained under conditions in Figure 16. Calculations of the VCD and IR spectra carried out with Gaussian 03 at DFT level with B3LYP functional and 6-31G(d) basis set for C, N, O, H and Ahlrich VTZ basis set for Co(II).

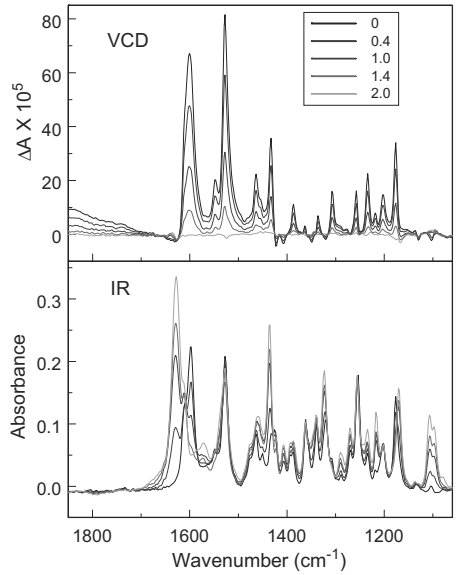

Fig. 19. Observed VCD (upper frame) and IR (lower frame) spectra of (R,R)-CoSA (30 mM) equilibrated with 0 to 2 molar equivalents of 1-methylimidazole as indicated, in the presence of O_2; 0.10 mm pathlength BaF_2 cell, 1 hour collection, 4 cm^{-1} resolution, PEM optimized at 1400 cm^{-1}. Spectral baselines corrected by subtracting solvent spectra.

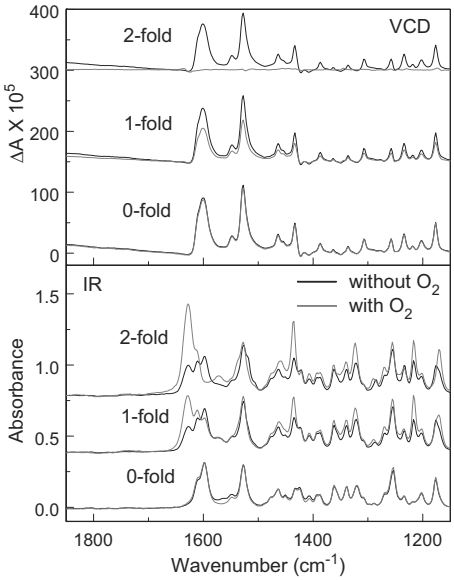

Fig. 20. Observed VCD (upper frame) and IR (lower frame) spectra of (*R,R*)-CoSA (30 mM) with 0, 1 and 2 fold of 1-methylimidazole with (red curves) and without (black curves) the presence of O_2. The spectra (optimized at 1400 cm^{-1}) were collected at 4 cm^{-1} resolution, 0.1 mm pathlength cell with BaF_2 windows, 1-h collection for solvent and sample. Spectral baselines corrected by subtracting solvent spectra. Spectra are offset in molar absorptivity for clarity.

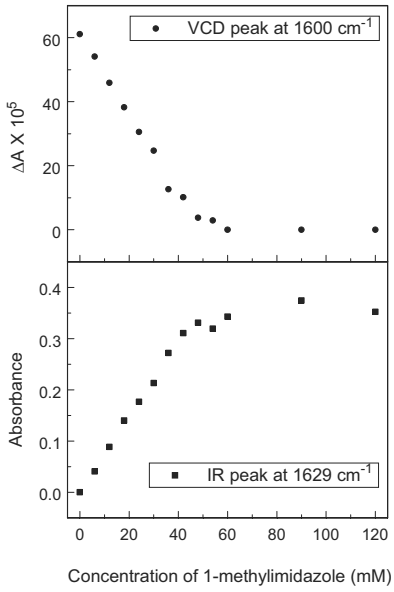

Fig. 21. Observed VCD intensity at 1600 cm^{-1} (upper frame) and IR intensity at 1629 cm^{-1} (lower frame) of (*R,R*)-CoSA in $CDCl_3$(30mM) equilibrated with various concentrations of 1-methylimidazole in the presence of O_2.

References

1. Freedman, T. B.; Cao, X.; Dukor, R. K.; Nafie, L. A. *Absolute configuration determination of chiral molecules in the solution state using vibrational circular dichroism*, *Chirality* **2003**, *15*, 743-758.
2. Stephens, P. J.; Devlin, F. J. *Determination of the structure of chiral molecules using ab initio vibrational circular dichroism spectroscopy*, *Chirality* **2000**, *12*, 172-179.
3. He, Y.; Cao, X.; Nafie, L. A.; Freedman, T. B. *Ab Initio VCD Calculation of a Transition-Metal Containing Molecule and a New Intensity Enhancement Mechanism for VCD*, *J. Am. Chem. Soc.* **2001**, *123*, 11320-11321.
4. Mason, S. F.; Peacock, R. D. *Complexes of Some First-row Transition Elements with (-)-Spartein*, *J. Chem. Soc. Dalton* **1973**, 226-229.
5. Bormett, R. W.; Asher, S. A.; Larkin, P. J.; Gustafson, W. G.; Ragunathan, N.; Freedman, T. B.; Nafie, L. A.; Balasubramanian, S.; Boxer, S. G.; Yu, N.-T.; Gersonde, K.; Noble, R. W.; Springer, B. A.; Sligar, S. G. *Selective Examination of Heme Protein Azide Ligand-Distal Globin Interactions by Vibrational Circular Dichroism*, *J. Am. Chem. Soc.* **1992**, *114*, 6864-6867.
6. Teraoka, J.; Nakamura, K.; Nakahara, Y.; Kyogoku, Y.; Sugeta, H. *Extraordinarily Intense Vibrational Circular Dichroism of a Metmyoglobin Cyanide Complex*, *J. Am. Chem. Soc.* **1992**, *114*, 9211-9213.
7. Che, C.-M.; Huang, J.-S. *Metal complexes of chiral binaphthyl Schiff-base ligands and their application in stereoselective organic transformations*, *Coord. Chem. Rev.* **2003**, *242*, 97-113.
8. Larrow, J. F.; Jacobsen, E. N. *Asymmetric Processes Catalyzed by Chiral (Salen)Metal Complexes*, *Topics Organomet. Chem.* **2004**, *6*, 123-152.
9. Bernardo, K.; Leppard, S.; Robert, A.; Commenges, G.; Dahan, F.; Meunier, B. *Synthesis and Characterization of New Chiral Schiff Base Complexes with Diimminobinaphthyl or Diiminocyclohexyl Moieties as Potential Enantialselective Epoxidation Catalysts*, *Inorg. Chem.* **1996**, *35*, 387-396.
10. Tsumaki, T. *Co.ovrddot.ordinate valency rings. IV. Some inner complex salts of hydroxyaldimines*, *Bulletin of the Chemical Society of Japan* **1938**, *13*, 252-60.
11. Floriani, C.; Calderazzo, F. *Oxygen adducts of Schiff base complexes of cobalt prepared in solution*, *Journal of the Chemical Society [Section] A: Inorganic, Physical, Theoretical* **1969**, 946-53.68 FIELD Section Title:Phase Equilibriums, Chemical Equilibriums, and Solutions
Cyanamid Eur. Res. Inst.,Cologny,Switz. FIELD URL:
written in English.
12. Calligaris, M.; Nardin, G.; Randaccio, L.; Ripamonti, A. *Structural aspects of the synthetic oxygen-carrier N,N'-ethylenebis(salicylideneiminato)cobalt(II): structure of the addition compound with oxygen containing dimethylformamide*, *Journal of the Chemical Society [Section] A: Inorganic, Physical, Theoretical* **1970**, 1069-74.70 FIELD Section Title:Crystallization and Crystal Structure
Ist. Chim.,Univ. Trieste,Trieste,Italy. FIELD URL:
written in English.
13. Fiammengo, R.; Bruinink, C. M.; Crego-Calama, M.; Reinhoudt, D. N. *Noncovalent Secondary Interactions in Co(II)Salen Complexes: O_2 Binding and Catalytic Activity in Cyclohexane Oxygenation*, *J. Org. Chem.* **2002**, *67*, 8552-8557.
14. Nakamoto, K.; Nonaka, Y.; Ishiguro, T.; Urban, M. W.; Suzuki, M.; Kozuka, M.; Nishida, Y.; Kida, S. *Resonance Raman and Infrared Spectra of Molecular Oxygen Adducts of N,N'-ethylenebis(2,2-diacetylenthyideneaminato)cobalt(II)*, *J. Am. Chem. Soc.* **1982**, *104*, 3386-3391.

15. Nakamoto, K.; Susuki, M.; Ishiguro, T.; Kozuka, M.; Nishida, Y.; Kida, S. *Resonance Raman Spectra of Molecular Oxygen Aducts of N,N'-Ethylenebis(salicylideniminato)cobalt(II), [BCo(salen)]$_2O_2$ (B = Pyridine, Pyridine N-Oxide, and Dimethylformamide)*, *Inorg. Chem.* **1980**, *19*, 2822-2824.
16. Djebbar-Sid, S.; Benali-Baitich, O.; Deloume, J. P. *Synthesis, characterization, and electrochemical behaviour of cobalt(II) and cobalt(III):O_2^- complexes, respectively, with linear and tripodal tetradentate lignads derived from Schiff bases*, *J. Molec. Struct.* **2001**, *569*, 121-128.
17. Cheeseman, J. R.; Frisch, M. J.; Devlin, F. J.; Stephens, P. J. *Ab initio calculations of atomic axial tensors and vibrational rotational strengths using density functional theory*, *Chem. Phys. Lett.* **1996**, *252*, 211-220.
18. Frisch, M. J.; Trucks, G. W.; Schlegel, H. B.; Scuseria, G. E.; Robb, M. A.; Cheeseman, J. R.; J. A. Montgomery, J.; Vreven, T.; Kudin, K. N.; Burant, J. C.; Millam, J. M.; Iyengar, S. S.; Tomasi, J.; Barone, V.; Mennucci, B.; Cossi, M.; Scalmani, G.; Rega, N.; Petersson, G. A.; Nakatsuji, H.; Hada, M.; Ehara, M.; Toyota, K.; Fukuda, R.; Hasegawa, J.; Ishida, M.; Nakajima, T.; Honda, Y.; Kitao, O.; Nakai, H.; Klene, M.; Li, X.; Knox, J. E.; Hratchian, H. P.; Cross, J. B.; Adamo, C.; Jaramillo, J.; Gomperts, R.; Stratmann, R. E.; Yazyev, O.; Austin, A. J.; Cammi, R.; Pomelli, C.; Ochterski, J. W.; Ayala, P. Y.; Morokuma, K.; Voth, G. A.; Salvador, P.; Dannenberg, J. J.; Zakrzewski, V. G.; Dapprich, S.; Daniels, A. D.; Strain, M. C.; Farkas, O.; Malick, D. K.; Rabuck, A. D.; Raghavachari, K.; Foresman, J. B.; Ortiz, J. V.; Cui, Q.; Baboul, A. G.; Clifford, S.; Cioslowski, J.; Stefanov, B. B.; Liu, G.; Liashenko, A.; Piskorz, P.; Komaromi, I.; Martin, R. L.; Fox, D. J.; Keith, T.; Al-Laham, M. A.; Peng, C. Y.; Nanayakkara, A.; Challacombe, M.; Gill, P. M. W.; Johnson, B.; Chen, W.; Wong, M. W.; Gonzalez, C.; Pople, J. A. *Gaussian 03*; Gaussian, Inc., Pittsburgh, PA, Revision B.03
19. Hoshina, G.; Tsuchimoto, M.; Ohba, S. *[N,N'-Bis(salicylidene)-1,2-diphenyl-(RS,SR)-1,2-ethanediaminato]-nickel(II)*, *Acta Cryst.* **2000**, *C56*, e122.
20. Nafie, L. A. *Dual polarization modulation: a real-time, spectral-multiplex separation of circular dichroism from linear birefringence spectral intensities*, *Appl. Spectrosc.* **2000**, *54*, 1634-1645.
21. Nafie, L. A.; Dukor, R. K. *The use of dual polarization modulation in vibrational circular dichroism spectroscopy*, *ACS Symposium Series* **2002**, *810*, 79-88.
22. Nafie, L. A.; Dukor, R. K.; Roy, J.-R.; Rilling, A.; Cao, X.; Bulis, H. *Observation of Fourier Transform Near-infrared Vibrational Circular Dichroism to 6150 cm^{-1}*, *Appl. Spectrosc.* **2003**, *57*, 1245-1249.
23. Cao, X.; Shah, R. D.; Dukor, R. K.; Guo, C.; Freedman, T. B.; Nafie, L. A. *Extension of Fourier transform vibrational circular dichroism into the near-infrared region: Continuous spectral coverage from 800 to 10000 cm-1*, *Applied Spectroscopy* **2004**, *58*, 1057-1064.
24. Schaefer, A.; Horn, H.; Ahlrichs, R. *Fully optimized contracted Gaussian basis sets for atoms lithium to krypton*, *J. Chem. Phys.* **1992**, *97*, 2571-7.
25. Dunning, T. H., Jr.; Hay, P. J. In Modern Theoretical Chemistry; Schaefer, H. F., III, Ed.; Plenum: New York, 1976; Vol. 3, pp 1-28.
26. Hay, P. J.; Wadt, W. R. *Ab initio effective core potentials for molecular calculations. Potentials for the transition metal atoms scandium to mercury*, *J. Chem. Phys.* **1985**, *82*, 270-83.
27. Stephens, P. J. *Theory of vibrational circular dichroism*, *J. Phys. Chem.* **1985**, *89*, 748-52.

28. Bak, K. L.; Devlin, F. J.; Ashvar, C. S.; Taylor, P. R.; Frisch, M. J.; Stephens, P. J. *Ab Initio Calculation of Vibrational Circular Dichroism Spectra Using Gauge-Invariant Atomic Orbitals*, *Journal of Physical Chemistry* **1995**, *99*, 14918-22.
29. Stephens, P. J.; Devlin, F. J.; Aamouche, A. *Determination of the structures of chiral molecules using Vibrational Circular Dichroism spectroscopy*, *ACS Symposium Series* **2002**, *810*, 18-33.
30. Nafie, L. A.; Freedman, T. B. *Vibrational Optical Activity Theory,* In Circular Dichroism, Principles and Applications (2nd Edition); Berova, N., Nakanishi, K. and Woody, R. W., Ed.; Wiley: New York, 2000, pp 97-131.
31. Nafie, L. A.; Freedman, T. B. *Vibronic Coupling Theory of Infrared Vibrational Intensities*, *J. Chem. Phys.* **1983**, *78*, 7108-7116.
32. Nafie, L. A. *Generalized Theory of Vibrational Circular Dichroism and Infrared Absorption: Extension to Include Molecules with Low-Lying Electronic States*, *J. Phys. Chem A* **2004**, *108*, 7222-7231.
33. Nafie, L. A. *Adiabatic Behavior Beyond the Born-Oppenheimer Approximation. Complete Adiabatic Wavefunctions and Vibrationally Induced Electronic Current Density*, *J. Chem. Phys.* **1983**, *79*, 4950-4957.
34. Neugebauer, J.; Baerends, E. J.; Efremov, E. V.; Ariese, F.; Cooijer, C. *Combined Theoretical and Experimental Deep-UV Resonance Raman Studies of Substituted Pyrenes*, *J. Phys. Chem. A* **2005**, *109*, 2100-2106.
35. Freedman, T. B.; Cao, X.; Young, D. A.; Nafie, L. A. *Density Functional Theory Calculations of Vibrational Circular Dichroism in Transition Metal Complexes: Identification of Solution Conformations and Mode of Chloride Ion Association for (+)-Tris(ethylenediaminato)cobalt(III)*, *J. Phys. Chem. A* **2002**, *106*, 3560-3565.
36. Holt, S. L.; DeIasi, R.; Post, B. *Crystal structure of the oxygen-inactive form of bis(salicylaldehyde)ethylenediiminecobalt(II)*, *Inorganic Chemistry* **1971**, *10*, 1498-500.
37. Huber, A.; Muller, L.; Elias, H.; Klement, R.; Valco, M. *Cobalt(II) Complexes with Substituted Salen-Type Ligands and Their Dioxygen Affinity in N,N-Dimethylformamide at Various Temperatures*, *Eur. J. Inorg. Chem.* **2005**, 1459-1467.
38. Hester, R. E.; Nour, E. M. *Resonance Raman Studies of Transition Metal Peroxo Complexes*, *J. Raman. Spectrosc.* **1981**, *11*, 49-58.